

Effects of Controlled Three-Dimensional
Perturbations on Boundary Layer
Transition

Thesis by
Steven Philip Schneider

In Partial Fulfillment of the Requirements
for the Degree of
Doctor of Philosophy

California Institute of Technology
Pasadena, California
1989
(Submitted March 10, 1989)

Acknowledgements

This work could not have been completed without the help and encouragement of many. I owe a debt of gratitude to all who helped, only some of whom it is possible to name here. Foremost among these is my advisor, Professor Hans W. Liepmann, whose direction, encouragement, and incisive advice has been a continual source of inspiration. After Dr. Liepmann took mandatory official retirement, Professor Anatol Roshko and then Professor Donald Coles were gracious enough to take over as my official advisor. Dr. Coles became more than an official advisor, giving generously of his time, advice, and encouragement. In particular, all through the course of the investigation, Dr. Coles has been a constant source of advice for mechanical design and general experimental design.

I am also indebted to many members of the GALCIT staff for their generous assistance and encouragement. George Lundgren, Howard McDonald, and Phil Wood of the Aeronautics shop have contributed a great deal of mechanical design assistance and encouragement. They also fabricated nearly all the hardware used. Herb Gaebler of the Hydrodynamics Lab has also been very helpful with the design and construction of mechanical hardware, as well as a patient instructor concerning the ins and outs of the FSWT¹ and its associated hardware. Harry Hamaguchi taught me some of the techniques of photography, while discussing and carrying out the photographic work involved in the project. Florence Kovacic, Jeri Chittum, Marcia Hudson, and Kathy Eriksen have made purchase orders, petty cash reimbursements, contract accounting, and the various other paper elements of the project go

¹Free Surface Water Tunnel

smoothly and easily. Betty Wood has drawn all the figures that were not produced on an automatic plotter. Jean Anderson has patiently searched out and provided many references. Many other staff members also contributed.

The following people have made special, specific contributions: Howard McDonald machined the flat plate model, and also contributed to its design. The late Professor Lester Lees helped form many of my early conceptions of boundary layer transition. His manner was always straightforward and encouraging. Dr. Thomas Sobota invested some of his time in encouraging and assisting me with the procurement of the power op-amps used in the redesign of the 32 channel power amplifier. My thesis follows the thesis of Dr. Harry Robey, who generously assisted my efforts to understand and rebuild his experiment. John Lee provided crucial assistance with the design and construction of nearly every piece of electronic equipment used. Dr. Les Mack of JPL provided a wide variety of his linear instability theory results, in machine-readable form.

Finally, I owe personal thanks to my parents and my wife, Lynette, for their support and encouragement. I also thank the good Lord, who gave me the love of learning and the curiosity to undertake this project, and the stubbornness to finish it.

Funding for this project was provided by the Office of Naval Research, under contracts #N00014-85-K-0205 and #N00014-87-K-0100.

Abstract

The laminar-turbulent transition in a flat plate boundary layer was studied experimentally using a spanwise array of computer-controlled surface heating elements. The elements were used to introduce disturbances at a point just downstream of the critical Reynolds number. When sinusoidal heating at an unstable frequency is carried out, instability waves develop and grow as they travel downstream. Measurements were made using flush-mounted hot-film wall shear sensors, and the later stages of transition were visualized using dye injection. Oblique Tollmien-Schlichting waves were successfully introduced, and their downstream development into the turbulent regime was studied. Exploratory studies of other types of 3D forcing are also reported.

Measurements of oblique waves in the linear region yielded phase speeds and wave angles that were consistent with the linear theory. Subharmonics of the oblique-wave wall shear were seen downstream, in the nonlinear region. Surprisingly, the amplitude of these subharmonic waves decreased abruptly with increasing oblique-wave angle, so that an oblique wave of about 10 degrees had a subharmonic amplitude which was an order of magnitude below that for a 2D wave. Waves of larger oblique angles did not produce detectable subharmonics. A simple explanation of this behavior is given, in terms of the wave-interaction theory.

The intermittency, defined as the fraction of time in which the wall shear is turbulent, was measured to determine the relative location of transition. These measurements, carried out further downstream, show that the introduction of a 2D wave is most effective in moving the transition point

upstream, for a given power input. This upstream movement of transition slowly decreases as the oblique wave angle is increased. The fact that there is no abrupt movement of transition corresponding to the abrupt disappearance of the subharmonic nonlinear breakdown mechanism suggests there should be a simpler explanation for the nonlinear breakdown.

Contents

Acknowledgements	ii
Abstract	iv
List of Figures	ix
List of Tables	xii
List of Symbols	xiii
1 Introduction	1
1.1 The Laminar-Turbulent Transition in Boundary Layers	1
1.2 An Overall Sketch of the Boundary Layer Transition Process	3
1.3 Three-Dimensional Effects in Boundary Layer Transition . . .	6
1.4 Apparatus for Introducing Controlled Three-Dimensional Perturbations	11
2 Experimental Apparatus	13
2.1 Water Tunnel	13
2.2 Flat Plate Model	15
2.3 Forcing Apparatus	15
2.4 Sensing Apparatus	18
2.5 Flow Visualization	20
2.6 Experimental Procedure	21
2.7 Discussion of Experimental Errors	22
3 Experimental Results and Discussion	25
3.1 Introduction	25
3.2 'Natural' Transition	25
3.2.1 Development of Natural Waves with Downstream Dis- tance	26
3.2.2 Two-Dimensionality of Natural Waves	32
3.3 Transition Caused by Oblique Wave Forcing	36
3.3.1 Linear Oblique Waves	37

3.3.1.1	Wave Amplitudes	37
3.3.1.2	Phase Speeds	49
3.3.1.3	Measured Angles	61
3.3.2	Nonlinear Oblique Waves	67
3.3.2.1	Higher Harmonics	69
3.3.2.2	Subharmonics	76
3.3.3	Late Nonlinear Region	85
3.3.4	Intermittent Region	87
3.4	Transition Caused by Forcing of Other Wave Patterns	89
3.4.1	Short Spatial Wavelength Patterns	93
3.4.1.1	Even/Odd Forcing	93
3.4.1.2	Pair Forcing	96
3.4.2	Long Spatial Wavelength Patterns	104
3.4.2.1	Half-Sine Distributed Amplitude Forcing	104
3.4.2.2	Bent Wave Forcing	105
3.4.2.3	Amplitude Jump Forcing	108
4	Summary of Results	110
	References	113
	Appendices:	
A	Detailed Description of Experimental Apparatus	118
A.1	General Apparatus and Procedures	118
A.1.1	Segmented Flat Plate Model	118
A.1.2	Experimental Control and Data Acquisition Program	121
A.2	Heating Apparatus for Introducing Perturbations	123
A.2.1	Computer-Controller Interface	123
A.2.2	Heater Array Signal Controller	126
A.2.3	32 Channel Power Amplifier	129
A.2.4	High-Current DC Power Supplies	133
A.2.5	Heater Array	134
A.2.6	Measurements of Perturbation Electronics Performance	138
A.2.6.1	Heater controller performance	138
A.2.6.2	Heater power output performance	143
A.3	Sensing Apparatus for Measuring Behavior	153
A.3.1	Hot Film Anemometer	153
A.3.2	Isolation Amplifier for Monitoring Heaters	157
A.3.3	Signal Conditioning and Data Acquisition	159
A.3.4	Pressure Transducer	161

B	Detailed Description of Experimental Procedures	164
B.1	Measurement of Freestream Turbulence	164
B.2	Calibration of Wall Shear Sensors	169
C	Detailed Description of Analysis Methods	175
C.1	Computation of Leading Edge Pressure Gradient Effects . . .	175
C.2	Computation of Intermittency	182
C.3	Computation of Power Spectra and Peak Amplitudes	185

List of Figures

1.1	Cartoon of Boundary Layer Transition	4
1.2	Oblique Wave Geometry	8
2.1	Free Surface Water Tunnel Schematic	14
2.2	Flat Plate Model Schematic: First Configuration	16
2.3	Block Diagram of Electronics	17
2.4	Flat Plate Model Schematic: Second Configuration	23
3.1	Linear Theory Amplification Rate Contours	27
3.2	Shear Trace of Natural Waves at S7, $Re_{\delta^*} = 1400$	28
3.3	Autocorrelation of Natural Instability Waves at S7	30
3.4	Spectra of Instability Waves at Four Streamwise Locations	31
3.5	Reduced Spectra of Natural Instability Waves	33
3.6	Naturally Occurring Waves at Two Spanwise Locations	34
3.7	Cross-Correlation of Shear at Three Spanwise Locations	35
3.8	Wall Shear Spectra in Linear Region at $Re_{\delta^*} = 1100$	38
3.9	Growth of Oblique Waves on Different Days	40
3.10	Growth of Oblique Waves vs. Downstream Distance	41
3.11	Amplitude of Oblique Waves for Different Forcing Amplitudes	42
3.12	Wall Shear Spectra at $Re_{\delta^*} = 1150$	44
3.13	Wall Shear Spectra at $Re_{\delta^*} = 1350$	45
3.14	Primary Response Amplitude vs. Forcing Power	47
3.15	Growth Rate of Primary Response vs. Wave Amplitude	48
3.16	Growth Rate of Waves Created with Same Forcing on Different Days	50
3.17	Cross-Correlation of Low Reynolds Number Phase Speed Data	53
3.18	Cross-Correlations for Extreme Frequency Data	54
3.19	Phase Speeds for Oblique Waves at $Re_{\delta^*} = 1100$	55
3.20	Linear Theory Results for Streamwise Phase Speeds	56
3.21	Cross-Correlation for High Reynolds Number Phase Speed Data	58
3.22	Streamwise Phase Speeds at $Re_{\delta^*} = 1400$	59
3.23	Typical Cross-Correlations for Nearby Sensor Wave Angle Data	62
3.24	Wave Angle Phase Lags for Nearby Sensors	63
3.25	Typical Cross-Correlations for $Re_{\delta^*} = 1300$ Wave Angle Data	64

3.26	Average Phase Shifts vs. Angle for Oblique Waves	66
3.27	Wall Shear Spectra for Highly Nonlinear Waves	68
3.28	Wall Shear Spectra Showing Second Harmonics	71
3.29	Amplitude of Second Harmonics vs. Primary	72
3.30	Amplitude of Primary and Second Harmonic vs. Angle	73
3.31	Time Trace of Nonlinear 2D Wave Showing Second Harmonic	75
3.32	Change in Subharmonic Amplitude with Surface Wave Damping	79
3.33	Primary and Subharmonic vs. Forcing Level	80
3.34	Decrease in Subharmonic Amplitude with Angle	82
3.35	Breaking of Triad Resonance for Oblique Primary Waves	83
3.36	Time Trace of Wall Shear for Late Nonlinear Wave	86
3.37	Photographs of Transition With and Without Forcing	88
3.38	Movement of Transition Caused by Oblique Wave Forcing	90
3.39	Sketch of Wave Patterns for 3D Forcing	92
3.40	Primary and Subharmonic Response to Even/Odd Forcing	95
3.41	Spectra for 2D Wave with Centerline Defect	98
3.42	Primary and Subharmonic Response to Centerline Defect	99
3.43	Nonlinear Response for Strong Centerline Pair Forcing	100
3.44	Spectra for Pair Forcing at Varied Spanwise Locations	102
3.45	Primary and Subharmonic Response to Pair Location	103
3.46	Subharmonic and Primary Response to Sine Wave in Amplitude	106
3.47	Primary Response to Bent Wave Forcing	107
3.48	Primary and Subharmonic Response to Amplitude Jump Forcing	109
A.1	Computer-Controller Interface Schematic	124
A.2	Heater Signal Controller Schematic	127
A.3	Old 32 Channel Power Amplifier Schematic	130
A.4	32 Channel Power Amplifier Schematic	131
A.5	Photograph of Heater Array	135
A.6	Controller Phase Shift Performance	140
A.7	Controller RMS Phase Shift Performance	141
A.8	Worst Case Performance of Mean Controller Phase Shifts	142
A.9	RMS DC Offset Errors for Controller and Power Amplifier	145
A.10	Quadratic Variation of Power Output with Instruction	148
A.11	Uniformity of Power Distribution Among Heaters	150
A.12	Hardnuts II Hot Film Anemometer Schematic	155
A.13	Pressure Transducer Calibrations	163
B.1	Spectrum of Freestream Turbulence in FSWT	168

B.2	Sample Calibration of Wall Shear Sensors	171
C.1	Surface Velocity Computed for Flat Plate Leading Edge	178
C.2	Falkner-Skan β for Flat Plate Leading Edge	179
C.3	Boundary Layer Thickness Corrected for Leading Edge	181
C.4	PDF of Shear for Intermittent Signal	184
C.5	Comparison of Intermittency Computation Procedures	186

List of Tables

3.1	Maxima vs. Frequency at Three Streamwise Locations	43
3.2	Wave Angles vs. Phase Lag Instruction for Oblique Waves . .	69
A.1	Power Output vs. Oblique Wave Angle	146
A.2	Power per Heater for Different 2D Forcing Levels	149
A.3	Typical Raw RMS Heater Voltage Record	151
A.4	Raw Voltage Proportional to Positive Current in Heater #1 .	152

List of Symbols

English Symbol	Definition
$^{\circ}C$	degrees Celsius
\vec{c}_{phase}	phase velocity
$c_{phase,x}$	phase speed in the x-direction
c_0	a constant
f	frequency, Hz
f_v	frequency of voltage forcing signal, Hz
F	nondimensional frequency, $F = (\omega\nu)/U_{\infty}^2$
\vec{i}	streamwise unit vector
\vec{j}	unit vector perpendicular to the wall
\vec{k}	spanwise unit vector
R	a Reynolds number
Re_x	$U_{\infty}x/\nu$, a Reynolds number
Re_{δ^*}	$U_{\infty}\delta^*/\nu$, another Reynolds number
t	time
u	streamwise velocity component
\vec{u}	fluid velocity
U_{∞}	freestream velocity
v	vertical velocity component
V	a voltage
w	spanwise velocity component
\vec{x}	vector of spatial coordinates
x	streamwise coordinate
y	coordinate perpendicular to the wall
z	spanwise coordinate

Greek Symbol	Definition
α	streamwise wavenumber
β	Falkner-Skan pressure gradient parameter, or spanwise wavenumber
δ^*	boundary layer displacement thickness
ϵ	a small number
θ	angle of oblique wave
$\vec{\kappa}$	wave number vector
λ	wavelength
μF	10^{-6} Farads
ν	kinematic viscosity
τ	fluid shear at the wall
ϕ	a phase shift
ϕ_v	phase shift in voltage signal
ω	angular frequency

Subscript	Definition
ζ_r	real part of ζ
ζ_i	imaginary part of ζ

Mathematical Operation	Definition
$\bar{\zeta}$	$\frac{1}{T} \int_0^T \zeta(t) dt$
ζ'	$\zeta - \bar{\zeta}$
ζ_{rms}	$\sqrt{\overline{\zeta'^2}}$
Correlation(ζ, η)	$\frac{1}{\zeta_{rms}\eta_{rms}} \frac{1}{T} \int_0^T \zeta(t)\eta(t + \tau) dt$
$\Re(\zeta)$	real part of ζ
\approx	approximately equal to
<i>h.o.t.</i>	higher order terms (in an expansion)

Chapter 1

Introduction

1.1 The Laminar-Turbulent Transition in Boundary Layers

The laminar-turbulent transition in boundary layers is a topic of great practical importance, due to the very different properties of the two boundary layer types. In a turbulent boundary layer, there is much more mixing between the fluid near the wall and the freestream fluid. This mixing makes for higher skin friction drag and higher heat transfer. It also makes the turbulent boundary layer much less likely to separate from the wall in an adverse pressure gradient. The ability to control these properties, through control of the position of the transition between the two types of flow, can be crucial to the design of everything from aircraft to lasers.

Better methods for controlling transition depend on improvements in our fundamental understanding of the transition process. Unfortunately, this understanding is still poor, despite the significant progress made by the many workers in this field; this can be seen from the fact that there is still no well-grounded method for predicting transition point location, even for a two-dimensional airfoil. Recent reviews of the extensive literature concerning wall-bounded shear flow transition can be found in Bayly and Orszag [1], Herbert [12], Kozlov and Levchenko [23], Narasimha [31], and Stuart [42]. Only a brief summary of the closely relevant elements of the literature will

be attempted here.

The first fundamental theory of boundary layer transition, developed by Prandtl's school in Germany, described the process in terms of the instability of small fluctuations in an idealized boundary layer, with disturbances of the form

$$\vec{u} = \Re \left(\vec{u}(y) e^{i(\alpha x + \beta z - \omega t)} \right).$$

A linearized eigenvalue equation for the stability of these waves, the celebrated Orr-Sommerfeld equation, was derived and solved. This work was done during the first third of the 20th century. The small fluctuations consist of simple linearized small-amplitude waves, with straight constant phase lines in the plan view, both two-dimensional and oblique. After Squire [41] showed that the two-dimensional waves become unstable at a lower Reynolds number than any oblique wave, work concentrated on the two-dimensional waves.

The instability theory was poorly accepted until the landmark experiments of Schubauer and Skramstad [38], who for the first time had available a wind tunnel with the small freestream noise level required to observe the linear growth of small boundary layer disturbances. By introducing controlled two-dimensional perturbations with a vibrating ribbon, they were able to corroborate the predicted growth rates of the nominally two-dimensional waves. Most experimental work thereafter followed this tradition of studying the convenient and well-defined waves which could be introduced using the vibrating ribbon technique.

A major improvement to the ribbon technique for generating controlled disturbances was introduced by Liepmann et al. [26], who used a flush-mounted surface heating strip to generate perturbations in water. As discussed in that paper, this technique provides greatly improved possibilities

for modulation of the perturbation in both time and space. For example, the heating can be made uniform in the spanwise direction within a few percent (see Appendix A.2.6), whereas the vibrating ribbon technique commonly results in a spanwise amplitude modulation of as much as 20% over a spanwise width of a few wavelengths [23, Figure 10]. Furthermore, the heaters present no disturbance to the flow when the current is turned off. This capability for creation of controlled three-dimensional disturbances was used by Robey [36] to study the development of single oblique waves in a boundary layer. The work reported here also uses this capability to study oblique waves, as well as some more complex patterns. This work with oblique waves and controlled three-dimensional forcing will be further discussed in Section 1.3. First, however, an overall sketch of the boundary layer transition process will be presented.

1.2 An Overall Sketch of the Boundary Layer Transition Process

The transition process in the boundary layer occurs over an extended streamwise distance, which can be divided into linear, nonlinear, and intermittent regions (see Figure 1.1). The small fluctuations considered by the linear instability theory enter the boundary layer from the freestream or from vibrations or imperfections of the plate, in a poorly understood process studied as ‘the receptivity problem’. If the disturbances enter primarily near the leading edge and are small, their growth as they travel down the plate will at first follow the linear disturbance theory, to good approximation.

The waves which develop from natural disturbances will in general have some finite coherence length, as indicated in Figure 1.1. The figure shows fuzzy dotted regions between the individual wave packets, for one would not

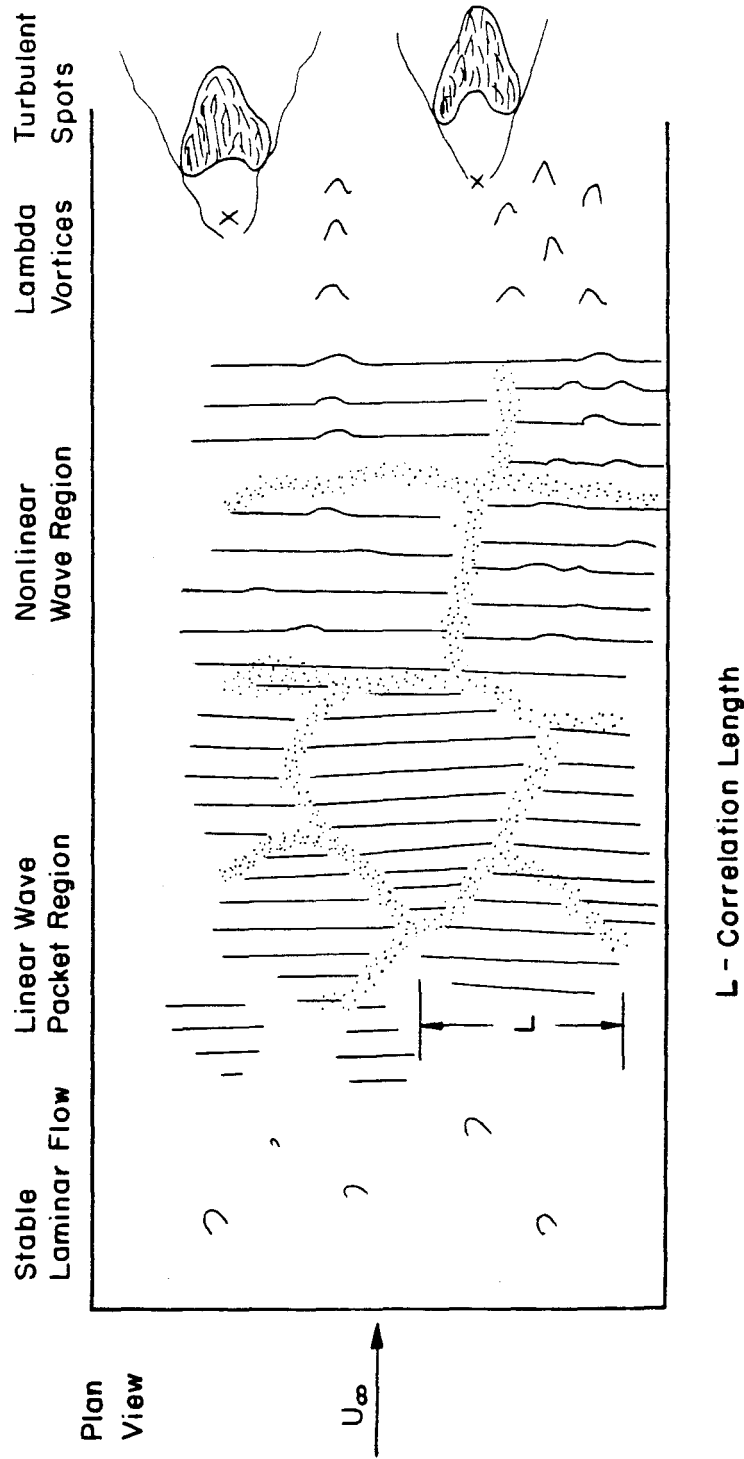


Figure 1.1: Cartoon of Boundary Layer Transition

expect the packets to have clearly defined boundaries. The coherence length of these packets might be expected to grow as the packets travel downstream, since they are passing through the narrow-band amplifier of the linearly unstable region. These spatial coherence issues are not yet well-understood. Of course, if waves are introduced by a two-dimensional wavemaker such as a vibrating ribbon, the spatial coherence length may be so large that spatial incoherency can be neglected.

The measurements of small amplitude instability waves reported here will be compared to the well-established linearized theory. The computation of results from the linear theory is not an easy process, and no complete compendium of results has yet been published. Fortunately, Dr. L.M. Mack of the Jet Propulsion Laboratory near Caltech was gracious enough to provide the results he had on hand [29], in machine readable format. It should be noted that two forms of the linear theory exist: the temporal case, where the waves are assumed harmonic in space, growing in time, and the spatial case, where the waves are assumed harmonic in time, growing in space. Since the frequency of waves in the spatial case remains constant as the waves grow downstream, and since this is also true in experiments, the spatial case was selected for comparisons. Mack's computer program is described in [28].

As the waves grow larger, the effect on the waves of changes in the mean flow field caused by the waves themselves can no longer be neglected, and the linear theory begins to fail. The now nonlinear waves begin to interact with themselves. The interaction of a single wave with itself causes distortion, while the interactions among single waves can cause wave resonance. As the waves become more strongly nonlinear, the wave patterns become more distorted, and strong spatial modulations of the once-straight waves develop. These usually look like the Greek letter Λ and are thus known as lambda

vortices. These lambda vortices can occur in a staggered hexagonal array, resulting in the presence of a subharmonic component in signals measured by a fixed sensor. The lambda vortices can also occur in a streamwise aligned array, which does not result in a subharmonic component. The circumstances that select a staggered or aligned pattern are currently a popular topic of research.

The strongly nonlinear lambda vortices break down into rapidly organized local turbulent fluctuations known as turbulent spots. The spots grow as they travel down the plate. The region in which these spots still cover only part of the flow, so that part is laminar and part turbulent, is called the intermittent region. After the spots have merged together, a fully turbulent boundary layer is formed, and the transition process is complete.

1.3 Three-Dimensional Effects in Boundary Layer Transition

Although the development of three-dimensionality is an essential element in the transition of boundary layers to turbulence, powerful experimental methods for studying the effects of controlled three-dimensionality have only recently been developed, following the introduction of the heated surface element technique. The development of three-dimensionality in the transition process has been a subject of much recent theoretical and numerical work, and one experimental approach has been to test these theories via suitably controlled experiments (see Corke [5]). Another approach, the one followed here at GALCIT¹, has been to study the experimental development of simple three-dimensional wave forms.

The only major study of such simple three-dimensional forms which has

¹Graduate Aeronautical Laboratories, California Institute of Technology

so far been carried out was done by Gaster ([42, Section 3.3] and [8]), who studied the development of spatially localized small disturbances in an unstable laminar layer. He carried out experiments describing the growth of such disturbances, and compared the measurements to the results of the linear instability theory. Since the disturbances can be described in terms of packets of instability waves using Fourier decomposition techniques, descriptions of their growth can be synthesized using linear combinations of the simple oblique and 2D waves of the standard linear theory. His results showed that linear superposition did hold while the disturbances were small, but failed when the disturbances became larger, and presumably nonlinear. Since the spatially localized linear wave packet must be described in terms of oblique waves, perhaps these oblique waves are an even more fundamental three-dimensional form.

Oblique waves are solutions of the linearized disturbance equations with straight but oblique constant-phase lines (see Figure 1.2). They were discussed very early by Squire [41], who derived a transformation which showed that the eigenvalues of an oblique wave were equal to the eigenvalues for an equivalent 2D wave at a lower Reynolds number, and thus that the mode which would be unstable at the lowest Reynolds number would be a 2D mode. However, oblique waves had never been a focus of experimental study prior to the work of Robey [34]. They are a major focus of the current work.

Oblique waves are not as trivial as is often thought. These waves contain all three components of both velocity and vorticity, as discussed for example by Craik [6]. The vortex lines for the oblique waves are distorted helices, with the helical axes parallel to the constant phase lines and the pitch of the helix windings decreasing from infinity as the oblique wave angle is increased from zero (see Robey [36, Figure 5]). Since the waves contain vortex lines

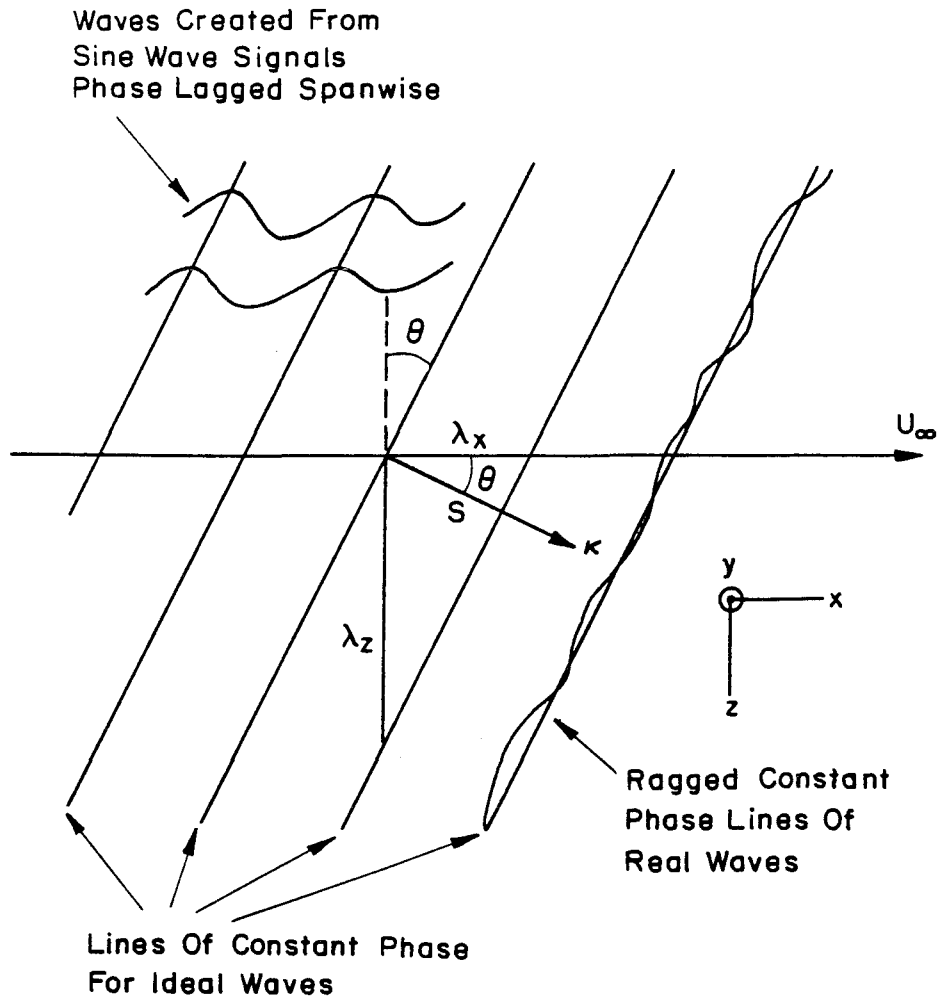


Figure 1.2: Oblique Wave Geometry

that are not all in the same direction, the vorticity now becomes directly subject to induced stretching and tilting. These nonlinear effects, which are not present in degenerate flows which have purely two-dimensional vorticity, can be extremely important. Moreover, the maximum of the vorticity moves away from the wall as the oblique wave angle is increased (see the detailed theoretical results of Hama [10] and the experimental results of Kachanov [16, Figure 5]). Furthermore, Gaster's studies of the development of wave packets involved an unexpectedly rapid growth of oblique waves: "... *the rapid development of oblique waves in the experimental results is not reproduced by the [linear] model.*" [8, p. 280]. There are thus good reasons for supposing that these oblique waves might become subject to strong nonlinear effects at much lower amplitudes than 2D waves; in other words, for supposing that these waves might behave much differently from the simple 2D waves.

Oblique waves are, however, difficult to generate experimentally. Some experiments have been done in which these waves were introduced via a vibrating ribbon which is positioned at an oblique slant to the freestream velocity (see Kachanov [16]). Similar experiments were done much earlier in a compressible boundary layer by Kendall [20]. This method has two drawbacks: first, the wave is introduced at a streamwise position which varies with spanwise position, so that the Reynolds number amplification history of the wave will vary across the span; and second, the oblique angle can be varied only with difficulty. Explicit computations of the linear instability of finite length waves of this sort, introduced by an oblique line source, have been done by Mack [28, Figure 6]. These computations show a severe distortion of the wave fronts at all spanwise locations except for a small region immediately downstream of the center of the wavemaker. This suggests that

the spanwise differences in Reynolds number history encountered by such a wave might be important. A method of generating the oblique waves entirely at one streamwise position would be desirable. Such a method will be presented in the next section.

The localized disturbances studied by Gaster and the oblique waves mentioned above would seem to be the two most fundamental instability wave patterns that might be studied. However, other wave patterns might also be of interest. For example, controlled spanwise modulations to the primarily two-dimensional waves produced by a vibrating ribbon were introduced by Klebanoff et al. [21] using cellophane strips, in their classic paper on the development of three-dimensionality in boundary layer transition. These modulations were introduced in order to fix the spanwise location of the development of three-dimensionality in growing 2D instability waves, in order to better study the onset of such three-dimensionality. Many other such patterns of 3D defects in primarily 2D waves might also be of interest. The author's apparatus, presented in the next section, was also capable of creating a variety of these more complex perturbation patterns, some of which were selected for a brief introductory study that will be presented in Section 3.4.

Since experiments are necessarily carried out in facilities with finite widths, it seems desirable to discuss the end effects which are encountered. The effects of the sidewalls on the development of transition in the boundary layer was first studied by Charters [3], who showed that a wedge shaped turbulent region with an included angle of about 11 degrees developed near such side walls. This edge contamination region was observed in the experiments reported here and may be seen in the photograph of the transition zone in Figure 3.37. This 11 degree angle is drawn on the plate layout sketches (Fig-

ures 2.2 and 2.4) for reference. A second edge effect is discussed by Mack [28, p. 130], who shows that the influence of the tips of a finite length source of instability waves is felt inside a wedge of half-angle 16 degrees, centered parallel to the flow direction. This 16 degree angle could also be drawn into Figures 2.2 and 2.4, where it would show that edge effects outside this angle will not affect even the farthest downstream sensor.

1.4 Apparatus for Introducing Controlled Three-Dimensional Perturbations

The essential element of the work described here is a new apparatus for introducing controlled three-dimensional disturbances into a laminar boundary layer. The apparatus used was developed from that of Robey [34], which in turn was inspired by the very different but related work of Trebitz [45]. Corke [5] has developed a somewhat similar apparatus, as has Meier et al. [30].

A flat plate model mounted in a water tunnel is used to form the boundary layer used as a basis for study. Heating is used as the method of introducing perturbations into the boundary layer. Instead of using a single two-dimensional strip spanning the boundary layer to introduce two-dimensional waves, however, an array of 32 small individual heating elements spanning the width of the boundary layer is used, to allow the introduction of three-dimensional perturbation patterns (see Figure 2.2). If sine waves of uniform frequency, amplitude, and phase are introduced into the 32 heaters, the heaters will all act in unison to produce a two-dimensional instability wave. However, if a uniform phase lag is introduced in the signals between adjacent heaters, the instability wave pattern produced will have constant phase lines which are delayed between one side of the plate and the other; i.e.,

the pattern will be an oblique wave (see Figure 1.2). Clearly, depending on the electronics used to drive the heating elements, a vast number of possible controlled three-dimensional perturbation patterns can be introduced. The growth of such three-dimensional patterns in the unstable boundary layer can be studied, and the effect on transition examined.

The present work extends the work of Robey [34], who completed qualitative studies of oblique and two-dimensional instability waves, covering the linear and nonlinear laminar regions of wave growth. The present work uses much improved forcing electronics to study quantitatively the development of two-dimensional and oblique instability waves through the linear and nonlinear regions and into the intermittent region. The development of the instability was studied using wall shear sensors, as in Robey, but more extensively, and using dye flow visualization of the intermittent region. In addition, studies of various other three-dimensional perturbation patterns were made.

Chapter 2

Experimental Apparatus

2.1 Water Tunnel

All the experiments were done in the Free Surface Water Tunnel of the Hydrodynamics Laboratory at GALCIT (see Figure 2.1 and the report of Ward [46]). The tunnel is operated as an open channel flow for these experiments. It has a 20 inch wide test section about 8 feet long, with plexiglas walls on three sides. Water exits from a 5:1 contraction directly into the test section¹. The water entering the test section was 21 inches in height as it left the contraction, and expanded into a greater height in the test section, creating some surface waves. A honeycomb of 4 inches depth with cells about $\frac{3}{16}$ inches wide is located just upstream of the contraction. For these low-speed tests a 20 mesh screen with blockage ratio 0.5 was attached to the honeycomb on the upstream side, to further smooth out the flow.

As mentioned, the tunnel is operated with the test section water level slightly above that in the contraction section². This overfilling was required in order to eliminate problems with high turbulence level which apparently were contributed to by air pockets on the top of the tunnel contraction section, or by a waterfall effect in the top of the honeycomb. The tunnel is equipped with a filter pump to clean the water, but this system was bypassed

¹The tunnel has a skimming system capable of removing the top wall boundary layer but this could not be used in the low speed experiments reported here

²test section running height 2.0 feet

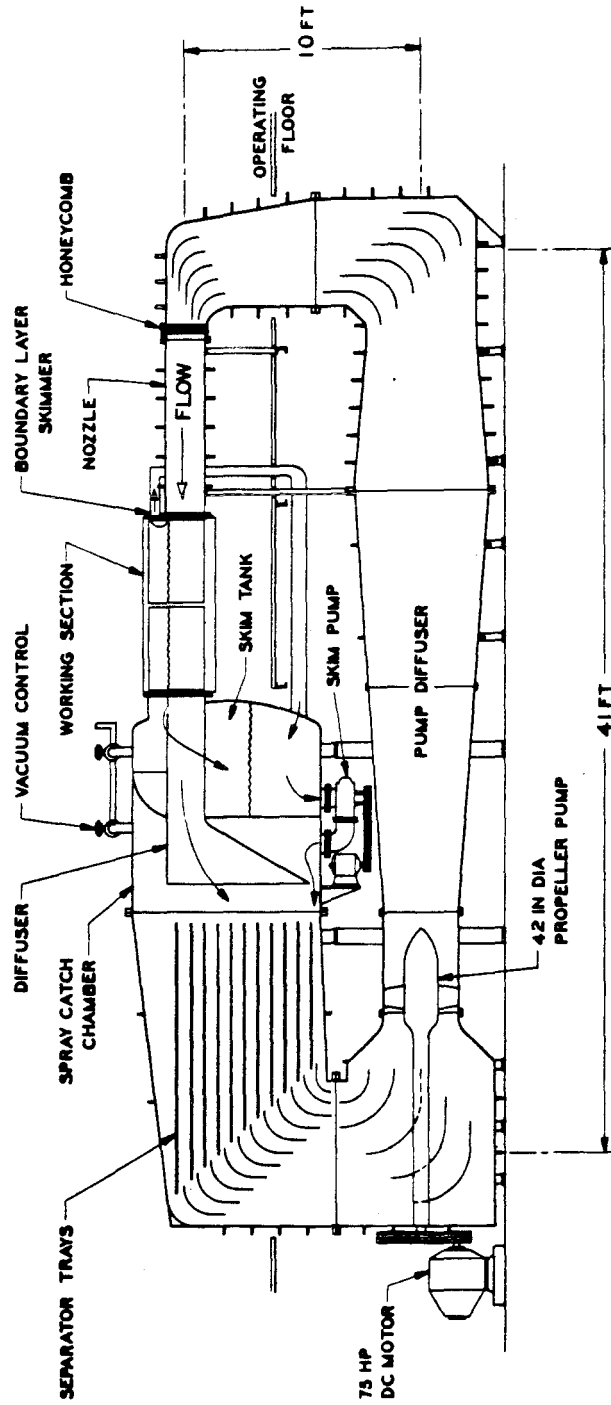


Figure 2.1: Free Surface Water Tunnel Schematic from Ward [46]

during the actual experiments in order to eliminate a source of disturbances in the flow just upstream of the last corner. Air bubbles were a continuing problem with the tunnel. When air was carefully drained out of all possible locations and the tunnel was run for a sufficient time to allow most of the air to leave, the air bubble content was acceptable. It was most important to keep the screen on the upstream side of the honeycomb clear of bits of grease and so on, which could greatly worsen the flow quality. When all these precautions were taken, the turbulence level in the test section was measured to be 0.15% (see Appendix B.1).

2.2 Flat Plate Model

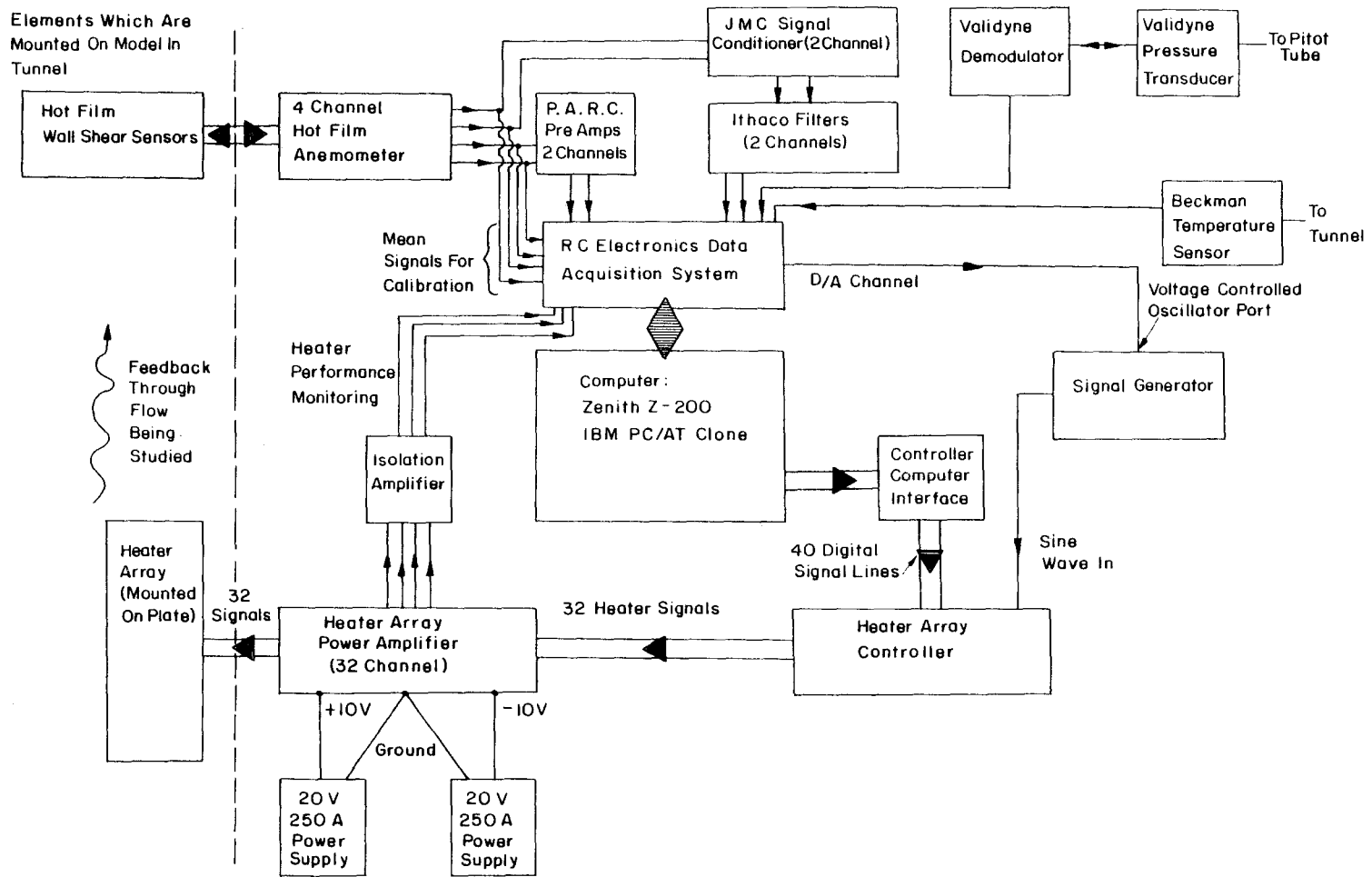
A modular flat plate model was fabricated for the experiments (see Figure 2.2, and Appendix A.1.1). The plate was one inch thick and 49 inches long and spanned the width of the test section. The plate was always located horizontally in the same position in the center of the test section. All electronic leads were brought out through the free surface above the plate. The bottom surface of the plate was the working surface whose boundary layer was studied.

2.3 Forcing Apparatus

The forcing apparatus used an array of 32 heating elements which was fastened to the working surface of the plate near the leading edge, as described in detail in Appendix A.2.5. The electronics used to drive the heaters is pictured along with the sensing electronics in Figure 2.3. A frequency generator³ supplied a sine wave signal to a computer controlled heater signal

³Hewlett Packard Model 3312A, or Exact Electronics Model 605

Figure 2.3: Block Diagram of Electronics



controller⁴, which generated 32 individual sine waves for the voltage on the 32 heaters. The amplitude of the sine wave on each heater could be selected from a set of 16 values, and the phase lag of the signal between one heater and the next could also be selected from a set of 16 phase lags. This controller was wired to a 32 channel power amplifier⁵ which supplied power gain to the signals from the controller and drove the heater array. Power for the 32 channel power amplifier was supplied by a pair of high-current DC power supplies (see Appendix A.2.4).

The perturbation-introducing system used was almost entirely new, having been almost completely rebuilt from the one inherited from Robey [34]. The system performance was improved by nearly an order of magnitude. The new system, whose performance is detailed in Appendix A.2.6, had an accuracy of the order of 1%; i.e., the uniformity among the heaters of both the power output and the signal phase lags is roughly 1%.

Since the signal placed on the heaters is a sine wave in voltage, and the heating power is proportional to the square of the voltage, the heating fluctuations occur at twice the frequency of the voltage fluctuations. Frequencies mentioned in the text as forcing frequencies are the frequencies of the heating power.

2.4 Sensing Apparatus

A Zenith Z-200 computer⁶ was used for control of the forcing apparatus and for data acquisition. The computer was equipped with a RC Electronics *Computerscope* 16 channel data acquisition system. An interface board⁷

⁴Appendix A.2.2

⁵Appendix A.2.3

⁶An IBM AT clone

⁷Appendix A.2.1

enabled the amplitudes and phase lags for each of the 32 individual heaters to be set automatically by computer. The performance of the heater electronics was monitored by the data acquisition system using an isolation amplifier⁸ to keep the small sensor signals from being corrupted by the high power heating electronics.

The tunnel flow velocity was first measured with a pitot-static tube and manometer, as detailed in Appendix B.1. For some later experiments a pressure transducer was used instead of the manometer; its behavior is described in Appendix A.3.4. The temperature of the tunnel water was at first measured only intermittently, since the tunnel resides in an air-conditioned basement room, and the water temperature varies only in the range of 22°C to 25°C. This variation interferes with precise measurements, and for later work the tunnel water temperature was measured using both a precision mercury thermometer⁹ and a precision resistance-temperature transducer¹⁰.

Flush mounted hot film anemometry was used for sensing the flow over the plate. The sensors measure surface shear, with excellent frequency response. They were calibrated as detailed in Appendix B.2, and were centered in the insert blocks, whose locations are sketched in Figures 2.2 and 2.4.

A twin sensor mounting was also fabricated, which held two sensors spaced 0.200 inches apart, the pair centered on the mounting insert. The sensors could be arranged to be in front (F) and to the rear (R) of the insert center. They could also be spaced apart spanwise from the insert center, in which case one was to the north (N), or heater #1 end of the plate, and the other was to the south (S) end of the plate. The sensor locations marked with an asterisk in Figure 2.2 sometimes contained these twin sensor inserts.

⁸Appendix A.3.2

⁹Fisher Scientific ST6208, -1 to 51°C

¹⁰Doric 610A, and later a Beckman substitute

When measurements made using the twin sensor pair are referred to in the text, the locations will be referred to as, for example, 'S1S'. This symbol denotes the south end sensor in a twin pair at location S1.

The anemometers used in the constant-temperature arrangement were built at GALCIT as described in Appendix A.3.1. Since the signals from such an anemometer are of generally low amplitude, with a large offset, signal conditioning equipment¹¹ was used to provide a signal suitable for digitization by the computer. This equipment also low-pass filtered the data in order to avoid aliasing in the computation of power spectra.

2.5 Flow Visualization

Flow visualization of the boundary layer was accomplished using dye bled in from the surface. This method clearly showed the regions of laminar and turbulent flow in the boundary layer, with the accompanying intermittent region filled with spots. It was not able to show the instability waves. Two methods of introducing the dye¹² were used. The first method used a plate section which had a manifold with 34 holes, each of 0.0135 inch diameter, to bleed dye into the boundary layer. A later design used a slot through which to bleed dye into the boundary layer, in an unsuccessful attempt to visualize the instability waves. The slot was 0.005 inches in width. A large mirror underneath the tunnel test section allowed photography of the working surface of the plate, which was accomplished on 35mm black and white film or with a video camera, using 500 watt studio fill lights. The upper side of the clear plexiglas plate was covered with white plastic film for the photography, so that the dark dye would be clearly visible against the white background.

¹¹Appendix A.3.3

¹²red or blue food coloring

The joints between the plate sections could not be easily so covered, and thus show up as dark strips in the photographs. The flow visualization was mostly used as a means of monitoring flow quality. It was also used for rough examinations of the effect of forcing on the movement of transition. Typical photographs are included as Figure 3.37.

2.6 Experimental Procedure

All of the results presented here were obtained using a data acquisition and control program¹³ which controlled the entire experiment. The program turned on the forcing, acquired data, turned off the forcing, computed intermediate results and summaries, fed back information to the operator, saved data to disk, and then continued to the next case. Using this automatic control, eight seconds of data for one forcing case could be acquired, examined, summarized, and saved to disk, in about $1\frac{1}{2}$ minutes, including the time required for equilibration between forcing cases. The data presented in this thesis represent roughly 1500 individual forcing cases produced over seven separate days of experiments.

The hot-film sensors were calibrated before and after each set of experiments, and estimates of the errors were made using the differences between the two calibration curves¹⁴. The heating and sensing electronics were also checked before and after each set of experiments, as was the pressure transducer or manometer. Several records of wall shear data without forcing were recorded during each set of experiments, and photographs or videotapes of the dye flow visualization were obtained for most experiments. Further details of the apparatus and its performance may be found in the appendices.

¹³described in detail in Appendix A.1.2

¹⁴Appendix B.2

The experiments reported here can be divided into two groups. The first group was conducted with the plate configured as shown in Figure 2.2. The sensors used in these experiments are labeled in the figure, and the experimental results will be referred to these sensor locations. This group used dye flow visualization, with the dye emitted as shown in the figure. Freestream velocities of $U_\infty = 3.50 \pm 0.02$ and $U_\infty = 3.68 \pm 0.02$ ft/sec were used. Approximately 1000 individual forcing conditions were examined in the course of the five separate days of experimentation included in this group.

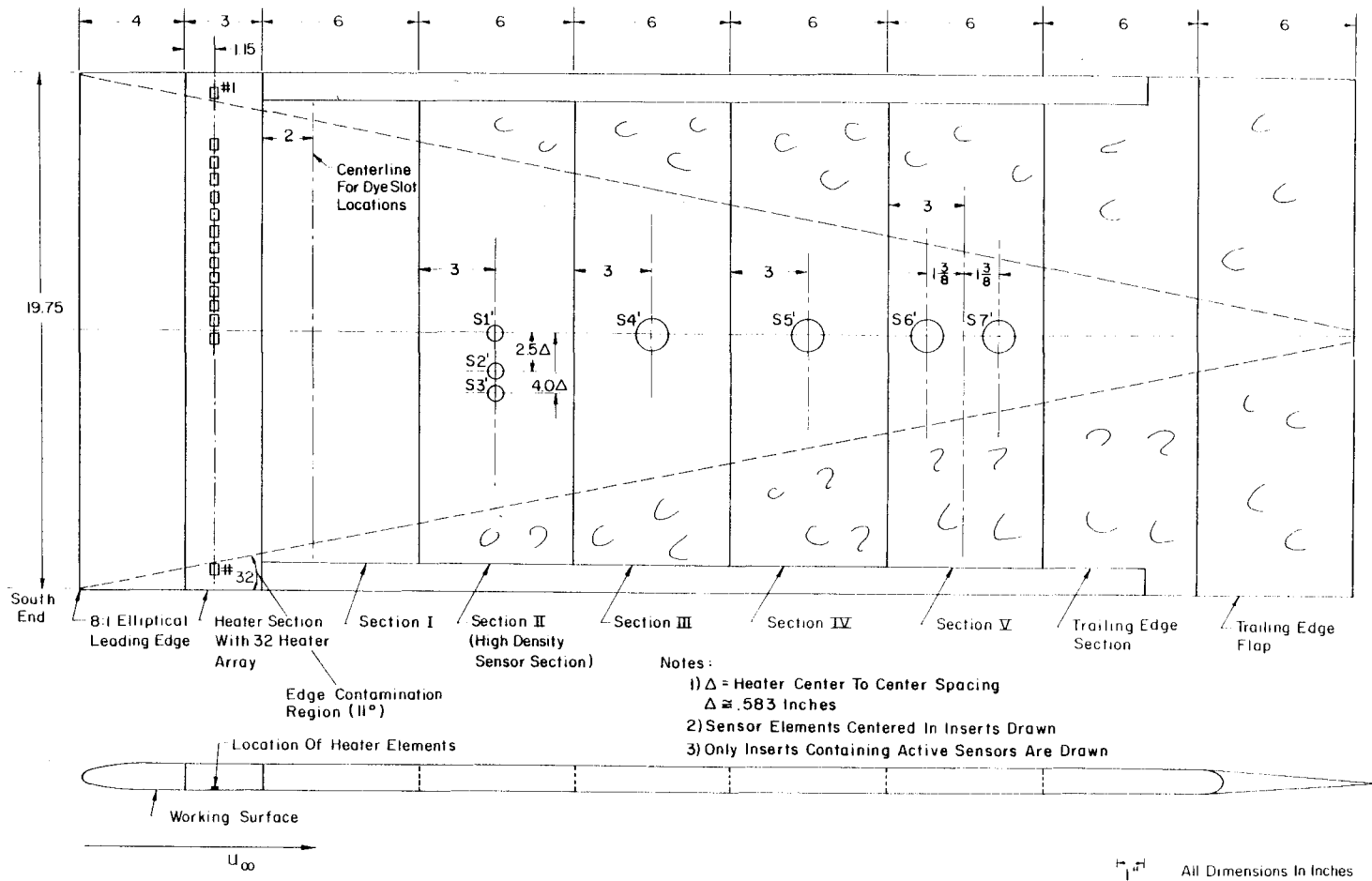
The second group of experiments incorporated improvements made following the analysis of the first group. These improvements are described in this chapter and in the appendices. This second group of experiments was conducted with the modular plate configured as shown in Figure 2.4. The experimental data obtained using this configuration will be referred to sensor locations shown on the figure. The dye flow visualization used in this group came from the dye slot shown in the figure. Most of the data was taken at freestream velocities of 3.69, 3.6, and 3.1 ft/sec. Perhaps 500 individual forcing conditions were examined using this improved apparatus, principally over the course of 3 days of major experimentation.

2.7 Discussion of Experimental Errors

Errors in the experimental equipment have been discussed in this chapter, and in the appendices, and have been estimated using the ideas of Kline [22].

Several special error sources are discussed in various sections. The effects of the free surface waves in the test section above the plate were examined in some experiments detailed in Section 3.2.1. The effects of the discrete geometry of the wave generator were examined in some experiments reported in Section 3.4.1.1.

Figure 2.4: Flat Plate Model Schematic: Second Configuration



In addition, an examination of the effects of the flush-mounted hot film sensors on the downstream flow was conducted. Two sensors 0.200 inches apart were used, with both natural instability waves and forced instability waves. In both cases, the signal from the downstream sensor did not change noticeably when the upstream sensor was turned on and off. This shows that heating of the flow due to the sensors has negligible effect on the flow.

Chapter 3

Experimental Results and Discussion

3.1 Introduction

The apparatus was primarily used to generate oblique instability waves, which were studied in the linear, nonlinear, and intermittent regions of the plate (see Figure 1.1). The apparatus was also used to examine the effects of various other three-dimensional perturbation patterns. The results presented in the following sections are divided by the general type of forcing used, and then subdivided by the region of the plate where the behavior was studied. The results for the natural, unforced, transition process will be discussed first.

3.2 'Natural' Transition

The term 'natural' transition is used for the transition observed on the plate without the introduction of special disturbances. Of course, the transition is then caused by the natural disturbances in this specific tunnel with this specific model. Although this limits the usefulness of the study of natural transition, it still seems useful to have some understanding of the transition process in a flow subject only to broadband incoherent disturbances, if only because the flow in applications is generally subject to such disturbances. The study of the natural transition should also shed some light on the background disturbance level in the facility, which is important for the forced

transition work.

Laminar flow was maintained in the center of the plate to above $Re_x \approx 1.4 \times 10^6$, as could be seen in the dye flow visualizations (Figure 3.37, upper photo). This value seems to be larger than that observed in the related experiments of Robey [34] and Nosenchuck [32, p. 35], who observed laminar flow up to about $Re_x \approx 1 \times 10^6$.

For comparison, a plot of the amplification rates given by linear instability theory for various frequencies and Reynolds numbers is given as Figure 3.1. The operating region for the work reported here is sketched on the figure. It is estimated from the highest and lowest forcing frequencies commonly used. The beginning of the operating region is chosen to be the heater array location; the freestream velocity used for normalization is the most common one, $U_\infty = 3.68$ fps.

3.2.1 Development of Natural Waves with Downstream Distance

A typical plot of the fluctuating shear for natural waves is shown in Figure 3.2¹. It should be noted that the large low-frequency component would not be seen in the usual AC-coupled oscilloscope traces. The other plotted trace, which shows the signal digitally filtered between 3Hz and 100Hz, is more akin to the usual oscilloscope traces shown. All the instability waves seen on the plate had this low-frequency component. It was first thought that these might be caused by the surface waves found on the free surface above the plate; however, experiments in which these waves were damped yielded natural instability wave spectra with no apparent differences. The

¹The code '5-5r06' found in the figure caption is a date code for the particular experiment in which that data was taken. Similar codes appear in all of the data plots. In this case, it refers to the sixth unforced run made during 5-5-88.

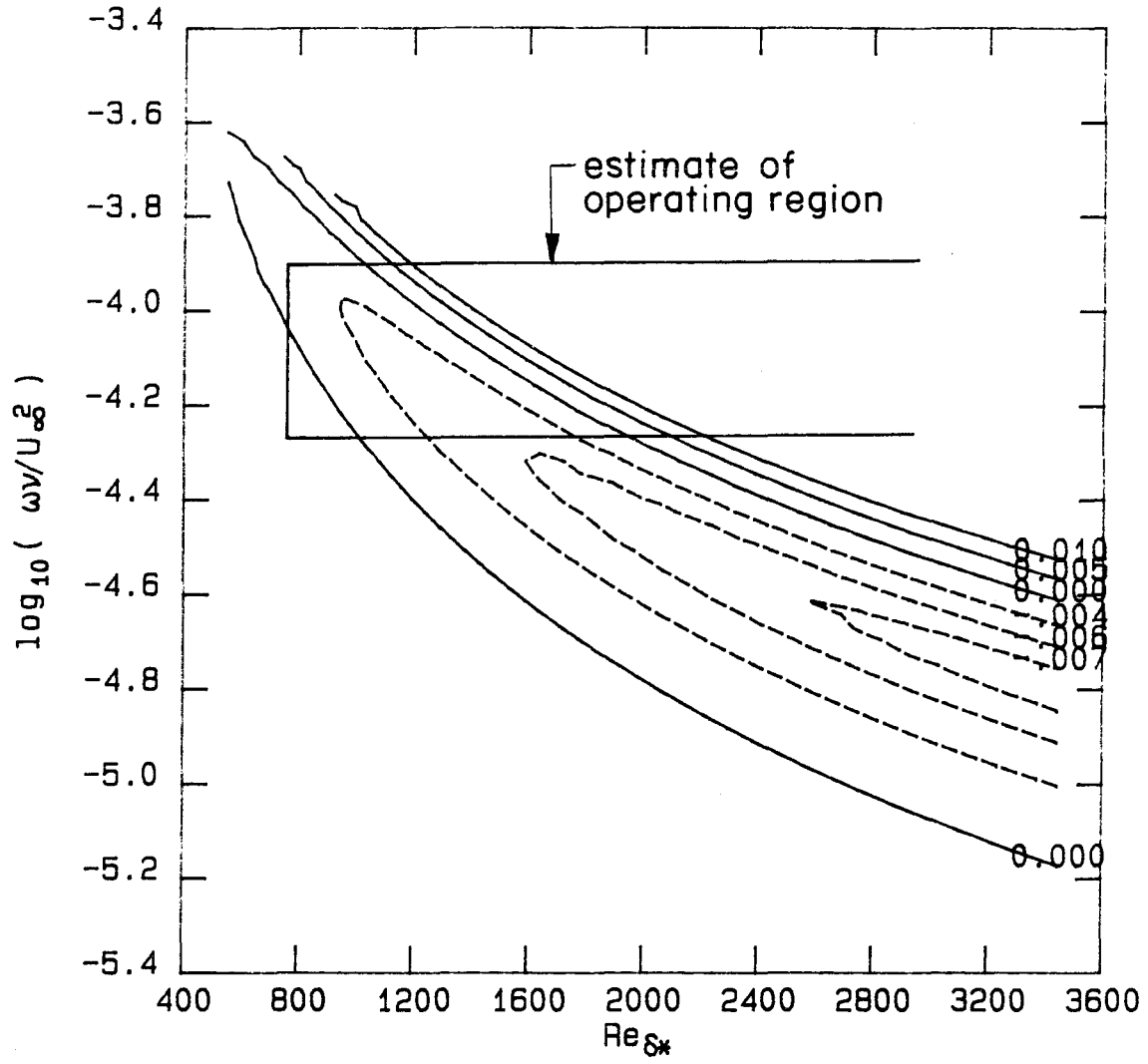


Figure 3.1: Linear Theory Amplification Rate Contours
from α_i data provided by L. Mack
see Section 3.2 for operating region estimate

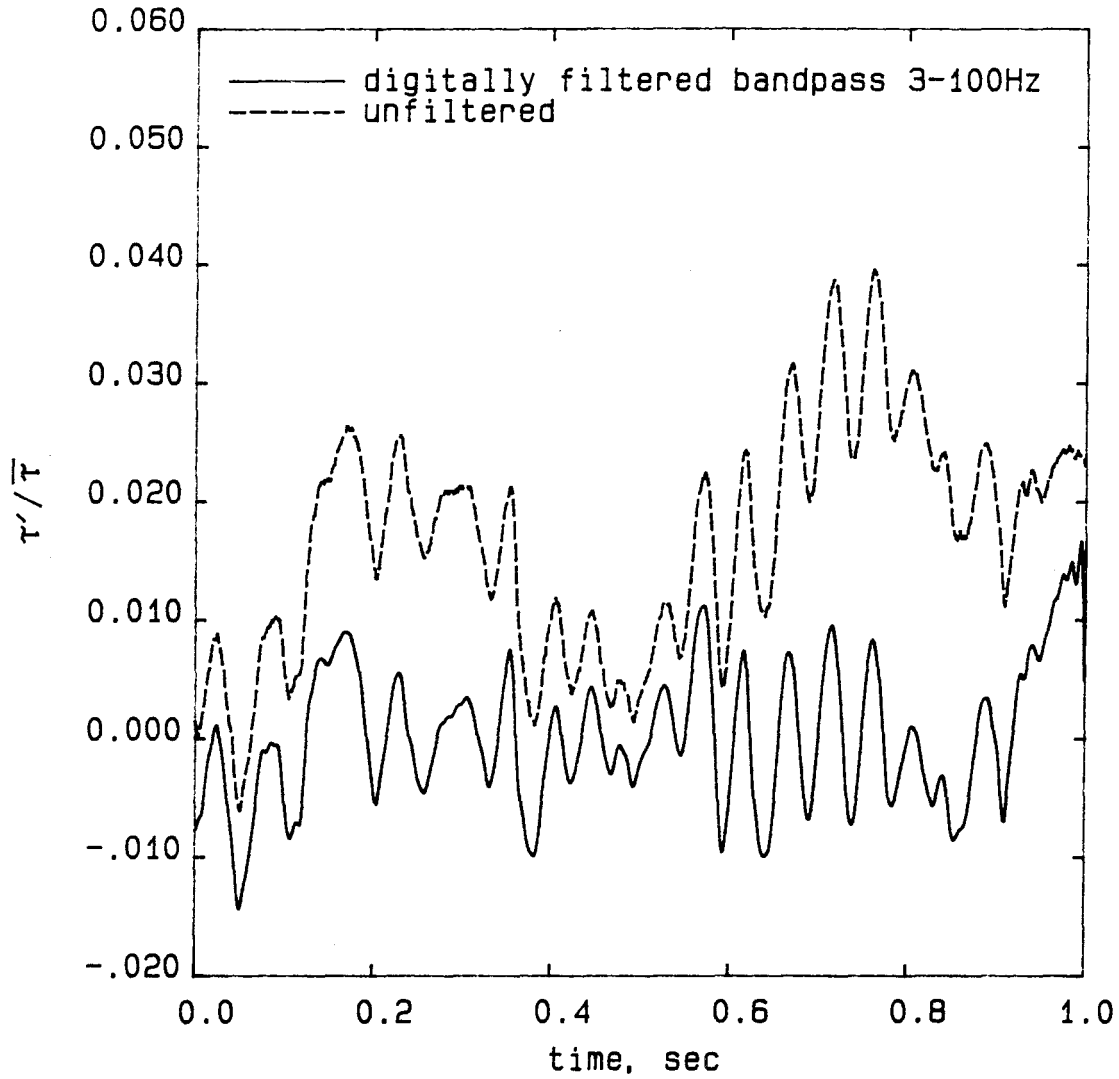


Figure 3.2: Shear Trace of Natural Waves at S7, $Re_{\delta^*} = 1400$
 $5 \cdot 5r06$, $U_{\infty} = 3.66$ fps

cause of this low frequency noise is unknown; it may be due to the large low frequency noise present in the facility, which can be seen in the freestream turbulence spectrum (Figure B.1). However, it is clear that the waves are not as clean as, for example, the ones observed by Liepmann et al. [26, Figure 3], who used a different facility of exceptional flow quality².

The unsteady nature of the waves is evident from the figure. An autocorrelation of the same data (Figure 3.3) clearly shows the rapid decay of coherence in the waves. After two cycles the periodic component of the correlation has become small. The waves seem to be composed of short coherent packets, a few cycles in length. These packets are not always of the same frequency, as one might expect from the fairly broadband nature of the instability, because the correlation function does not have a pure sine wave carrier. Thus either the packets are of different frequencies, or even individual packets do not have a single frequency. This unsteady poorly correlated nature is reflected in the broadband nature of the spectra presented below.

Spectra³ of the unforced disturbances computed from data taken at several positions down the plate during the same run are shown in Figure 3.4. The logarithm of the power in the shear fluctuations is plotted against the frequency. The large amount of power at low frequency was discussed above, and varies for the four spectra at very low frequencies due to differences in the high pass filters used. The peaks at 60Hz are due to line noise and may be safely ignored. These line noise peaks are two orders of magnitude in power, or one order of magnitude in amplitude, below the natural disturbances that account for the bumps in the spectra around 20Hz. It can be seen that these bumps peak at about 10^{-6} in power, or 0.1% in amplitude

²See also Appendix C.1

³For method of computation see Appendix C.3

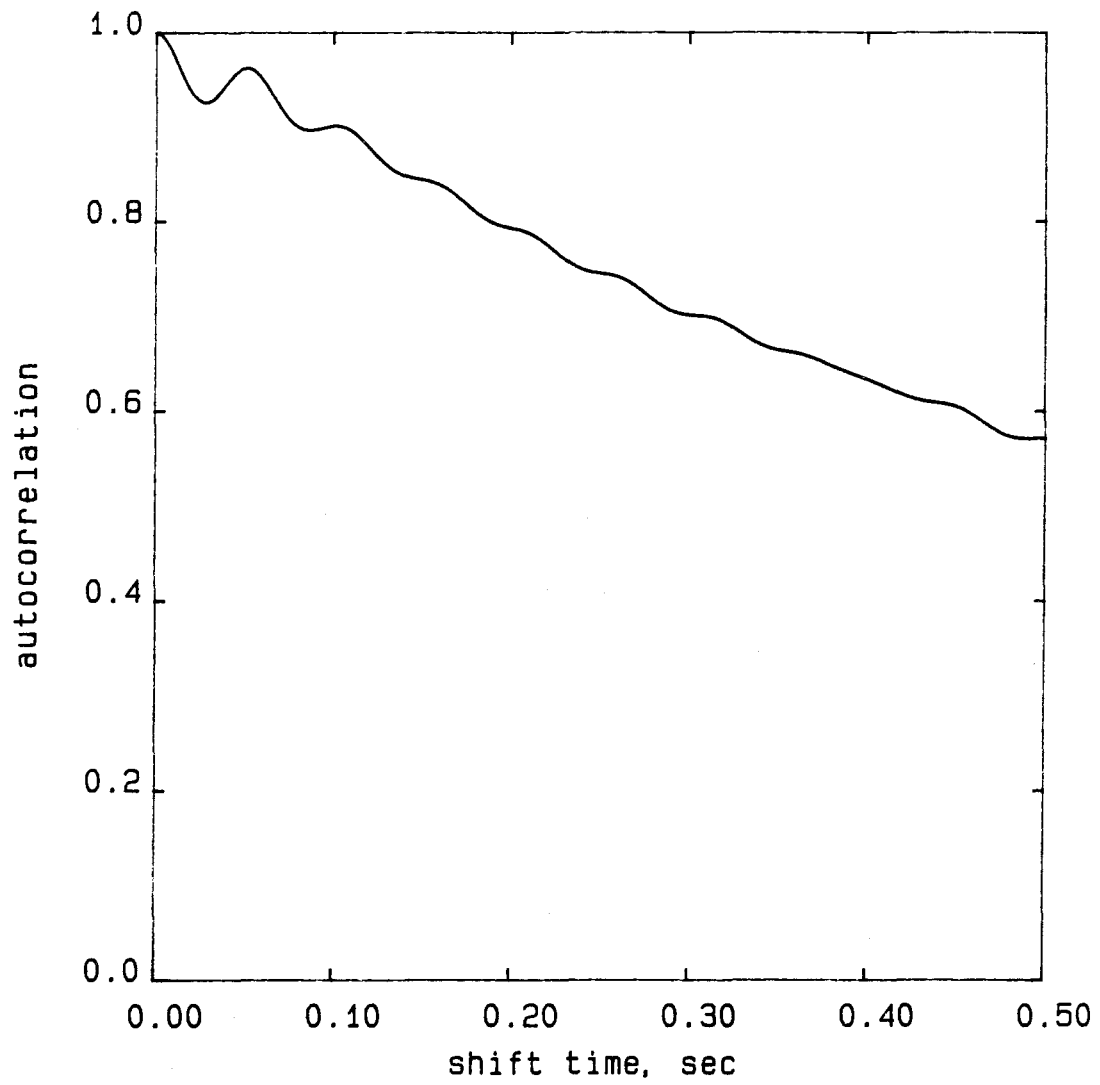


Figure 3.3: Autocorrelation of Natural Instability Waves at S7
($Re_{\delta^*} = 1400$, $5-5r06.c22$, $U_{\infty} = 3.66$ fps)

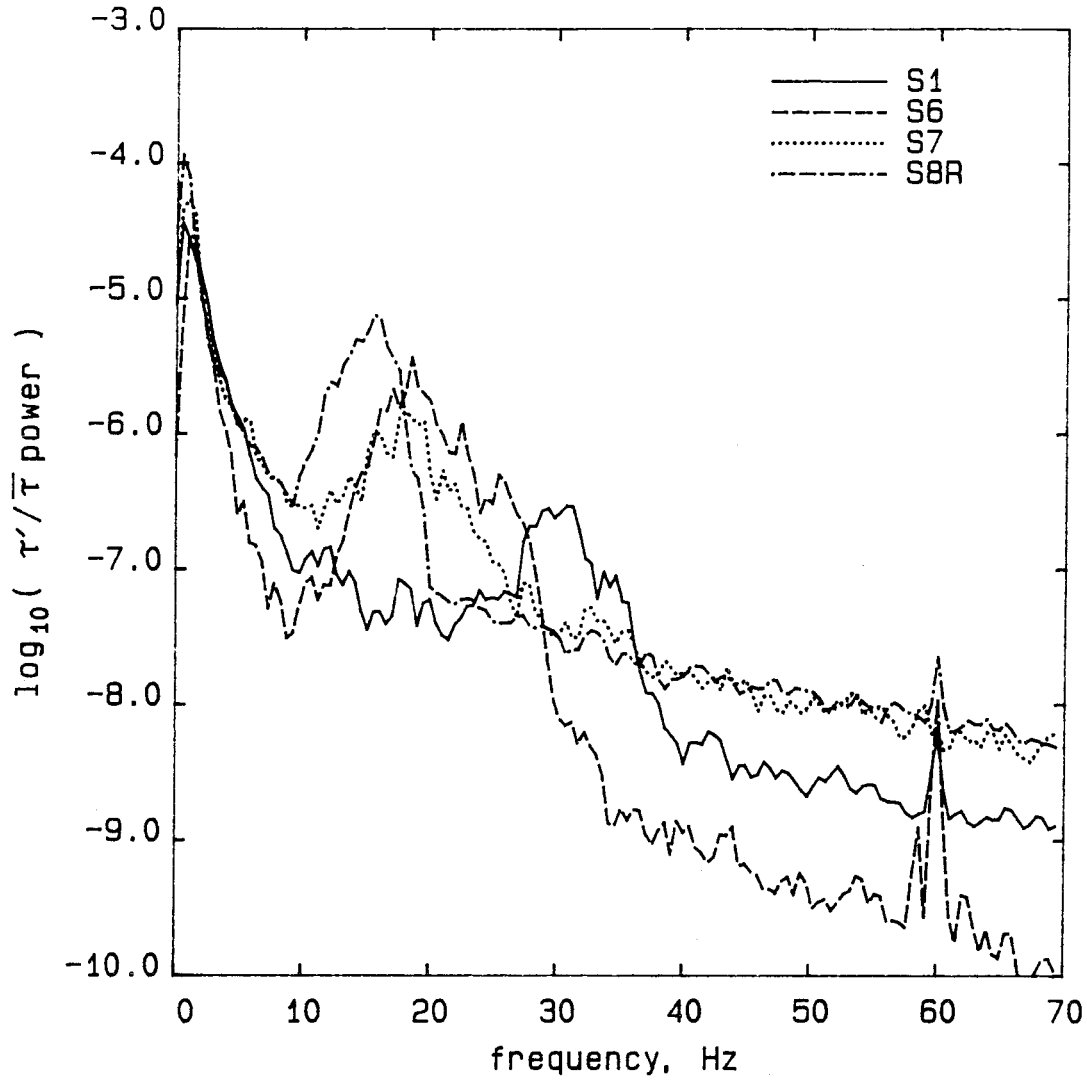


Figure 3.4: Spectra of Instability Waves at Four Streamwise Locations
($Re_{\delta^*} = 1100, 1350, 1400, 1750, 5-5r06$, $U_{\infty} = 3.66$ fps)

($\tau'_{rms}/\bar{\tau} = 0.1\%$). The bumps are about an order of magnitude in amplitude above the background noise in nearby spectral ranges.

A decrease in wave frequency with downstream distance is evident, and would be expected from the linear theory. One attempt to collapse this shift is shown in Figure 3.5, which shows the spectra plotted with frequency reduced by the local parameters δ^* and U_∞ . The three downstream spectra collapse well, but the upstream data do not. If the spectra are instead collapsed with the distance from the leading edge, the farthest downstream sensor does not collapse well, while the three upstream sensors do. The linear theory predicts a transfer function that could be used to predict the downstream spectra given the upstream spectra, and assuming that all the disturbances enter near the leading edge. However, this prediction is a complex process, involving the eigenvalues of the Orr-Sommerfeld equation for a variety of frequencies and Reynolds numbers, and has not yet been carried out.

3.2.2 Two-Dimensionality of Natural Waves

A typical plot of the fluctuating shear measured at two spanwise locations for natural waves is included as Figure 3.6. The irregularity of the waves is evident, as is the lack of spanwise uniformity. The cross-correlations plotted in Figure 3.7 show quantitatively the amount of spanwise correlation. It can be seen that the correlation is always less than about 0.2, even for nearby sensors which are 2.375 inches or about 3 wavelengths apart. This result can be contrasted to the result of Nosenchuck [32, p. 97], in which the cross-correlation has a maximum of about 0.8 and decreases very slowly with time. The two-dimensionality of that flow can also be seen in Liepmann et al. [26, Figure 3], where excellent similarity of the wall shear time

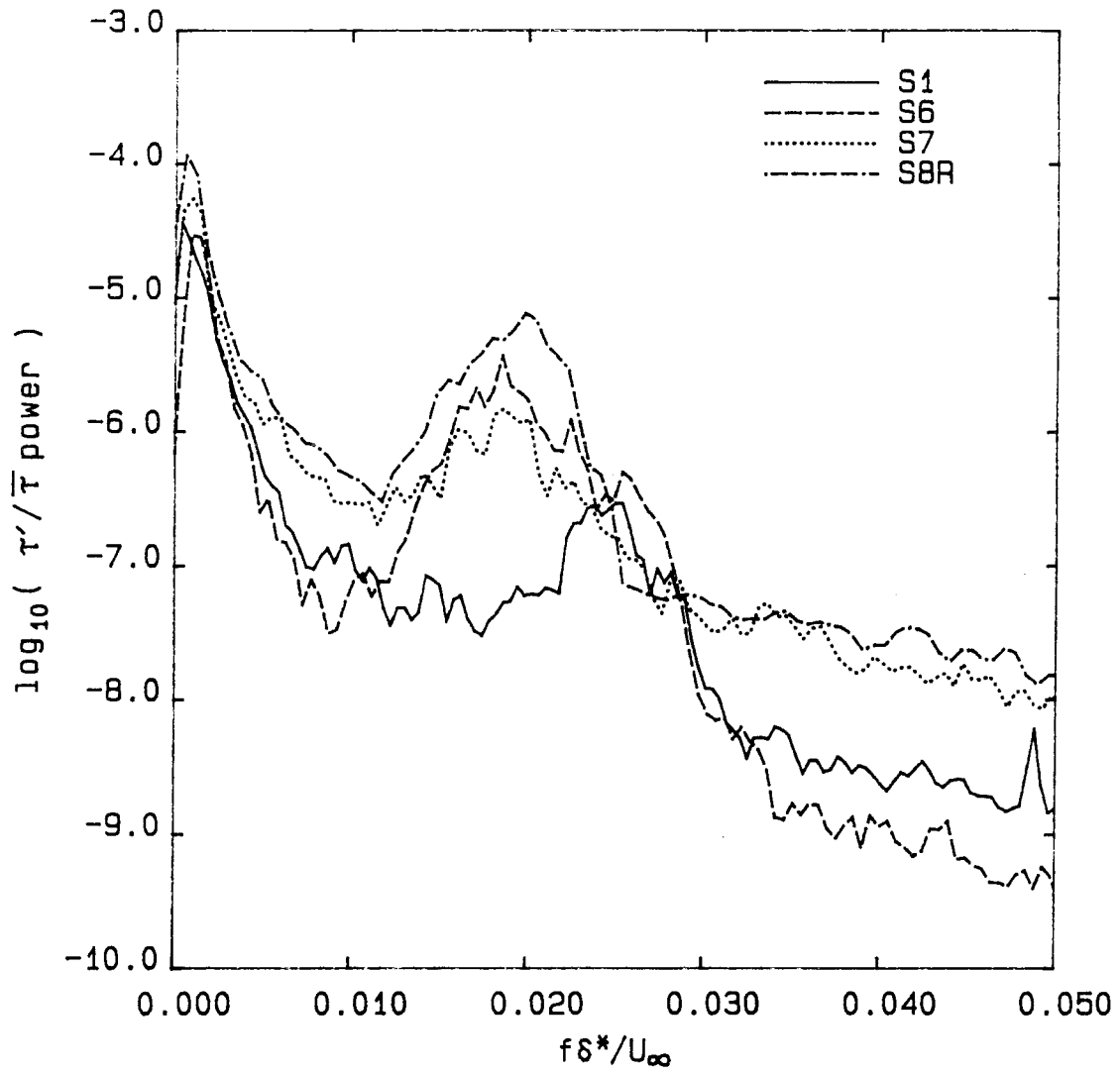


Figure 3.5: Reduced Spectra of Natural Instability Waves
(same conditions as in previous figure)

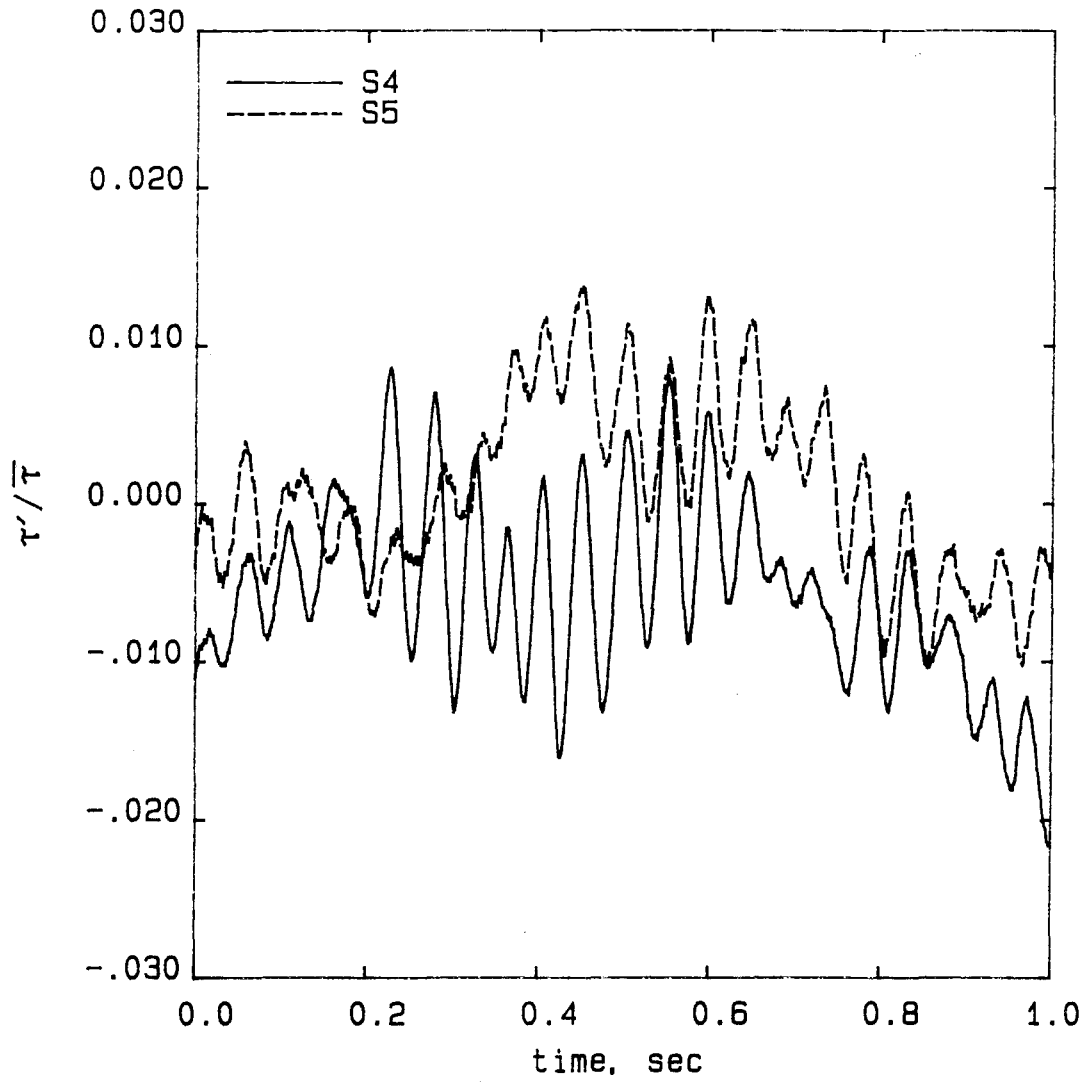


Figure 3.6: Naturally Occurring Waves at Two Spanwise Locations
($Re_{\delta^*} = 1300$, 4-13mr01, $U_{\infty} = 3.50$ fps)

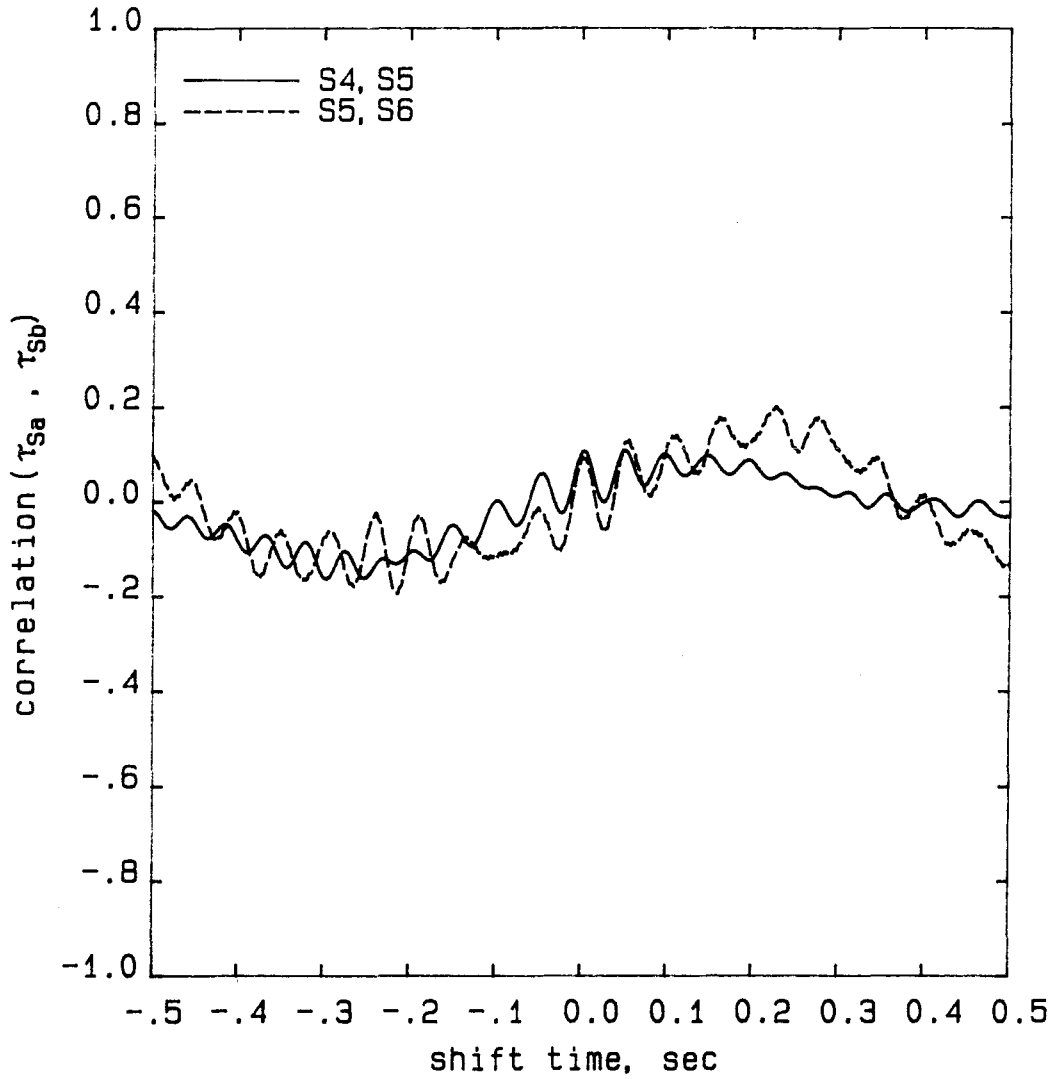


Figure 3.7: Cross-Correlation of Shear at Three Spanwise Locations
($Re_{\delta^*} = 1300$, 4-13mr01, $U_{\infty} = 3.50$ fps)

traces is demonstrated at two spanwise positions. However, it can also be seen in the Liepmann time trace data that there is a phase shift between the two spanwise positions, showing that even in that flow the waves are not always perfectly 2D but can have some oblique angle. The difference might be due to the blunter leading edge used in that work, which gives rise to a 2D region of highly unstable flow just behind the shoulder and thus perhaps more 2D waves⁴. The difference might also be due to the better flow quality in the facility⁵ used in the Liepmann et al. experiments; if the disturbance spectrum consists mainly of low-frequency disturbances that are highly correlated across the span of the leading edge of the plate, one would expect highly two-dimensional disturbances to be created near the plate leading edge, leading to highly two-dimensional waves downstream. Robey [34] does not give a cross-correlation, so that it is difficult to compare his sample time traces. That his results seem similar to Nosenchuck's is not surprising, since their work was carried out in the same facility.

3.3 Transition Caused by Oblique Wave Forcing

Most of the experiments studied the behavior of straight waves, both 2D and oblique. For these wave patterns all 32 heaters in the heater array were forced with sine waves of the same amplitude. A constant phase shift between the heaters was imposed, in order to make waves of different angles, ranging from 2D to about 32 degrees (see Figure 1.2). Oblique waves were chosen for most of the studies for three reasons. First, they are solutions of the linear theory, so that they can be easily compared to it. Second, they are simple forms, and for this work it seemed best to start with the simplest

⁴see Appendix C.1

⁵GALCIT High Speed Water Tunnel

three-dimensional forms possible. Third, even these simple forms are here a focus of quantitative experimental study for the first time, the only previous experimental work having been rather qualitative.

The first intensive experimental study of these waves was carried out by Robey [34]. The current work differs in that the waves are created more precisely, and their behavior is more carefully characterized. Also, the growth of the waves is studied here all the way into the intermittent region of the plate. However, the current apparatus is not capable of creating waves quite as large as those made by Robey (see Appendix C.1).

The waves were studied as they developed downstream, using various combinations of the wall shear sensors discussed above. They evolve through linear, nonlinear, and intermittent regions, which will be discussed in turn.

3.3.1 Linear Oblique Waves

The operational definition of the linear region is that the spectra contain spikes only at the primary forcing frequency. Typical spectra can be seen in Figure 3.8. This plot shows five spectra for waves forced at five different frequencies. The response to the forcing shows up as sharp spikes, whose amplitude varies according to the frequency of forcing. The rest of the spectra are similar to the unforced spectra discussed previously. The results for the linear region fall into three main groups: results for the amplitudes of the waves, results for the angles of the waves, and results for the phase speeds of the waves.

3.3.1.1 Wave Amplitudes

At all measurement locations, the oblique wave amplitudes were slightly less than the 2D wave amplitudes. It was not possible to compute accurate

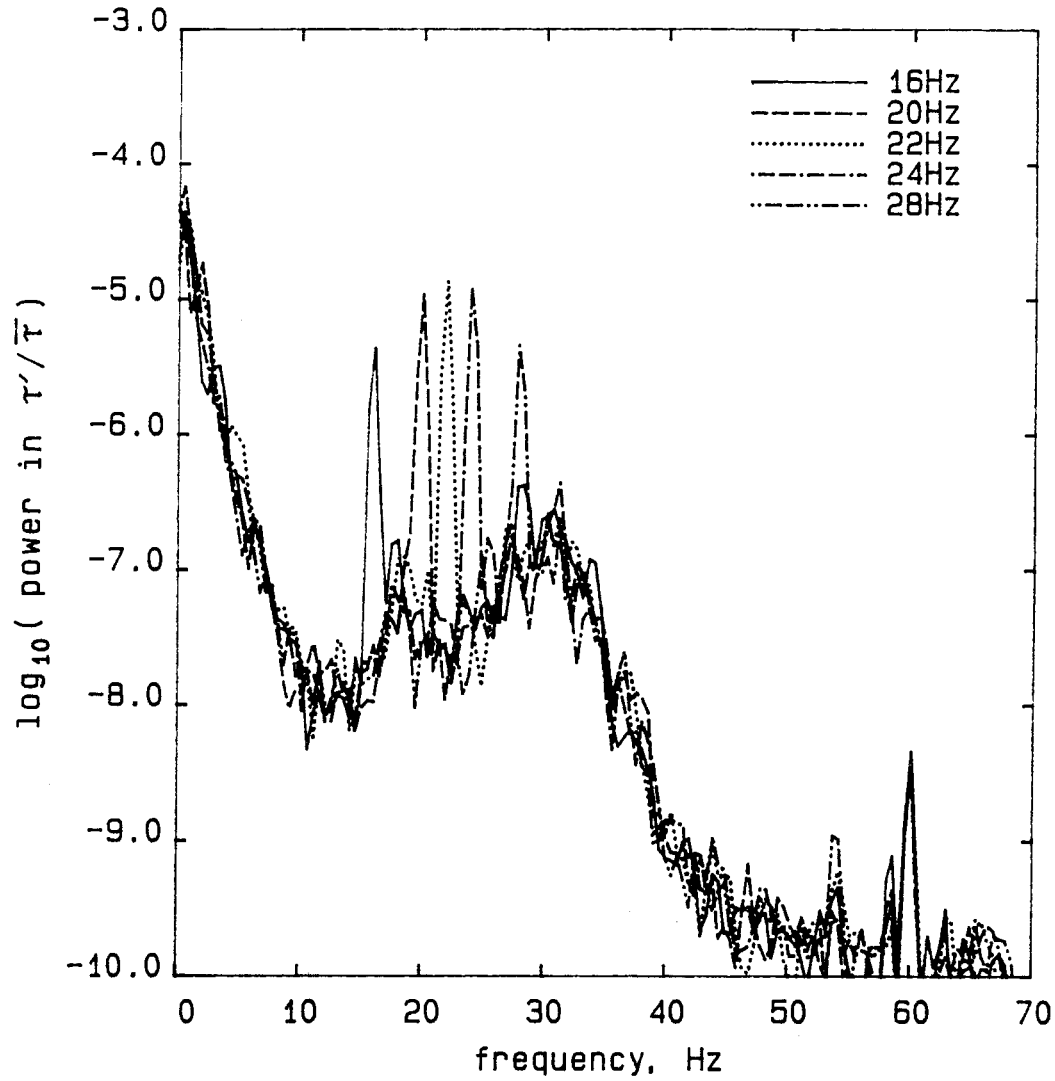


Figure 3.8: Wall Shear Spectra in Linear Region at $Re_{\delta^*} = 1100$
Five Spectra for Different Heat Frequencies
(83 watts total power, S1, 2D forcing, 4-22, $U_{\infty} = 3.68$ fps)

growth rates for the waves due to the lack of precision in the wall shear measurements. The growth of the oblique waves can be measured relative to the growth of 2D waves, but such a measurement is difficult to compare to the linear theory without extensive linear theory results and accurate measurements of the local boundary layer thickness. No such comparisons were therefore attempted.

Figure 3.9 shows the amplitude⁶ of the wave response at the same downstream location using the same heating on different days (this allows the reader to estimate the scatter in the data). These data show that although there is significant scatter in the apparatus, the amplitude of response decreases with increasing angle, consistently for different days, and the amount of change is very consistent. This trend is the same one reported by Kachanov [16] in his vibrating ribbon experiments. This decrease in response amplitude with increasing oblique wave angle may be caused by a decrease in growth rates; but it may also be caused by a decrease in the receptivity to the heating. There is no reason to expect that a given heater power input will produce the same amplitude instability waves independent of the obliqueness of the waves.

Figure 3.10 shows the amplitude of the waves on sensors at various locations downstream for different angles of forcing. These data show that the larger-angle oblique waves remain smaller as they travel down the plate. Figure 3.11, which shows the amplitude of the waves on one sensor for different forcing amplitudes, appears similar to Figure 3.10. This result shows that the larger angle oblique waves remain smaller than the 2D waves as the wave amplitude is increased, at least up to wave amplitudes of a few percent. All the data show that the higher angle waves have lower amplitude, as one

⁶For method of computation see Appendix C 3

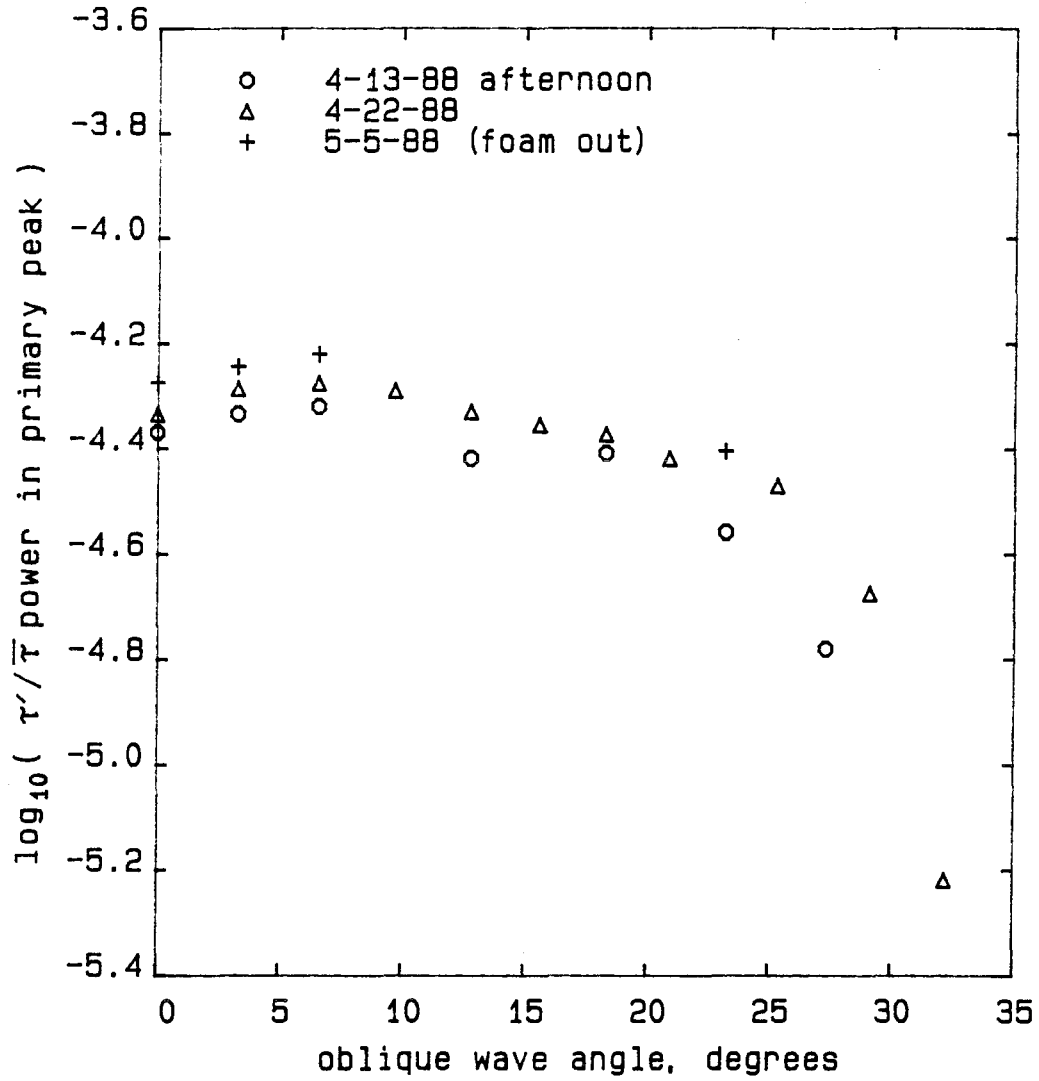


Figure 3.9: Growth of Oblique Waves on Different Days
Primary Response at S1 to 20Hz 192 watt forcing
 $U_{\infty} = 3.68$ fps, $Re_{\delta^*} = 1100$

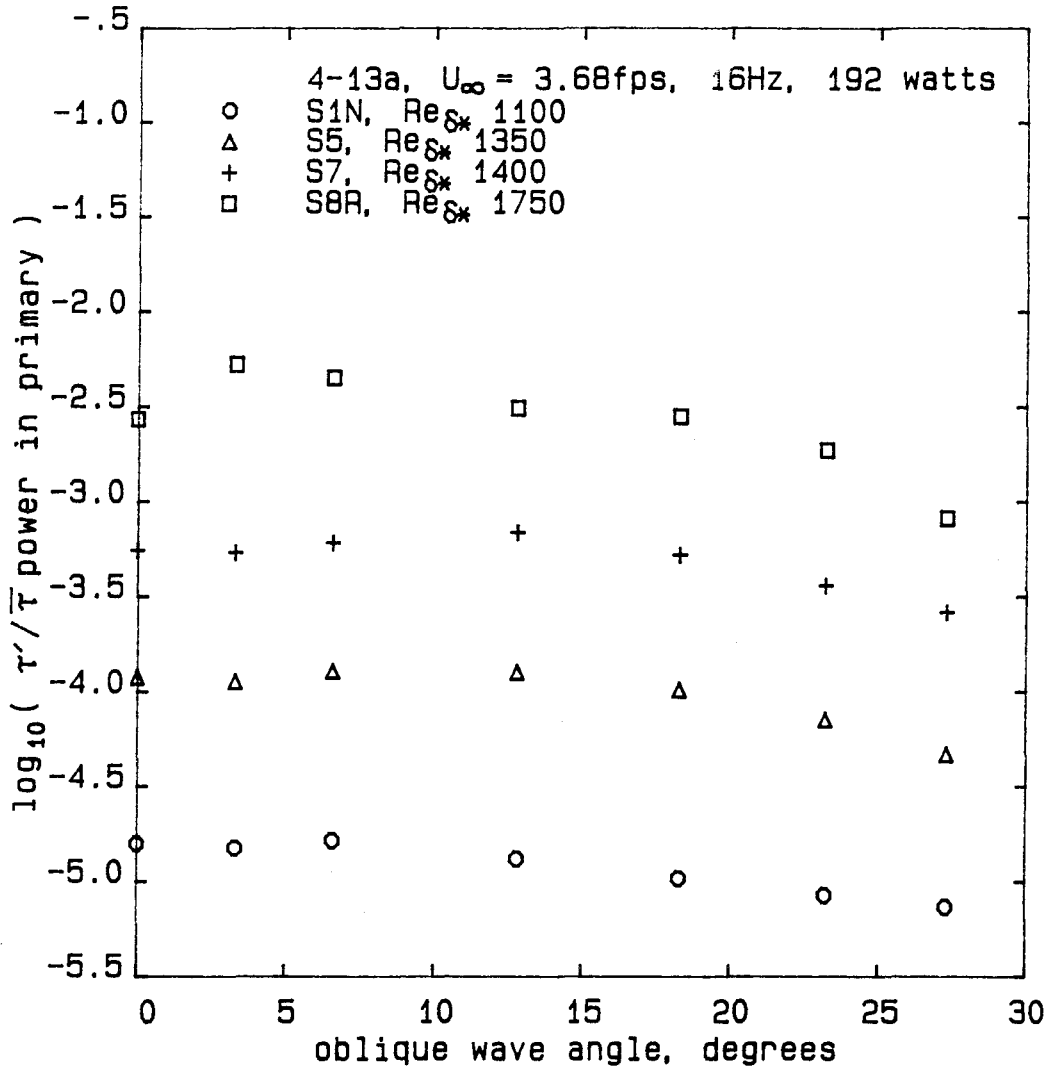


Figure 3.10: Growth of Oblique Waves vs. Downstream Distance
 $U_\infty = 3.68$ fps, 16Hz, 192 watts, 4-13a

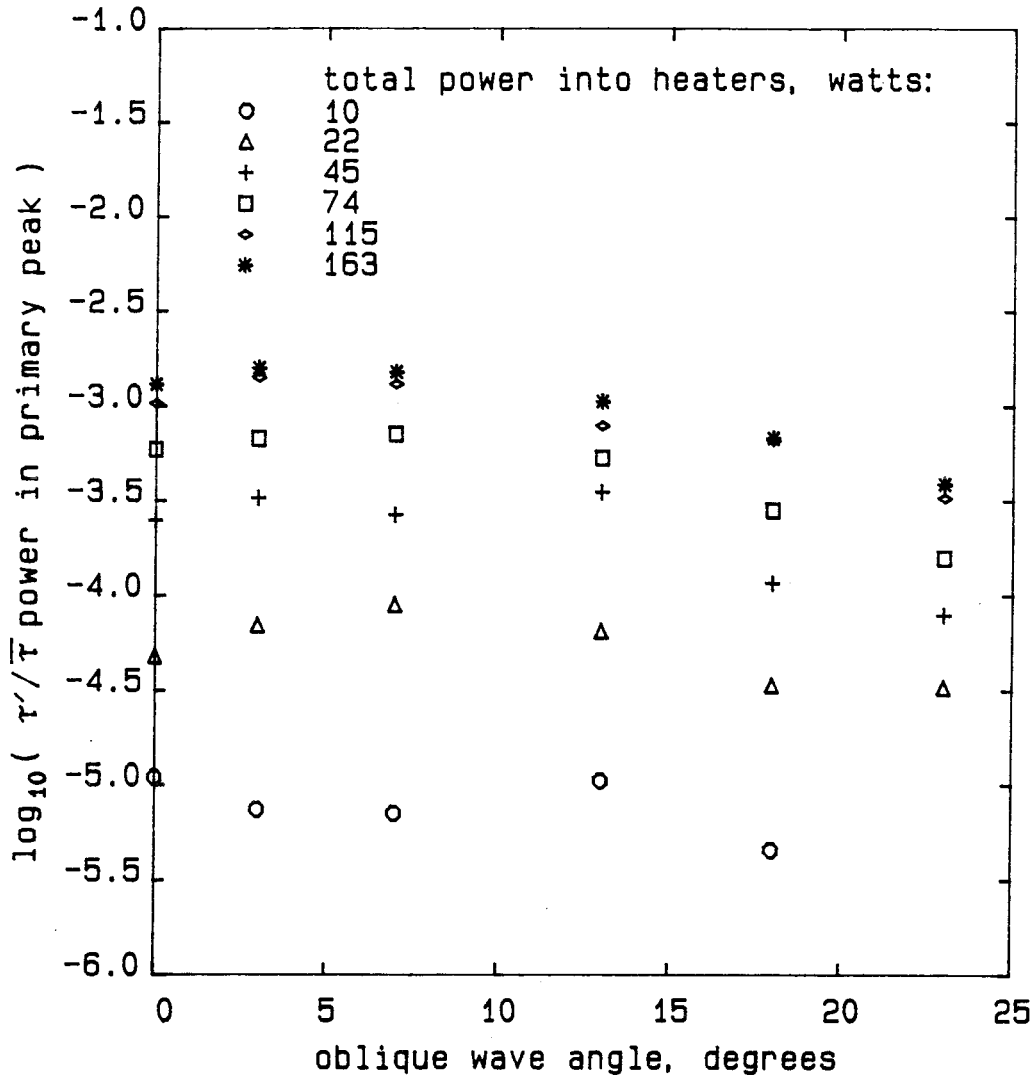


Figure 3.11: Amplitude of Oblique Waves for Different Forcing Amplitudes
 $S4'$, $Re_{\delta^*} = 1600$, $U_{\infty} = 3.69$ fps, $f_v = 10Hz$, 9-2-88 data

Sensor #	Frequency(Hz) and Power($\times 10^5$)								Maxima	
	Data ($U_\infty = 3.68\text{fps}$)									
S1	8.03	0.65	10.00	1.50	10.98	1.82	11.99	1.78	22.75	1.80
S2F	8.03	1.21	10.00	3.18	10.98	3.83	11.99	3.20	22.01	3.81
S5	8.03	8.58	10.00	15.1	10.98	10.4	11.99	2.79	19.23	13.83

Table 3.1: Maxima vs. Frequency at Three Streamwise Locations

might expect from the linear theory. The 2D waves are slightly smaller than the smallest angle oblique waves, presumably because the power in the perturbation producing the waves is slightly less for 2D forcing than for oblique forcing (Appendix A.2.6).

The wave frequencies which are most amplified between the heater and sensor depend on the streamwise positions of the two. This result is evident from Figures 3.12 and 3.13, which show spectra from the same experiments as Figure 3.8, but computed from data taken on sensors farther downstream.

It is evident, particularly from Figure 3.13, which is significantly farther downstream than the others, that the most amplified wave has shifted to lower frequency. These data are summarized in Table 3.1, which shows the frequency and power of the forced waves on three streamwise sensors, as well as the frequency and power of the most amplified wave, estimated by interpolating the maximum value⁷. When the frequency of forcing was increased or decreased from the most amplified frequency, the wave amplitude decreased smoothly. This was true for all the data taken on all sensors for a variety of frequencies, although no detailed study of the frequency dependence of the amplification was made.

This reduction in most amplified frequency with downstream location can be very striking when the most amplified waves at very distant streamwise

⁷see Hildebrand [15, p. 75]

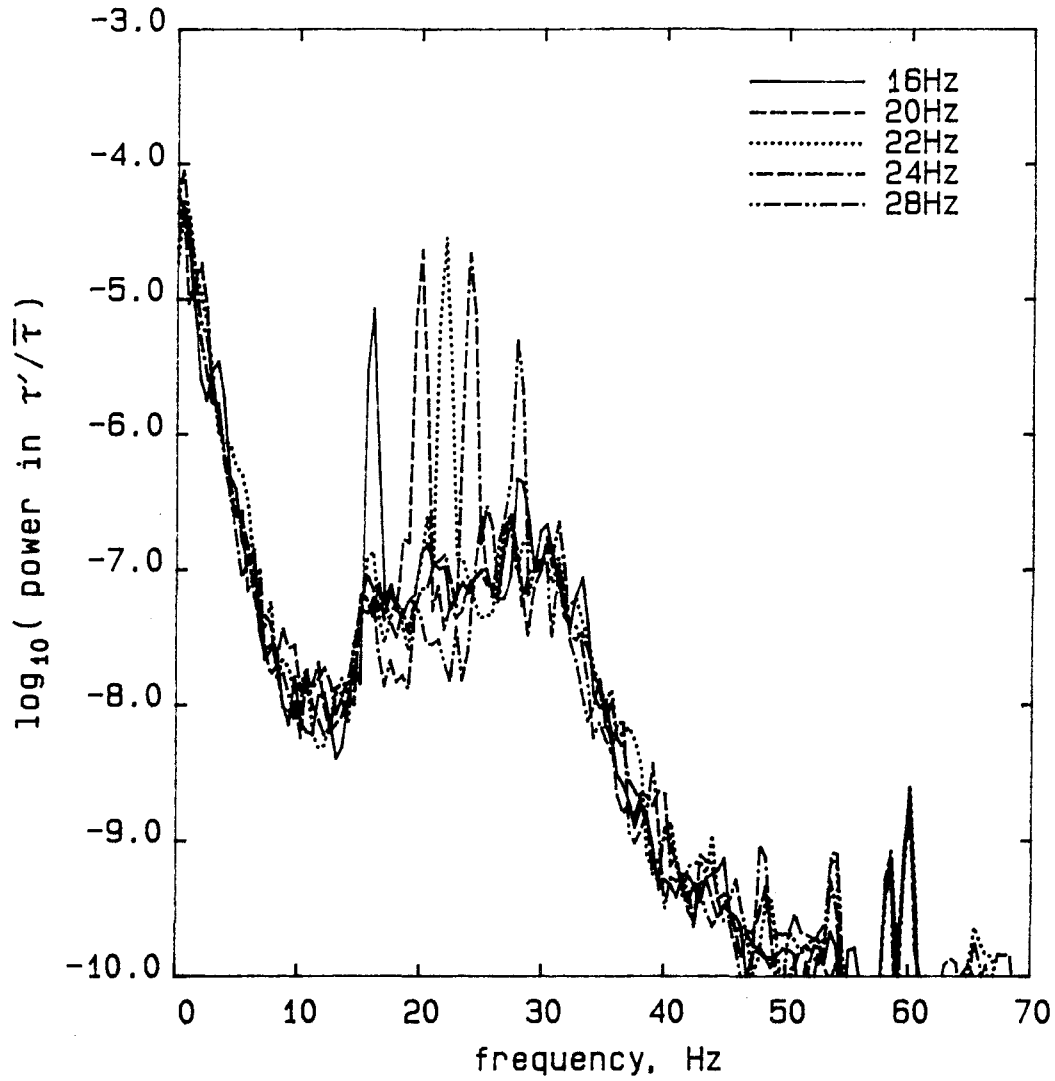


Figure 3.12: Wall Shear Spectra at $Re_{\delta^*} = 1150$
for five different heating frequencies
2D forcing, 83 watts, S2F, 4-22, $U_{\infty} = 3.68$ fps

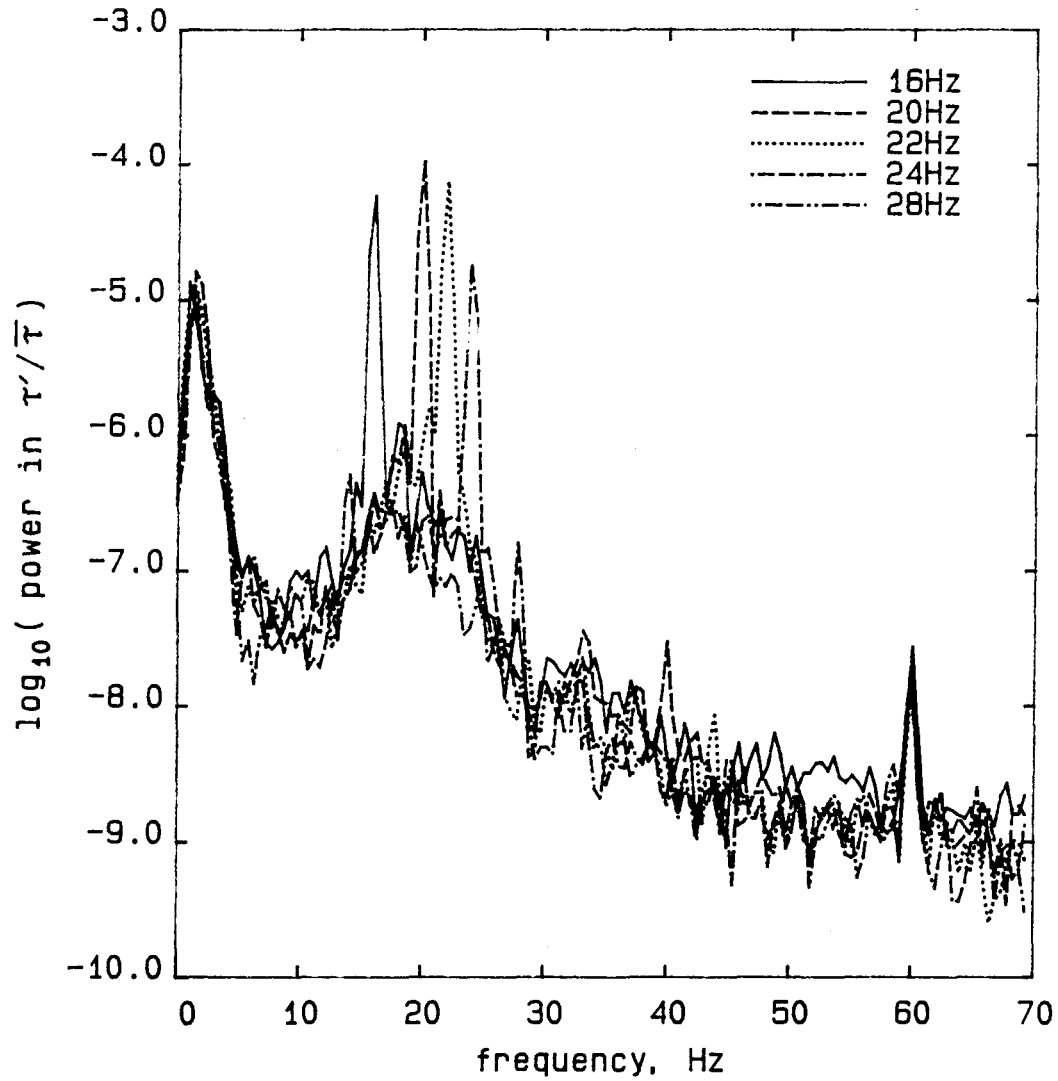


Figure 3.13: Wall Shear Spectra at $Re_{\delta^*} = 1350$
for five different heating frequencies
2D forcing, 83 watts, S5, 4-22, $U_{\infty} = 3.68$ fps

locations are compared. It often happens that waves that are large at the early sensors have grown irregular and caused transition by S8, whereas lower frequency waves that grow slowly upstream give rise to very large amplitude waves on S8. These are, however, still clean instability waves without much broad-band turbulence.

The amplitude of response by one sensor to different amplitudes of forcing is shown in Figure 3.14. The figure shows that the response downstream increases less than linearly with the power input to the heaters. This behavior is the same as that observed by Robey [34, Figure 3.4], who suggested that the decreased sensitivity of the flow to increasing power was caused by the smaller temperature dependence of the viscosity of water at higher temperatures. The growth of the waves between two streamwise sensors as a function of the amplitude at the first sensor is shown in Figure 3.15. In this figure an amplitude is changed by changing the forcing level. The figure shows that the growth rate is constant for different wave amplitudes. Thus in this sense the waves are still linear, even to rms wall shear amplitudes of about 2%. According to the results of Robey [34, p. 12],

$$\tau'/\bar{\tau} \approx \frac{5}{2}(u'_{max}/U_{\infty}),$$

so the corresponding maximum velocity amplitude is about 0.8%.

The data for wave amplitudes could also be used to compute growth rates of the waves. However, this can only be done to a limited extent due to errors in the data. Since no sensors capable of being traversed along the plate surface were built, the growth rates must be estimated from the amplitudes found on separate sensors which have separate calibrations. Unfortunately, the sensor accuracy was not what might be hoped for (see Appendix B.2). Results for the growth rates of waves made under the same conditions on

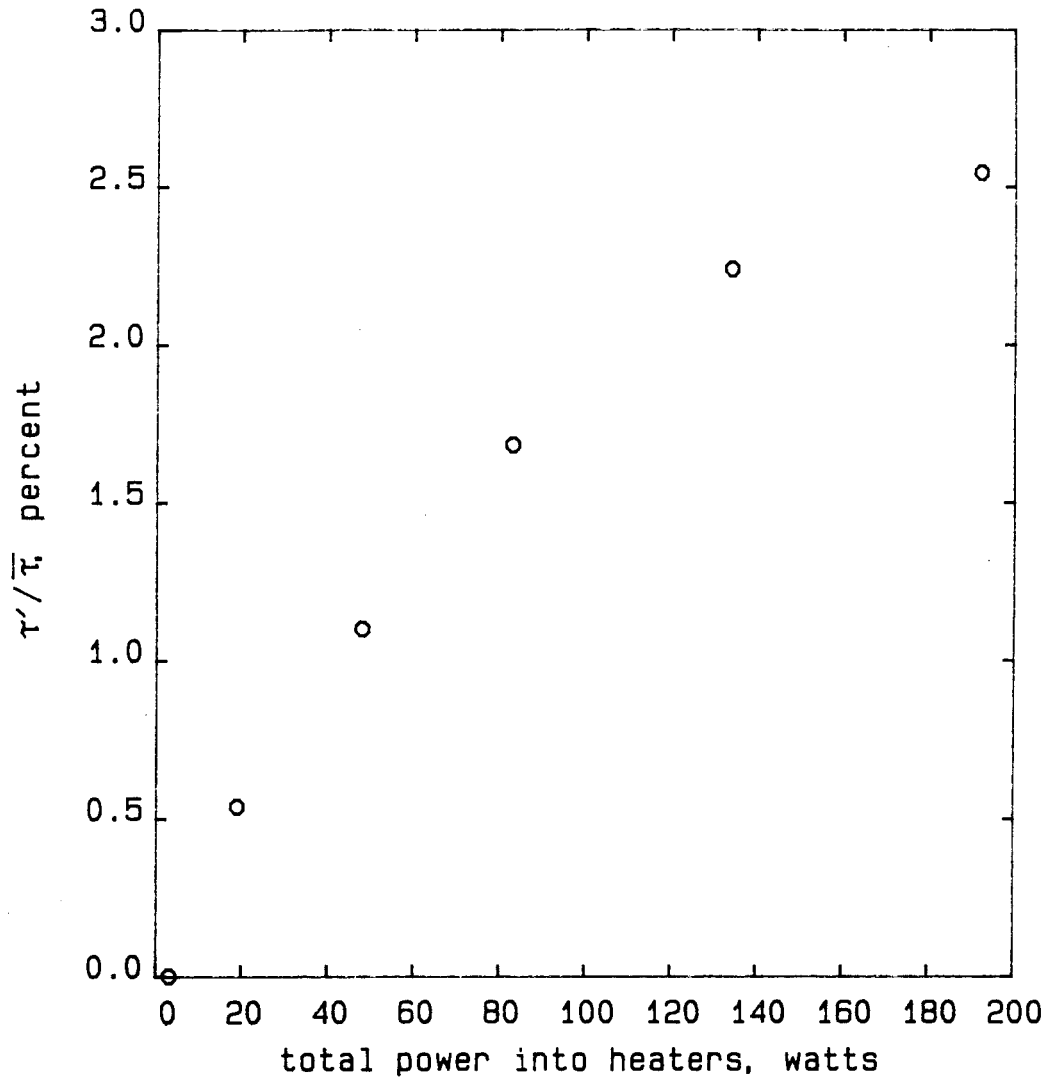


Figure 3.14: Primary Response Amplitude vs. Forcing Power
10Hz 2D forcing S6, 4-13mII, $Re_{\delta^*} = 1300$

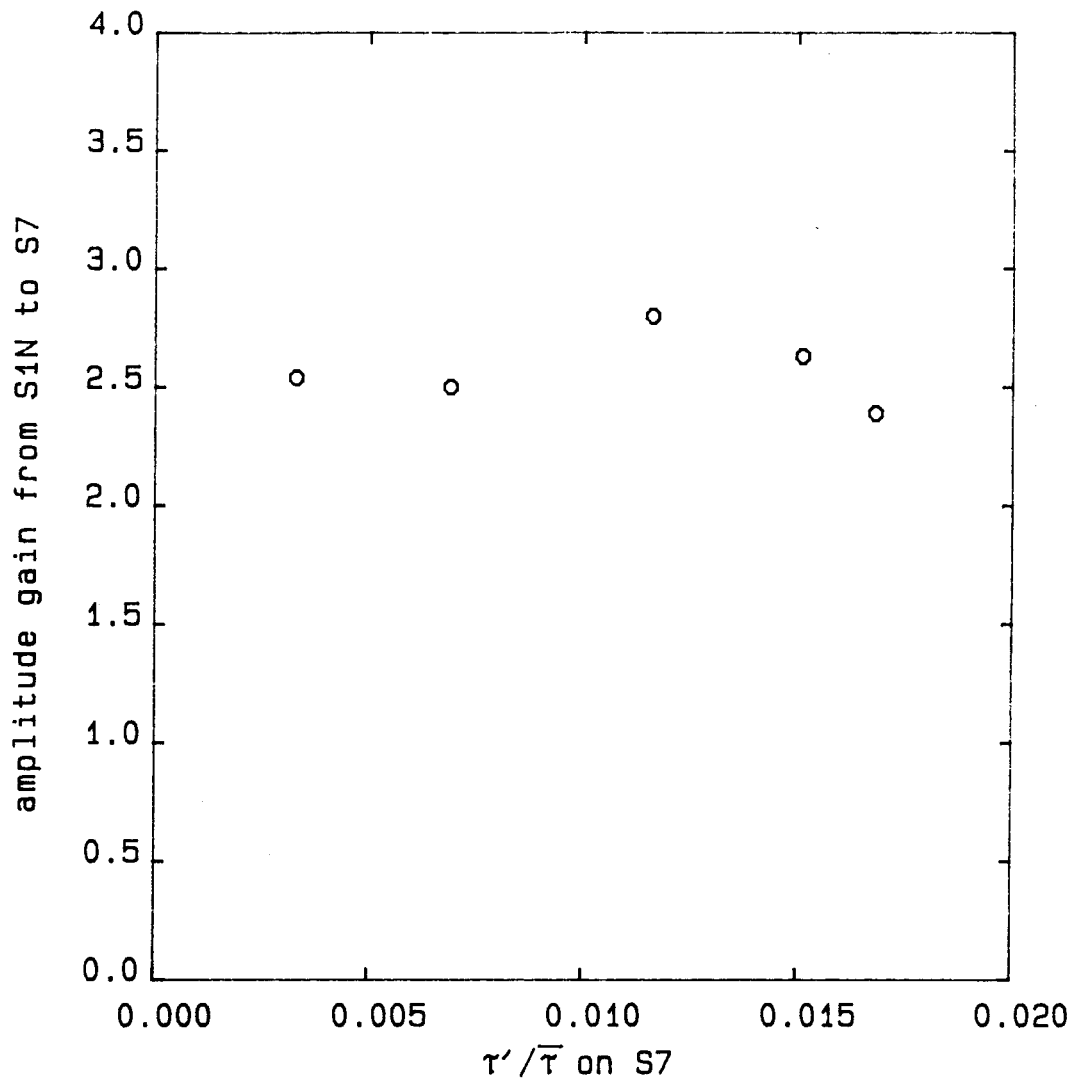


Figure 3.15: Growth Rate of Primary Response vs. Wave Amplitude
 $U_{\infty} = 3.50$ fps, 20Hz, 4-13mII
 $Re_{\delta^*}(S1N) = 1050$, $Re_{\delta^*}(S7) = 1350$

different days can be plotted to estimate the errors. The data scatter not only because of errors in the sensor calibrations, but also because of errors caused by small changes in the power output by the heaters, small differences in the tunnel water temperature which can cause large integrated changes in Reynolds number and growth rate, and small changes in tunnel velocity or freestream noise. For estimation of absolute growth rates, as opposed to relative growth rates, all these errors must be small. A plot of the shear response to a given forcing type using data taken on several different days from several sensors is shown in Figure 3.16. The data clearly shows the large growth of the instability waves down the plate, but has too little accuracy to give absolute local growth rates.

3.3.1.2 Phase Speeds

Phase speeds for oblique waves can be defined using the relation

$$\vec{c}_{phase} = \frac{\omega}{(|\vec{\kappa}|)^2} \vec{\kappa},$$

where $\vec{\kappa}$ is the wave vector for the wave (see Whitham [48, p. 365]). But for spatially growing oblique waves with

$$\vec{u} = \Re \left(\vec{u}(y) e^{i(\alpha x + \beta z + \omega t)} \right),$$

where β and ω are real, we have that

$$\vec{\kappa} = \alpha_r \vec{i} + \beta \vec{k},$$

since

$$\vec{u} = \Re \left(\vec{u}(y) e^{i(\vec{\kappa} \cdot \vec{x} + \omega t)} e^{-\alpha_i} \right).$$

Thus

$$|\vec{\kappa}| = \sqrt{\alpha_r^2 + \beta^2}.$$

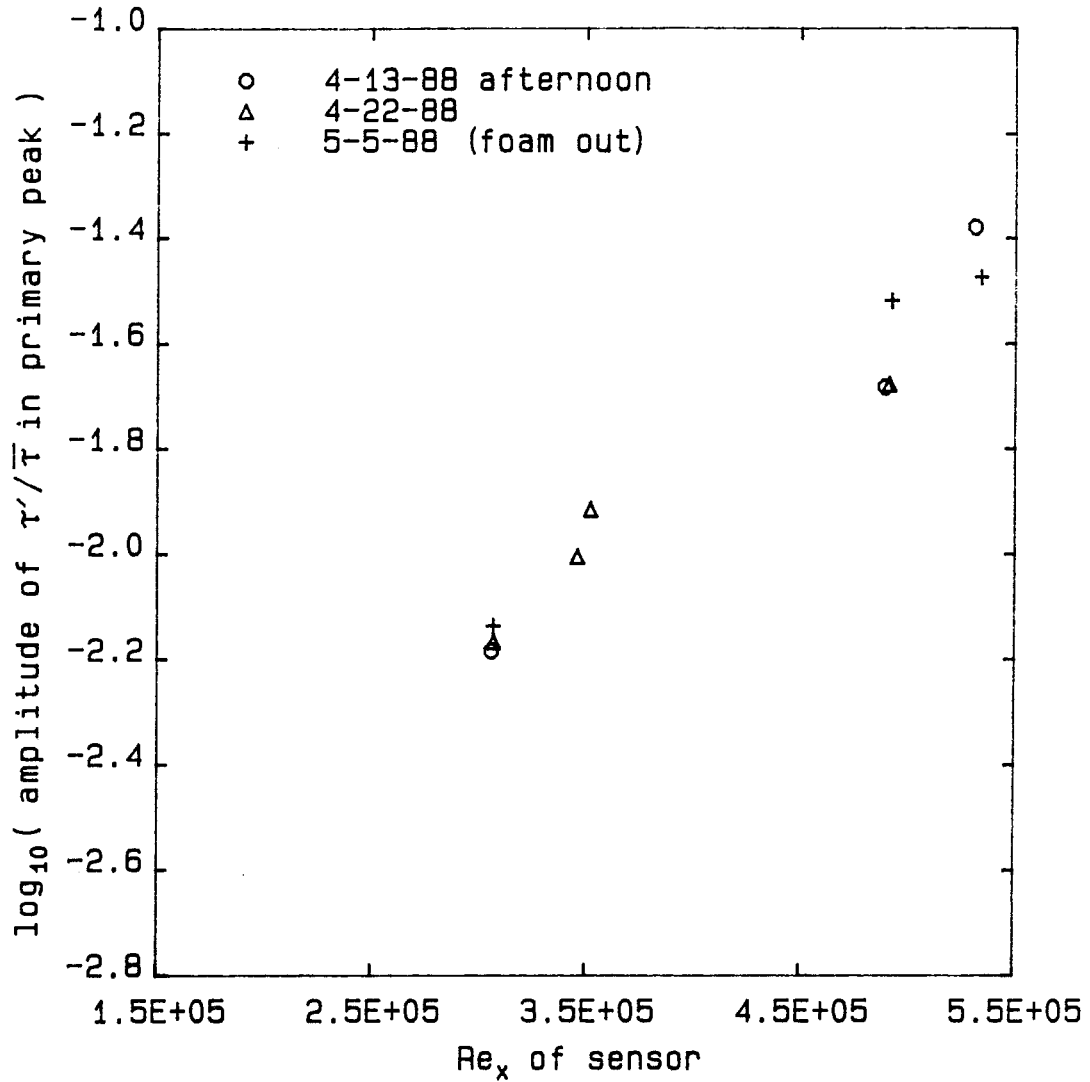


Figure 3.16: Growth Rate of Waves Created with Same Forcing on Different Days
192 watts, $U_\infty = 3.68$ fps, 2D 20Hz,
heater at $Re_x = 1.5 \times 10^5$

The phase speed is therefore

$$\vec{c}_{phase} = \frac{\omega\alpha_r\vec{i} + \omega\beta\vec{k}}{\alpha_r^2 + \beta^2}.$$

However, the phase speed of the waves along the x direction is *not* $\vec{c}_{phase} \cdot \vec{i}$. This formula, which gives the component of the phase speed vector along the x-direction, does not give the speed of the constant phase lines along the x-direction. This formula instead gives a value which decreases relative to \vec{c}_{phase} as the wave angle is increased, whereas the correct formula gives a value which increases relative to \vec{c}_{phase} as the wave angle increases. The correct formula for the speed of constant wave phase lines in the x-direction (which is here called the 'phase speed in the x-direction', or $c_{phase,x}$), can be easily derived from first principles, and is

$$c_{phase,x} = \frac{\omega}{\vec{k} \cdot \vec{i}}$$

or

$$c_{phase,x} = \frac{\omega}{\alpha_r}.$$

This phase speed in the x-direction is what was measured in the experiments reported here.

This phase speed in the x-direction was obtained using time-of-flight measurements of the wave travel between streamwise sensors. Eight second data records were digitized at 1000Hz on several sensors for a set of forcing conditions. Cross-correlations of these records were computed, and the time-of-flight taken from the average shift of the position of the first few peaks in the correlations away from the positions which would occur for an autocorrelation of these periodic signals. The exact time of the peaks was interpolated from the cross-correlation data.⁸ The rms variation (among the correlation

⁸see Hildebrand [15, p. 75]

maxima) of the shift was generally less than a few percent. Since the distance between the sensors is known very accurately, and the timing can be measured precisely, the phase speed results should be precise.

For one set of measurements, three sensors, S1F, S1R, and S2 were used. The first pair were located 0.200 inches apart, which is considerably less than one streamwise wavelength of the waves. The results from these nearby sensors were not very accurate, but served to give an estimate of the phase speed within about 10%.

The second pair of sensors, which are slightly more than one wavelength apart, were used to give a more exact value, the time corresponding to one wave period being added into the time-of-flight to give the total phase shift between the two sensors. Two typical cross-correlations for the data from these sensors are given in Figure 3.17. The cross-correlation for the 2D wave shows the large fluctuations which would be expected for a highly coherent wave. The correlation for the 32 degree wave, however, shows much smaller fluctuations, indicating that these large angle waves remain much less coherent as they travel downstream across the two sensors. From this and from similar data for the scatter in the time-shifts among the individual peaks, one expects the phase speed data for the higher angle waves to have more scatter. That this is true also, but to a lesser extent, for the extreme high and low frequency wave data, can be seen from Figure 3.18 which shows cross-correlations for the extreme frequency waves forced with 2D phase. Figure 3.19 shows the phase speed results for these sensors for the highest amplitude forcing used. An increase of phase speed with frequency is evident, as is a fair amount of scatter. The values cluster around 0.4, a value can be compared to the linear theory (see Figure 3.20). The experimental values are a little higher than the linear theory, but the agreement is good,

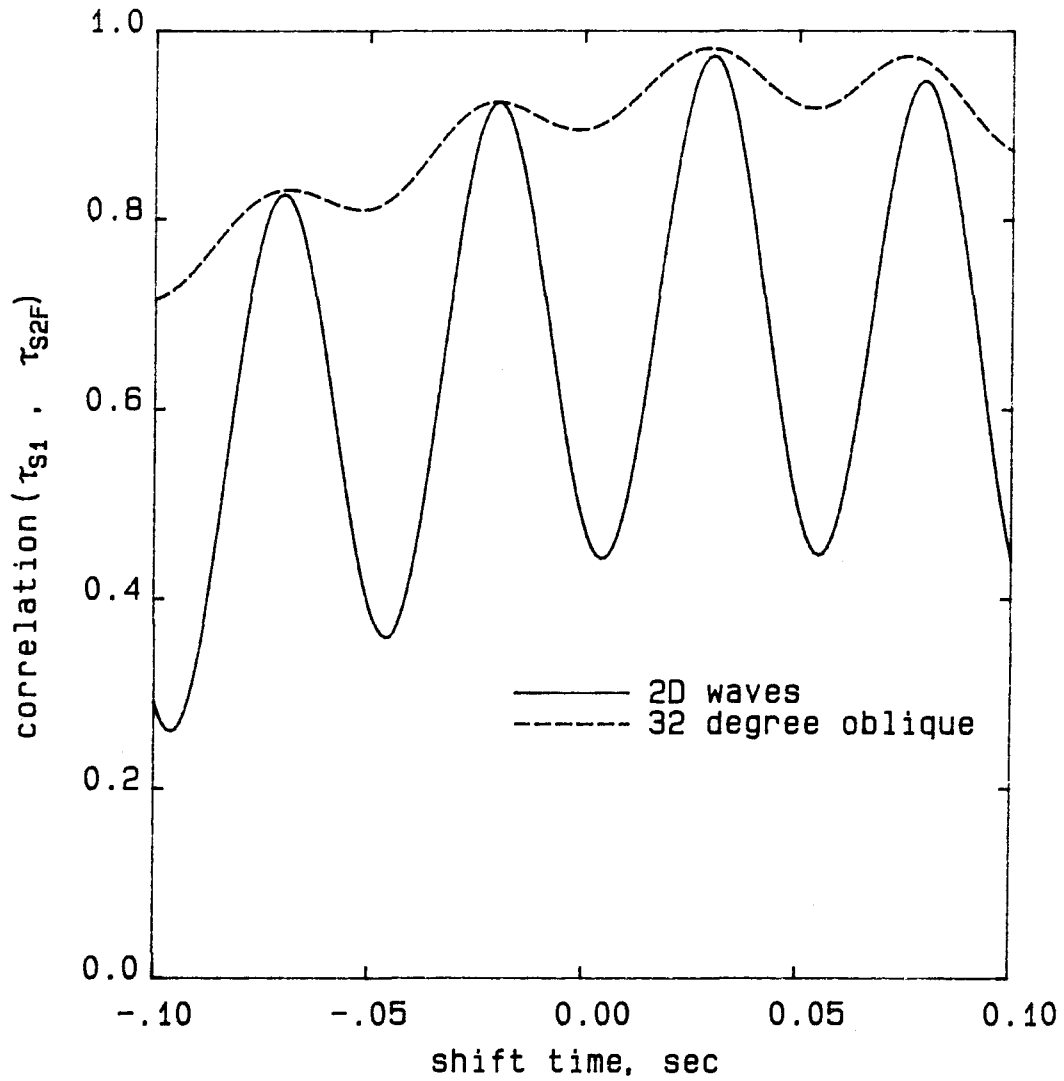


Figure 3.17: Cross-Correlation of Low Reynolds Number Phase Speed Data
20Hz 192 watt forcing, S1 and S2F, 4-22
 $Re_{\delta^*}(S1) = 1100$, $Re_{\delta^*}(S2F) = 1150$, $U_{\infty} = 3.68$ fps

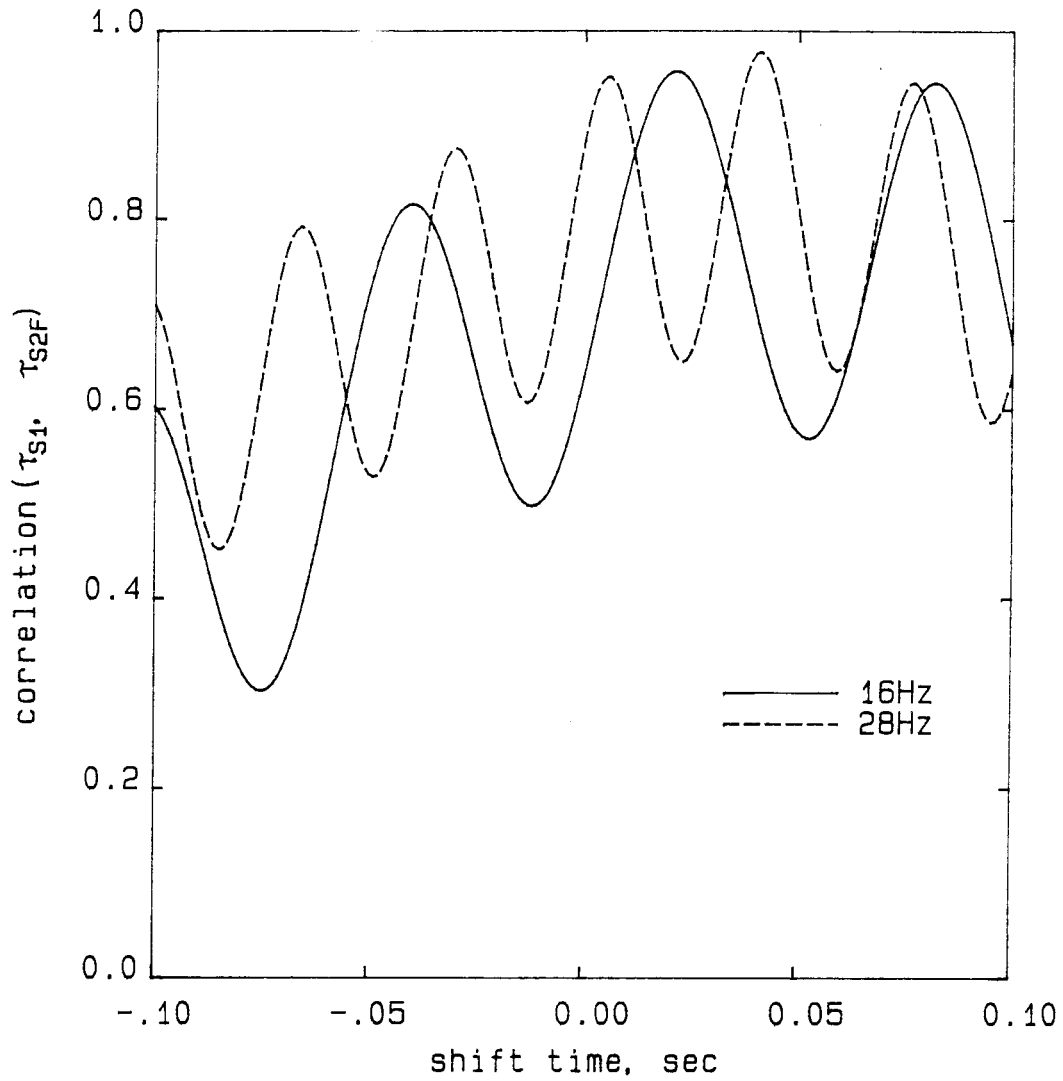


Figure 3.18: Cross-Correlations for Extreme Frequency Data
192 watt 2D forcing, S1 to S2F, 4-22
 $Re_{\delta^*}(S1) = 1100$, $Re_{\delta^*}(S2F) = 1150$

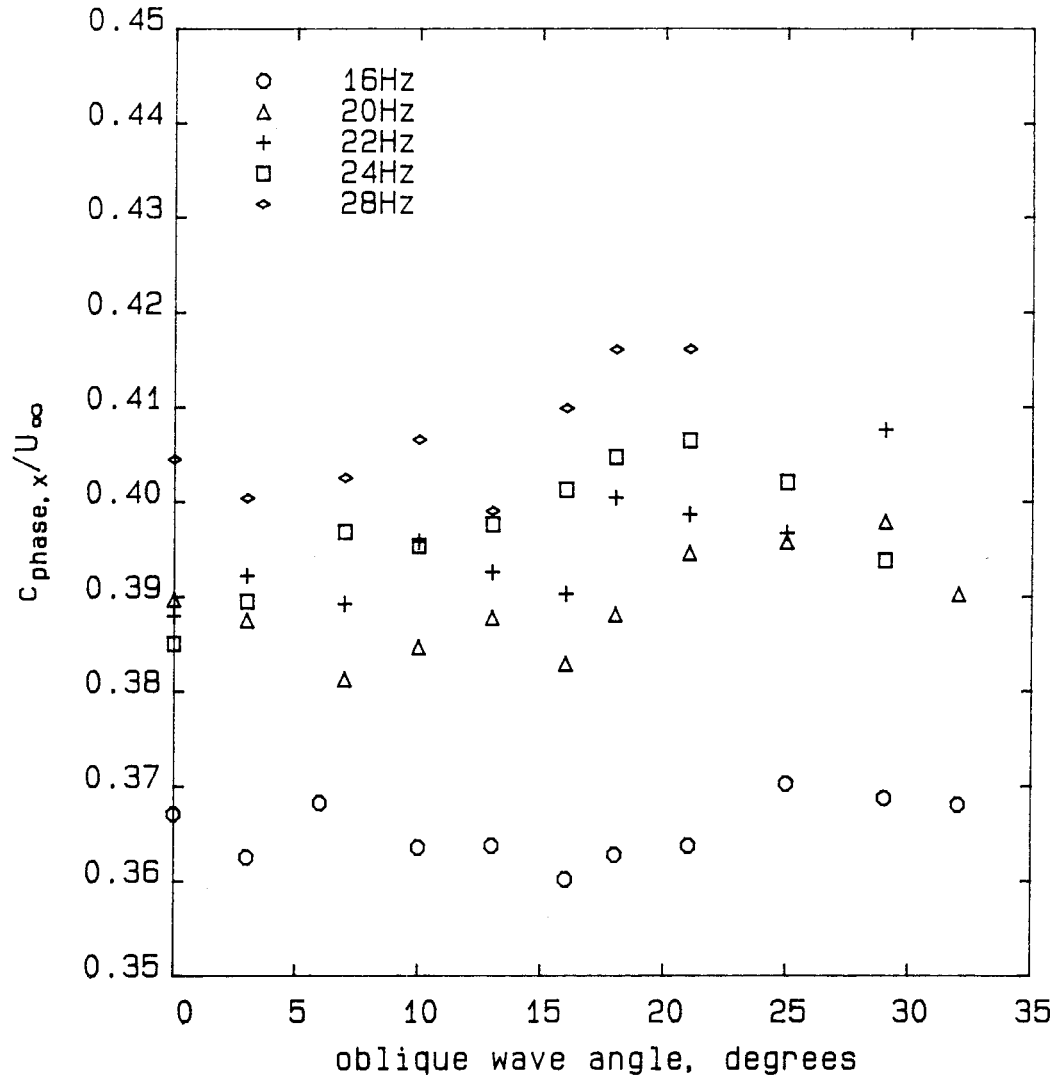


Figure 3.19: Phase Speeds for Oblique Waves at $Re_{\delta^*} = 1100$
at five heating frequencies, from S1 to S2F
192 watts, 4-22, $Re_{\delta^*}(S1) = 1100$, $Re_{\delta^*}(S2F) = 1150$

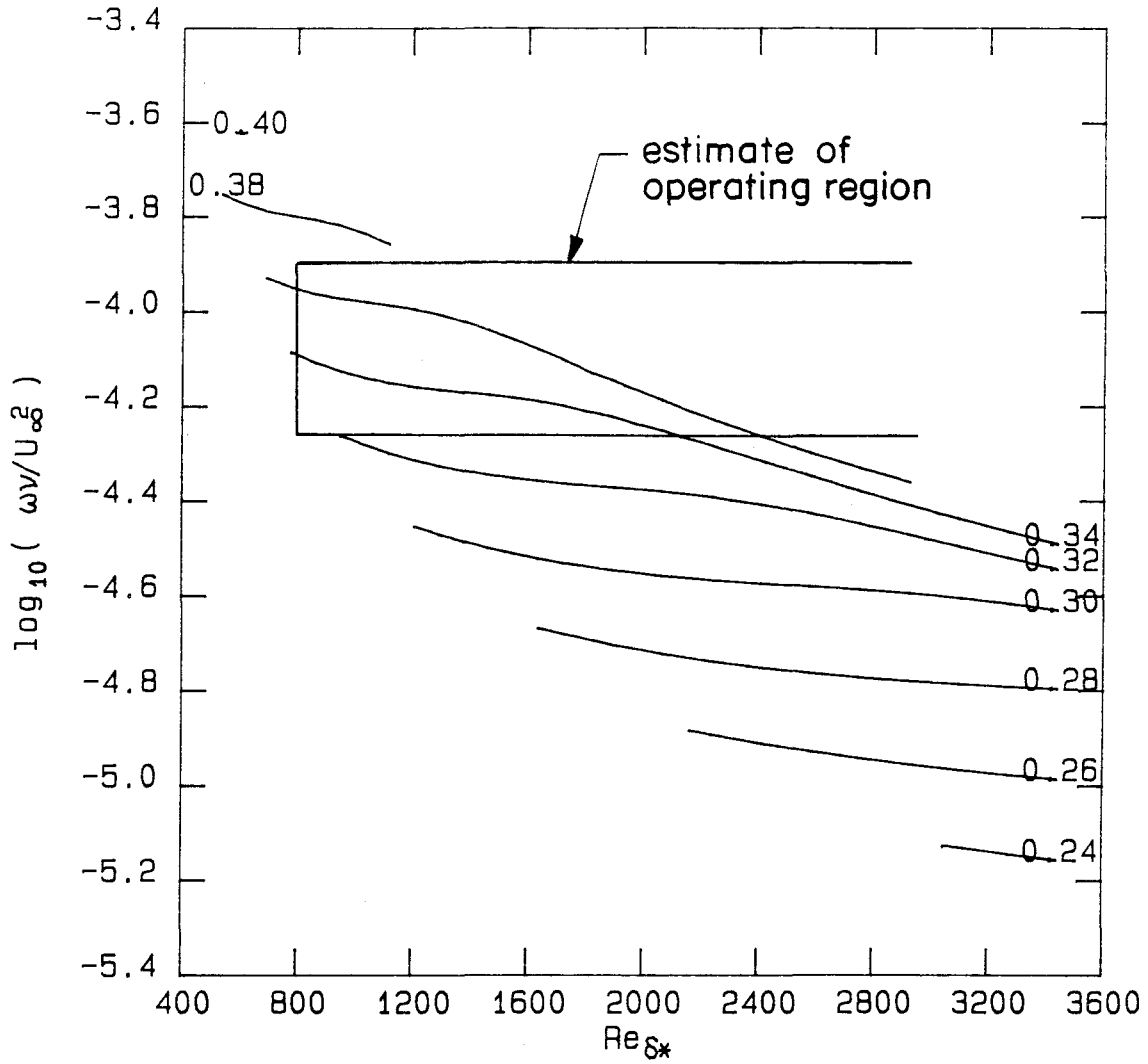


Figure 3.20: Linear Theory Results for Streamwise Phase Speeds
contours of $c_{phase,x}/U_\infty$ at 0.02 intervals
2D linear theory results from L. Mack
see Section 3.2 for operating region estimate

considering that the linear theory has not been corrected for the leading edge pressure gradient, and does not contain non-parallel flow corrections. Neither is the experimental Reynolds number a precise quantity, since no direct measurements of the boundary layer thickness were made. The data for the lower forcing amplitudes are similar, except they generally have more scatter due to the less coherent waves generated.

Measurements were also made using data from sensors S5 and S7, somewhat further downstream. The cross-correlation between these sensors is stronger, as may be seen from Figure 3.21. The cross-correlation carrier wave amplitude for the 2D wave is almost double that which was observed for the upstream data and remains fairly large for the largest angle oblique wave forced. The phase speed results are given in Figure 3.22. The values are noticeably smaller than for the lower Reynolds number data plotted above, and the scatter is less. The decrease in scatter is presumably due to the increased coherency of the waves. The decrease in phase speed with increasing Reynolds number agrees with linear theory, as does the increase in phase speed with frequency.

The increase in phase speed with wave angle which is evident in the figure can be expected from Squire's theorem (for the temporal case) [41, Equation 25]. This theorem states that the relation $F(\alpha, R, c)$ which gives the eigenvalue c , and thus the phase speed, can also be used for oblique waves of spanwise wavenumber β , if one uses the transformation $\bar{\alpha} = \sqrt{\alpha^2 + \beta^2}$ and $\bar{R}\bar{\alpha} = R\alpha$. It is important to note that in both cases $c = \omega/\alpha$, so that in both cases c is actually the streamwise phase speed. Thus the phase speed of a given oblique wave is the same as the phase speed of a 2D wave with a higher streamwise wavenumber and a lower Reynolds number. Since the theoretical phase speeds for the temporal case increase with decreasing Reynolds number

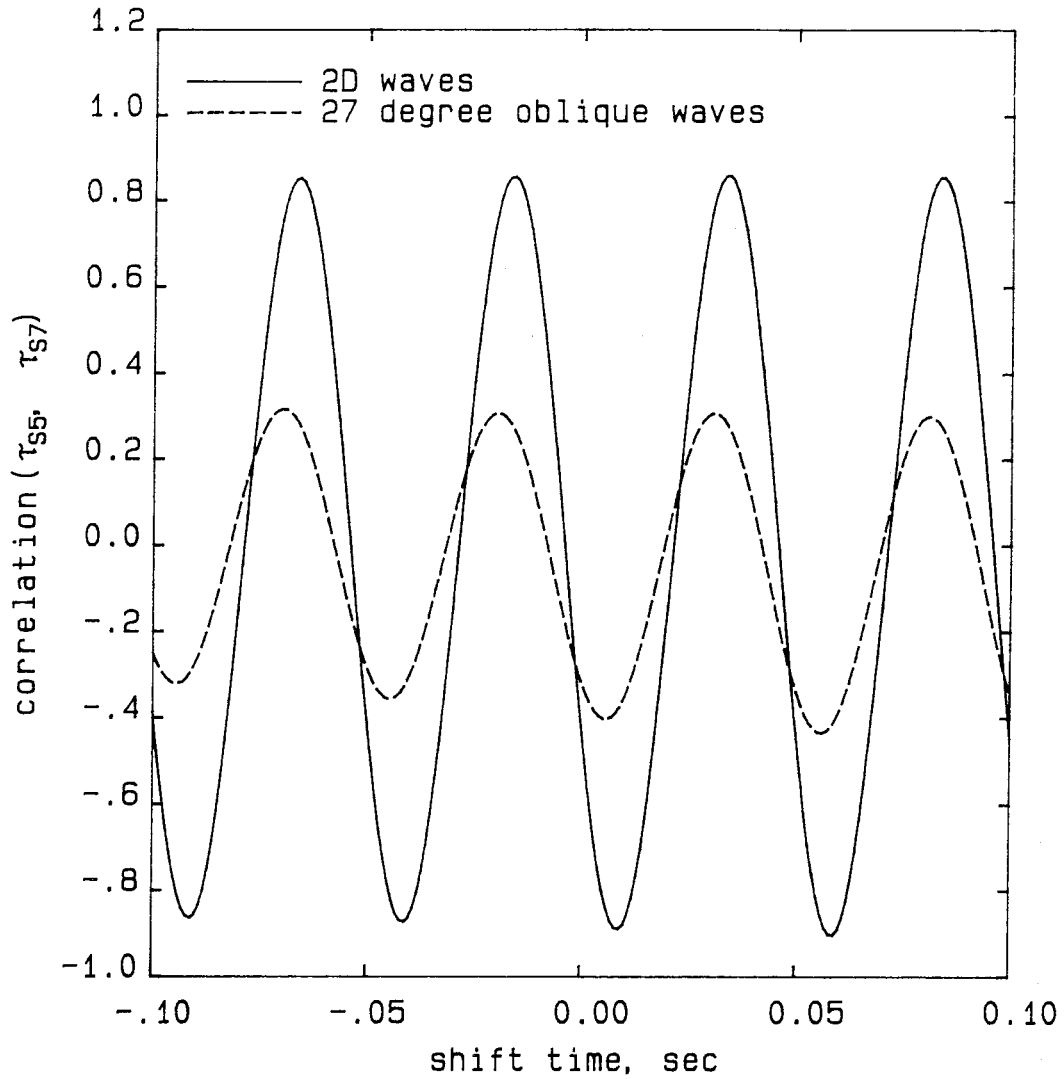


Figure 3.21: Cross-Correlation for High Reynolds Number Phase Speed Data
20Hz 192 watt forcing, S5 to S7, 4-13a, $U_\infty = 3.68$ fps,
 $Re_{\delta^*}(S5) = 1350$, $Re_{\delta^*}(S7) = 1400$

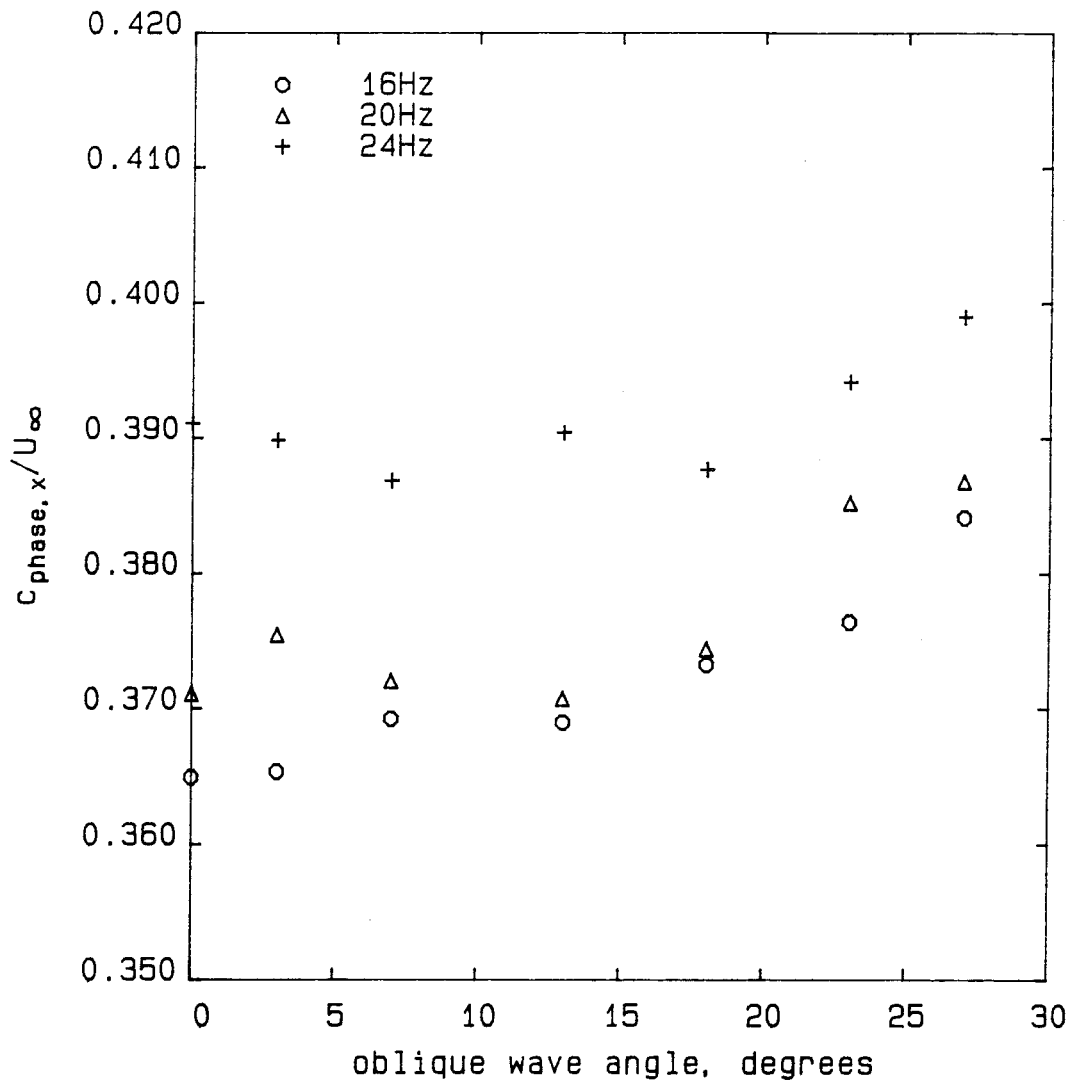


Figure 3.22: Streamwise Phase Speeds at $Re_{\delta^*} = 1400$
 $U_{\infty} = 3.68$ fps, $d = 1.375$ inches, 192 watts,
sensors S5 and S7, $Re_{\delta^*}(S5) = 1350$, $Re_{\delta^*}(S7) = 1400$, 4-13a

and increasing streamwise wave number (see e.g. Wazzan et al. [47]), the theory agrees with the experimental result that the streamwise phase speed increases with angle. Computations for the spatial case linear theory supplied by Mack [29] also show an increase of the streamwise phase speed, which for oblique waves of angle 30 degrees is about 5% above the 2D value⁹. The magnitude of this increase agrees well with the experimental data which shows an increase of about 0.02 in a value of about 0.38. The data for the lower amplitude forcing cases are again similar.

This change of phase speed with angle for oblique waves was previously measured by Kachanov [16, Figures 4,5] using a vibrating ribbon generator at two oblique angles, and also using an undefined spectral decomposition of wave packets. His results show a decrease in phase speed with increasing wave angle, the opposite trend to that reported here, although his measurements may refer to the phase speed perpendicular to the wave fronts. He reports an increase of phase speed with frequency; the same trend reported here. It is unclear whether his results for the phase speed, taken from the spectral decomposition, were corroborated by the single oblique wave data.

The phase speed results reported here are the first to cover a range of oblique angles. They agree well with the linear theory, and thus give a strong indication that the apparatus is really making the oblique waves about which we have extensive knowledge from study of the linear theory. The results also indicate that it is possible to make such linear oblique waves in a real flow. This is the first time that this has been shown to be possible.

⁹available computations, for $F = 6.0 \times 10^{-5}$ and $Re_{\delta^*} = 1380$. Experiment is at $F = 9.2 \times 10^{-5}$ and $Re_{\delta^*} = 1400$, which is not quite the same. However, the trend with oblique angle should be quite similar.

3.3.1.3 Measured Angles

The angles of the oblique waves were measured using data from sensors spaced apart spanwise at the same streamwise location. The phase lag of wave arrival at the different spanwise locations provides the angle. Cross-correlations were used to obtain the mean phase lag between the sensors. These give the average phase lag over the eight seconds of data acquired (roughly 150 cycles). The method of computing the phase lag is the same as that used for the phase speed analysis above.

The first experiment used sensors S1N and S1S, which were spaced 0.200 inches apart. These sensors are fairly far upstream, where the waves are not yet well-developed, as can be seen from the typical cross-correlations plotted in Figure 3.23. The results for the phase lags between the sensors are presented in Figure 3.24. The phase lag increases with the increase in the heater phase lags, as expected, but then drifts away from the expected curve. This is presumably due to the effects of irregularities in the wave fronts (see Figure 1.2). This unexpected behavior may also be at least partially due to the weakly formed nature of the waves at the far upstream station where these data were taken. Many of the stray points in these plots can be traced to the weak cross-correlations which exist for weakly amplified waves.

The experiment was then repeated using sensors S4, S5, and S6, which are spaced 2.375 inches apart farther downstream. The cross-correlations for these data (see Figure 3.25) are much stronger, in spite of the fact that the sensors are ten times as far apart as the ones used above. This increased spatial coherency is presumably due to the longer fetch the waves travel through before they reach the measuring station. The importance of this effect of fetch should be emphasized, since it is an effect rarely discussed in

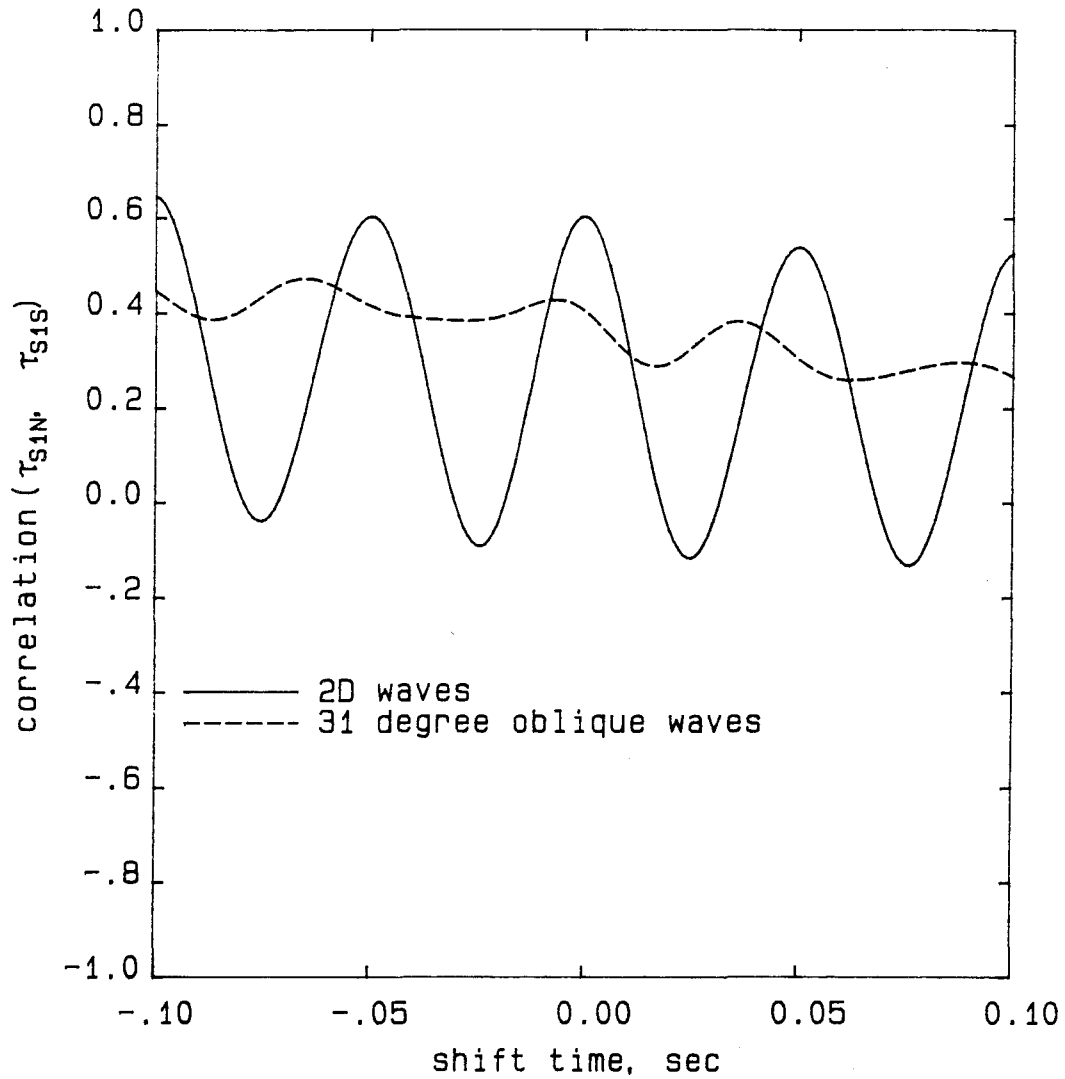


Figure 3.23: Typical Cross-Correlations for Nearby Sensor Wave Angle Data
20Hz 192 watt forcing, S1N and S1S, 0.200 inch spacing,
 $Re_{\delta^*} = 1050, 4-7$

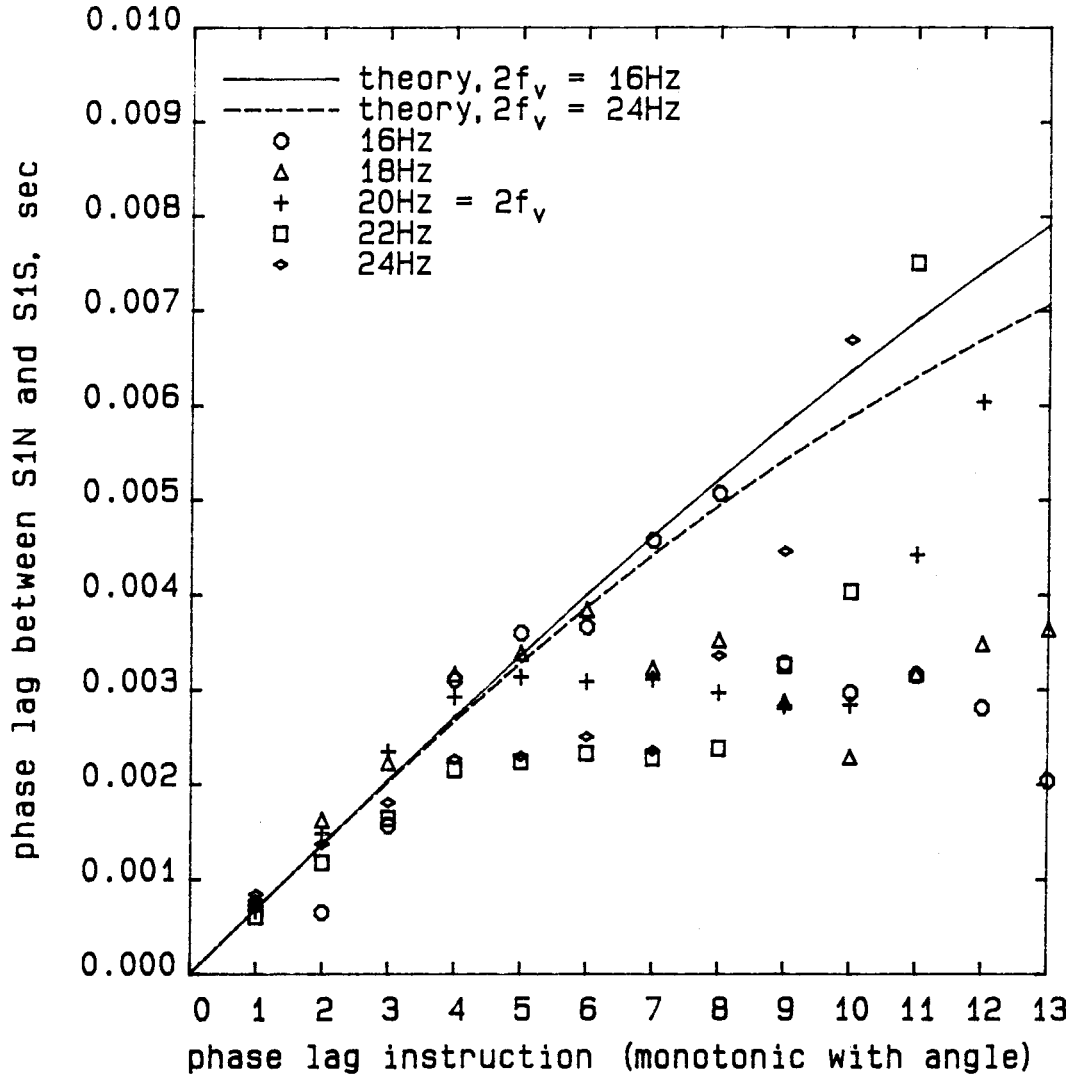


Figure 3.24: Wave Angle Phase Lags for Nearby Sensors S1N and S1S, $Re_{\delta^*} = 1050$, 192 watts, 4-7
theory (Equation 3.2) uses $c_{phase,x} = 0.38U_{\infty}$, $U_{\infty} = 3.52$ fps

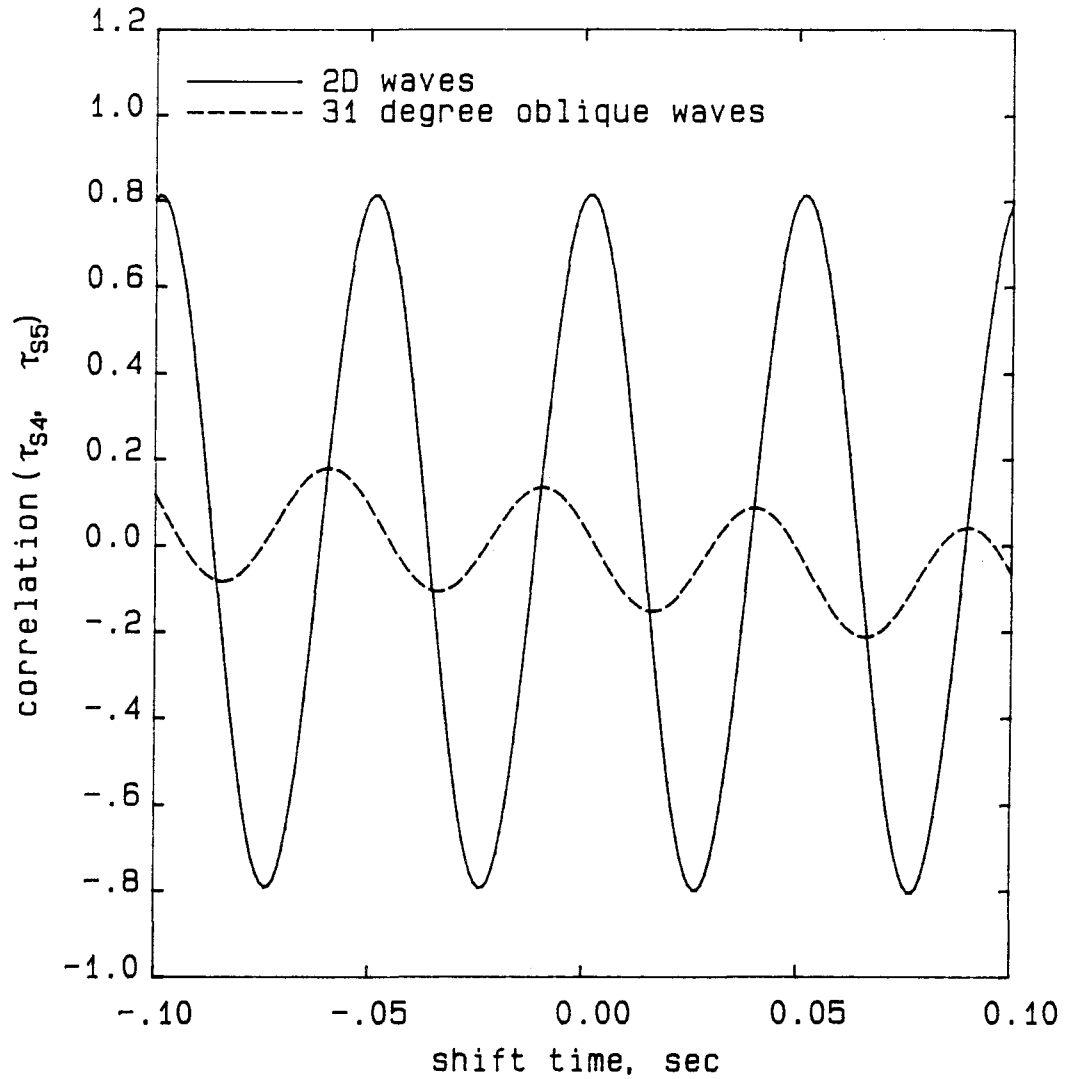


Figure 3.25: Typical Cross-Correlations for $Re_{\delta^*} = 1300$ Wave Angle Data
20Hz 192 watt forcing, 4-13mI data

the literature. The results for the phase shift are given in Figure 3.26. The results for the other phase shift combinations possible with the three sensor records are very similar and show that the wave angles measured downstream match those that the apparatus was expected to generate¹⁰. Thus, the apparatus is really making oblique waves at the angle expected. This, again, is the first measurement of this kind and shows both that the apparatus is capable of making oblique wave fronts, and that they can develop in a reasonably stable fashion in the boundary layer.

The angles used in the experiment are controlled by the phase lag instruction issued by the computer. In order to determine the actual angles, a table of the oblique wave angles that correspond to a given phase lag instruction was computed. For this purpose, the angles can be computed from the theory, which as shown above closely fits the data. The theory is based on the phase lag created by the controller circuitry¹¹, and on the phase speed of the instability waves, which is taken to be $0.38U_\infty$, a good approximation to the measured phase speed data. The theory uses the equation

$$\tan \theta = \frac{\lambda_{streamwise}}{\lambda_{spanwise}},$$

where

$$\lambda_{streamwise} = U_\infty \frac{c_{phase}}{U_\infty} \frac{1}{2f_v},$$

and

$$\lambda_{spanwise} = \frac{2\pi b}{32(2\phi_v)}.$$

Here b is the spanwise distance between the end heaters of the 32 heater array, and ϕ_v is the phase shift in the voltage signals between adjacent heaters; that

¹⁰Although it is the spanwise wavenumber β , and not the wave angle θ , which should really be constant as the waves travel downstream – see Mack [27, Sec. 2.6.1]

¹¹see Appendix A.2.2

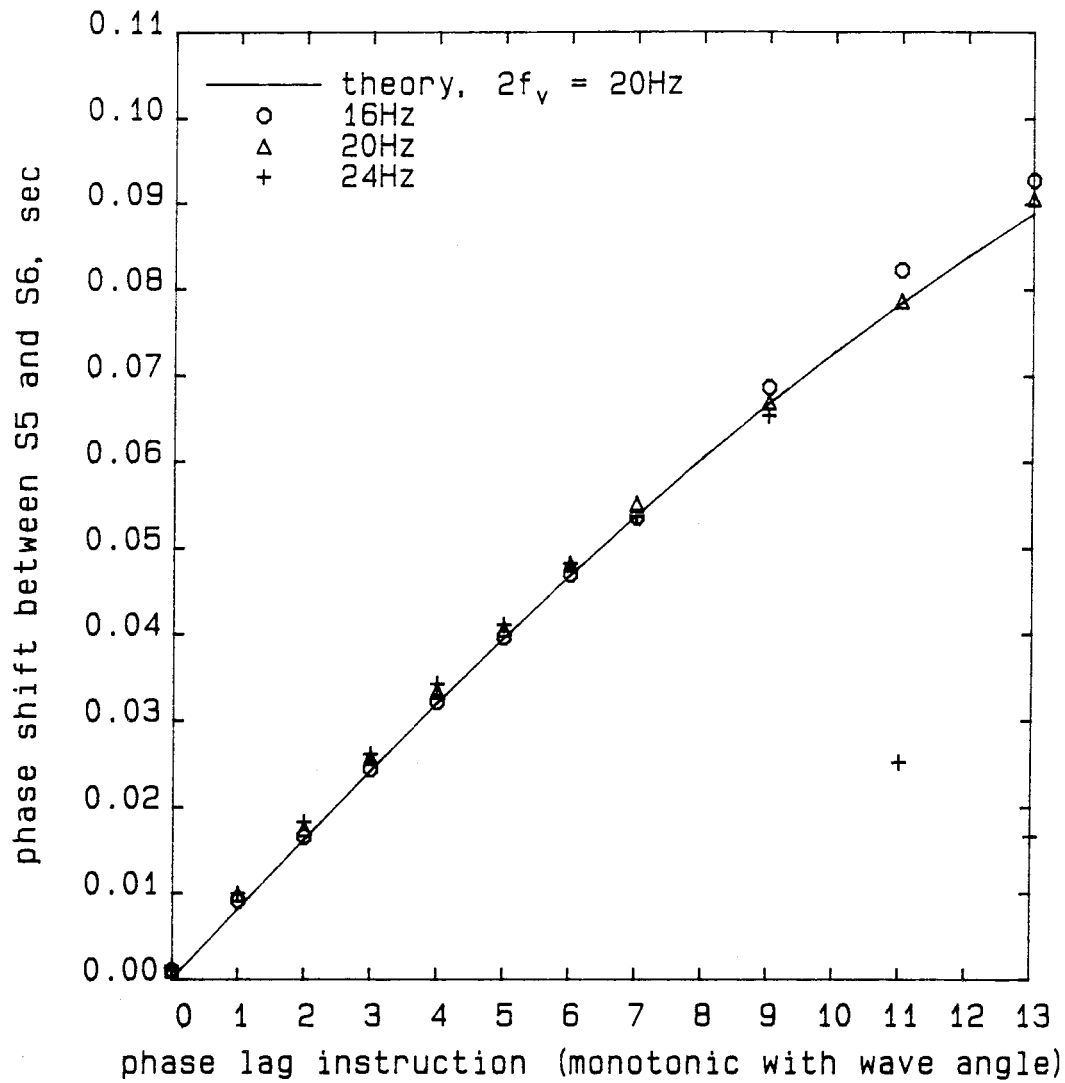


Figure 3.26: Average Phase Shifts vs. Angle for Oblique Waves
S5 and S6, $U_{\infty} = 3.50$ fps, 192 watts
 $Re_{\delta^*} = 1300$, phase lag instruction 13 is 31 degree waves
theory (Equation 3.2) uses $c_{phase,x} = 0.38U_{\infty}$
the 24Hz large angle waves have weak cross-correlations

is

$$\phi_v = 2 \arctan(2\pi f_v nRC), \quad (3.1)$$

where f_v is the voltage forcing frequency in Hz, R and C are resistor and capacitor values installed in the controller, and n is the instruction for the phase lag. When the proper values are substituted, the following equation for the angles results:

$$\tan \theta = \frac{U_\infty(c_{phase}/U_\infty) \arctan(0.00628nf_v)}{1.8285f_v}. \quad (3.2)$$

Equation 3.2 is used to compute the values used in this thesis. For small nf_v , it is evident that the angle θ is independent of the forcing frequency, an observation that simplifies the data analysis considerably. For the largest angles used in this thesis, the angles differ for the different frequencies only by about $\pm 5\%$, which does not seem material. Angles quoted in the thesis will be given for waves with $f_v = 10\text{Hz}$. The wave angle results for the two freestream velocities most commonly used are in Table 3.2.

3.3.2 Nonlinear Oblique Waves

The instability waves grow along the plate until they become nonlinear. This can be seen from plots of their spectra, made from data taken from sensors placed farther downstream. Figure 3.27 shows the spectrum of a set of particularly nonlinear waves. The plot shows spectra of 2D waves for three different forcing frequencies. One can clearly see the subharmonics and second and third harmonics¹², as well as $\frac{3}{2}$ harmonics.

Robey [34, Figure 5.10] observed a general filling in of the subharmonic region of the spectra for large oblique waves, with the amount of this low-

¹²If the primary frequency is f , the second harmonic is defined to be $2f$, the third $3f$, and so on. See Webster's New International unabridged dictionary, second edition, under 'harmonic'. Subharmonics are here usually $f/2$.

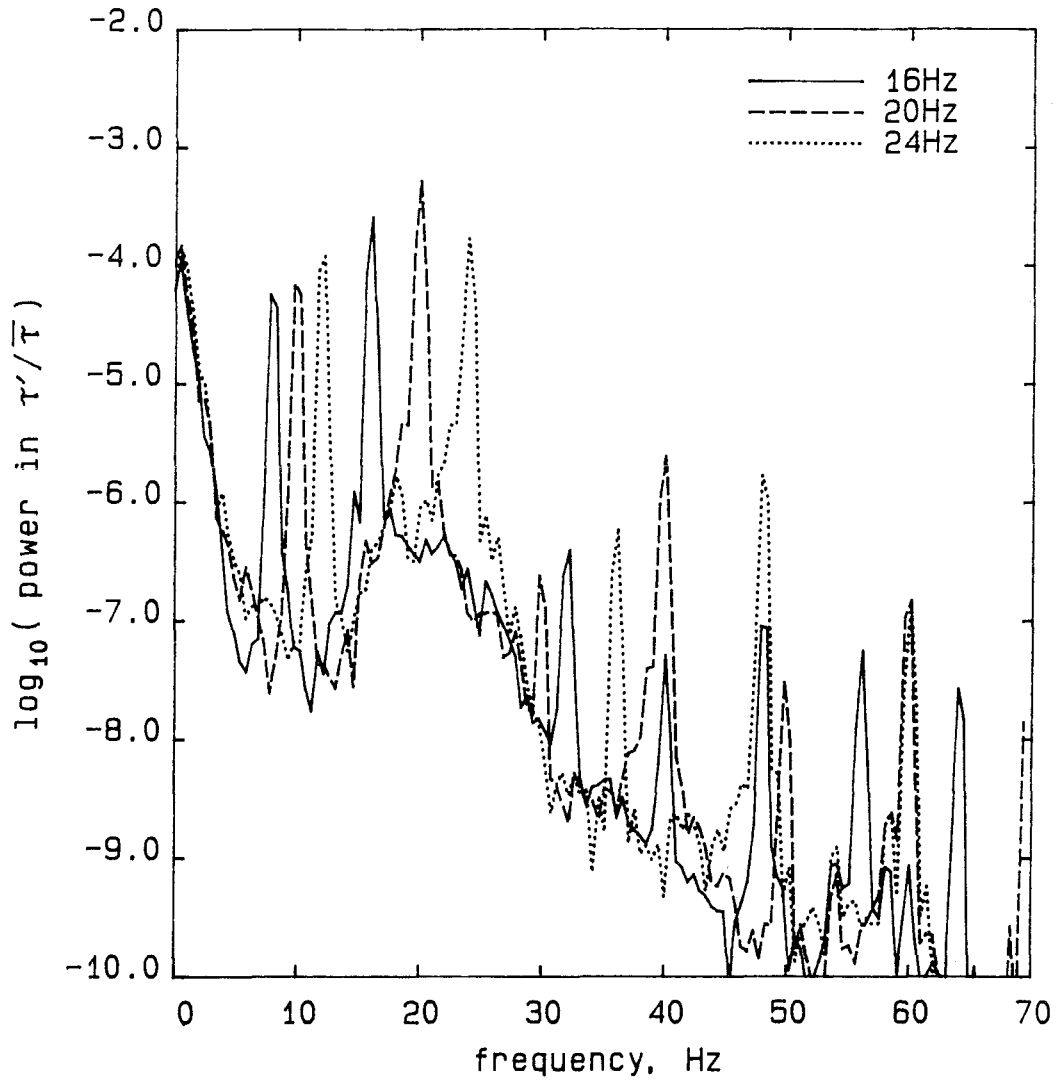


Figure 3.27: Wall Shear Spectra for Highly Nonlinear Waves
S4, $Re_{\delta^*} = 1300$, $U_{\infty} = 3.50$ fps, 4-13mII
192 watts

n	$f_v = 10\text{Hz}$		$f_v = 8\text{Hz}$
	$U_\infty = 3.69\text{ft/sec}$	$U_\infty = 3.50$	$U_\infty = 3.69$
	θ	θ	θ
0	0 degrees	0 degrees	0 degrees
1	3.3	3.1	3.3
2	6.6	6.2	6.6
3	9.7	9.2	9.8
4	12.8	12.1	12.9
5	15.6	14.9	15.8
6	18.3	17.5	18.6
7	20.9	19.9	21.3
8	23.2	22.1	23.7
9	25.3	24.2	26.0
10	27.3	26.1	28.2
11	29.1	27.8	30.1
12	30.7	29.4	32.0
13	32.2	30.9	33.6

Table 3.2: Wave Angles vs. Phase Lag Instruction for Oblique Waves

frequency content increasing dramatically as the oblique wave angle was increased. This behavior was supposed to result from the increased non-linearity of the oblique waves. Although for some large waves this spectral filling in was also observed in the current work, there was no evidence to support the trend with oblique angle reported by Robey. Robey [35] later suggested that this might be due to the larger waves he could create. Detailed comparisons are impossible because of the lack of quantitative information in Robey's reports.

3.3.2.1 Higher Harmonics

Second harmonics are always seen on all sensors located in the nonlinear region and are in fact the clearest sign that the waves have entered the nonlinear region. A typical set of spectra showing second harmonics only is

attached as Figure 3.28. The figure shows spectra for five forcing frequencies of 13 degree oblique waves. Second harmonics are visible for all five frequencies.

At smaller amplitudes of the primary wave, the harmonics are smaller. Figure 3.29 shows the amplitude of the second harmonic vs. the square of the amplitude of the primary wave for 20Hz waves of various oblique angles, created using differing initial perturbation amplitudes. It can be seen that the second harmonic increases quadratically with the primary response, as might be expected if it is caused by a simple nonlinear interaction (see e.g. Robey [34, Figure 3.8]). If the shear consists of a single harmonic,

$$\tau = \epsilon \sin \omega t,$$

then a quadratic nonlinearity which goes like $c_0\tau^2$ will produce a signal

$$\tau = \epsilon \sin \omega t + \frac{c_0\epsilon^2}{2}(1 - \cos 2\omega t).$$

Plotting the square of the amplitude of the fundamental against the amplitude of the second harmonic should then give a linear curve that increases with the fundamental, as is seen in the figure. It is also evident from the figure that there is no marked change in the coefficient c_0 for oblique waves, at least for small angles.

The amplitudes of the primary and the second harmonic decrease slowly with increasing oblique angle, as shown in Figure 3.30. It can be seen that the harmonic persists with increasing angle, remaining at a nearly constant ratio to the primary even for angles larger than those plotted in Figure 3.29.

It was hoped that this kind of study of the second harmonic would provide a clear indication of the primary amplitude at which the wave becomes nonlinear (through some sudden change in the behavior of the second harmonic at a threshold value of the primary). However, the evidence is that

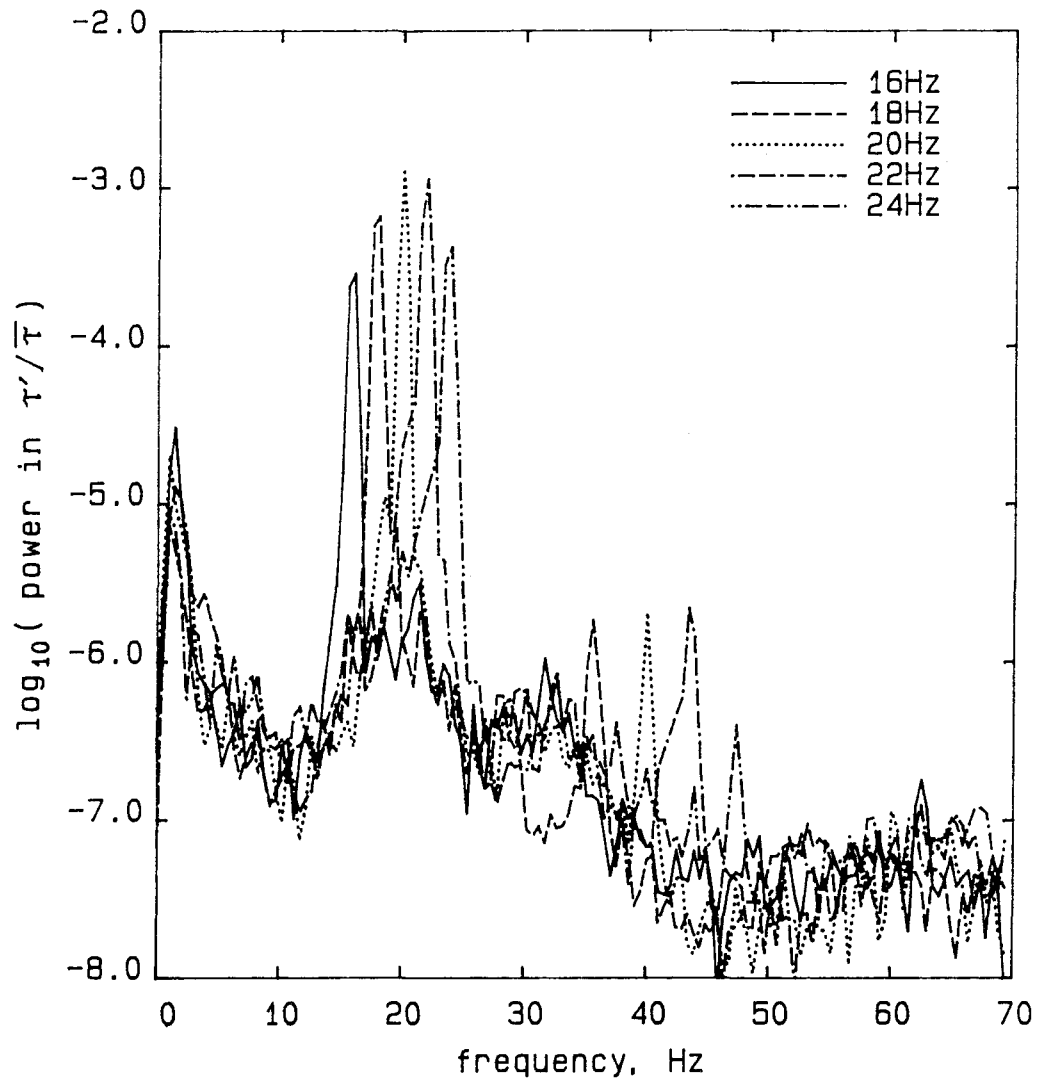


Figure 3.28: Wall Shear Spectra Showing Second Harmonics
S7, $Re_{\delta^*} = 1400$, 192 watts, 2D waves, 4-13a

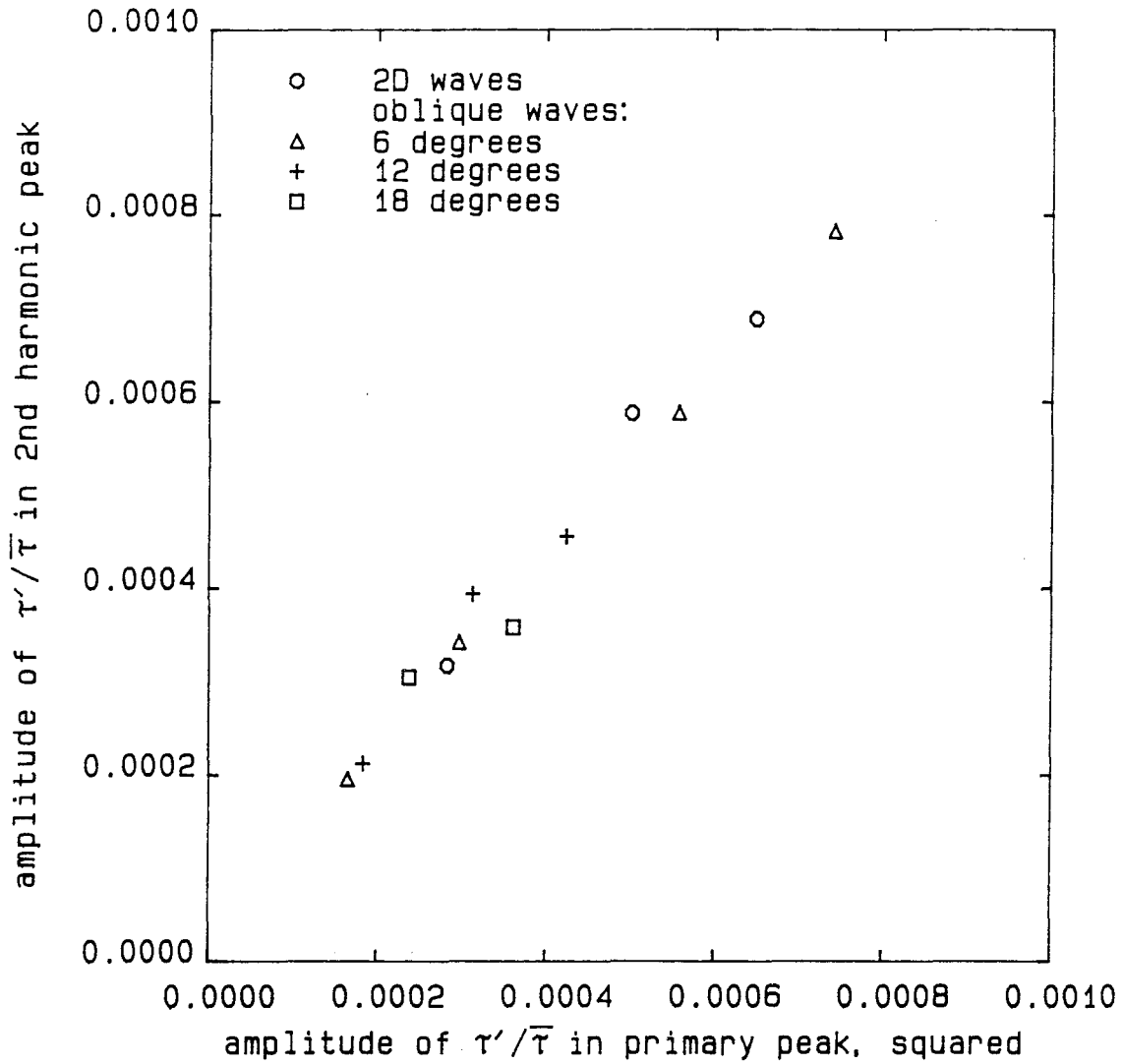


Figure 3.29: Amplitude of Second Harmonics vs. Primary
20Hz, S6, $Re_{\delta^*} = 1300$, 4-13mII, varied heater power

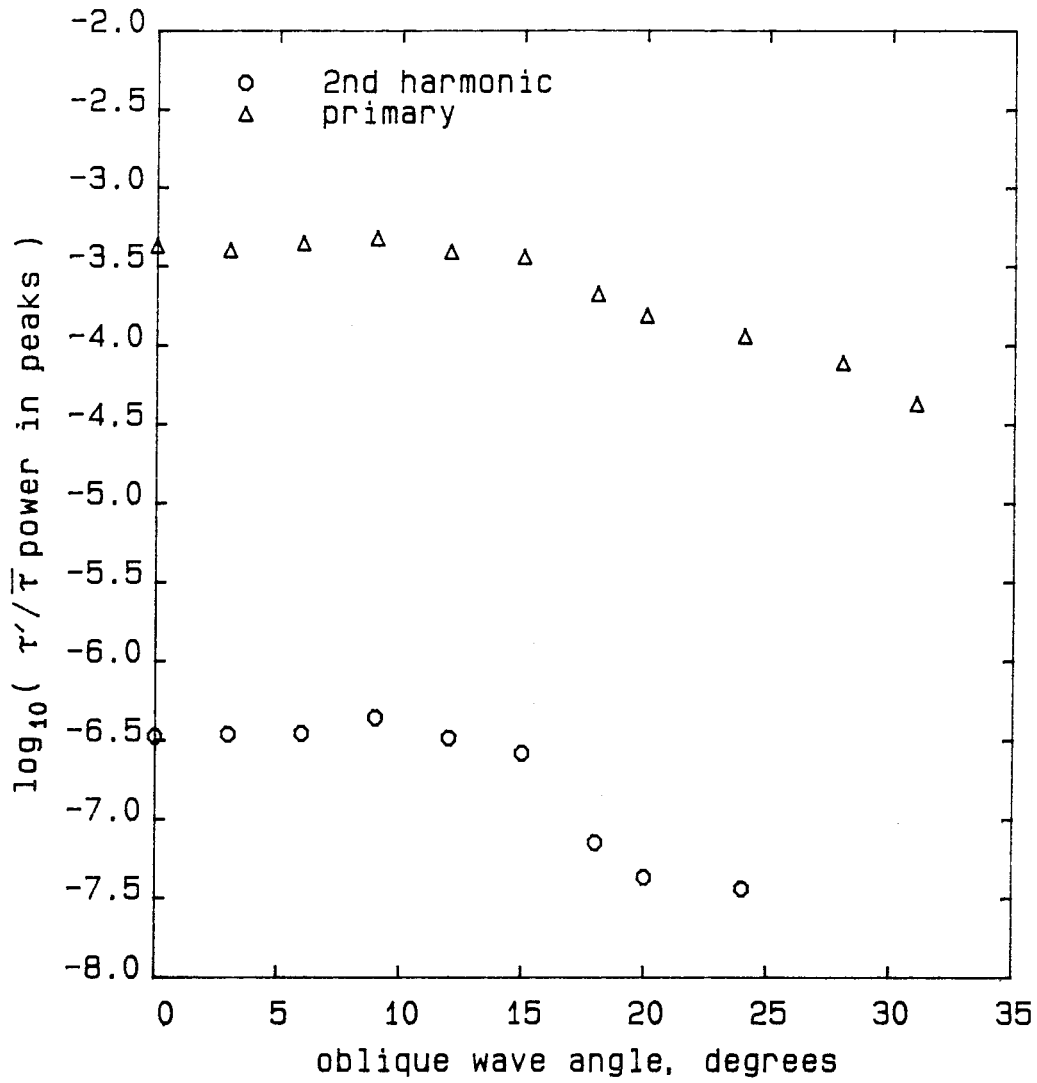


Figure 3.30: Amplitude of Primary and Second Harmonic vs. Angle
S5, $Re_{\delta^*} = 1300$, $U_{\infty} = 3.50$ fps, 20Hz,
192 watts, 4-13m

the amplitude of the second harmonic increases slowly with the amplitude of the primary, the amplitude at which it first becomes visible being dependent only on the noise level in the spectra. Thus, there does not seem to be any threshold at which the second harmonic suddenly appears; rather, the development of nonlinearity is a continuous process, at least in so far as the second harmonic is concerned. This smooth development of the second harmonic can also be seen in the experimental results of Kachanov et al. [17, Figure 4d].

A typical time trace showing the signal for a weakly nonlinear wave is shown as Figure 3.31. The signal digitally filtered around the second harmonic is also plotted to bring out phase relation of the two signals. It can be seen from the phase of the second harmonic that the nonlinearity generally seems to act to increase the shear in the trailing edge (later time) face of the waves, above the value for sinusoidal waves (see especially the central portion of the figure, away from the edge effects of the filter). A similar effect can be seen in the streamline computations for large amplitude 2D instability waves by Lessen [25, Figure 4], which show a stretching out of the streamlines behind the maximum of the wave.

If one looks again at Figures 3.27 and 3.28 (and at Figures 3.41 and 3.44), it can be seen that the individual peaks for the fundamental and higher harmonics tend to slope down more gradually on the low frequency side than on the high frequency side, at least for frequencies somewhat away from the central maxima. No explanation of this behavior has yet been found.

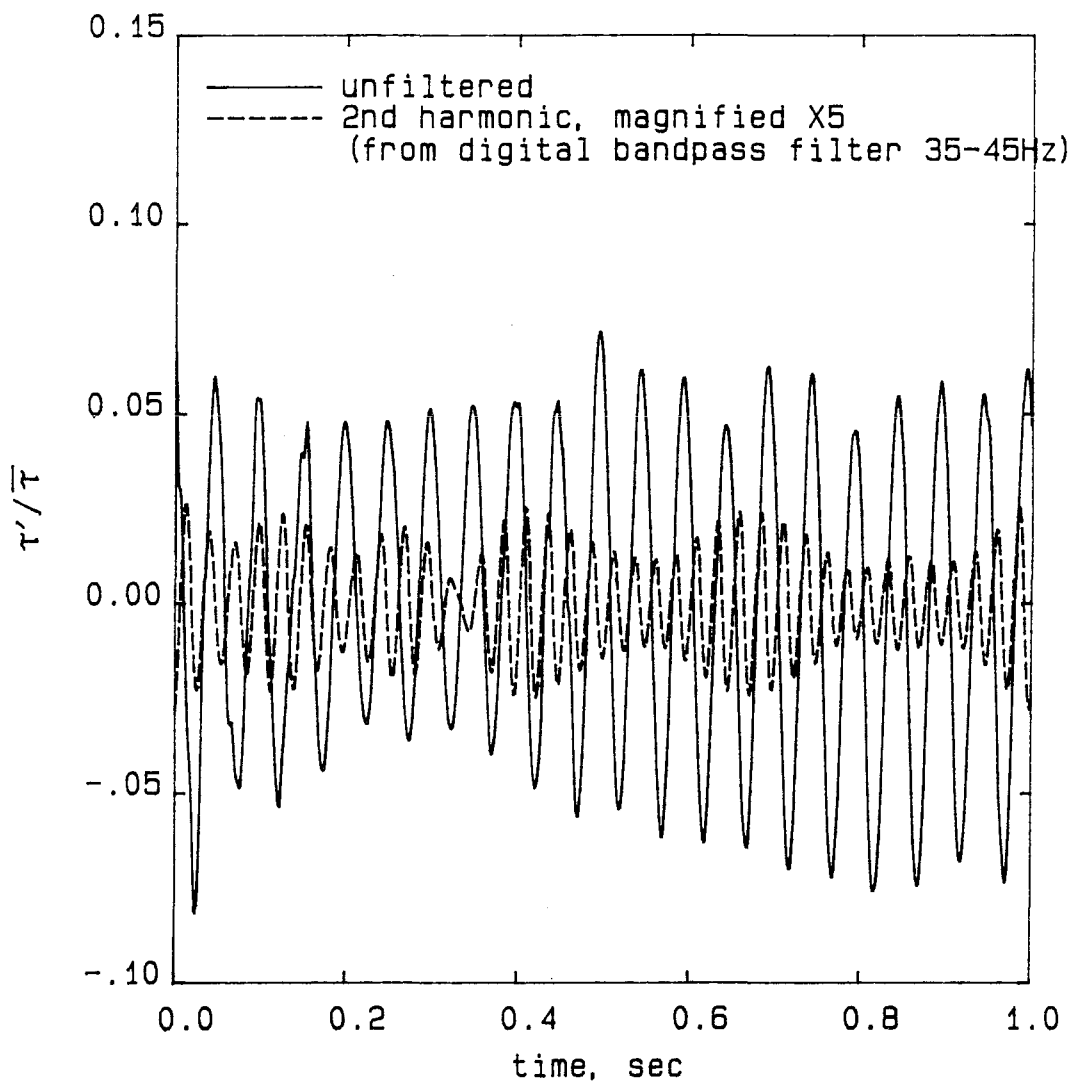


Figure 3.31: Time Trace of Nonlinear 2D Wave Showing Second Harmonic
S7, $Re_{\delta^*} = 1400$, $U_{\infty} = 3.68$ fps, 20Hz 2D, 4-13a

3.3.2.2 Subharmonics

Subharmonics are often seen on the sensors in the nonlinear regime¹³, starting downstream of the region where the second harmonic is first seen. Subharmonics are not seen at all spanwise locations, but seem to vary in amplitude across the span in a random fashion, the location where they are seen depending on the day, but remaining uniform in the course of a day. This behavior is not surprising for an effect which can be expected to depend on the details of three-dimensional irregularities in the freestream flow. These irregularities depend strongly on the amount of contaminants blocking the turbulence damping screen upstream of the honeycomb, and so the pattern of irregularities can be expected to depend on the particular contaminant pattern existing on a particular day. If the surface waves above the plate affect the irregularities, they will change depending on the leads to the back side of the plate that are used on a particular day. Finally, the uniformity of the heater power output, while good, is not perfect, and the irregularities change slowly with time as heaters corrode or as the electronic circuits drift.

One would expect the appearance of the subharmonics to vary across the span, since they are a three-dimensional effect of late transition. One might expect the position to vary with time; however, if the spanwise location of the subharmonic is phase-locked to three-dimensional nonuniformities in the freestream flow or in the heaters, it might well be located in a fixed spanwise position. A flow with a perfectly uniform staggered pattern of lambda vortices might be expected to show subharmonics everywhere. However, one of the standard references for subharmonic transition in a boundary layer reports a variation of subharmonic amplitude with spanwise position large

¹³On roughly one-third of the sensors in this loosely defined region

enough that the subharmonic vanishes at the spanwise node (see Kachanov [19, Figure 14b]). Moreover, flows with subharmonic components often show a mixed transition pattern where some of the lambda vortices are in-line and some are staggered, with the pattern varying across the span (see Spalart et al. [40, Figure 2h]).

The subharmonic results given here were very carefully checked to make sure they were not an artifact. This check is important because the frequency of the forcing voltage is half the heating frequency and is the same frequency as the response subharmonic. Weak electronic pickup from the heating electronics can thus easily masquerade as a flow subharmonic. The following checks were carried out, among others: First, the forcing electronics were carefully isolated from the sensing electronics, as described in the Appendices. Second, the pair forcing results of section 3.4.1.2 show that the amplitude of the subharmonic varies in a reasonable fashion as the location of the forced pair of heaters is varied across the span. Third, the subharmonic results presented were seen on all the sensors, at different times, and using many different combinations of signal conditioning elements. Fourth, $\frac{3}{2}$ harmonics can be seen in Figure 3.27, which must occur through interaction of the primary and subharmonic frequencies. These frequencies would not interact if the subharmonic was caused by electrical pickup, and thus independent of the flow.

Finally, the most cogent check on possible electrical coupling was made in connection with the surface wave damping experiments also mentioned in section 3.2.1. Oblique waves were forced both with and without styrofoam blocks placed on the free surface at the entrance to the test section to damp out the surface waves that formed most strongly there. No other changes were made. A plot of the primary and subharmonic amplitudes computed

from the resulting spectra for a sensor which had subharmonics is plotted as Figure 3.32. It can be seen that although the primary amplitude changes little with the addition of the surface wave damping, the subharmonic amplitude is consistently smaller for the smaller surface wave case, but has the same trend with angle. This change with surface waves is presumably caused by the small three-dimensional perturbations introduced by surface waves, acting through changes in the delicately triggered three-dimensional breakdown process. However, the important feature here is that the subharmonic changes very significantly (about 50% in amplitude) when a purely fluid mechanical change is made. This finding seems clear evidence that the subharmonic is not some obscure form of electronic pickup from the heating apparatus, for one would expect such pickup to be independent of the surface wave amplitude or the presence of styrofoam on the surface.

The amplitude of primary and subharmonic is plotted for several values of the output power in Figure 3.33, to show that the subharmonic is present at all forcing levels, instead of appearing only at higher forcing levels. It is also evident that the subharmonic increases much less rapidly with forcing than does the primary amplitude. These results do not show a sudden growth of the subharmonic after the primary reaches some critical amplitude, as seen in classic subharmonic studies [13, Figure 3]. However, that work studies the growth of the subharmonic with streamwise distance rather than with input amplitude, as in the present work. It should be noted that the DC offset error in the sinusoidal heater voltage signals provides a subharmonic perturbation of about 1% of the primary perturbation (see Appendix A.2.6). This subharmonic seeding may or may not be significant to the subharmonics observed downstream in the nonlinear region.

The most interesting observation is that when subharmonics are seen,

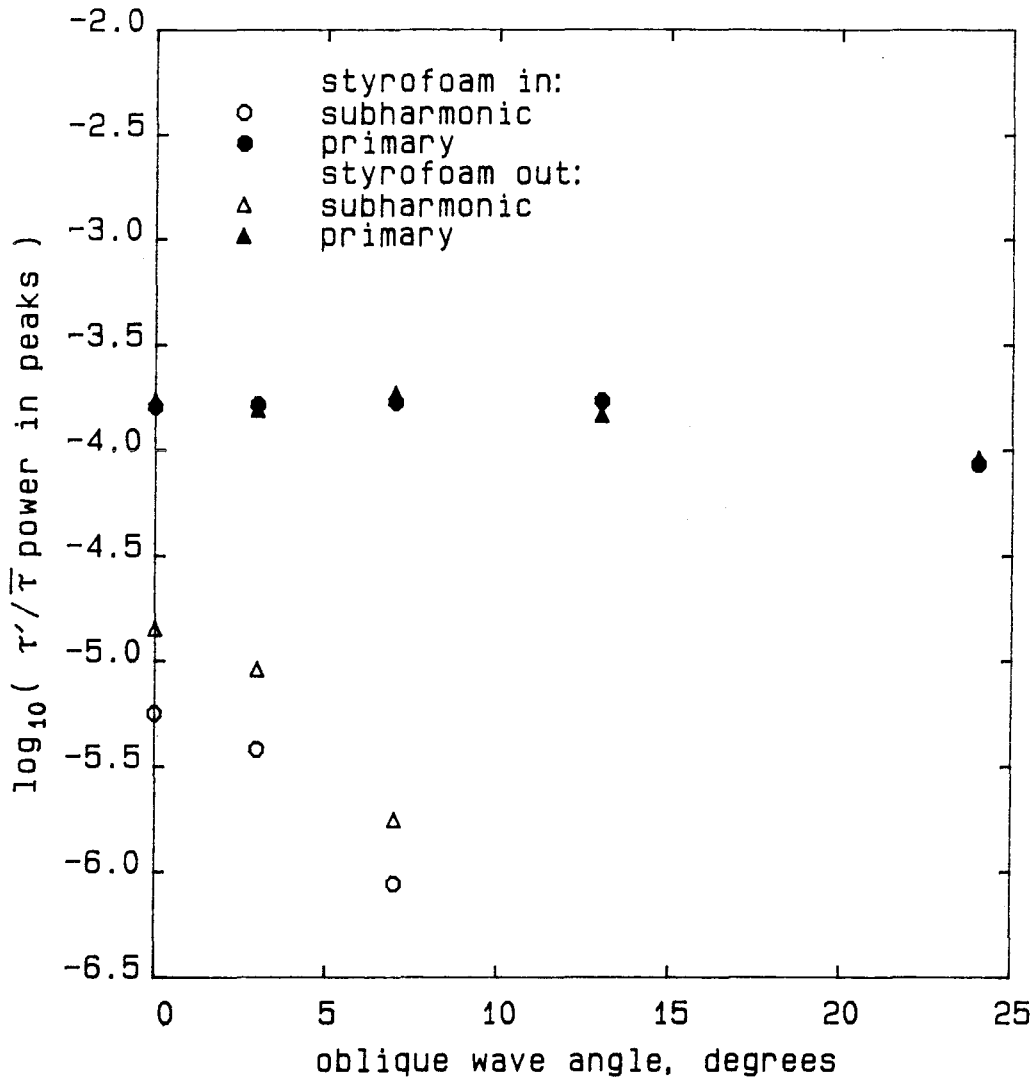


Figure 3.32: Change in Subharmonic Amplitude with Surface Wave Damping
16Hz 83 watt forcing, S6, $Re_{\delta^*} = 1350$, 5-5, $U_{\infty} = 3.69$ fps

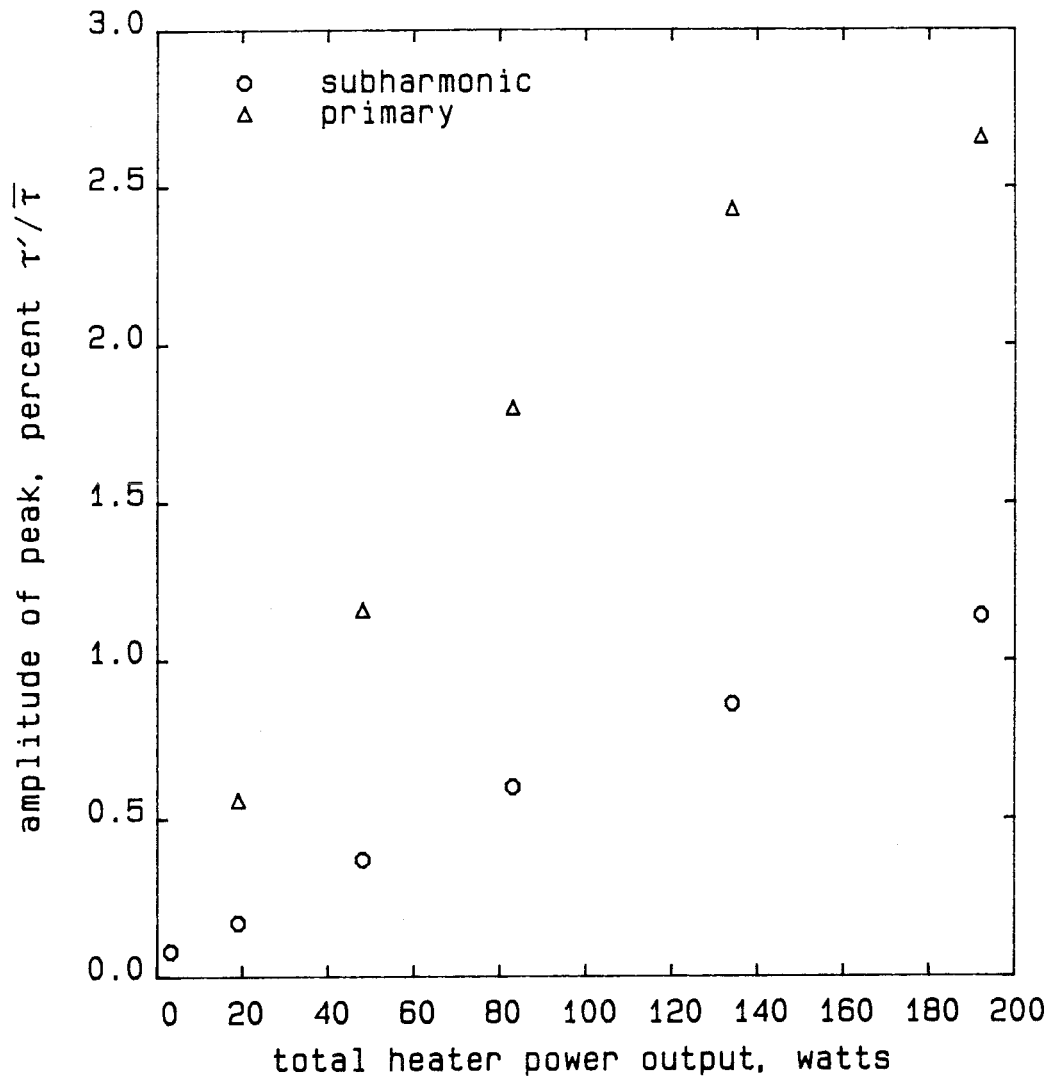


Figure 3.33: Primary and Subharmonic vs. Forcing Level
S4, $Re_{\delta^*} = 1300$, $U_{\infty} = 3.50$ fps, 2D waves, 4-13mII

they are strongest for 2D forcing, and decrease rapidly in amplitude for oblique forcing of increasing oblique angle, so that for an oblique wave of perhaps 5 degrees the subharmonic amplitude has decreased by an order of magnitude from the 2D value (Figure 3.34). Never are the subharmonics seen to increase with angle, and therefore it seems highly unlikely that the location is simply moving spanwise. This behavior is very striking, and so an explanation was sought in terms of the theories for nonlinear instability wave breakdown.

Subharmonics are a feature of several analyses of the secondary instability of Tollmien-Schlichting waves and are also the subject of several experiments (see for example Herbert [12] and Corke [5]). In all these cases, the instability of a strong two-dimensional primary wave is studied. Figure 3.35 (adapted from Hama et al. [10, Figure 33]) shows the triad resonance explanation of the appearance of subharmonics. A pair of oblique waves of equal and opposite angles can be traveling with the same phase speed as a primary 2D wave, if the oblique angle is correct. This triad of waves can then resonate nonlinearly, causing an increase in mutual growth rate. The figure shows how such a triad can exist with a simple phase-locked arrangement of the waves. The triad-resonance theory is based on an analysis of the weakly nonlinear instability of this arrangement. The regions marked A and B have opposite phases, so that the nonlinear interaction is capable of amplifying these regions differently, causing the appearance of a subharmonic component. However, the drawing shows how even a small angle oblique wave can no longer have a phase locked relationship to such a pair of oblique waves, so that this triad interaction can no longer exist. One could conceive of a triad interaction of two oblique waves of slightly different wave angles with a slightly oblique primary wave, but the two waves of slightly different angles would not have

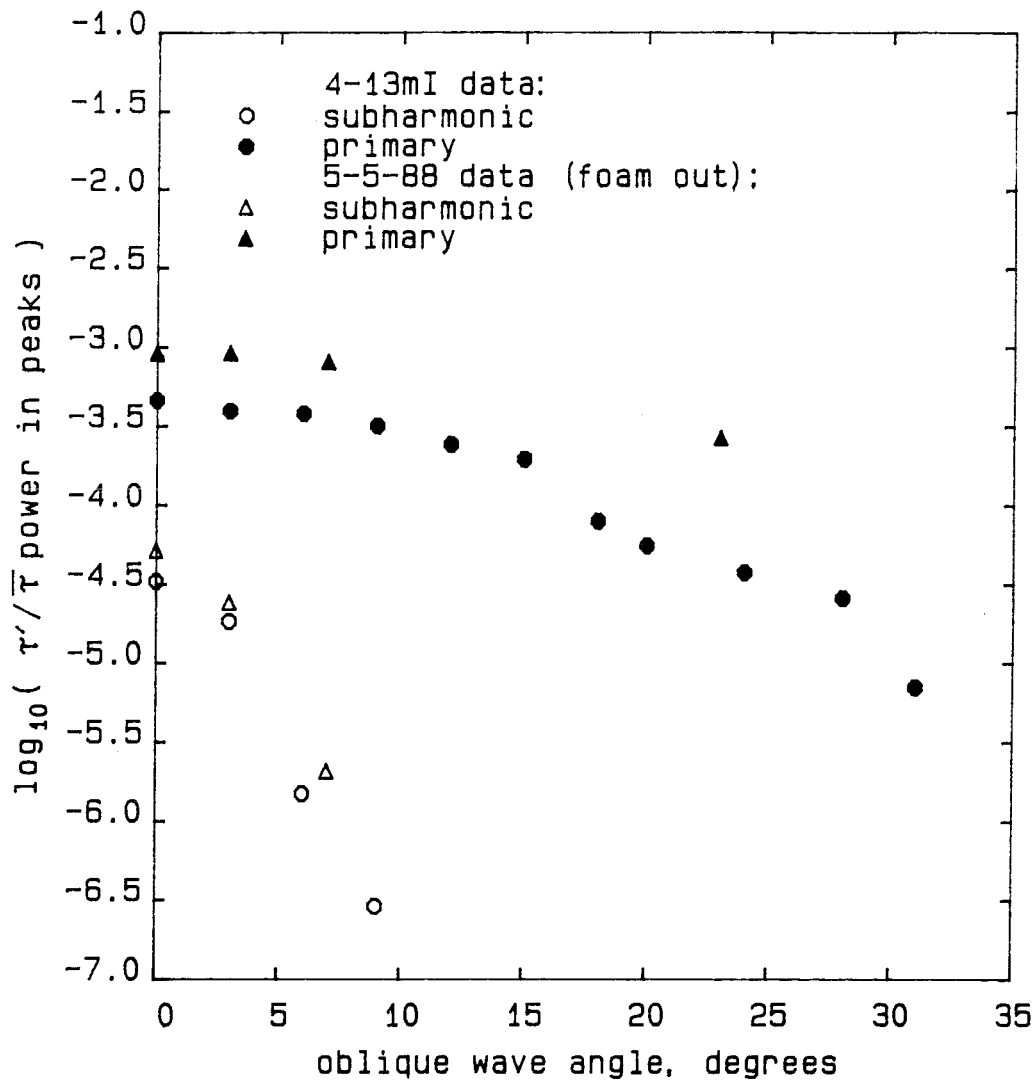


Figure 3.34: Decrease in Subharmonic Amplitude with Angle
20Hz 192 watt forcing,
4-13mI data: S4, $Re_{\delta^*} = 1300$, $U_{\infty} = 3.50$ fps
5-5-88 data: S6, $Re_{\delta^*} = 1350$, $U_{\infty} = 3.68$ fps

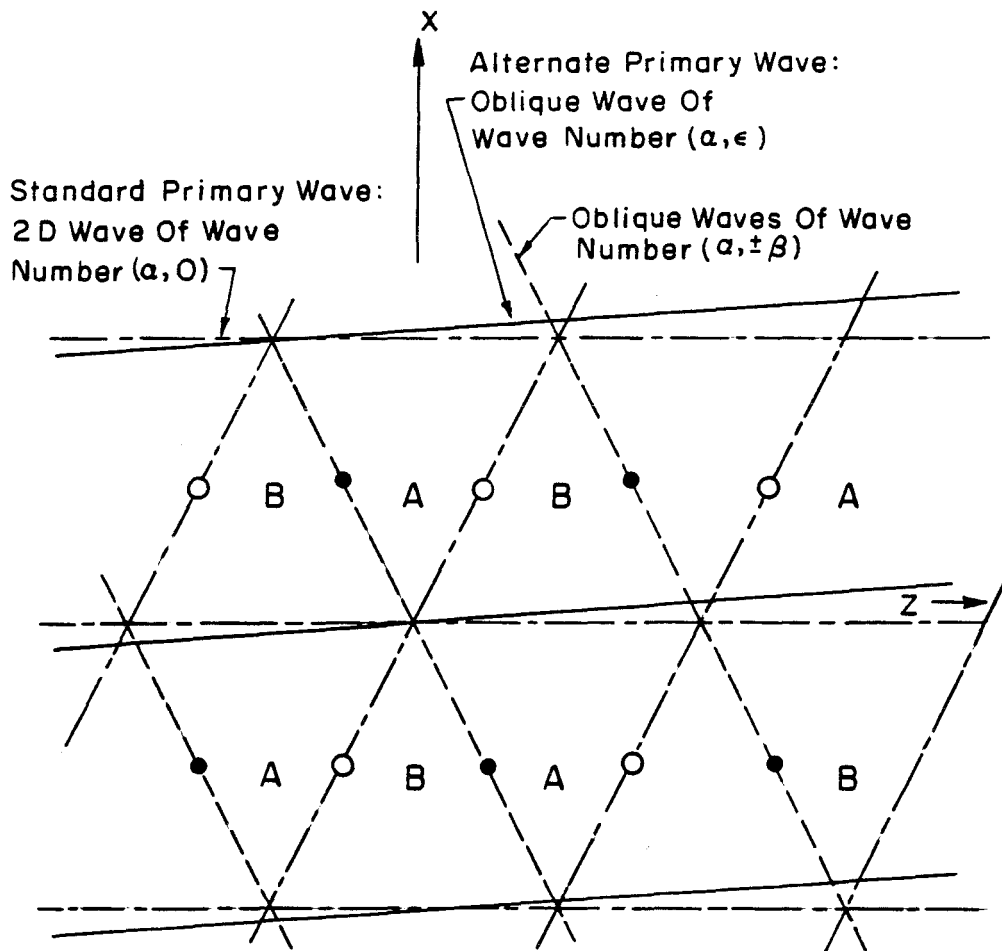


Figure 3.35: Breaking of Triad Resonance for Oblique Primary Waves (after Hama et al. [10, Figure 33])

the same phase speeds, and so could not long exist in a resonant phase locked condition.

Thus it can be seen that a strong single frequency fundamental wave of even slightly oblique angle (13 degrees) which is nearly as large in amplitude as the similar 2D wave (because it has nearly the same integrated growth rate) has a very different secondary instability. This secondary instability does not show subharmonics in the nonlinear region and cannot be explained by the wave triad resonance concept. The wave breakdown may instead be explained by the different properties which are evident even for small angle oblique waves, such as their fully three-dimensional vorticity and the movement of the vorticity maximum away from the wall (see the linear eigenfunctions of Hama et al [10, Figure 2]). However, this change in the observed secondary instability of these waves does not cause a dramatic change in their overall transition to turbulence, since there is no sudden movement of the boundary layer transition point corresponding to this sudden change in secondary instability (see Figure 3.38). This result suggests that there is a more fundamental explanation for the nonlinear breakdown of instability waves that does not rely on a mechanism applicable only to 2D waves.

The subharmonic amplitude changes in an unpredictable fashion with frequency. The changes may be associated with spanwise movement of the subharmonic maxima. This spanwise motion could not be studied with existing instrumentation.

It is very difficult to study the spanwise structure of these waves through point measurements alone, without flow visualization photos. However, the difficulty of visualizing small amplitude instability waves is well known, and the usual techniques are not easily used in our facility as configured. As will be discussed in the summary, further work should focus on developing

such a flow visualization apparatus to operate concurrently with the three-dimensional perturbation apparatus.

3.3.3 Late Nonlinear Region

Eventually the waves break down into local large fluctuations. These are nonlinear, fully three-dimensional, and apparently random. Thus, at the least, a two-dimensional photograph or sensor array is needed to study them; however, several things can be noted here. A typical trace of such a late nonlinear signal is shown in Figure 3.36, which shows the large unsteady fluctuations typical of this region. Also, dye streak flow visualization showed spanwise fluctuations in the streamwise dye streaks just before they were lifted off the plate by turbulence, in a manner similar to the behavior described by Liepmann et al. [26, Figure 7]. Neither of these behaviors were studied in detail.

It should also be noted that one would not expect to see the 'spikes' first studied by Klebanoff et al. [21] in the flow near the wall, as shown in their Figure 26. Finally, turbulent spots appear in videotape records of the transition¹⁴ both for forcing patterns that have subharmonics and for forcing patterns that do not. Moreover, the surface shear downstream is in all cases intermittent, as will be discussed in the following section. These observations do not agree with those of Kachanov [18, p. 45], who states that the subharmonic transition is fundamentally different and occurs by a smooth increase of fluctuations instead of through the formation of turbulent spots.

¹⁴photographing the dye sheet emitted by the dye slot

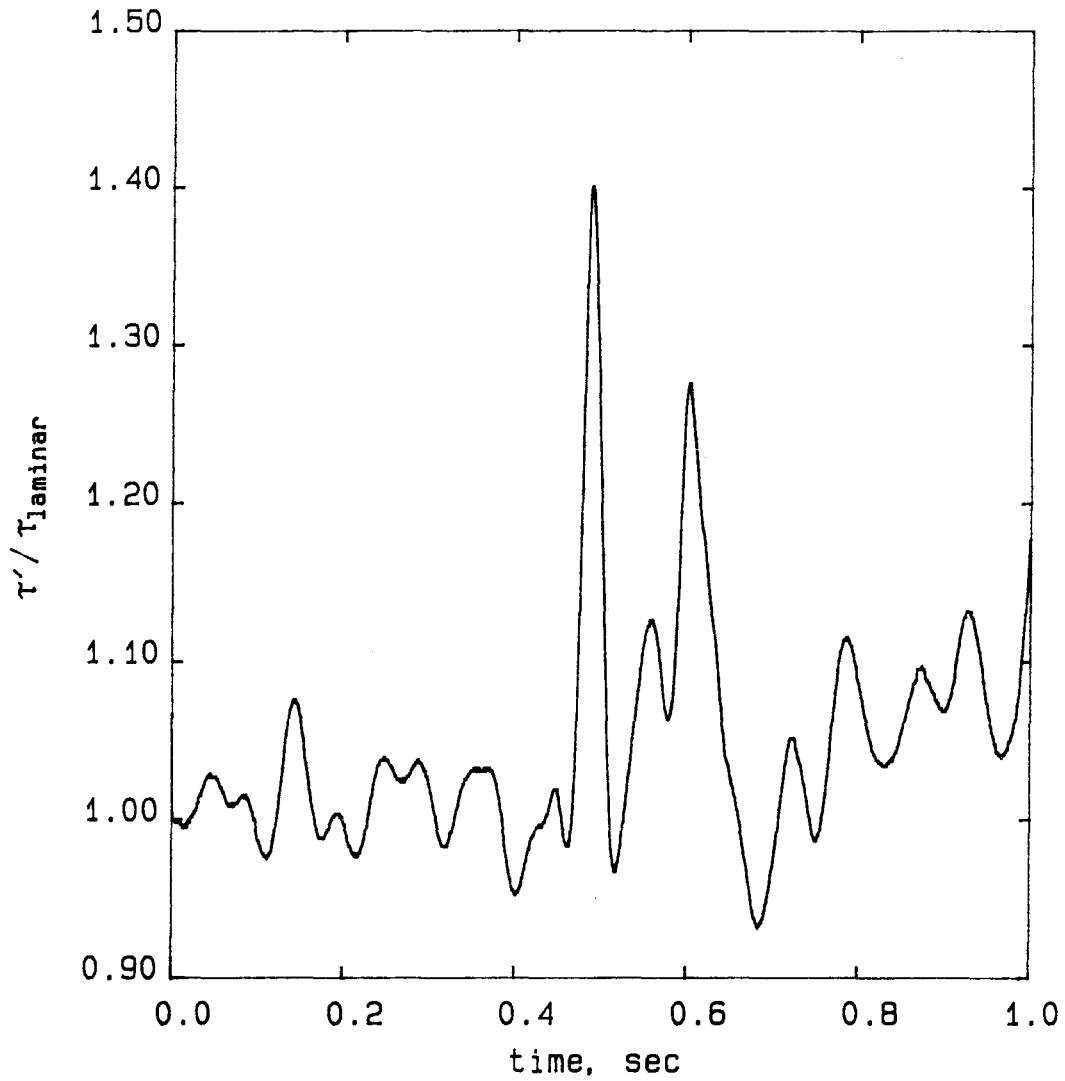


Figure 3.36: Time Trace of Wall Shear for Late Nonlinear Wave
2D 20Hz waves, 192 watt forcing, S8, $Re_{\delta^*} = 1750$, 4-13a

3.3.4 Intermittent Region

Eventually the waves break down into turbulent spots in an intermittent fashion that seems to be of the classically intermittent kind (see, for example, Narasimha [31]). Dye flow visualization of this region shows a transition between laminar flow regions marked by dye from upstream and turbulent flow regions where the dye is being or has been washed away. This interface is ragged and unsteady. The interface moves upstream markedly when significant forcing is turned on, corresponding to an upstream movement of the transition point. Two photos of the intermittent region are attached in Figure 3.37, which shows the dye for forced and unforced waves. The arrow shape of the dye in the unforced case is caused by the edge contamination in the tunnel, which creates wedge-shaped turbulent regions near both walls of the tunnel. The raggedness of both dye fronts is evident, as is the upstream movement of transition in the forced case. However, it is difficult to see any clear effect of small changes in forcing with this technique, because the transition marked by the dye fluctuates so much.

If a sensor is placed in this fluctuating region, the fraction of time when the flow is turbulent can be computed. The result is known as the intermittency¹⁵. If the wall shear is measured over a sufficiently long period of time, the fluctuations in the intermittency computed for shorter times will average out, causing the intermittency to converge to a long-time average value, close to the value that would be found using infinite averaging. The length of time required for good convergence does not seem to have been discussed in the literature.

The intermittency is known to increase with downstream distance until

¹⁵for method of computation, see Appendix C.2

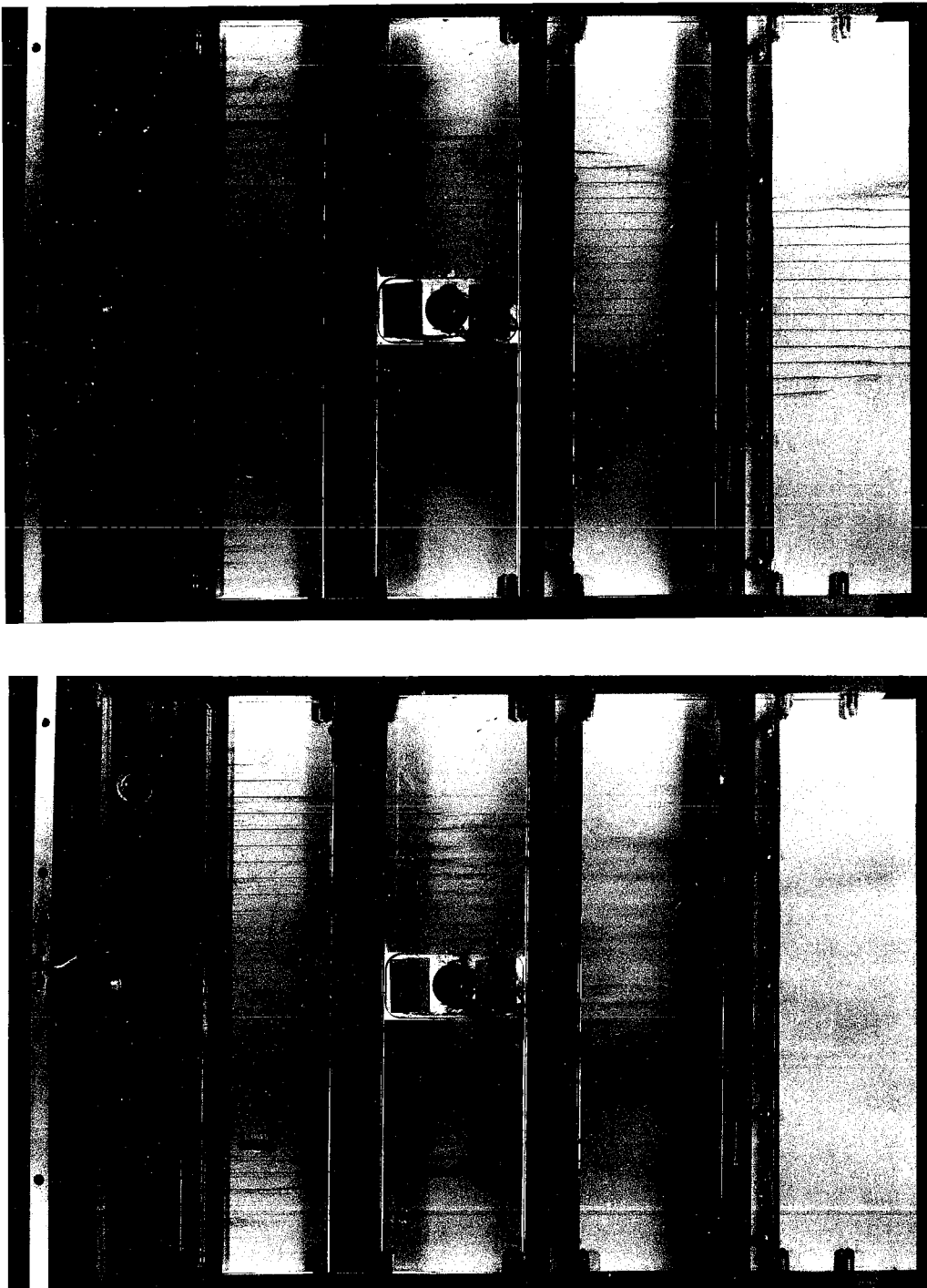


Figure 3.37: Photographs of Transition With and Without Forcing
Upper Photo: unforced
Lower Photo: Forced 192 watts 16Hz 12 degree oblique wave
Both Photos: $U_{\infty} = 3.50$ fps, 4-13m, flow is from left to right

the flow is fully turbulent. Here, the intermittency is measured at two fixed sensors, and the change in intermittency with forcing is used to quantify the movement of transition caused by the forcing. Extensive experiments were done with oblique wave forcing in order to get a sufficient record to get good statistics. In the present experiment, it turned out that 5 records of about 300 instability wave cycles each were required in order to get the intermittency to converge, so that the rms variation among the records is about 0.1. Figure 3.38 shows that, as the angle of oblique wave forcing is increased, the transition point moves upstream less and less. Thus two-dimensional forcing has the largest effect on the movement of the transition point. It is important to remember that this forcing is located at a fixed streamwise location, near the critical Reynolds number.

This result is not surprising, in view of the generally smaller oblique wave amplitudes measured at the end of the linear region. The nonlinear effects that favor the growth of oblique waves, as discussed in the introduction, are evidently not sufficient to overcome their smaller linear growth rates and possibly weaker receptivity to the heating. This experiment is the first time the development of such waves has been observed all the way into the intermittent region.

3.4 Transition Caused by Forcing of Other Wave Patterns

Work was concentrated on the study of the oblique waves because of their theoretical simplicity. However, some experiments were done using various other perturbation patterns in an exploration of possible effects. A major difficulty lies in choosing among the vast variety of patterns that can be studied, even using the present rather limited signal generation apparatus.

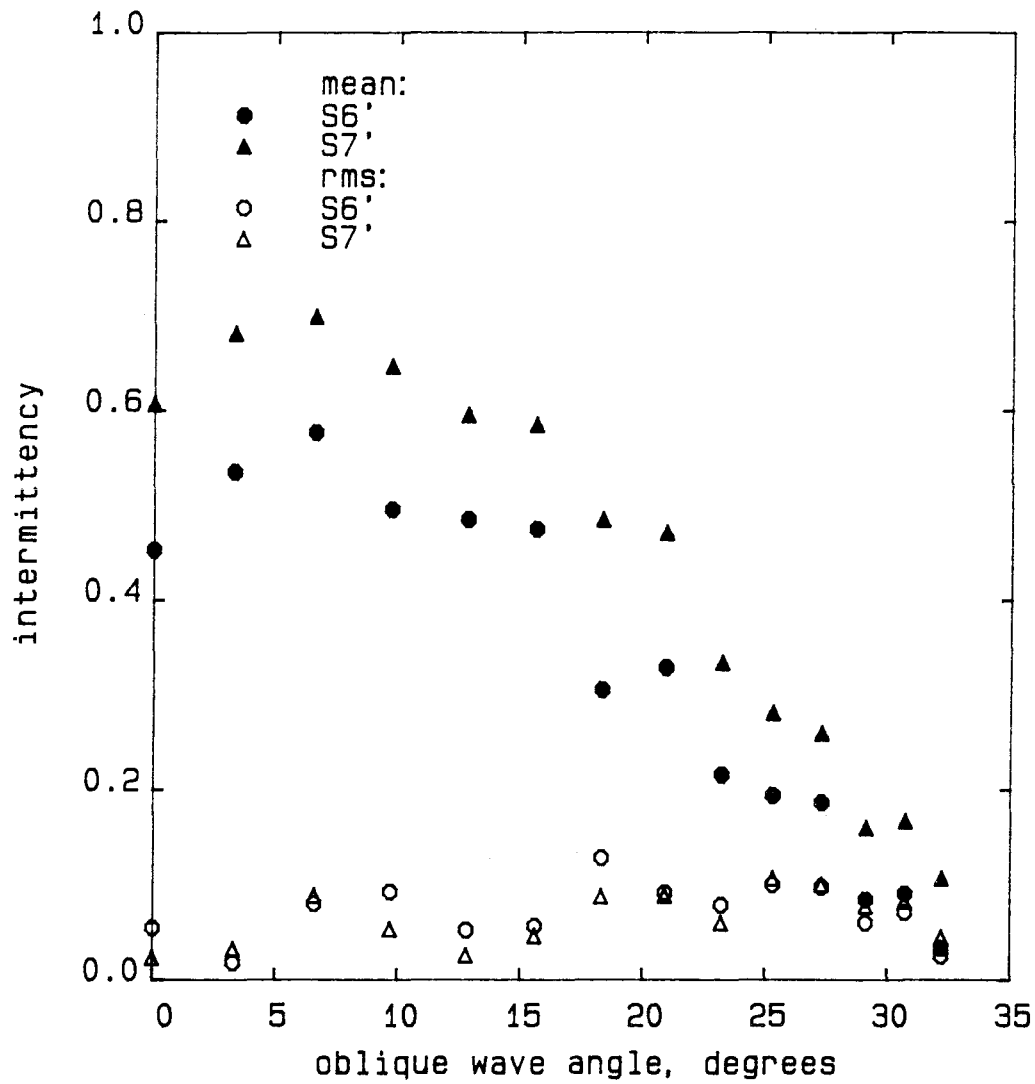


Figure 3.38: Movement of Transition Caused by Oblique Wave Forcing
20Hz 163 watt forcing, $U_\infty = 3.69$ fps, 9-2d2-6
S6': $Re_x = 1.0 \times 10^6$ S7': $Re_x = 1.1 \times 10^6$
5 records of 16 seconds each, intermittency I computed for each
'mean' is the average I over the 5 records (80 seconds)
'rms' is the rms variation of I among the 5 records

A second difficulty lies in choosing a region in which to study the instability wave growth, given a particular wave pattern.

Most of the non-oblique wave pattern data was acquired in the course of one long experiment which was part of the first experimental set. Five fundamental wave patterns were studied, each only briefly. Four sensors were operating for these studies, so that some record of the pattern development was recorded in the linear, nonlinear, and intermittent regions. One sensor was located off the centerline, to give some record of the spanwise variation in the flows generated. These experiments were carried out at the same freestream velocity as most of the rest of set I, 3.69 ± 0.02 ft/sec. Some further experiments using one of the forcing patterns were carried out during the second set of experiments using the second plate configuration.

The farthest downstream sensor, S8, was intermittent for some of these runs, and an attempt was made to look at the movement of transition caused by the various forcing patterns through measurements of the intermittency on this sensor. Unfortunately, the length of the records acquired, 8 seconds or about 160 instability wave cycles, was insufficient to obtain an accurate value for the intermittency. The scatter among intermittencies computed for the repeated records taken during the set of runs discussed in this section was large, of the order of the intermittencies measured. The intermittencies measured for oblique waves, discussed in section 3.3.4, required ten times this amount of data to reach good statistical convergence. Thus, no intermittency plots have been included in this section. However, the data are of some value for indicating gross trends, and such trends will be discussed.

The wave patterns used are divided into two groups for this discussion (see Figure 3.39 for sketches of the patterns). The first group consists of wave patterns in which the spatial variation is all at short wavelengths. An

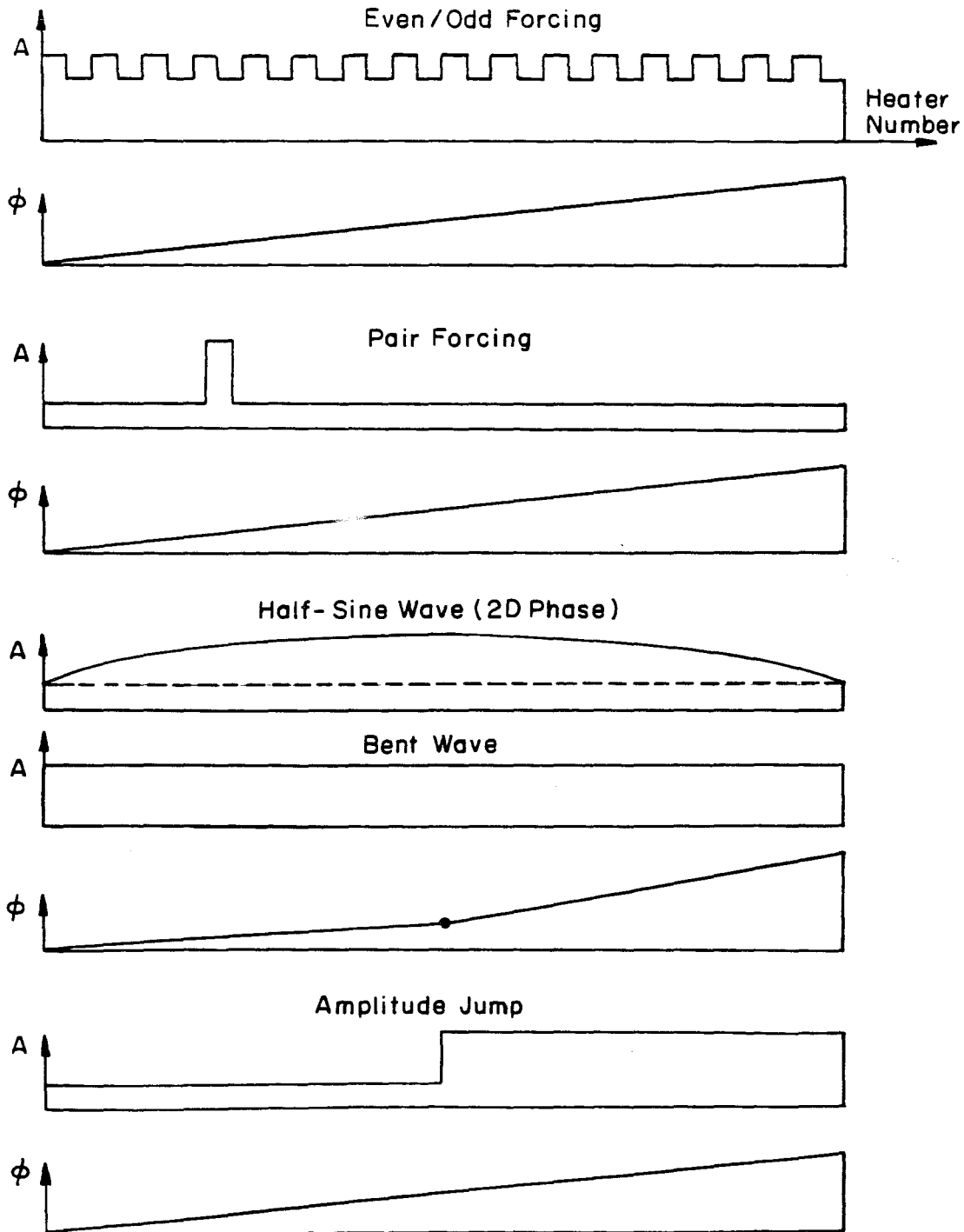


Figure 3.39: Sketch of Wave Patterns for 3D Forcing
 ϕ - phase shift from first heater; A - amplitude

example from this group is a pattern in which alternate heaters are offset in amplitude. The second group consists of wave patterns in which the spatial variation contains long spatial wavelengths as well as short ones. An example from this group is a pattern in which the amplitude jumps from one value to another at mid-span. The distinction is somewhat arbitrary, but it is the only one that seems of obvious significance. As far as the author is aware, this is the first time that the development of any such controlled three-dimensional patterns has been studied at all.

3.4.1 Short Spatial Wavelength Patterns

Two of the wave patterns generated come under this classification. The first of these is a pattern in which straight waves are generated, very much like the oblique waves used in the main text, except that every other heater is offset in amplitude from its neighbors. That is, all the even numbered heaters are at one amplitude, and all the odd numbered heaters are at another. The phase shift between the channels could have various values, but is uniform among the heaters. This pattern has been called *even/odd forcing*, for lack of a better term. The second pattern is one in which all the heaters are forced in phase, as if to make a 2D instability wave, except that a neighboring pair of heaters is offset in amplitude from the rest. The location of this offset pair was varied across the span. This pattern has been called *pair forcing*, for obvious reasons. *Even/odd forcing* will be discussed first.

3.4.1.1 Even/Odd Forcing

Even/odd forcing was studied for one base amplitude of the odd numbered heaters, two angles of obliqueness, and four values of the offset of the even numbered heaters, for three frequencies. Subharmonics were observed at

sensor S6, located in the nonlinear regime. A plot of the amplitudes of the primary and subharmonic responses to the forcing for this sensor is attached as Figure 3.40. The figure plots the power in the spectral peaks against the amplitude offset of the even-numbered heaters, for two angles of obliqueness, and for one typical frequency. Also plotted are some reference data for the response at this sensor to standard straight oblique wave forcing, measured on the same day. Looking first at the primary response, it is evident for all angles that the response increases with the offset of the even heaters. This is to be expected, since the total power entering the flow is increasing. The increase with power is smooth and not dramatic, and the change in response with increasing power is very similar to that for standard oblique waves. Looking next at the subharmonic response, one sees that they also increase with power input, as might be expected, but not dramatically. Clearly the oblique wave forcing results in much lower amplitude subharmonics than in the 2D phase case. This is the same behavior as for uniform amplitude oblique wave forcing, showing that the nonuniformity in spanwise heating does not change this effect. The other sensors in the linear and nonlinear regime show similar behavior, but without the subharmonics.

For this pattern, the furthest downstream sensor showed intermittency, although as mentioned above, sufficiently long records to achieve good statistics were not taken. However, the data do show that the the intermittency increases with forcing power, and also that the *even/odd forcing* pattern did not have a dramatic effect on the forward movement of transition.

The results seem to show that there is no major effect of this short wavelength spanwise amplitude modulation on the flow development. This finding was at first a surprise. It seems that since the short wavelength modulation is created in the early linear amplification region, the wave must travel through

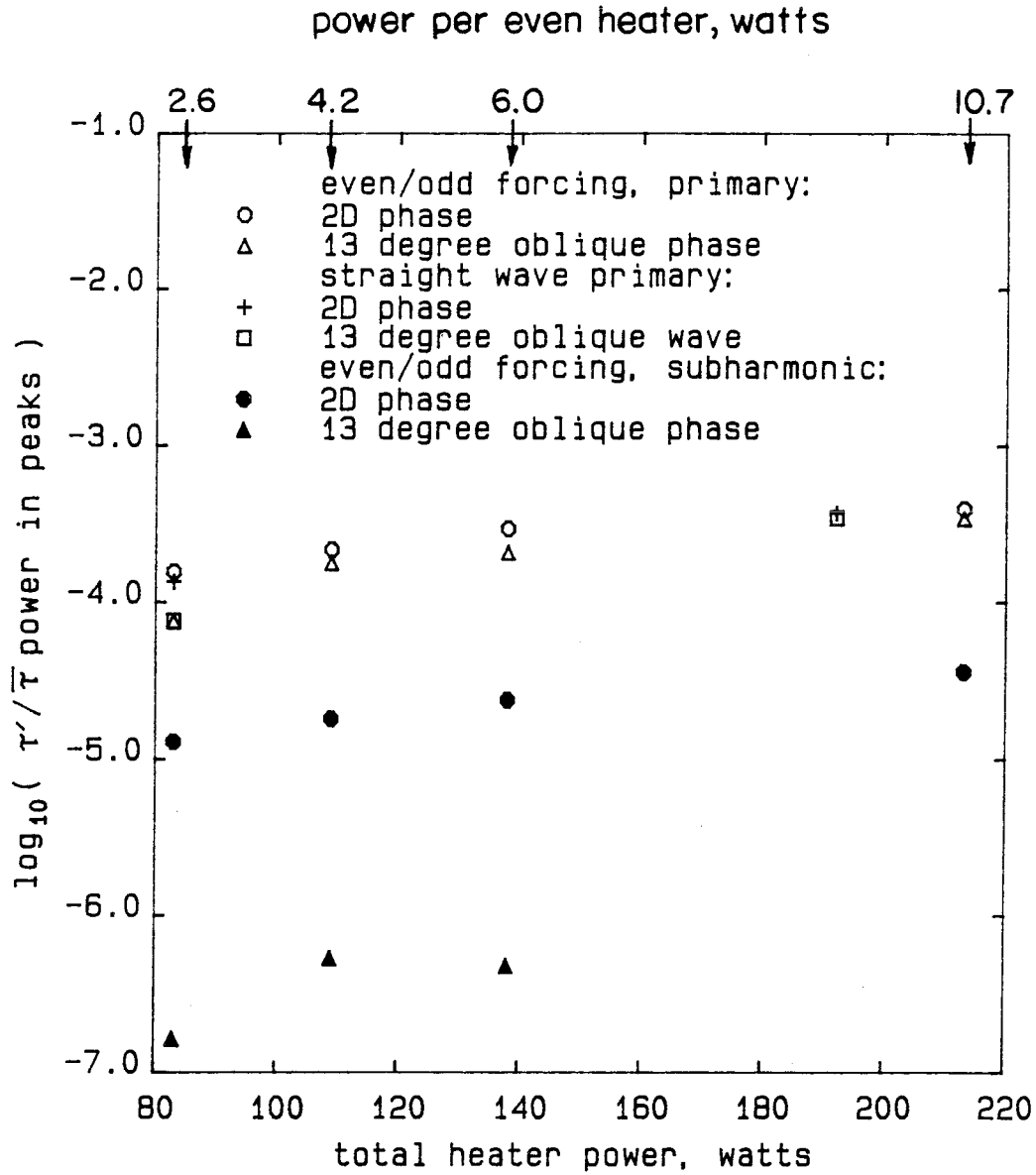


Figure 3.40: Primary and Subharmonic Response to Even/Odd Forcing S6, $Re_{\delta^*} = 1350$, 20Hz forcing, odd heaters at 2.6W each, 5-5d2, straight wave forcing is standard oblique wave

a long linear amplification region before any nonlinear effects can come into play. In this linear amplification region, the large angle oblique waves into which the modulation can be decomposed do not grow much, if at all. Thus the wave modulation tends to smooth out, with the wave pattern approaching that of the elementary, growing, straight wave shape. This means that when the wave reaches the nonlinear and intermittent regions, it is very much the same wave as that created by a simple straight wave forcing and so behaves similarly. Additional implications of this observation will be discussed later. It should be mentioned that there are reassuring implications for the wave creation technique, inasmuch as small differences between the wave pattern generated by the 32-element array and a perfect oblique wave pattern should smooth out in a similar fashion.

3.4.1.2 Pair Forcing

A considerable amount of pair forcing data was acquired, using both the first and second plate configurations. The pair forcing was investigated for two purposes. The first was to see if a local perturbation, or a local perturbation to a strong straight wave, has a large effect. The second was to look at the subharmonics generated by the perturbation and to see if they varied in a reasonable way as the perturbation location was varied across the span, in order to check that the subharmonics generated were not caused by electrical pickup from the heater electronics.

The first results to be presented are for large amplitude 2D forcing perturbed by a small offset, either positive or negative, in the amplitude of the centerline pair. It was thought that this pattern would provide a localized defect for growth of secondary disturbances in the 2D wave. Spectra for the sensor located in the nonlinear region on the centerline downstream are

shown in Figure 3.41. It is readily seen that there is very little difference between the spectra for the three cases, with no change for a positive or negative defect in the forcing, even at this location directly downstream of the defect. Evidently this forcing pattern behaves the same as the even/odd forcing; the small disturbance is created in the early linear region so that by the time the wave has grown through the linear region the disturbance has been smoothed out. Figure 3.42 shows the amplitudes of the primary and subharmonic responses on the off-centerline sensor. It is evident that the primary signal on this off-centerline sensor increases only very slowly with the amplitude of forcing on the centerline, while the subharmonic increases slightly more rapidly. The anomalously low primary response to the positive offset 12Hz wave does not have an obvious explanation. The subharmonics are strong here, as they usually are for forcing with 2D phase on sensors where subharmonics are seen, but there is again no dramatic change with the introduction of the defect.

The second set of data to be presented is for a very low amplitude 2D wave perturbed by a large offset in amplitude for the centerline pair of heaters. This forcing pattern is almost the same as if only the centerline pair of heaters was forced. Figure 3.43 shows the primary and subharmonic amplitudes measured from data taken from the off-centerline sensor in the nonlinear region. It is evident that large subharmonics are present for this 2D phase forcing, and that the amplitude of the subharmonics again increases with frequency. The amplitude of subharmonic response increases smoothly and slowly with increasing offset amplitude of the centerline pair being forced, while the primary amplitude scatters anomalously. It is notable that the subharmonic increases to a point where it has a higher amplitude than the primary response. The reason for this is not clear.

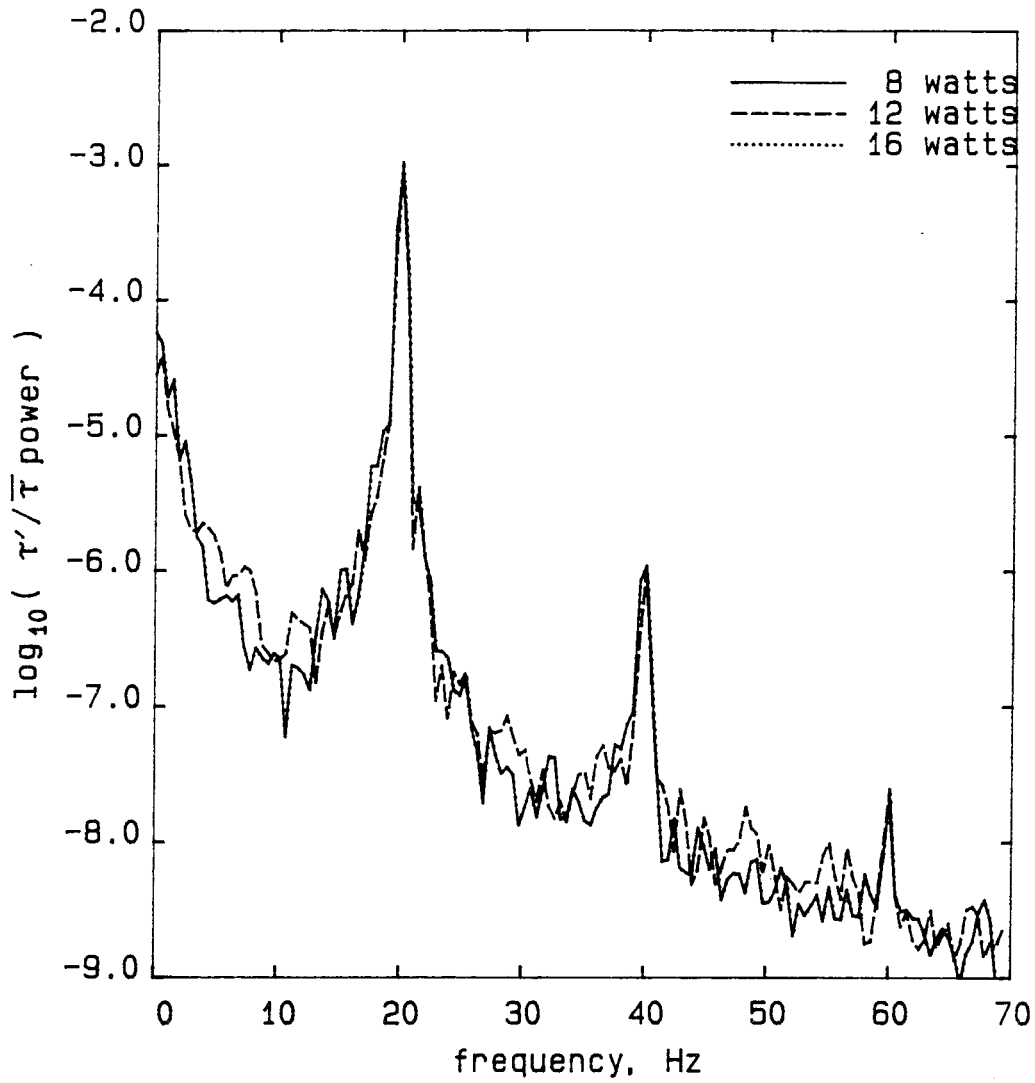


Figure 3.41: Spectra for 2D Wave with Centerline Defect
20Hz 2D forcing, Offset Center Pair, 5-2d9
S7, $Re_{\delta^*} = 1400$, $U_{\infty} = 3.69$ fps, base 6W/heater
Power listed in legend is the power
on the center pair of heaters

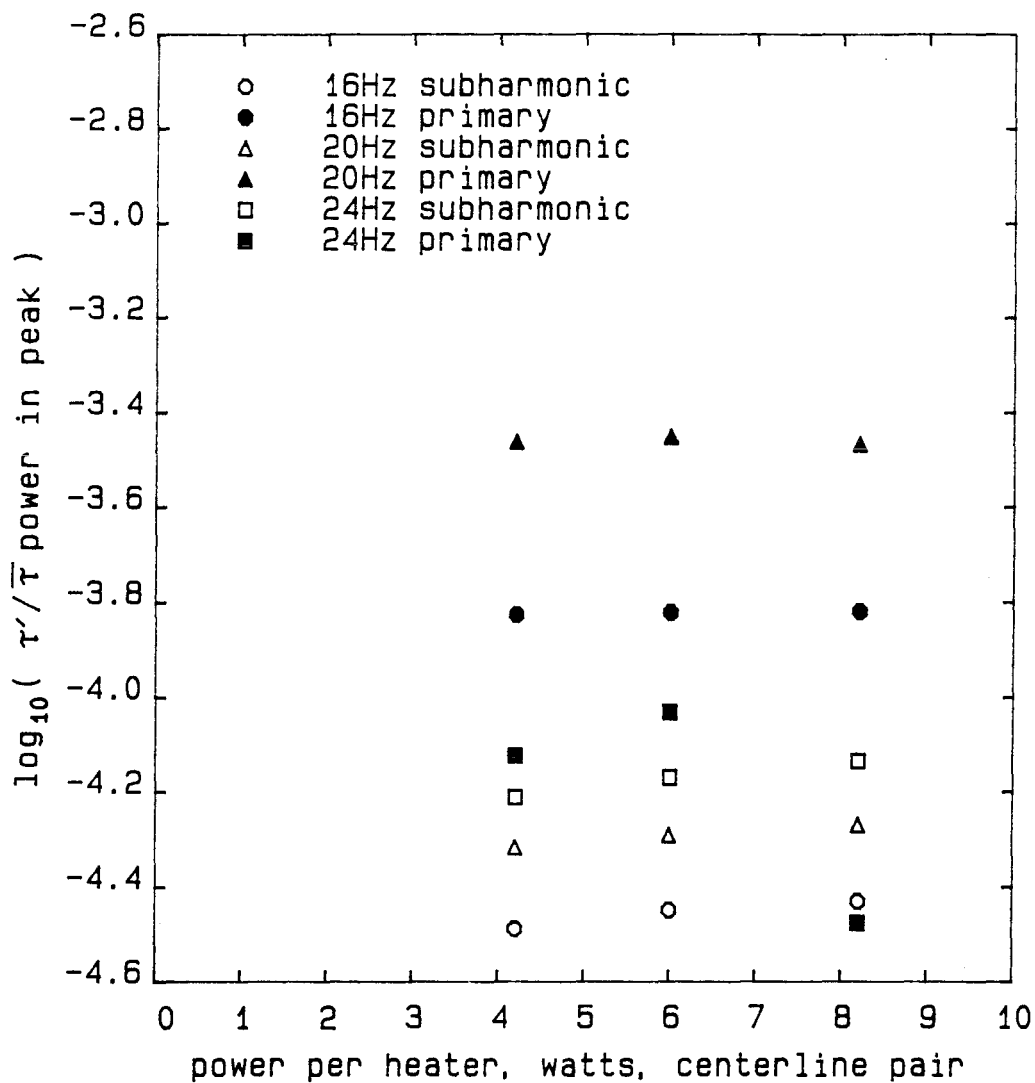


Figure 3.42: Primary and Subharmonic Response to Centerline Defect
Other heaters 6.0W each, 2D phase, 5-2d9
S6, $Re_{\delta^*} = 1350$

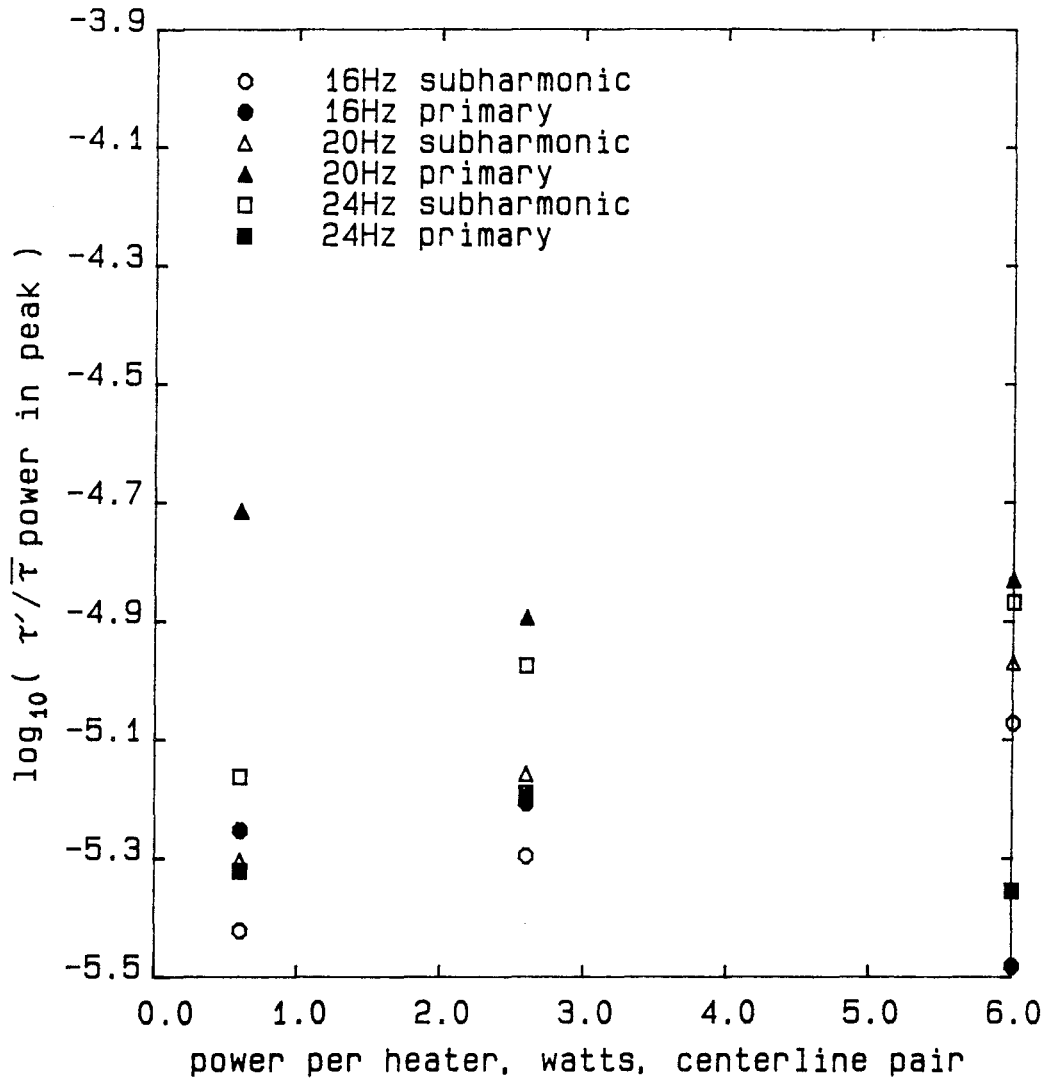


Figure 3.43: Nonlinear Response for Strong Centerline Pair Forcing
background heaters 0.6W each, 5-2d8
S6, $Re_{\delta^*} = 1350$, $U_{\infty} = 3.69$ fps

The last type of forcing to be discussed in this section is that of a pair strongly offset from a negligibly small 2D wave. The amplitude and frequency of the pair heating is kept constant, and the location of the pair is varied across the span. Data are acquired on a fixed sensor, as always, here located on the plate centerline. Figure 3.44 shows spectra at the sensor for four locations of the pair forcing. It can be seen that the amplitude of the primary response changes greatly with the spanwise position of the forcing, as might be expected, since the disturbances convect downstream. When the forcing is carried out directly upstream of the sensor, the disturbance is large enough to show a strong second harmonic. Subharmonics can be seen in all the spectra, and they decrease only slowly as the location of forcing is moved away from the centerline. This behavior can be seen more clearly in Figure 3.45, which shows the variation in amplitude of both the primary and subharmonic response with the location of the forced pair. The primary response varies rapidly with the movement of the forced pair away from the centerline. The amplitude of the primary response is lost in the natural wave noise for distances greater than about 2 inches. However, the subharmonic varies only a factor of about 3 in power as the location of the excited pair is moved all the way from the centerline to the edge of the tunnel. This large subharmonic is rather surprising. No explanation for this rather strange behavior has yet been found.

It seems that short spatial wavelength patterns introduced at the heater upstream of the linear region smooth out before the variations have a chance to be important in the nonlinear region. These variations may be sufficient to trigger a spatial localization of the beginning of three-dimensionality, as in Klebanoff et al. [21], but they are not sufficient to change the overall transition process. This conclusion has implications for boundary layer receptivity

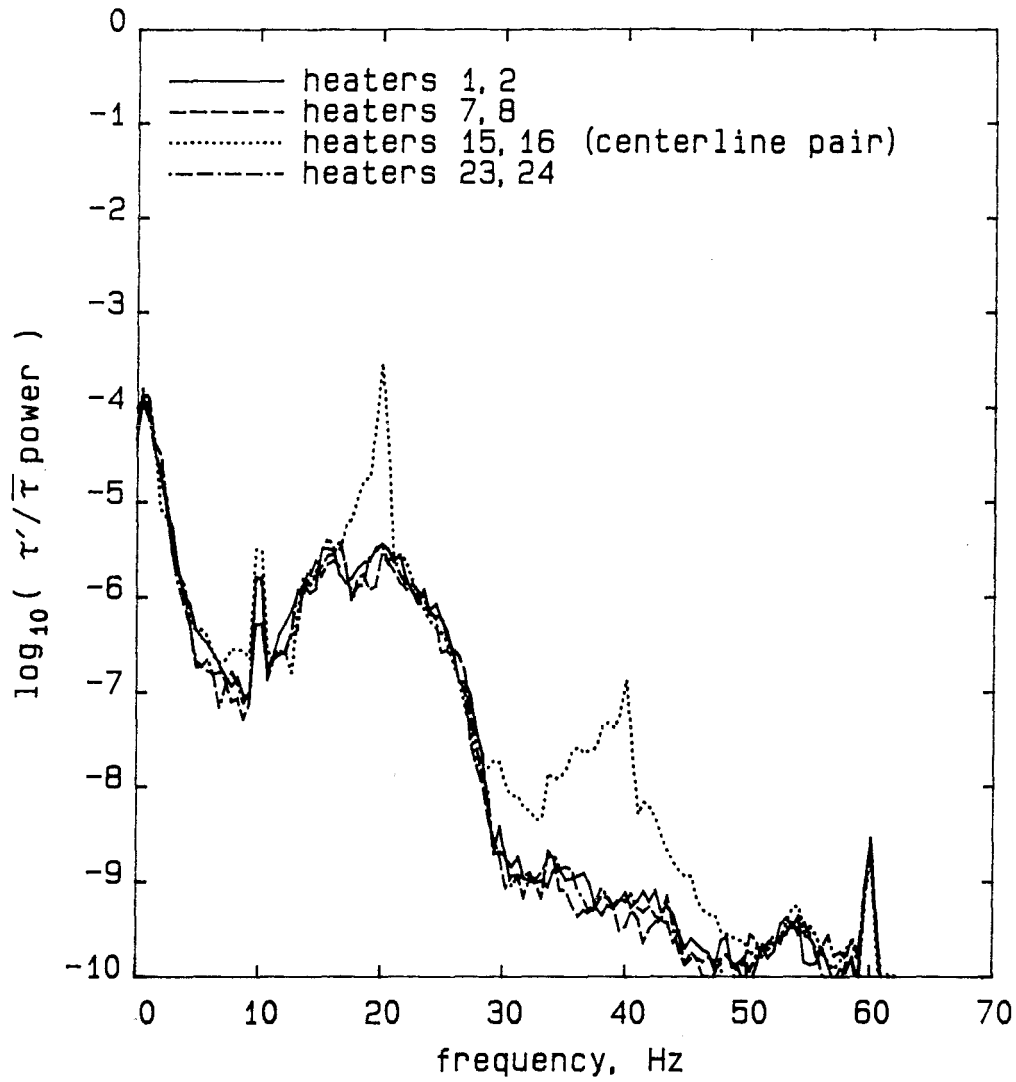


Figure 3.44: Spectra for Pair Forcing at Varied Spanwise Locations
background heaters 0.1W each, pair 6.0W/heater, 9-12d5
 $S1'$, $U_\infty = 3.1$ fps, 20Hz

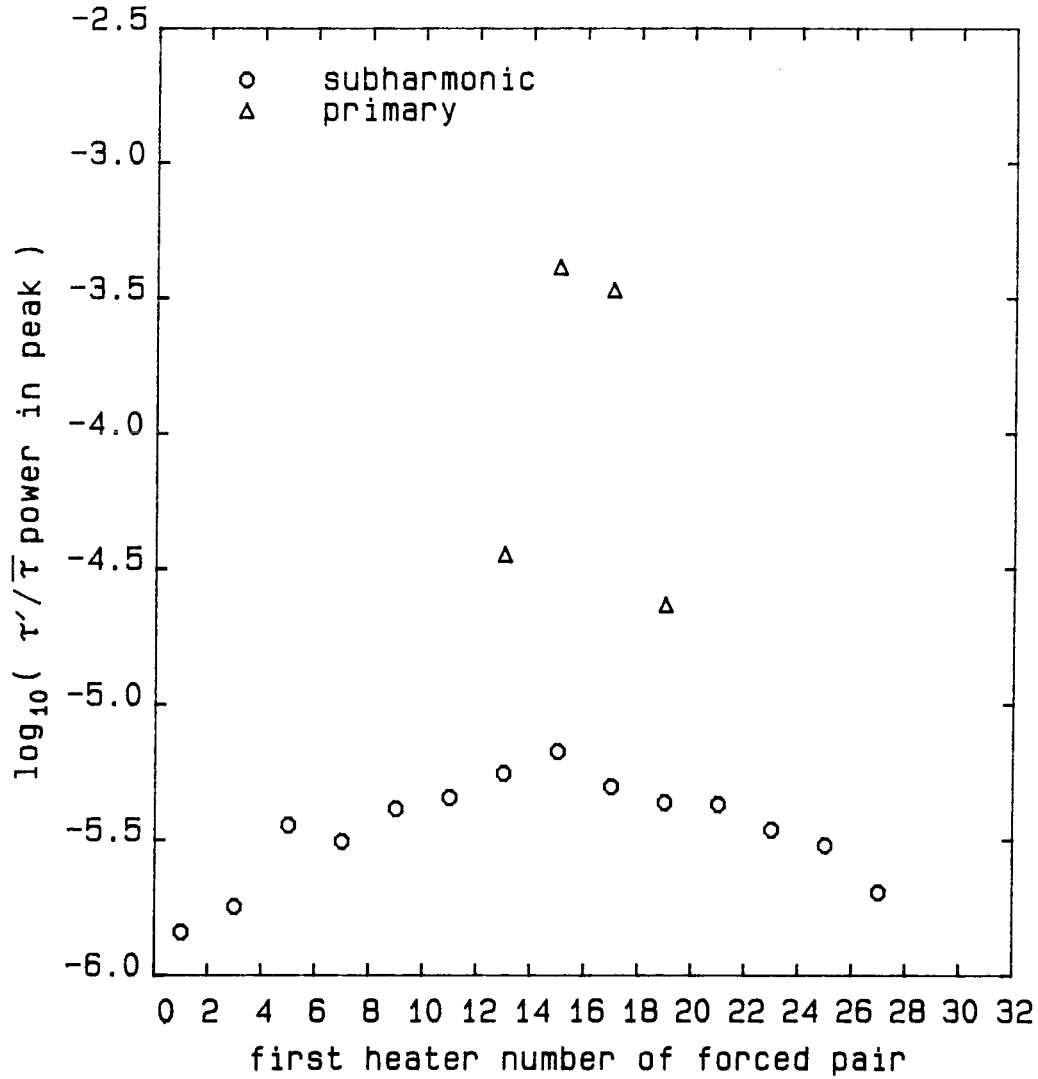


Figure 3.45: Primary and Subharmonic Response to Pair Location
background heaters 0.1W each, pair 5W each, 9-12d5
S1', $U_{\infty} = 3.1$ fps, 20Hz

to disturbances, because it suggests that 3D disturbances that enter through the outer layer in the nonlinear region might be more important for triggering 3D effects than disturbances that enter near the leading edge and are thus heavily damped before they become relevant.

3.4.2 Long Spatial Wavelength Patterns

Three of the non-oblique wave patterns that were generated can be classified under this heading. The first was an attempt to mimic the output of a vibrating ribbon. In this *sine wave in amplitude* pattern, the heaters are all forced in phase to make a 2D wave. However, the amplitude of forcing is varied across the span so that the power output on the heaters varies like a half-period sine wave across the span. This forcing can only be done to a rough approximation because of the limited range of discrete forcing levels available. The second pattern has a uniform amplitude across the span, with uniform phase shifts on either side of the plate centerline, interrupted by a jump in the phase shift at the centerline. This *bent wave* forcing thus consists of two straight line segments of oblique forcing interrupted by a kink in angle at the centerline. The third pattern is similar to the second but has a jump in amplitude at the centerline, with uniform phase lag across the entire span. This is called *amplitude jump forcing*. These last two types were suggested by Professor A. Leonard.

3.4.2.1 Half-Sine Distributed Amplitude Forcing

The half-sine forcing was carried out for three frequencies and for two types. In the first, a large base 2D wave was forced, with a small amplitude half-sine distribution added to it. This was to be a model of a vibrating ribbon with the fixed ends located outside the tunnel, so that the amplitude does not

decrease to zero at the edge of the tunnel. No unusual effects were observed for this case. The second case used a very low base amplitude, to which was added a large amplitude sine wave offset. Results for the off-centerline sensor S6, which showed subharmonics, are plotted in Figure 3.46. Evidently the primary response increases with the peak offset of the sine wave, which is expected since the total heat does also. Results for standard oblique waves are also plotted on the figure, for comparison. It can be seen that the increase in response with heating power is very similar for the two forcing patterns. The subharmonic is large, as we can expect for this 2D phase case, and increases in amplitude with heater power in a manner very similar to that seen for oblique waves. This forcing type did not cause any intermittency on the downstream sensor. Thus, on the whole, no surprising results were found for this forcing pattern.

3.4.2.2 Bent Wave Forcing

Bent wave forcing was carried out for one amplitude, three frequencies, and the nine combinations of angles possible using three different angles on each side of the plate. Figure 3.47 shows the results for the primary response on the centerline sensor S7, in the nonlinear region. The horizontal axis gives the wave angle generated on the north side of the plate, and primary response amplitudes are plotted for several settings of the wave angle on the south side of the plate. It can be seen that the amplitude for the three straight wave combinations falls off with increasing angle, just as was found in the oblique wave forcing work. The other results are somewhat confusing. It appears that the amplitude generally increases with the oblique angles of the segments, but that the larger oblique angles tend to reduce the amplitude if they cause too much of a kink on the centerline. It is obviously impossible

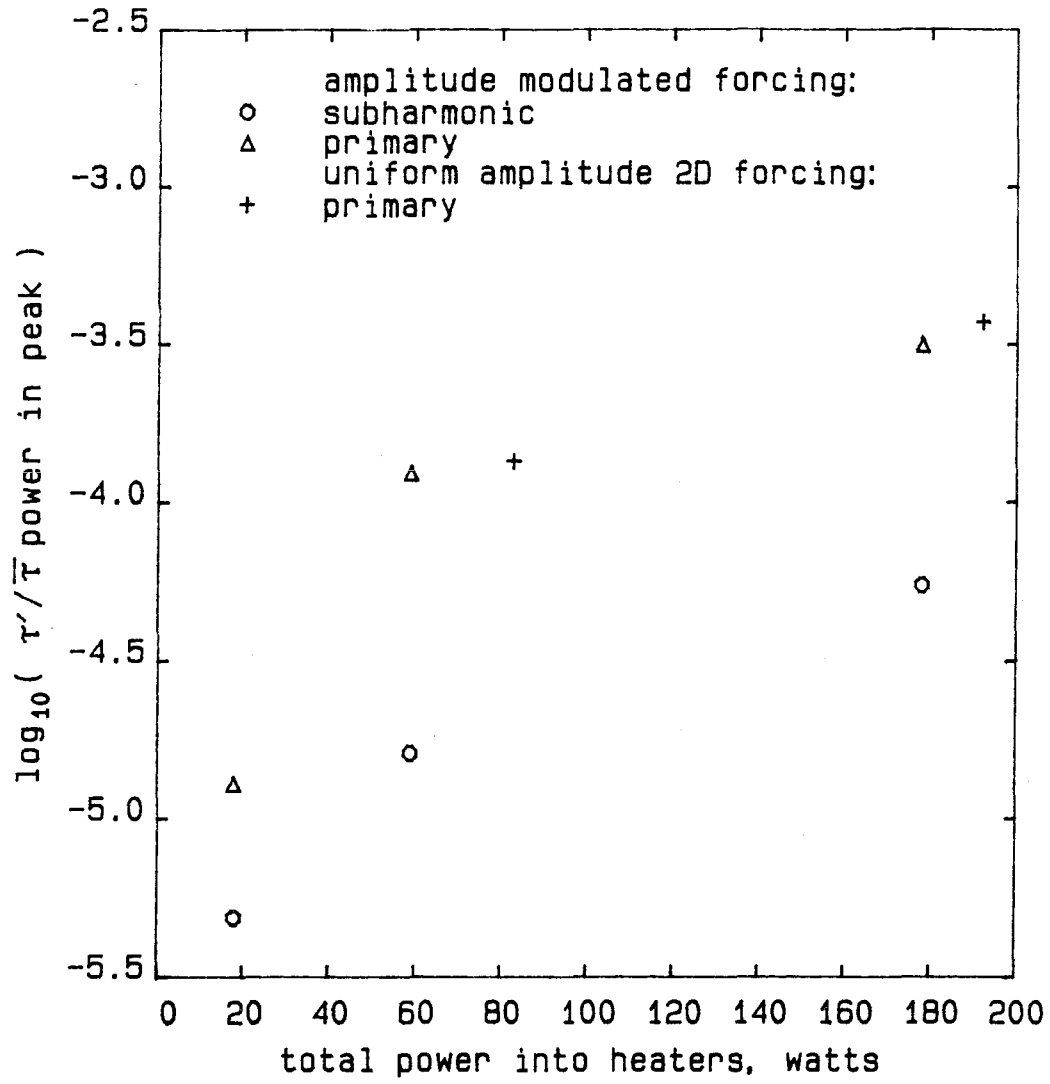


Figure 3.46: Subharmonic and Primary Response to Sine Wave in Amplitude
S6 $Re_{\delta^*} = 1350$, 20Hz waves, 5-2d6, base amplitude L1

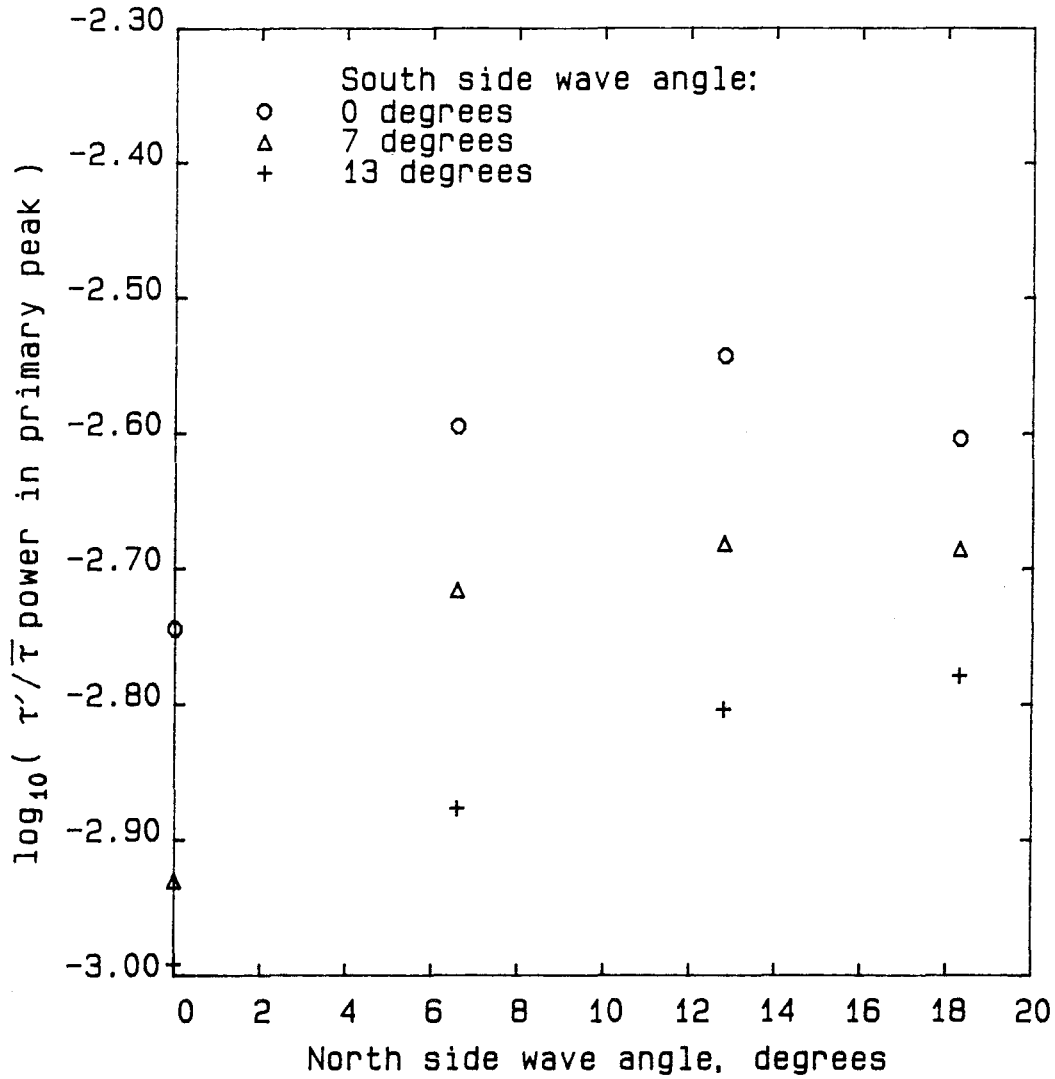


Figure 3.47: Primary Response to Bent Wave Forcing
20Hz 192 watt forcing, 5-2d4, S7, $Re_{\delta^*} = 1400$

to understand this flow without having a much better idea of its three-dimensional structure. It should be remembered that reversing the angles between the north and south sides does not produce the same wave, since one is convex downstream and the other convex upstream (see Figure 3.39).

This forcing caused the flow on the downstream sensor S8 to be intermittent. The intermittency varied with the forcing in a manner very similar to the variation of wave amplitude plotted above, not a surprising result since the data are from records on two sensors for the same experiment. Evidently the primary response on the centerline upstream is a good diagnostic for the eventual transition position downstream.

3.4.2.3 Amplitude Jump Forcing

Amplitude jump forcing was carried out for three frequencies, two wave angles, one amplitude of forcing on the north side of the plate, and four amplitudes of forcing on the south side. The results for the primary and subharmonic amplitudes on S6, the off-centerline sensor that often showed subharmonics on this day, are shown in Figure 3.48. Evidently, all amplitudes increase with the level of forcing, an increase which is to be expected since more power is being put into the flow. The increase in response with heater power is again very similar to that observed for standard oblique waves. Again, it is evident that the subharmonic amplitude is much larger for the 2D-phase waves than for the oblique waves. No striking differences from the oblique wave results can be seen.

The flow on the downstream sensor became intermittent for this forcing, for the most amplified frequency. The level of intermittency again varies with the forcing in a manner very similar to the variation of wave amplitude upstream. No dramatically large intermittencies were observed.

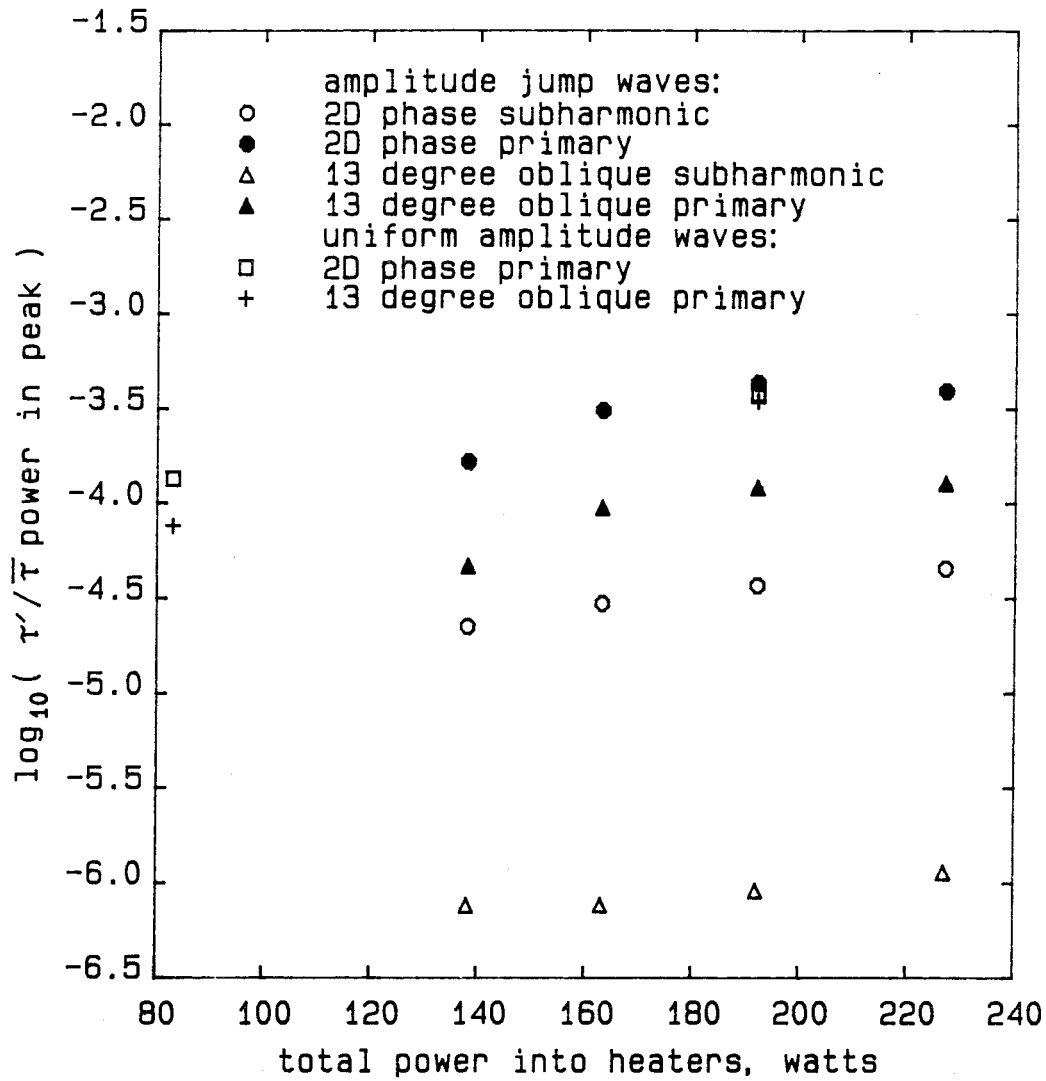


Figure 3.48: Primary and Subharmonic Response to Amplitude Jump Forcing
S6, $Re_{\delta^*} = 1350$, 20Hz forcing, North side always 96W, 5-2d3

Chapter 4

Summary of Results

Experiments exploring some effects of well-controlled three-dimensional forcing on boundary layer transition are reported. A new apparatus was developed, and the accuracy of the perturbation introduced has been improved by an order of magnitude both in phase and in amplitude.

The apparatus was first used to generate oblique instability waves, both as a study in themselves and as a test of the apparatus. The wall shear fluctuations on a fixed sensor in the linear region downstream decreased with increasing oblique angle, as might be expected from Squire's transform. Results for the streamwise phase speeds of these waves agree with the linear theory, showing an increase with both frequency and oblique wave angle. Measurements of the angles of the waves show that the average angle agrees well with the expected value. Thus, single oblique waves can be successfully generated and do agree with the linear theory, at least in overall properties.

The development of the oblique waves was observed through the nonlinear region. Second harmonics in the wall shear response were observed to scale as the quadratic of the primary amplitude. Subharmonics were also observed at some spanwise locations. When subharmonics were observed, their amplitude was largest for 2D forcing and decreased rapidly with increasing oblique angle, decreasing by an order of magnitude as the oblique angle was increased from 0 to 13 degrees. This result suggests that the

nonlinear secondary instability of even small angle oblique waves is very different from that of 2D waves. A simple explanation of this effect in terms of the triad wave interaction theory has been proposed. Since the small angle oblique waves are almost as probable in a real flow with some natural three-dimensionality, because of their very similar growth rate, the mechanism of their breakdown should be almost as important as that for large 2D waves and deserves further study.

One might expect oblique waves to become nonlinearly unstable at lower amplitudes than 2D waves, because they contain all three components of vorticity and are thus subject to vortex stretching effects, and because the maximum of vorticity moves away from the wall for these waves. However, measurements of intermittency at a fixed downstream location show that 2D forcing, carried out near the beginning of linear instability, causes the largest upstream movement of the transition point; this upstream movement decreases with increasing oblique angle. Thus any such nonlinear effects are not sufficient to overcome the somewhat larger amplitudes which the 2D waves had at the end of the linear region.

What seems the most important conclusion arises from consideration of both of the above results. As the oblique wave angle is increased, there is an abrupt change in nonlinear breakdown mechanism, but no correspondingly abrupt change in the movement of the transition point. Thus, there must be a more fundamental explanation for the 3D nonlinear breakdown of instability waves that does not rely on a mechanism applicable only to 2D waves, and in which the presence or absence of the subharmonic or staggered pattern is not a crucial factor.

Studies of more complex wave patterns were also made. These do not show any behavior dramatically different from that of the 2D and oblique

waves. The early linear region of wave growth in the boundary layer apparently acts as a narrow band filter in both time and space, damping those disturbances with temporal or spatial wavenumbers that are not in the linear amplification region. This property is evident also in the oblique wave results, which show the waves becoming more coherent as they travel through the linear region. Only in the late nonlinear region do the waves again become more incoherent as they begin to break down into spots.

Further work should incorporate apparatus capable of visualizing the small amplitude instability waves themselves, so that the three-dimensional effects in these waves can be seen directly. This is essential for study of the three-dimensional nonlinear region, where the distortions in the wave patterns are complex and very difficult to infer from measurements at a few points. A detailed Appendix is attached that describes the three-dimensional forcing apparatus, to facilitate further work. Some useful improvements to the forcing apparatus are also suggested in the Appendix.

Bibliography

- [1] B. Bayly, S. Orszag, and T. Herbert. Instability mechanisms in shear-flow transition. *Annual Reviews of Fluid Mechanics*, 20:359–392, 1988.
- [2] G. L. Brown. Theory and application of heated films for skin friction measurement. In *Proceedings of the 1967 Heat Transfer and Fluid Mechanics Institute*, Stanford Press, 1967. pp. 362-381.
- [3] A. C. Charters. *Transition between Laminar and Turbulent Flow by Transverse Contamination*. Technical Note 891, National Advisory Committee for Aeronautics, 1943.
- [4] J. M. Cimbala. *Large Structure in the Far Wakes of Two-Dimensional Bluff Bodies*. PhD thesis, California Institute of Technology, Pasadena, California, 1984.
- [5] T. C. Corke. Measurements of resonant phase locking in unstable axisymmetric jets and boundary layers. In *Nonlinear Interactions in Fluids. Proceedings of the December 1987 ASME Winter Annual Meeting, Boston, Mass.*, 1987. pp. 37-65.
- [6] A. Craik. Boundary-layer transition: theory and experiment. In Eppler and Fasel, editors, *Laminar-Turbulent Transition. Proceedings of the First IUTAM Symposium, Stuttgart*, Springer-Verlag, 1979. pp. 218-222.
- [7] L. M. Fingerson and P. Freymuth. *Fluid Mechanics Measurements*, chapter four. Hemisphere Publishing Corporation, Washington, 1983.
- [8] M. Gaster. A theoretical model of a wave packet in the boundary layer on a flat plate. *Proceedings of the Royal Society, Series A*, 347:271–289, 1975.
- [9] J. G. Graeme. *Applications of Operational Amplifiers*. McGraw-Hill Book Company, New York, 1973.
- [10] F. R. Hama, U. Rist, U. Konzelmann, E. Laurien, and F. Meyer. Vorticity field structure associated with the 3D Tollmien-Schlichting waves.

Sādhanā, 10:321–348, August 1987. A Journal of the Indian Academy of Sciences.

- [11] R. J. Hansen and J. G. Hoyt. Laminar-to-turbulent transition on a body of revolution with an extended favorable pressure gradient forebody. *Transactions ASME: Journal of Fluids Engineering*, 106:202–212, 1984.
- [12] T. Herbert. Secondary instability of boundary layers. *Annual Reviews of Fluid Mechanics*, 20:487–526, 1988.
- [13] T. Herbert. Secondary instability of plane shear flows - theory and application. In V.V. Kozlov, editor, *Laminar-Turbulent Transition. Proceedings of the Second IUTAM Symposium, Novosibirsk*, Springer-Verlag, 1984. pp. 9-20.
- [14] J.L. Hess and A.M.O. Smith. Calculation of potential flow about arbitrary bodies. *Progress in Aeronautical Sciences*, 8:1–138, 1967.
- [15] F. B. Hildebrand. *Introduction to Numerical Analysis*. Dover Publications, New York, second edition, 1987.
- [16] Y. Kachanov. Development of spatial wave packets in boundary layer. In V.V. Kozlov, editor, *Laminar-Turbulent Transition. Proceedings of the Second IUTAM Symposium, Novosibirsk*, Springer-Verlag, 1984. pp. 115-123.
- [17] Y. Kachanov, V. Kozlov, V. Levchenko, and M. Ramazanov. On nature of K-breakdown of a laminar boundary layer. New experimental data. In V.V. Kozlov, editor, *Laminar-Turbulent Transition. Proceedings of the Second IUTAM Symposium, Novosibirsk*, Springer-Verlag, 1984. pp. 61-73.
- [18] Yu. S. Kachanov. On the resonant nature of the breakdown of a laminar boundary layer. *Journal of Fluid Mechanics*, 184:43–74, 1987.
- [19] Yu. S. Kachanov and V. Ya. Levchenko. The resonant interaction of disturbances at the laminar-turbulent transition in a boundary layer. *Journal of Fluid Mechanics*, 138:209–247, 1984.
- [20] J. M. Kendall. Supersonic boundary layer stability experiments. In W.D. McCauley, editor, *Boundary Layer Transition Study Group Meeting, Volume II: Session on Boundary Layer Stability*, Aerospace Corporation, 1967. Air Force Report No. BSD-TR-67-213, Vol II.

- [21] P.S. Klebanoff, K.D. Tidstrom, and L.M. Sargent. The three-dimensional nature of boundary-layer instability. *Journal of Fluid Mechanics*, 12:1-34, 1962.
- [22] S. J. Kline and F. A. McClintock. Describing uncertainties in single-sample experiments. *Mechanical Engineering*, 75:3-8, January 1953.
- [23] V.V. Kozlov and V.Y. Levchenko. Laminar-turbulent transition control by localized disturbances. In H. Liepmann and R. Narasimha, editors, *Turbulence Management and Relaminarization. Proceedings of IUTAM Symposium, Bangalore, India*, Springer-Verlag, 1987. pp. 249-269.
- [24] P. Leehey, C. Gedney, and J. Her. The receptivity of a laminar boundary layer to external disturbances. In V.V. Kozlov, editor, *Laminar-Turbulent Transition. Proceedings of the Second IUTAM Symposium, Novosibirsk*, Springer-Verlag, 1984. p. 283.
- [25] M. Lessen and P. Koh. Instability and turbulent bursting in the boundary layer. In V.V. Kozlov, editor, *Laminar-Turbulent Transition. Proceedings of the Second IUTAM Symposium, Novosibirsk*, Springer-Verlag, 1984. pp. 39-51.
- [26] H.W. Liepmann, G.L. Brown, and D.M. Nosenchuck. Control of laminar-instability waves using a new technique. *Journal of Fluid Mechanics*, 118:187-200, 1982.
- [27] L. M. Mack. Boundary layer linear stability theory. In *Special Course on Stability and Transition of Laminar Flow*, Advisory Group for Aerospace Research and Development, 1984. AGARD Report No. 709.
- [28] L. M. Mack. Instability wave patterns from harmonic point and line sources in laminar boundary layers. In V.V. Kozlov, editor, *Laminar-Turbulent Transition. Proceedings of the Second IUTAM Symposium, Novosibirsk*, Springer-Verlag, 1984. pp. 125-132.
- [29] L.M. Mack. Computations of spatial case linear instability theory for low Reynolds number boundary layers. Private communication of results for various frequencies, spanwise wave numbers, and Reynolds numbers, 1986-1988.
- [30] H.U. Meier, Li Jing-bai, and A. Maier. *Boundary Layer Transition Controlled by Flush Mounted Electro Acoustic Generators*. Technical Report IB 222-87 A 33, DFVLR, Göttingen, West Germany, 1987. In

- English. See also references therein to earlier work with pulsed heating wires in air.
- [31] R. Narasimha. The laminar-turbulent transition zone in the turbulent boundary layer. *Progress in Aerospace Science*, 22:29–80, 1985.
 - [32] D. M. Nosenchuck. *Passive and Active Control of Boundary Layer Transition*. PhD thesis, California Institute of Technology, Pasadena, California, 1982.
 - [33] W. H. Press, B. P. Flannery, S. A. Teukolsky, and W. T. Vetterling. *Numerical Recipes: The Art of Scientific Computing*. Cambridge University Press, Cambridge, 1986.
 - [34] H. F. Robey. *On the Nature of Oblique Instability Waves in Boundary Layer Transition*. PhD thesis, California Institute of Technology, Pasadena, California, 1986.
 - [35] H.F. Robey. Discussions of experimental results for oblique waves. Private communication, 1988.
 - [36] H.F. Robey. On the nature of oblique instability waves in boundary layer transition. In H. Liepmann and R. Narasimha, editors, *Turbulence Management and Relaminarization. Proceedings of IUTAM Symposium, Bangalore, India*, Springer-Verlag, 1987. pp. 187-198.
 - [37] H. Schlichting. *Boundary-Layer Theory*. McGraw-Hill Book Company, New York, seventh edition, 1979.
 - [38] G.B. Schubauer and H.K. Skramstad. Laminar boundary-layer oscillations and stability of laminar flow. *Journal of the Aeronautical Sciences*, 14:69–78, 1947.
 - [39] A.M.O. Smith and J. Pierce. *Exact Solution of the Neumann Problem. Calculation of Non-Circulatory Plane and Axially Symmetric Flows About or Within Arbitrary Boundaries*. Report ES 26988, Douglas Aircraft Company, 1958.
 - [40] P.R. Spalart and K. Yang. Numerical study of ribbon-induced transition in Blasius flow. *Journal of Fluid Mechanics*, 178:345–365, 1987.
 - [41] H. B. Squire. On the stability for three-dimensional disturbances of viscous fluid flow between parallel walls. *Proceedings of the Royal Society, Series A*, 142:621–628, 1933.

- [42] J. Stuart. Instability of flows and their transition to turbulence. *Zeitschrift für Flugwissenschaften und Weltraumforschung*, 10:379–392, 1986. (in English).
- [43] S. Taylor. *The Effects of Large-Eddy Manipulator Devices on the Turbulent Spot and the Turbulent Boundary Layer*. PhD thesis, California Institute of Technology, Pasadena, California, 1986.
- [44] B. Thwaites, editor. *Incompressible Aerodynamics*. Clarendon Press, Oxford, 1960.
- [45] B. O. Trebitz. *Acoustic Transmission Imaging for Flow Diagnostics*. PhD thesis, California Institute of Technology, Pasadena, California, 1982.
- [46] T. M. Ward. The Hydrodynamics Laboratory at the California Institute of Technology. *Transactions ASME: Journal of Fluids Engineering*, 98:740–748, 1976.
- [47] A.R. Wazzan, T.T. Okamura, and A.M.O. Smith. *Spatial and Temporal Stability Charts for the Falkner-Skan Boundary-Layer Profiles*. Report DAC-67086, Douglas Aircraft Company, Long Beach, California, 1968.
- [48] G.B. Whitham. *Linear and Nonlinear Waves*. Wiley-Interscience, New York, 1974.

Appendix A

Detailed Description of Experimental Apparatus

A.1 General Apparatus and Procedures

A.1.1 Segmented Flat Plate Model

The flat plate model used for the experiments was designed to be composed of interchangeable sections, for flexibility. A sketch of the plate is included as Figure 2.2. The overall width is 19.75 inches, which allows 0.125 inches of space on either side between the plate and the wall of the tunnel test section for a Tygon tubing seal. The plate has a total length of 49 inches, this being the longest length for which the center of the plate at the trailing edge is still free of edge contamination from the tunnel sidewalls. It is made principally of one inch thick plexiglas, cut into sections 6 inches x 17.75 inches. There are three extra sections beyond those needed for the makeup of the plate, to allow new elements to be fabricated without losing the use of the plate. Machining of the individual sections is much easier due to their small size. The sections can be interchanged, allowing sensors and flow visualization equipment to be easily moved upstream or downstream. These capabilities were very useful during the course of the experiments.

The sections are held together by two brass rails, which make up the sides of the plate. These rails have grooves in the outside in which tubing is inserted to make a good seal with the sidewalls. There was no evidence

of any flow past the seals in the flow visualization. The rails are threaded to accept four pieces of threaded rod from which the plate as a whole is suspended. The threaded rods are attached to a pair of crosspieces across the top of the tunnel, and adjusted so that the plate working surface is in the desired position.

The smoothness of the plate is important. The critical problem with making a plate out of sections is to minimize any possible discontinuity at joints of the working surface, especially near the leading edge where the boundary layer is thinner. This problem is made more difficult by the poor dimensional stability of plexiglas. The solution is use of stainless steel joint pieces that are bolted to flats machined on the back of both sections at each joint. The flats were very carefully machined so that the distance between the working surface of the section and the flat on the back is constant along each section and also among the sections. The final cut was done on all the sections without changing the setup of the milling machine, and a uniformity of better than 0.002 inches was achieved. The plate was cut out of two pieces of plexiglas, with the working surface for all sections being taken to be the flatter side of the original pieces, which were themselves selected from stock for flatness. When the plate is assembled the discontinuity in smoothness between sections has been measured to be within 0.001 inches. In the worst cases, the joint has a jump of 0.001 inches in one direction on one side of the plate and 0.001 inches in the other direction on the other side. Since the boundary layer thickness at the first joint is above 0.020 inches (see Appendix C.1), and since the roughness present in the joints is in any case nearly two-dimensional, this seemed acceptable.

Two special sections are located on the front of the plate. The leading edge is an 8:1 ellipse, extending 4 inches in the streamwise direction. This

is bolted to the heater section, which is 3 inches long in the streamwise direction, and to which is mounted the heater array that creates the perturbations. The leading edge to heater section joint is adjustable, and the working surface smoothness at the joint can be adjusted to better than 0.001 inches. This was done by feel, with the results occasionally checked with a dial gauge. The heater section attaches to the first of the standard sections with the same joint used between the standard sections. A shim at this joint accommodates the different thicknesses of the heater arrays used during the course of the experimental development.

A tapered trailing edge flap is incorporated into the plate and is adjustable via a strut which extends from the top of the tunnel to the back of the flap. This flap is used to control the position of the stagnation point at the leading edge of the plate, in order to force it onto the working surface side. If the stagnation point should come to be on the back side of the plate, the flow has to turn through a local strong adverse pressure gradient region at the tip, making the flow very susceptible to freestream disturbances. A small deflection of the flap has a large impact on the movement of the transition point, while further motion has little further effect. For the experiments discussed in this thesis, the flap was fixed at a position in which its bottom surface was parallel to the working surface of the plate. Measurements show that the static pressure difference at the plate between a station at $x = 10$ inches and at $x = 34$ inches is less than 0.025 feet of water at $U_\infty = 3.8$ fps, for all but very large deflections of the flap (45 degrees or more). This figure corresponds to a Falkner-Skan β of less than 0.03.

The plate was always located with its leading edge $28\frac{1}{2}$ inches from the entrance to the tunnel test section. The plate was suspended accurately from above, so that it was parallel to the test section horizontal surfaces within

0.02 inches in 49 inches. The leading edge tip was located $9\frac{1}{4}$ inches from the bottom wall of the test section.

A.1.2 Experimental Control and Data Acquisition Program

The data acquisition and control program controlled the entire experiment. The set of forcing patterns desired was entered into the program. The program set the frequency generator to the correct frequency, using closed loop feedback from the heater monitoring apparatus. It then set the controller to the forcing pattern desired. After waiting for a flow to equilibrate to the forcing (wait was a minimum of 8.0 sec), it triggered the data acquisition system. Four channels of signal conditioned hot film anemometry were acquired for every run, along with two channels of heater data and two channels of unconditioned hot film anemometry. The software plotted the data on the computer screen to give rapid feedback on the system behavior, and then saved the data to disk. Only a summary of some of the less important data was saved to disk, in order to save space and processing time. The software then proceeded to the next forcing case. This software allowed data to be acquired much more rapidly and with less error than by hand. The program loops over a set of oblique wave angles, for example, and when finished with all the angles for a particular amplitude, goes on to the next forcing amplitude, until finished with all the forcing amplitudes to be done. It then proceeds to the next frequency, until all the frequencies are done. The length of time required to complete a typical set of forcing patterns was about 2-4 hours (100-200 cases, at about 1-2 minutes per case). The sequence in which the cases were carried out was sometimes staggered, so that the effect of ordering could be examined. The program was used in two versions, which

differ in their particulars.

The original setup from which data are presented here did not pause between forcing cases; thus, the heaters were on for the whole course of the experimental set, which might cover a few hours. Only when the frequency was being changed was the heater output turned down low. This constant heating could potentially cause some contamination of later runs through the heat generated by earlier runs. For the second set of experiments the data acquisition program was changed in order to turn off the heating for 8.0 sec between runs, in order to eliminate this possibility.

The second version of the program added some further features. The program was changed in order to plot spectra on the screen for immediate feedback. Also, after taking 8 seconds of data on the 8 channels during the forcing, data were taken for one second on 8 different channels without forcing, to study changes in the mean hot film signals, the tunnel temperature, and the freestream stagnation pressure. Only summaries of the second eight channels were saved to disk. As in the first version, full time traces were saved of the first eight channels of data acquisition only for the wall shear sensor time fluctuations, the other information (two channels of mean hot film, and the heater performance) being summarized only (saving the mean, maximum, minimum, and rms variation). The second version saved the phase of the heater signal, in addition to the frequency, which was saved by both versions. The second version also ran a repeated reference case at the beginning of every loop over forcing amplitude, so that the drift of performance for a fixed forcing type could be checked. The second case also reduced the digitization rate to 500Hz from 1000Hz, so that longer records could be taken.

A.2 Heating Apparatus for Introducing Perturbations

A.2.1 Computer-Controller Interface

The heater array controller was designed by Dr. Harry Robey to interface directly with the HARDNUTS II computer. The controller accepts input from an 8 bit data bus, and from 32 data ready lines, one for each heater channel, which are set high one at a time when the particular heater is to latch data from the data bus. It was necessary to build an interface between this controller and the Zenith Z-200 PC/AT clone that was used as a data acquisition and control computer. This interface was designed and built by H. Robey. A schematic drawn from a sketch supplied by Robey is attached as Figure A.1. The description following is based on information supplied by Robey.

The individual heater channels on the controller are addressed by writing 8 bit bytes to 32 individual I/O ports that are reserved by the Zenith for user I/O. Port addresses 340-35F are used to represent heaters 1-32. These are nominally free addresses for I/O and do not conflict with the operation of the COMPUTERSCOPE A/D board¹. The 8 bit byte on the data line is decoded by the controller hardware into 4 bit nibbles for the heater phase lag and amplitude, so the only work the interface need do is to decode a write signal for a port address into a write signal on one of the 32 controller data ready lines.

The first 74LS244 serves as a buffer and line driver for the 8 bit data bus, and has no other function. The second and third 74LS244's serve to buffer the computer input of the port address. The second buffers the I/O write and address enable lines of the bus, and the 5 higher order bits of the port

¹Z-200 Tech Manual Table 6-2 or IBM AT Technical Reference Manual

ZENITH Z-200 PC/AT TO HEATER CONTROLLER INTERFACE

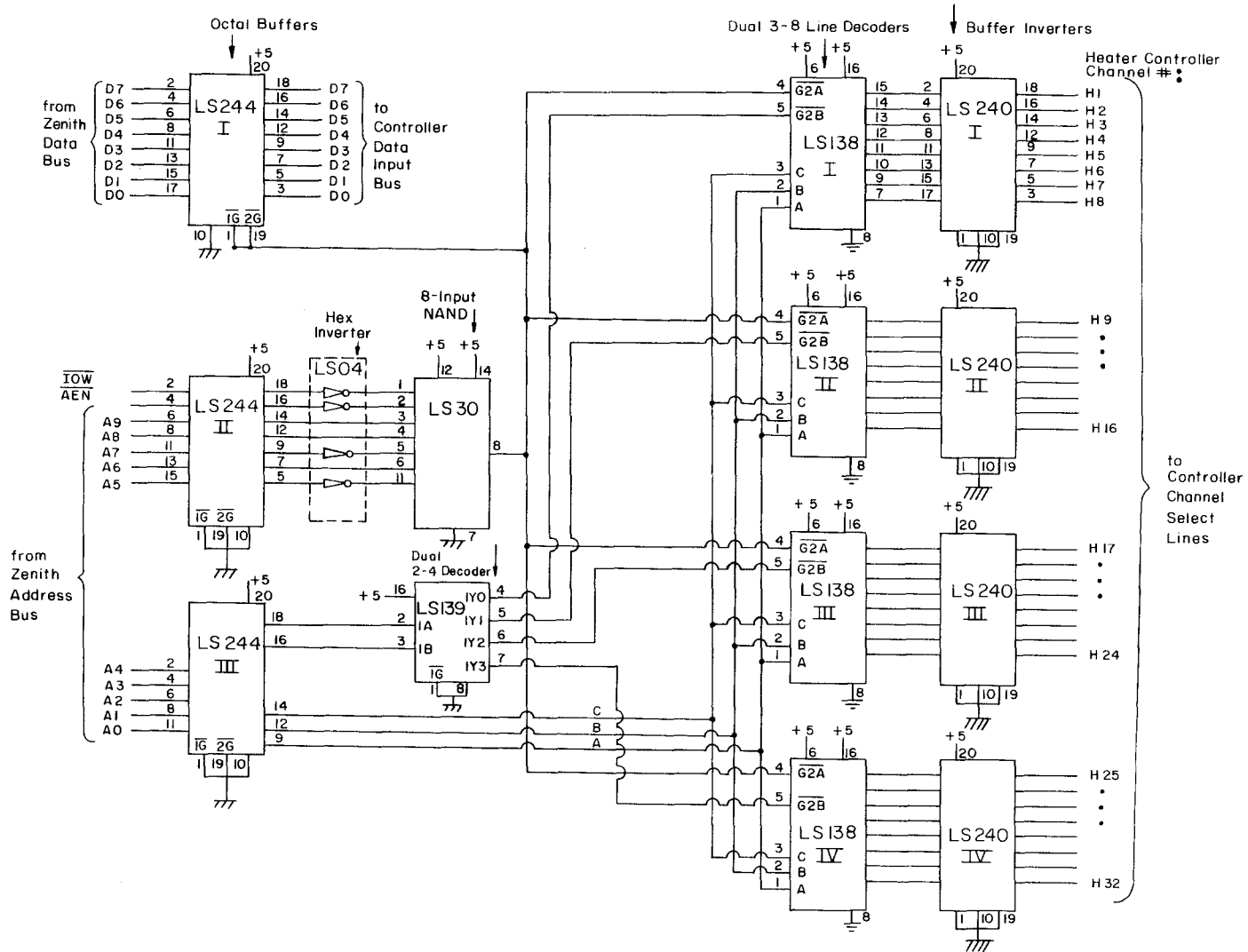


Figure A.1: Computer-Controller Interface Schematic

address. The third buffers the 5 lower order bits of the address. Only the lowest 10 bits of the address bus are decoded since these should be enough to make the address unique.

The 74LS30 is an 8 input positive NAND gate. Some of its input signals are first inverted using a 74LS04. The output of this NAND gate is a write enable signal for writing to a port. It is high when the following is true: IO write is high, address enable is high, bits 6, 8 and 9 of the address are high, and bits 5 and 7 of the address are low. When the 5 low order address bits are selected, this will pick out an address between 340 hex and 35F hex, where the controller channels are addressed. Since bits 10 and 11 of the address are not decoded, one cannot distinguish address 340 hex and address 540 hex, for example, but this is not important since the allowable addresses run only up to 3FF anyway. The LS138 and 139 chips are decoders that are arranged to turn the 32 possible states of address bits A0 to A4 into a high signal on one of 32 channel select lines when the channel select lines are enabled by a high signal on the interface write enable line. The LS240's are buffer inverters that give the output the correct logic. The write enable line was also connected to the enable line on the data buffer chip so that the data buffer only tracks the data line when data are being written to the controller, greatly reducing the noise on the data line.

In operation, the interface works as follows: An OUTP instruction from C or BASIC is used to write a data byte to one of the relevant ports. The LS244's hold the information. If the port address is correct, the hardware logic puts one of the channel select lines high, and the controller latches the byte on the data bus into the selected channel.

A.2.2 Heater Array Signal Controller

The heater controller was adapted from that used by Robey [34]. It is worth noting that the schematic in [34] gives $0.035\mu F$ for the phase shift setting capacitors although the installed value was $0.1\mu F \pm 20\%$ or so. Several modifications were made to improve accuracy, stability, and ease of use.

A schematic for an individual controller circuit is attached as Figure A.2. The controller is made up of 32 of these circuits, mounted on eight wire-wrapped circuit cards that are connected with edge connectors into a vented cabinet. The controller is part digital and part analog. It takes the sine wave input from a signal generator (usually 5V and about 10Hz) and produces 32 channels of sine waves, one for each heater, with 16 possible discrete amplitudes for each channel, and 16 possible discrete phase lags between each channel and the next. The choices of amplitudes and phase lags are made by computer control through the interface card. The output amplitudes can be adjusted to match the heater resistances using an individual trimpot on each channel.

The circuit schematic will be described starting from the control side: Each 74LS373 latches in an 8 bit control word from the interface card in the computer when the chip select line for that channel is set high by the computer. The most significant (MS) 4 bits control the setting of 16 possible phase shifts, and the least significant (LS) 4 bits control the 16 possible amplitude settings. The control word is converted from TTL to CMOS levels by the first pair of TL074 op-amps. These signals are used to control the CD4066 quad digital switch chips. These chips switch the discrete resistances in and out of the two principal op-amp circuits, which use a third quad TL074 chip to supply the op-amps shown on the right side of the schematic.

CIRCUIT DIAGRAM OF THE PHASED HEATER CONTROL ELECTRONICS

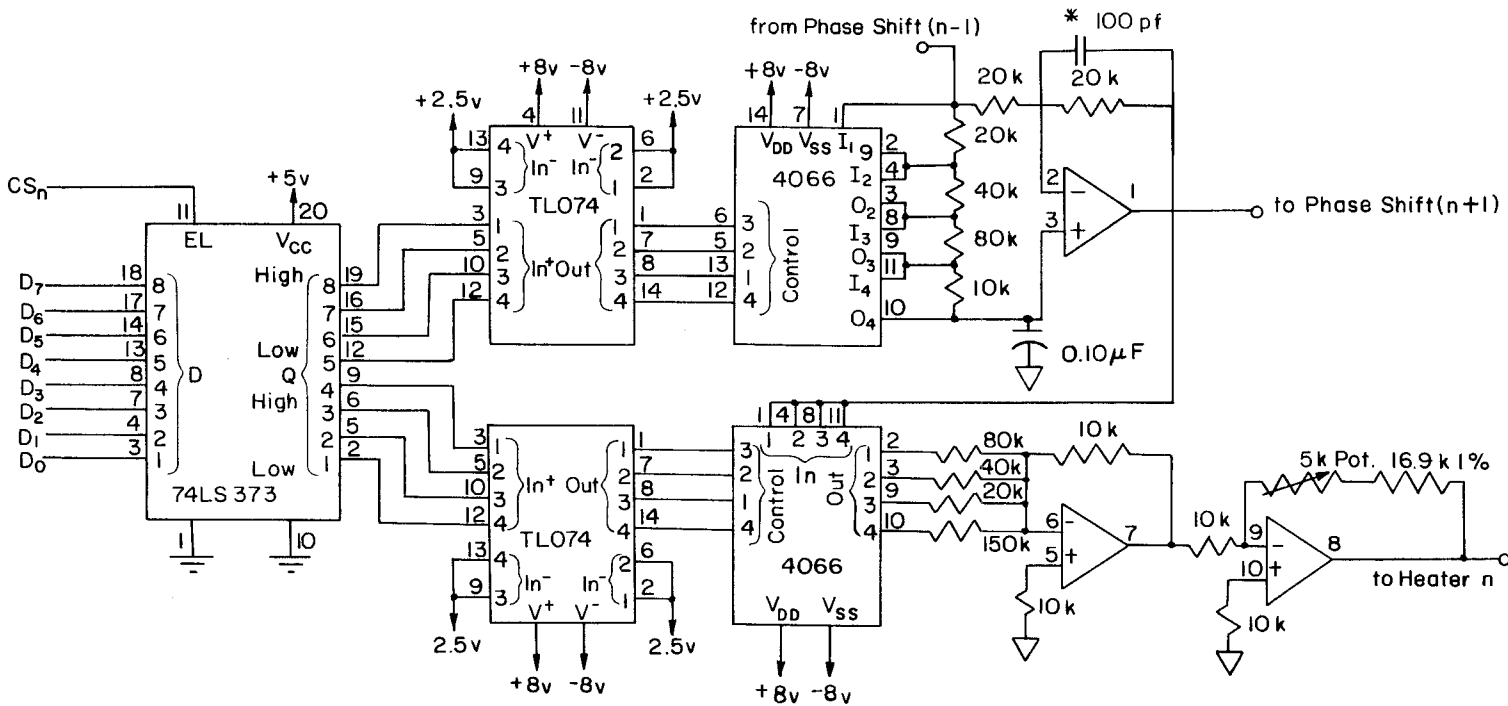


Figure A.2: Heater Signal Controller Schematic
 * - this component installed in every fourth circuit

The upper phase shift circuit is described by Graeme [9, pp. 102-103], and gives phase shifts of 0/16 to 15/16 of the maximum shift, as the phase shift instruction is varied from 0-15. The phase shift signals are chained from each circuit to the next, and are also passed to the lower, amplitude setting, circuit. This is a standard inverting amplifier circuit, which gives gains of 0/16 to 15/16 as the 4 bit digital amplitude instruction varies from 0 to 15. The output of this circuit is passed to a buffer stage that provides an adjustable gain. This adjustable gain was used to fine-tune the voltage outputs for the individual heaters, so that the heater array would produce a uniform power output in spite of the variation in heater resistances.

Several specific problems and modifications will be detailed. The chained phase shift circuits developed high frequency (MHz range) oscillations under some circumstances. These heated the chips and distorted the output sine waves, causing the output op-amps to fail fairly often. Small (100pF) capacitors were installed in the feedback loop of every fourth phase shift circuit to roll off the gain at high frequencies and remove this problem. They have no appreciable affect on the frequencies of interest.

The output pot originally allowed adjusting the gain from 0 to 5 in 20 turns, making fine adjustments very difficult. It was usually set to a gain of about 1 to drive the original 0.5 ohm heaters with up to 5V. This pot was replaced by a 5K pot in series with a 16.9K fixed resistor allowing adjustment of the gain over a range of about 1.7 to 2.2. The output maximum desired is about 10V with the 1 ohm heater elements in the later designs, but the CMOS digital switches can only switch voltages up to about 7V. A 5V signal is therefore standard throughout the controller up to this output stage. If the circuit were to be rebuilt, digital switches capable of switching 15V would probably be used.

The original capacitors in the phase shift circuit were $0.1\mu F \pm 20\%$. The tolerance caused a large variation in the phase shift between the channels. Early measurements of the rms variation among the channels gave about 20%. These capacitors were replaced with new ones of the same value but with 1% accuracy. The rms variation of phase shift among the channels is now about 1%, a value in line with the 1% accuracy components used throughout.

The circuits still fail fairly often, usually by the development of stray resistances in the contacts between circuit cards. The resistance in the contacts causes anomalous phase shifts in some of the circuits. The controller monitoring interface and software allow the performance to be easily checked and make maintenance much easier. The controller performance is evaluated in Appendix A.2.6.

A.2.3 32 Channel Power Amplifier

Preliminary experiments were carried out using a modified version of the amplifier described by Robey [34]. A corrected schematic for this amplifier is attached as Figure A.3. This simple design can be adjusted with considerable effort to give good accuracy at one forcing level, but gives large errors at different forcing levels ($O(10\%)$). The errors are due both to crossover distortion and to DC offset problems. The DC offset was introduced when the battery power sources used developed different voltages during loading and over the course of a set of runs. A new power amplifier was therefore designed. The new apparatus reduced these important errors by an order of magnitude (see Appendix A.2.6.2 for discussion).

The central element in the new power amplifier is a set of Burr-Brown OPA501 power operational amplifiers. These chips are capable of sourcing

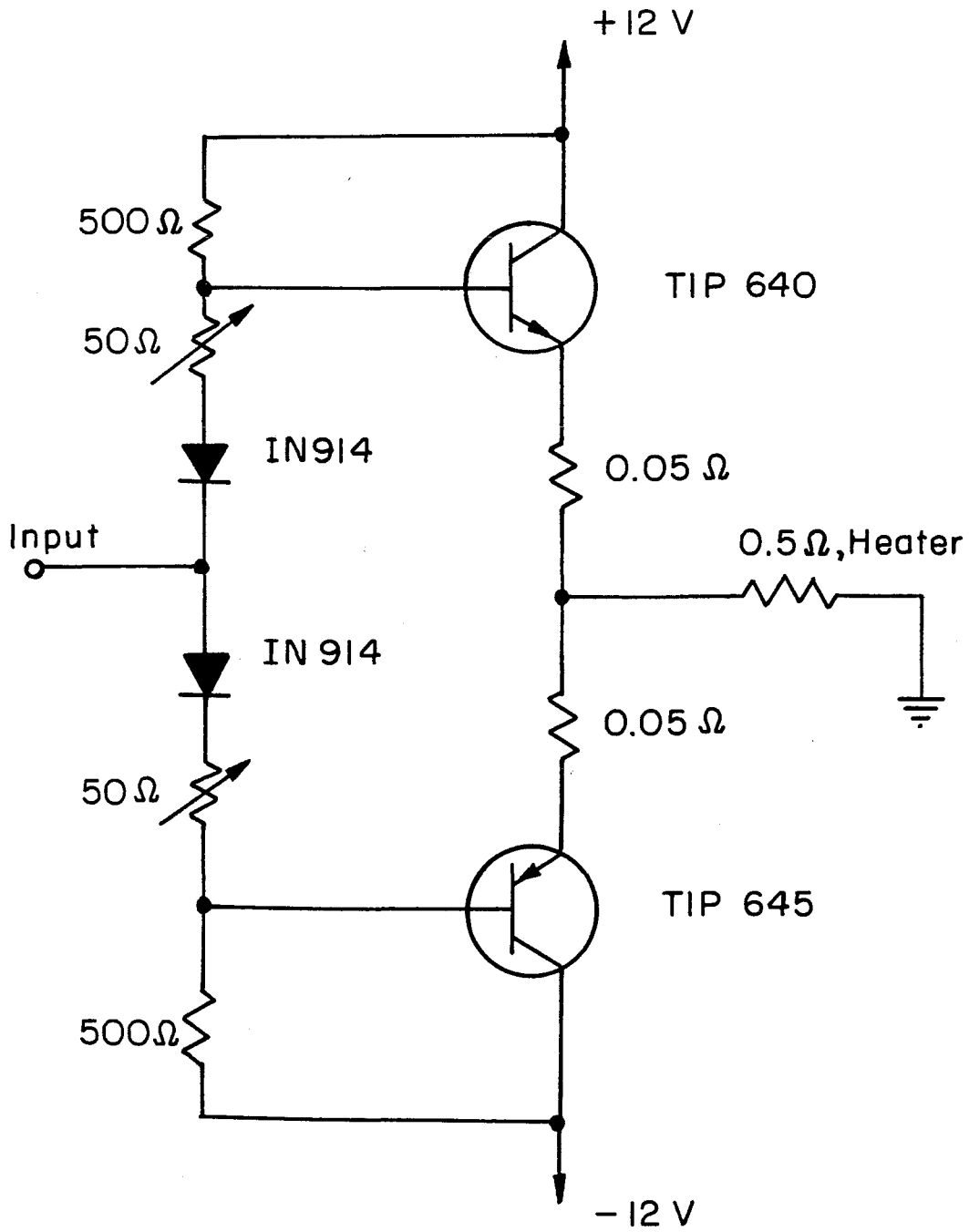


Figure A.3: Old 32 Channel Power Amplifier Schematic

CIRCUIT FOR 32 CHANNEL POWER AMPLIFIER

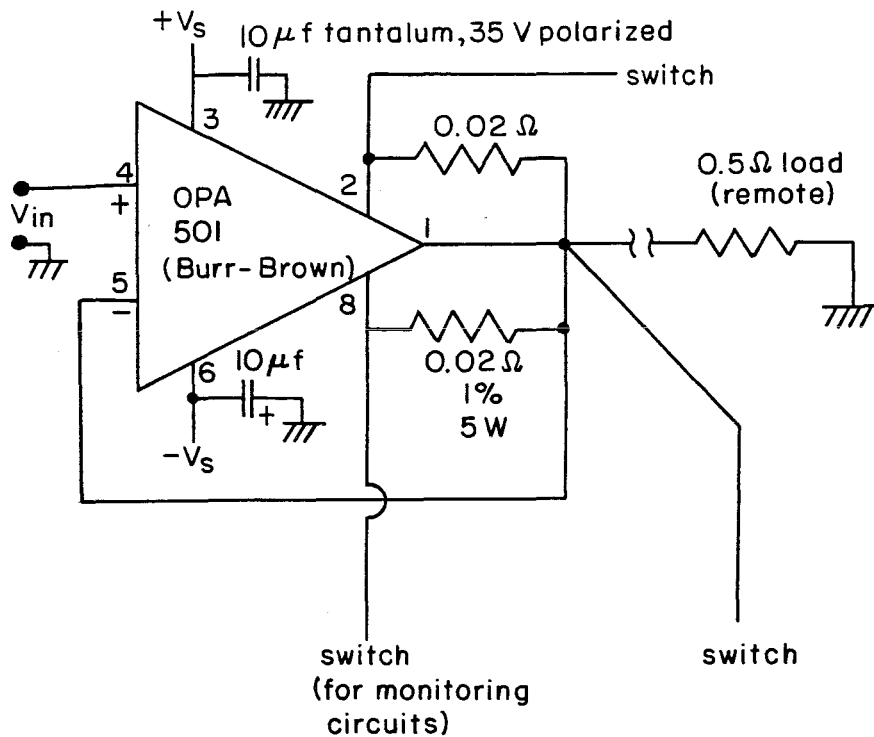


Figure A.4: 32 Channel Power Amplifier Schematic

10A and of dissipating 80W and cost about \$50 each. The individual amplifier circuits designed around these chips are shown in Figure A.4. An OPA512 op-amp was also tested and would have been preferable due to a higher power capability, but it was unstable to high frequency oscillations. These op-amps are very accurate, despite the high power levels: for example, total harmonic distortion for the OPA501 is quoted at 0.2% by the manufacturer for frequencies below 500Hz. The circuits required no adjustments

to maintain accuracies well within about 1% in all tests conducted. The op-amps reject the 3V spikes that occur in the power supply lines due to the highly varying load, passing no evidence of them to the output.

The individual circuits are kept very simple. The unity gain design requires no gain-setting components. The current limiting resistors are required by the op-amp design and turned out to be very useful. The only other components in the circuit are power-supply bypassing capacitors used to insure against oscillation.

Construction techniques were important for the chassis, since the amplifier set can draw as much as 320A and dissipate as much as 1000W in normal operation. The op-amps must be kept below about 75°C to stay in the manufacturer's safe operating area. The op-amp circuits were mounted in blocks of eight on 2x5 inch aluminum channel that was drilled to mount the op-amps and the current limiting resistors. Four of these blocks are mounted parallel to the front of a commercial metal chassis, bolted to the aluminum base. One side of the chassis holds a large perforated plate vent, and in the other side are two large 4.5 inch diameter 120V, 0.35A fans for cooling. In steady operation at full load, the base of the box gets warm but not hot. The circuits are fused on both the (+) and (-) power supply sides, in pairs, for a total of 32 fuses.

The current-limiting 0.02 ohm 1% resistors are used as ammeter shunts for measuring the output currents, since they carry full output current. One carries the positive-sense current and the other the negative-sense current; they will be called the (+) and (-) resistors. The effective resistance of the (+) resistor is slightly higher due to the longer length of 18ga wire required to reach it. Pins 2, 8, and 1 of each op-amp are wired to 3 pole rotary switches, one for each block of amplifier circuits. Each rotary switch is

wired to a master switch, which connects to external banana jacks. A fourth external banana jack is wired to the power supply ground reference for use in monitoring the outputs. Thus the (+) and (-) currents and the output voltage for each circuit can be monitored by switching external switches. The individual amplifier blocks can be removed for repair by disconnecting the master switch, the fuse lines, the input lines, and the output lines, and removing the block together with its associated rotary switch. Due to the low impedance of the load, quality of the output connections proved to be crucial, and spade lugs with terminal strips are used and have proven satisfactory. Heavy-gauge wiring is used on all low impedance paths. The inputs from the controller are brought in via a standard 34 pin ribbon cable connector.

The output monitoring banana jacks are connected to the Computerscope A/D board for monitoring the forcing electronics, using an isolation amplifier (see Appendix A.3.2). A data-taking program was written that prompts the operator to switch the rotary switches while the program takes and processes data for the output voltage and current for each channel. In this way the output current and voltage on all 32 channels can be checked at one forcing level in a matter of a few minutes, allowing frequent checks during the experimental series. This capability proved essential to the improvement and maintenance of the complex forcing apparatus.

A.2.4 High-Current DC Power Supplies

Two high-current DC power supplies running off 230V line power were used to power the heater system. These supplies are capable of 20V and 250A peak output. They are model number TCR20T250 supplies from Electronic Measurements, Inc. and use linear SCR technology. Although this technology is not really designed to maintain power to a 10Hz fluctuating load

such as the one in the present experiments, they functioned satisfactorily. It would have been much more expensive to obtain switching power supplies of the same current output, and it was feared that the noise output of switching supplies would interfere with the experiment. The voltage supplied by the Electronic Measurements supplies fluctuated about 3V peak-to-peak around a 10.5V mean when operating with a 160 amp peak load at about 10Hz. This large noise component was successfully rejected by the power op-amps used in the amplifier array, however, and no trace of it was evident in the output. The power supplies were a major improvement to the previously used lead-acid batteries, mostly because they allowed the experiment to be operated indefinitely.

A.2.5 Heater Array

The heater array is manufactured using standard printed circuit technology. A photo of the current version of the array is attached as Figure A.5. All arrays used in the course of these experiments were manufactured by Proto Systems, of Alpharetta Georgia, from artwork created at GALCIT.

The artwork for the arrays used in the preliminary work was a photographic copy of the artwork used for Robey's array [34], enlarged so that the array would span the 20 inch test section of the FSWT instead of the 13 inch test section of the HSWT². This original array design had a thinner ground bus and wider heater lines, as well as heater pads that extended much farther in the streamwise direction. It was found during tests of the current distribution in the array, with only one end of the ground bus connected to external ground, that the voltage drop in the ground bus under 2D forcing caused a large difference in the power delivered to the heaters at different

²High Speed Water Tunnel

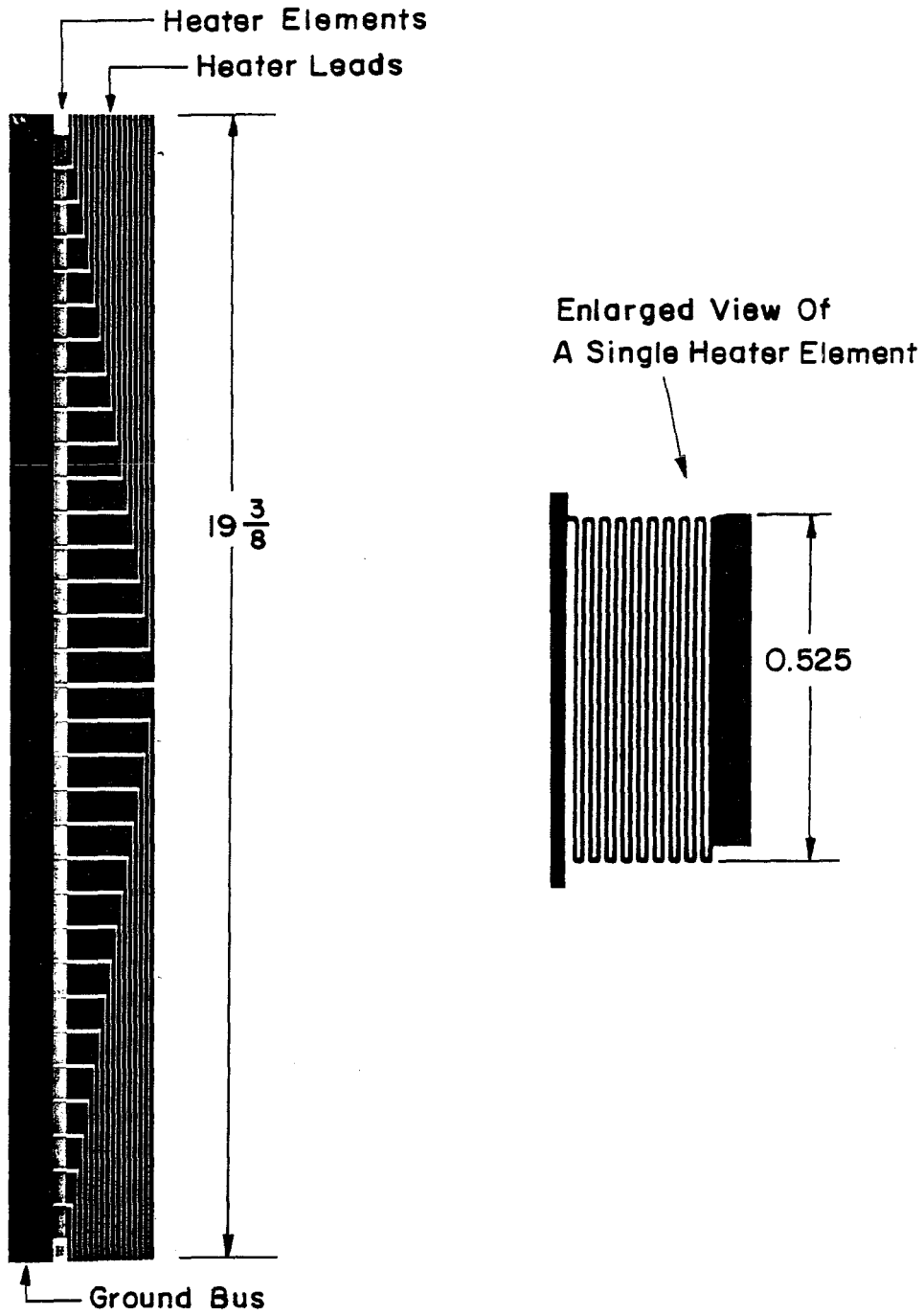


Figure A.5: Photograph of Heater Array
(dimensions in inches)

ends of the array. Modeling of this problem indicated that this would still be a large effect with both ends grounded, and so the design of a new array was undertaken. Since Robey did not measure the current distribution in his heaters under load, and since although he grounded both ends of his array he used 28ga ribbon cable for leads, the uniformity and consistency of the actual output from his heaters has to be considered questionable. Differences between the current results and those of Robey could well be attributable to this factor.

The final design was an adaptation of the old one. The heater array is not insulated from the water, so that it can be thinner and so that heat transfer to the water can proceed more easily, but this element of the design has the drawback of requiring the heaters to be very low resistance, if high voltages and consequent electrolysis are not to be a problem. With the current design, the heater resistances are about 1 ohm, and peak voltages reach about 3-5V. Under these conditions, if the water resistance is lowered by adding a small amount of bleach, the heaters begin electrolyzing. Future designs should incorporate an insulating coating so that the resistance can be increased without causing electrolysis. The difficulty of having low resistance heaters lies in keeping the lead resistance small compared to the resistance of an array of 32 heaters in parallel.

The array used in the experiments reported here has 32 heaters, the width of which is dictated by the need to span the 20 inch test section of the tunnel, leaving enough room near the edges to attach leads. The spacing between the heater pads is the minimum amount that will not create difficulties in fabrication. The center-to-center spacing of the heaters is designed to be 0.575 inches, with 0.050 inch spacing between pads. The streamwise dimension of the heaters affects the diffusion of the heat into the boundary layer. This

dimension was chosen to be somewhat less than $10\delta^*$, following the empirical suggestion of Nosenchuck [32, p. 49]. The heater resistance elements consist of a 'winding' of 17 lengths of 0.005 inch wide copper spaced 0.012 inches on centers, taking up a streamwise distance of about 0.22 inches. The minimum width of the heater lines is dictated by the ability of the technology to reproduce fine detail. The board was made from stock copper to make production simpler. It could be made out of several materials, or the lead section of the board could be plated after etching to reduce the lead resistance. These expedients were avoided for simplicity. The leads were made as wide as possible, keeping the total streamwise length of the board small enough so that it can be fastened to the 3 inch long flat plate section designed to hold it.

The artwork for the photoreproduction of the heater was created on an E size HP plotter (courtesy of Prof. Eric Antonnson) using a file of HP-GL instructions made up using a custom program. This procedure allowed careful determination of the sizes of the elements and was fairly simple. John Lee helped with the use of the plotter. Narrow titanium ball india ink pens (0.35mm and 0.25mm) were used in the plotter to make the fine lines in the artwork that make up the resistive elements. A wider pen was used to do the filling to make the leads. The artwork was sent to Proto Systems, who did a 2X reduction down to the 20 inches x 3 inches full size, and printed the board. The actual board came out about 1.5% oversize. In the future, the photolithography mask should be created directly, using a Gerber photoplotter, since this 2X reduction was very difficult for the finely detailed board.

Preliminary versions of the array were manufactured on Kapton film, also by Proto Systems. This film is flexible, and could be used to attach an array to bodies such as airfoils or cylinders. The array was then epoxied to the

plexiglas section of the flat plate. However, both times this was done the film eventually peeled away from the plate, after repeated rewettings and dryings.

The current heater array was then obtained on 0.062 inch (nominal) FR-4 using one ounce copper, which is about 0.0014 inches thick. This 0.0014 inches protrudes into the flow about 5% of the local boundary layer displacement thickness (see Figure C.3) or about 1.3 wall units. The board was drilled and countersunk for 2-56 flat head screws, which were mounted smooth or just below the surface. High vacuum grease was used in an attempt to seal the interface between the FR-4 and the plexiglas. The remaining depressions were filled with Strip-Calk, 3M part number 8568, and scraped smooth using a piece of plexiglas having a milled edge. All protrusions were measured using a micrometer to be no more than 0.001 inches above the neighboring copper. Any remaining depressions are estimated to likewise be no more than 0.001 inches below the FR-4. The leading edge of the heater pads themselves was measured to be 1.04 inches from the leading edge of the heater section. The uncoated copper experiences only minor corrosion, because it is under water only during the actual tests.

A.2.6 Measurements of Perturbation Electronics Performance

A.2.6.1 Heater controller performance

The phase shifts of the various signals to be put on the heater array depend primarily on the phase of the outputs from the heater controller alone, since there is very little capacitance in the heaters, the frequency is very low, and the heater power amplifiers are very precise.

The controller output was monitored before and after all runs. The con-

troller worked well except for some connection problems mentioned in Appendix A.2.2. The baseline controller performance is exhibited in Figure A.6 which shows the variation of phase shift with forcing instruction for phase shift. The plot shows the normalized phase shift averaged over several cycles, and averaged over the 32 heaters. The solid line is the theory (equation 3.1) for the circuit, and it can be seen that the data fit the theory well. In particular, the phase shift is independent of the frequency. The behavior is very steady with time. The rms scatter of phase shift among the heaters is shown in Figure A.7, which shows that the deviation among the channels is about 1% of the mean phase shift, except when the mean phase shift is small. The controller was rechecked before each new set of runs to see that it did not drift from this behavior. The only problem noticed was one in which the phase shift on certain channels on one board became significantly different from the other channels. This problem turned out to be associated with the connections of the board to the instrument. At worst, this effect caused a doubling of the rms deviation of phase among the channels for even forcing instructions. The effect also caused a small shift in the mean, again only for even forcing instructions. Any large deviations of this type were generally noticed before any experiments were done, and the plots attached may be regarded as accurate descriptions to within about 20% in the rms deviation or 1 or 2% in the mean phase shift. In the worst case, a problem developed during a run or during a week between runs. A plot of the controller performance after such a run when a problem was discovered is attached as Figure A.8.

The frequency put out by the controller is selected by the frequency generator. The computer puts a voltage on the voltage controlled oscillator and uses feedback from the heaters to set the frequency. The frequency is

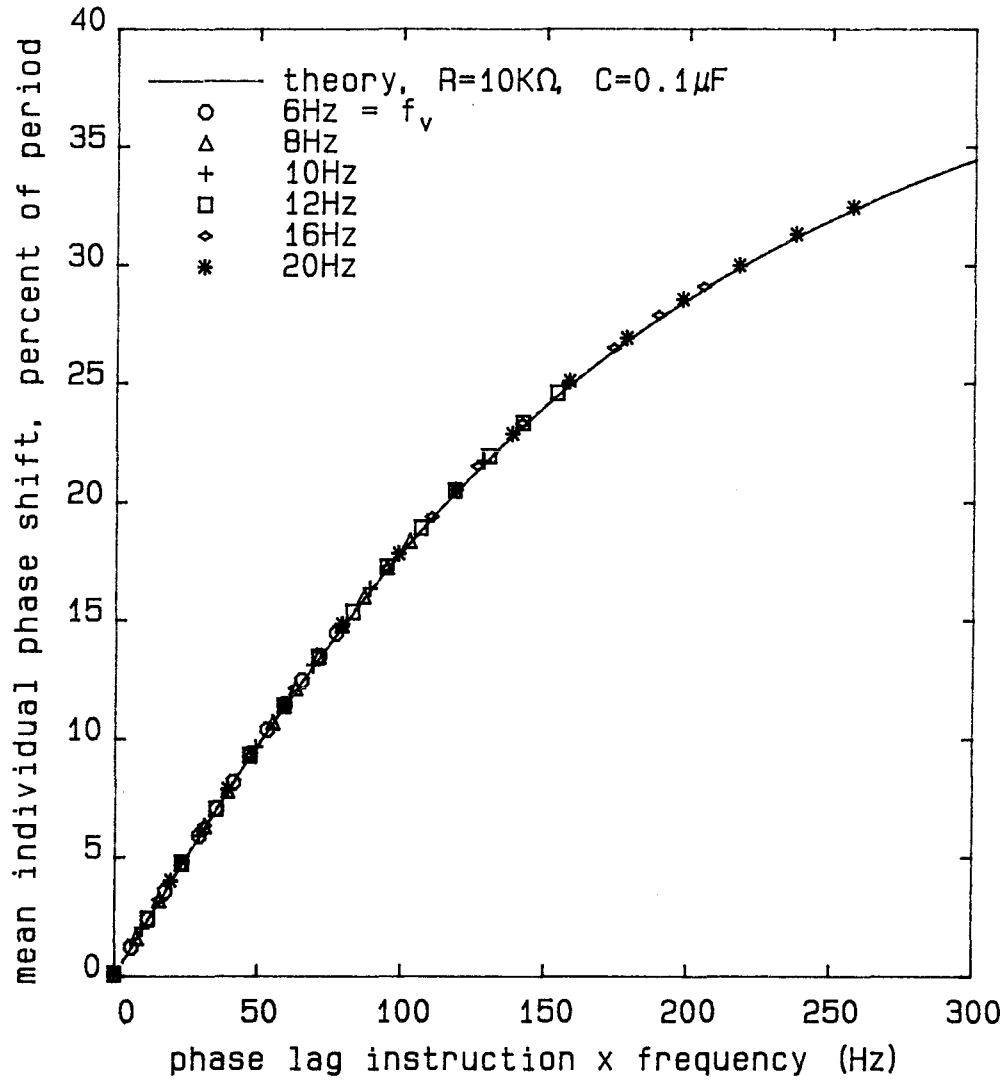


Figure A.6: Controller Phase Shift Performance
All level 10, phase lag instructions 0-13, 3-11-88
theory is Equation 3.1

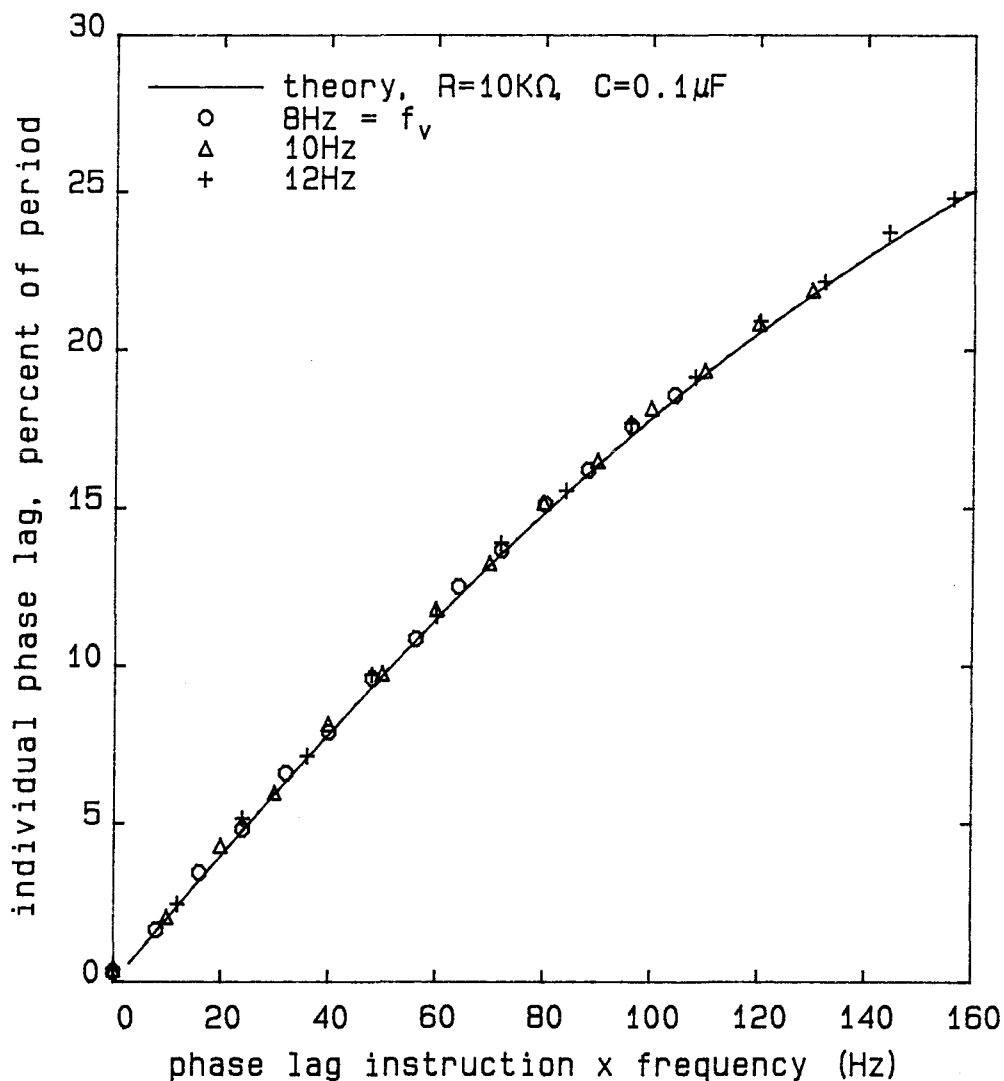


Figure A.8: Worst Case Performance of Mean Controller Phase Shifts
5-5-88 data, theory is Equation 3.1

accurate to within $\pm 0.03\text{Hz}$, and is stable over a set of runs to the same figure.

A.2.6.2 Heater power output performance

The power levels on the various heaters are very much determined by the heater power amplifiers and heater array, as well as by the controller.

The heater power output was measured using hardware described in Appendices A.2.3 and A.2.1. The necessary data were acquired on the computer, before or after a set of runs, during normal operation of the entire forcing system. In addition, one of the heater channels was monitored during all runs to provide data on the drift of the heater system. The current data are limited in accuracy, to perhaps 5%, because of inaccuracies in the resistances used for current measurement. In addition, a ground offset caused by the separate ground of the data acquisition system, which for some reason is different for each current sign, causes an additional error. The voltage data should be considerably more accurate, perhaps to 1%.

Several corrections were used in computing the power delivered to the heaters. Since the heater resistances are low, the lead resistances even for fairly heavy leads are not negligible compared to the heater resistances. The leads to ground from each side of the heater array board involved about 3 feet of 8 gauge wire from the board to outside the tunnel and about 8.5 feet of 4 gauge wire from the tunnel to the power supplies, for a total resistance of about 0.0040 ohms on each side. The parallel resistance of the 32 one ohm resistors is about 0.03 ohms, so there is about 7% of stray resistance, worth correcting for. The lines to the individual heaters from the power amp consist of about 6 feet of 20 ga. wire, used because larger gauge wire would be difficult to attach to the heater board. The resistance in these lines is

about 0.061 ohms, which is roughly 6% of the heater resistance. The voltage drop in this line was also corrected for in computing the heater power. The only correction remaining would be to correct for the voltage drop in the ground bus on the heater board in the water, which causes an error in the power distribution estimate. However, numerical studies of the heater board during its design showed this error to be about 5% or less, and it is not easily corrected for, since it depends on the current pattern as a function of time. Since the heater studies were validated by the power distribution being as uniform as expected, this correction was not made.

It is important to eliminate the DC offset in the sinusoidal voltage going into the heaters. Since the power put into the heaters varies like V^2 , if the voltage is $V_0 + V_1 \sin \omega t$, then the offset V_0 will produce an error in the power:

$$P = V_0^2 + 2V_1V_0 \sin \omega t + V_1^2 \sin^2 \omega t,$$

or

$$P = V_0^2 + 2V_1V_0 \sin \omega t + V_1^2 \left(\frac{1}{2}(1 - \cos 2\omega t) \right).$$

The second term involves the voltage forcing frequency or the subharmonic of the actual heat forcing frequency. The nonlinear development of subharmonics then becomes difficult to distinguish from the linear growth of this spurious subharmonic. This offset cannot be checked through the use of the isolation amplifier and computer because of the ground isolation problem. To eliminate all possibility of ground loops during this measurement, the DC offset was measured with a battery powered Fluke multimeter to obtain the values attached as Figure A.9. The offset of the controller output was also measured in a similar fashion and is included in the same figure. It is apparent that the offset is very small, always less than about 1%. Most of this offset comes from the controller, which is not quite as accurate as the

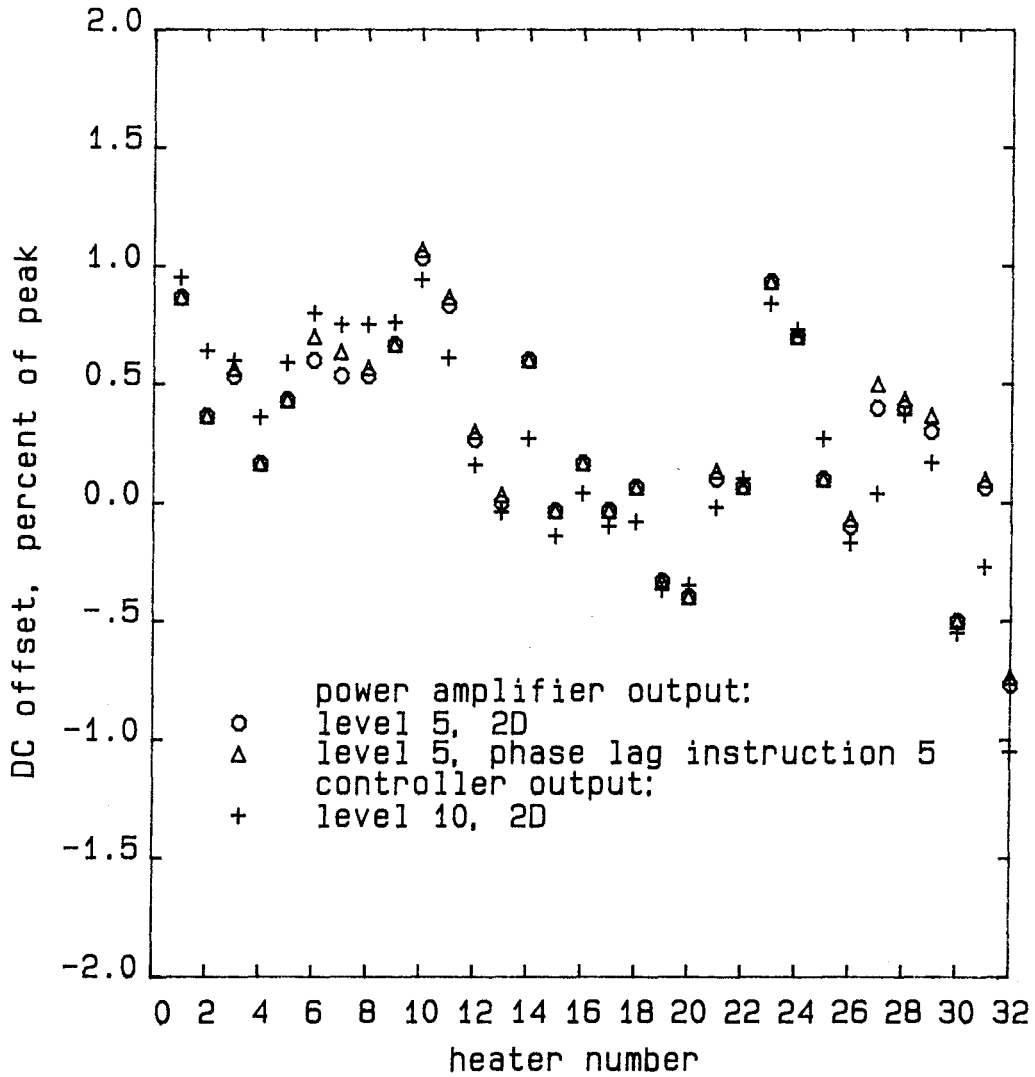


Figure A.9: RMS DC Offset Errors for Controller and Power Amplifier
power amp data taken 4-7-88; controller data taken 3-9-88

forcing angle	Total power output, watts
0	73
1	85
2	84
4	83
8	83

Table A.1: Power Output vs. Oblique Wave Angle, 9-2-88 data

power amplifier.

Another difficulty that had to be addressed and that required considerable apparatus development was the problem of keeping the heater power output constant when the forcing is changed from 2D to oblique. In 2D forcing, all the heaters are forced at the same level, in phase, so all the current (as much as 200 amps) flows out through the ground bus and ground wiring. For even the smallest oblique angle forcing, the heater currents are out of phase, and so the current flows from one heater supply into another heater supply. Thus one type involves a large voltage drop in the ground wiring, whereas the other type does not. Although this problem was overcome in terms of the uniformity of power distribution among the heaters, there remains a difference in net power delivered to the heaters when they are driven at the same computer commanded voltage levels but at different angles. Table A.1, which shows the variation of power with angle, shows a 13% drop in power delivered to the heaters for the 2D forcing as opposed to any of the oblique forcing cases. The power is very uniform among the oblique cases. This difference is not corrected for since what is presumably a linear shift in disturbance amplitude cannot easily be used to correct nonlinear effects such as intermittency or the development of subharmonics.

The amplitude of heating for the heater board is controlled by computer, and all the saved data is indexed by the forcing instruction issued to the

controller. It remains to assign a power output level to these controller instructions. There is a significant variation (as much as 15%) in the power delivered to the heaters for the same forcing instruction on different days. About half of this variation seems to be due to errors in setting the amplitude of the frequency generator, most of the rest apparently being caused by increases in the effective resistance of the heaters as they oxidize. This variation presents a further correction issue. It appears, however, that the variability is only between two groups, in each of which the delivered power is fairly constant. In the first group, the power outputs are about 15% higher than they are in the second³. Thus, separate tables of forcing level instruction vs. forcing power were made, one for each of these groups. This procedure appears to give the correct values within an error of less than 5%. The reason for the difference seems to be the difference in voltage output between two different signal generators using different procedures for setting their amplitudes.

The values for the power output for different amplitude instructions should increase as the square of the amplitude instruction, if all else were perfect, since the amplitude instruction should be linear in the heater voltage (see Appendix A.2.2). As can be seen from Figure A.10 (2D phase), this statement is fairly accurate for a given forcing type from a given group. Since the best data are for 2D forcing, values are given in the text for power for 2D forcing, with forcing using oblique phase having power higher by about 13%, also noted again in the text where this is an important issue. The error in these values, with all these corrections having been made, is perhaps $\pm 10\%$ or ± 0.1 watt. The values used for converting the level instructions to power are given in Table A.2.

³Group #1: 4-7 to 5-5; Group #2: 9-2 to 9-14

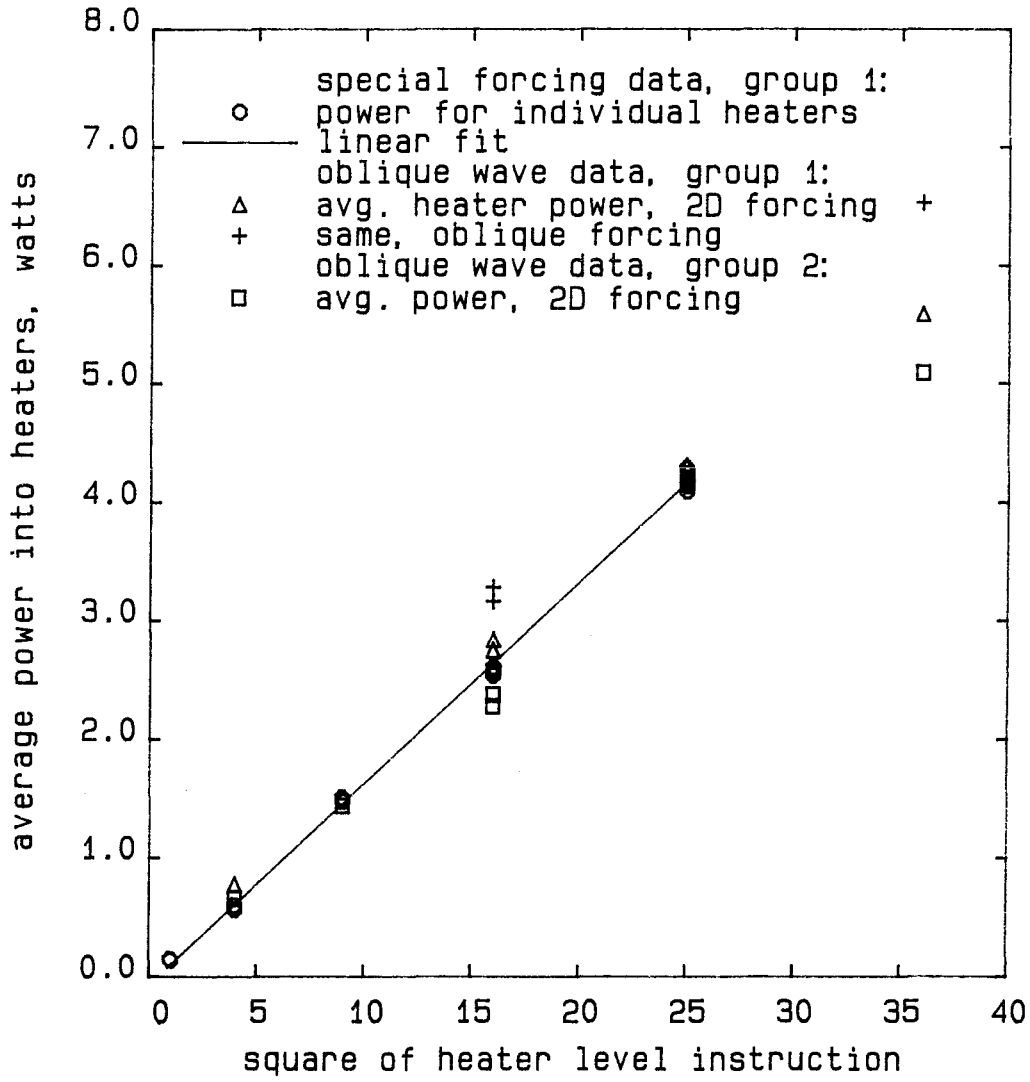


Figure A.10: Quadratic Variation of Power Output with Instruction
special forcing data from ha5-2

level instruction	power per heater, watts	
	group #1	group #2
1	0.1	0.3
2	0.6	0.7
3	1.5	1.4
4	2.6	2.3
5	4.2	3.6
6	6.0	5.1
7	8.2	6.9
8	10.7	9.0

Table A.2: Power per Heater for Different 2D Forcing Levels

The evenness of power distribution among the heaters was a major concern in the development of the apparatus, as discussed in Appendices A.2.2 and A.2.3. Using the test equipment described in Appendix A.3.2, the power output for each of the 32 heaters was measured. Some sample data are plotted as Figure A.11. The rms variation among the heaters of the corrected power output varies from 1.1% to 4.3% in the 20 test runs made; the later runs being worse due to developing problems. The average rms variation in the corrected power is 2.3%. This plot also shows how the heater voltages were fine-tuned in order to provide uniform power output in spite of heater-to-heater variations in resistance.

It would be desirable to compute the temperature on the heaters from the current and voltage measured with the above equipment in order to improve on the crude theoretical estimates that can be made following Robey [34]. However, despite serious attempts involving smoothing, correcting, and averaging, it was only possible to get a crude estimate. The errors in the measurements of current and voltage are of the order of 5%, which is of the same order as the resistance change due to the estimated temperature rise. The data show a resistance change of about 10% at the peak of the forcing

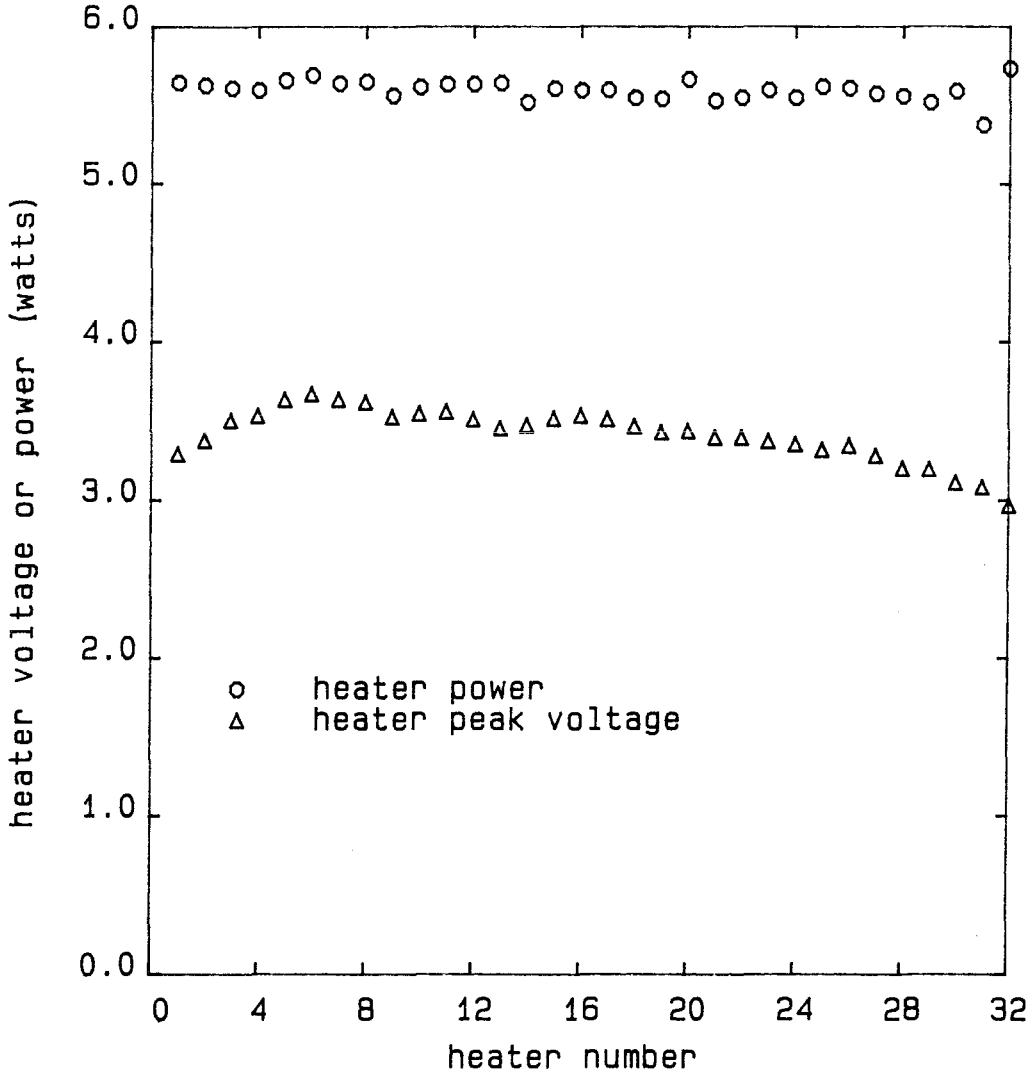


Figure A.11: Uniformity of Power Distribution Among Heaters
group 1 data, 4-7-88, 192 watts, 2D

Level Number	Frequency Hz	Angle Instruction						
		0	1	2	4	6	8	10
2	8.00Hz	0.883	0.883	0.882	0.882	0.882	0.882	0.881
2	9.00Hz	0.883	0.883	0.883	0.882	0.882	0.882	0.882
2	10.00Hz	0.883	0.883	0.882	0.883	0.882	0.882	0.882
2	6.00Hz	0.883	0.883	0.883	0.883	0.882	0.883	0.882
2	11.00Hz	0.882	0.881	0.881	0.881	0.881	0.881	0.880
2	12.00Hz	0.881	0.882	0.783	0.004	0.004	0.004	0.000
2	10.00Hz	0.882	0.882	0.882	0.882	0.883	0.882	0.882
4	8.00Hz	1.764	1.764	1.763	1.763	1.762	1.762	1.761
4	9.00Hz	1.765	1.765	1.764	1.763	1.763	1.763	1.762
4	10.00Hz	1.766	1.763	1.762	1.764	1.763	1.760	1.763
4	6.00Hz	1.765	1.765	1.764	1.764	1.763	1.763	1.763
4	11.00Hz	1.764	1.761	1.763	1.760	1.760	1.761	1.758
4	12.00Hz	1.764	1.763	1.763	1.763	1.760	1.761	1.760
4	10.00Hz	1.763	1.765	1.762	1.761	1.761	1.760	1.762
6	8.00Hz	2.648	2.647	2.646	2.646	2.645	2.645	2.643
6	9.00Hz	2.649	2.648	2.647	2.647	2.646	2.646	2.645
6	10.00Hz	2.650	2.646	2.648	2.647	2.647	2.643	2.645
6	6.00Hz	2.649	2.648	2.648	2.647	2.647	2.646	2.647
6	11.00Hz	2.644	2.643	2.644	2.641	2.640	2.640	2.638
6	12.00Hz	2.645	2.647	2.647	2.643	2.645	2.643	2.643
6	10.00Hz	2.649	2.649	2.647	2.648	2.647	2.645	2.646

Table A.3: Typical Raw RMS Voltage Record on Heater #1

signal, giving a peak temperature rise of roughly 25°C. This temperature rise is in rough agreement with the crude theoretical estimates.

The stability of power output with time during one day is most easily seen through examination of the heater performance data taken during the forcing runs. For example, Table A.3 shows the heater voltage and Table A.4 the heater currents for heater #1 during 4-13-88.

Level Number	Frequency Hz	Angle Instruction						
		0	1	2	4	6	8	10
2	8.00Hz	0.109	0.116	0.116	0.116	0.117	0.118	0.116
2	9.00Hz	0.109	0.116	0.115	0.116	0.116	0.117	0.116
2	10.00Hz	0.109	0.116	0.115	0.116	0.116	0.116	0.116
2	6.00Hz	0.108	0.115	0.116	0.116	0.116	0.117	0.116
2	11.00Hz	0.108	0.117	0.116	0.116	0.117	0.116	0.116
2	12.00Hz	0.108	0.117	0.110	0.015	0.016	0.016	0.000
2	10.00Hz	0.108	0.116	0.115	0.115	0.116	0.115	0.116
4	8.00Hz	0.210	0.221	0.221	0.223	0.224	0.223	0.222
4	9.00Hz	0.211	0.222	0.221	0.222	0.222	0.224	0.222
4	10.00Hz	0.210	0.222	0.221	0.222	0.223	0.222	0.223
4	6.00Hz	0.209	0.218	0.223	0.223	0.221	0.224	0.223
4	11.00Hz	0.209	0.222	0.222	0.223	0.223	0.222	0.222
4	12.00Hz	0.210	0.222	0.222	0.223	0.222	0.223	0.223
4	10.00Hz	0.210	0.222	0.221	0.221	0.222	0.221	0.222
6	8.00Hz	0.308	0.321	0.322	0.325	0.327	0.326	0.323
6	9.00Hz	0.307	0.323	0.322	0.323	0.325	0.326	0.323
6	10.00Hz	0.308	0.324	0.322	0.323	0.324	0.322	0.324
6	6.00Hz	0.307	0.317	0.324	0.325	0.322	0.326	0.324
6	11.00Hz	0.307	0.324	0.323	0.325	0.325	0.323	0.323
6	12.00Hz	0.307	0.325	0.324	0.325	0.324	0.324	0.325
6	10.00Hz	0.307	0.324	0.321	0.323	0.323	0.323	0.325

Table A.4: Raw Voltage Proportional to Positive Current in Heater #1

The voltages are steady to less than 1%, as are the currents. The only jump is the one from 2D forcing to oblique forcing that was mentioned before. Occasionally there was a problem with the heaters acting up for some reason, and these records of the heater power were used to eliminate the results for those cases from further analysis (e.g. the results for level 2, 12Hz forcing, for angles 4-10, which as can be seen in the table are anomalous).

A.3 Sensing Apparatus for Measuring Behavior

A.3.1 Hot Film Anemometer

The constant temperature anemometer circuits used for the preliminary experiments were adapted from those described by Robey [34]. These were originally contained in a screen mesh box, and all the connections except for the output were soldered. This instrument was difficult to repair and test since the circuits were accessible only with difficulty. Also, the high current drain of the cylindrical hot film sensor used for the freestream turbulence experiments caused the circuit in question to go into a high-frequency oscillation. The overheat adjustment was made with a 20 turn trim pot, making it difficult to set the overheat to a fixed or repeatable value. Overheats were set by setting the anemometer to a fixed DC voltage with no flow over the sensor.

The circuits were rebuilt in another box, with connectors on all lines from the circuit boards so that they could be easily removed. Ten turn pots and dials were installed. The 2N2270 transistor was replaced by a TIP 121 Darlington transistor, which eliminated the oscillation problem. Both of these instruments were air-cooled and powered by 12V auto batteries. This instrument worked tolerably well. However, it was subject to occasional random failures; the voltage on a channel would sometimes suddenly jump up or down. The overheat was extremely sensitive to the adjustment of the 10 turn 100 ohm potentiometers, so that even touching these would give a large variation in the overheat setting and destroy calibrations in progress. Calibrations were done while the velocity was being increased preparatory to an experiment and again while decreasing the velocity. The two calibration curves would usually be nearly parallel, but there was always a large

DC offset. This set of anemometers was used for preliminary experiments, including the freestream turbulence results presented in Appendix B.1.

Three channels of TSI anemometers were available, but it was desired to use four channels. Moreover, these TSI anemometers were old, and the resistance decades were unreliable.

New anemometers were therefore designed and built during fall 1987 – spring 1988, initially with the help of an undergraduate student, Todd Murray. The schematic for the circuit is attached as Figure A.12. This circuit has several small changes from the previous circuit.

The circuit is a very simple but high-quality implementation of the standard constant temperature anemometer servo-balanced bridge. A 0-999 ohm digidecade resistance decade is used to set the overheat. This is a thumb-wheel switched set of fixed resistances supplied by the Digitran Co., and previously used successfully at GALCIT in hot wire anemometers. The switches use gold contacts for high reliability. The discrete nature of the resistance shift makes for high repeatability and excellent resistance to laboratory vibrations. The bridge is in a 100-1 ratio, so that the resistance decade side draws very little current and does not warm appreciably. Also, the switch resistance and contact resistance became smaller relative to the decade resistance. Vishay temperature stable resistors are used for the 40 ohm resistor on the sensor side of the bridge. These are quoted as having a temperature coefficient of 1-3 ppm/°C.

The circuit is servo-driven into balance by a OP-27 op-amp driving a TIP 121 Darlington transistor pair. The combination has very high gain and slewing rate, which seems to improve the stability of the circuit. When the Darlington is sourcing 300mA to the bridge, it is drawing only 0.3mA or so, due to its high gain. The op-amp is thus drawing currents of the

order of nA, which are small even compared to the small currents on the resistor decade side of the bridge. The OP-27 is the highest quality op-amp easily available here, with low offset voltages and so on. A small capacitor is connected across the feedback loop of the op-amp to roll off the gain at high frequencies (MHz) to doubly ensure stability. This capacitor should have negligible effect at the frequencies of the order of 1KHz which are of interest.

An AD524 instrumentation amplifier is used as a unity gain buffer for the output. It also has a high common mode rejection ratio which helps to take out ground line noise. A 500mA milliammeter is used to give an immediate visual sign of the circuit operation to the user. The power supplies to the IC's are capacitor buffered to reduce 60Hz noise, and a resistor R_{CL} can be inserted if it is desired to limit the sensor current below the maximum of $\frac{1}{3}$ amp. An Acopian model TD15-250VM power supply is used to power the amplifiers. This power supply is much more convenient than the previously used batteries. The supply has less than 2mV P-P of 60Hz noise. The circuit boards are shielded from the magnetic field of the power supply using a piece of 1/4 inch cold-rolled steel plate, which reduces the field at the circuit boards by a factor of 5, using measurements made with a coil of wire and an ammeter. The normal noise level during operation is roughly 5 mV P-P with a DC output of about 4V.

Attention was also paid to the mechanical design of the chassis, which follows the same lines as the TSI anemometers. The power supply and fan are installed in the back of a commercially available aluminum box. Individual anemometer channels are wired on separate single-sided circuit boards and attached to separate small front sub-panels, which are bolted in a large cutout in the front panels. Most wiring is soldered directly from the circuit boards to the front panel meter, resistance decade, and output and sensor BNC

connectors. Only the power supply leads from the rear are not soldered, and they use screw terminals. Yet the individual channel is easily removed for tests and repair or is accessible in-place via removal of the top cover.

The hot films were wired to the anemometers using TSI model 1159-15 cables for the TSI model 1237W probes. Duct tape was used to form makeshift splitter plates for these cables, to reduce vibration problems. A specially double-shielded cable of twisted pairs was used for the older TSI 1268 probes, along with a twisted pair from the probes to screw terminals and BNC's from the cable to the anemometers. The cables were about 10 feet long. A typical probe overheat was about 5% or about 30°C . The calibration procedure is discussed in Appendix B.2.

A.3.2 Isolation Amplifier for Monitoring Heaters

One of the principal experimental difficulties encountered during the development of the apparatus came in reducing the noise levels in the sensor signals. It was desired to reliably identify subharmonics and superharmonics which were reduced an order of magnitude or more in amplitude from the primary response, which was itself a signal of only 10-20mV peak to peak riding on a DC voltage of perhaps 7V. A principal element of the sensor noise comes from electronic coupling between the forcing electronics and the sensing electronics. Since the forcing electronics puts a voltage sine wave on the heaters, and the heating is proportional to V^2 , the heat going into the flow fluctuates at twice the frequency of the voltage. Any direct electronic coupling of the high-power heating electronics to the sensitive sensing electronics appears as a false subharmonic of the instability wave. This error source is discussed further in section 3.3.2.2.

Experience suggested that the main source of noise coupling between the

heater circuitry and the sensor signals was through ground loops. The sensor apparatus is grounded to an AC line circuit separate from that used by the heater apparatus. This fact is important because many of the instruments used have their output ground connected in some manner to line ground. The heater apparatus puts out so much current (as much as 200A peak) that the line ground to which it is referenced can be expected to fluctuate significantly. It was desired to monitor the output of the heater apparatus, and thus to monitor signals that are referenced to the heater ground. The Computerscope A/D instrumentation has 16 single ended channels, that is, all the channels share a common ground. Thus, any current flowing into the ground from one channel, say a heater monitoring channel, will interfere with the signal on another channel, say a sensor output channel, and produce noise. The isolation amplifier is a very simple circuit that serves primarily to isolate the ground of the heater electronics from the sensor ground while allowing the monitoring of the heater performance during runs. It also serves to amplify some of the heater channels to levels more suited to the A/D board.

The isolation amplifier consists of three Analog Devices AD524 instrumentation amplifiers. These instrumentation amplifiers are powered by a source connected to the sensor ground and have their output referenced to the sensor ground. The inputs are connected to the output monitoring jacks on the 32 channel power amp. The AD524's present a high impedance load to the power amp, so as to not disturb it, and amplify only the difference between the input signals, as long as neither of the input signals gets too near one of the power line rails. Since the ground fluctuation between the power and sensor circuits was small, this possible proximity was not a problem. The AD524's are arranged to output the three difference signals of

interest from the four output jacks of the power amp and to amplify the two current monitoring signals by a pin selectable gain of 10.0 in order to bring them to an appropriate range for the A/D converter. The AD524's have a gain accuracy of better than 1%, and this specification was taken to be good enough without a calibration.

A.3.3 Signal Conditioning and Data Acquisition

The signals from the hot film anemometer (Appendix A.3.1) were filtered, offset, and amplified so that they could be accurately digitized by an RC Electronics Computerscope A/D converter board, which digitized to 12 bit accuracy over the range -10 to 10V. All data was computer-acquired using this board, except as specifically mentioned. The apparatus used for signal conditioning consisted of several elements:

1. Two channels of signal conditioning were made up of Princeton Applied Research Model 113 Preamplifiers. These instruments have switch selectable adjustable gain. The bandwidth of amplification can be limited by low-pass and high-pass filters, which are set at the -3dB points of 6db/octave filters. No additional filtering capable of handling signals up to the -10 to 10V range of the A/D converter was available, so these filters were the only ones used to eliminate aliasing. The units were always used in single-ended mode, since the A/D converter was single ended. These units were used for signal conditioning low amplitude instability waves exclusively since the large DC component of the hot film signal was removed by high-pass filtering. For this purpose, the high-pass filtering was set usually to 0.1 or 0.3 Hz, an order of magnitude below the frequencies of interest. Since data acquisition was usually done at 1000Hz, the low-pass filter point was usually set to

either 100Hz or 300Hz, far enough below the Nyquist frequency of the sampling so that the filter does not allow much power to pass into the A/D converter above the Nyquist frequency.

2. Downstream anemometer channels used a different system of signal conditioning, since only two channels of the above type were available, and because the hot-film sensors that were located well downstream often had large amplitude irregular low-frequency fluctuations, such as spots. These signals were severely distorted by the high-pass filtering used on the PARC preamplifiers.

For these channels an instrument built by Dr. John M. Cimbala [4] was used for primary signal conditioning. This instrument could add in a selectable DC voltage, multiply by a gain, and output to the A/D converter. The instrument has LED's that show when the amplified signal is out of the range 0-10V, a feature that is very useful for showing the operator when a signal is being clipped by the digitizer, especially when the clipping is happening to rare large amplitude events that might otherwise not be noticed in a sample portion of the record.

Since the JMC signal conditioner incorporated a low-pass filter only at 500Hz, and it was not desired to change this, and since it was desired to use a high-pass filter on these channels when they were measuring low-amplitude waves in order to remove low-frequency fluctuations, these channels were piped into a pair of Ithaco 4213 Variable Electronic Filters. These filters can handle signals of up to $\pm 10V$ and have variable 4 pole Butterworth (24db/octave) high-pass and low-pass filters that were set at 1Hz high-pass and 200Hz low-pass for most of the tests, where the channel contained low amplitude instability waves. When

the signal was of higher amplitude and included spots and so on, the high-pass filter was set OUT, and the low pass filter only was used.

The accuracy of these instruments was checked several times before and during use. In particular, an automatic test program was written using the data acquisition board to supply a test sine wave signal of varying frequency to the signal conditioning apparatus and to save the output of the various instruments. The program also computed the gain of the various instruments and wrote out the zero crossings of the outputs so that phase shifts in the instruments could be computed. Such tests indicate that the phase shift introduced by the signal conditioning was 1 msec or less for all frequencies of interest, and that the gain for the various instruments was less than the value set by about 3-7%, so that the difference among the instruments would be about $\pm 2\%$. The phase shift was primarily caused by the proximity of the high-pass filter 3dB knee point, and thus was very similar for the two different kinds of filters used. These data have not been further analyzed since it seemed that these errors would not be significant to the results. None of the results presented in this thesis have been corrected for these effects. The data acquisition board itself was checked against other instruments and, for the experiments presented here, was working well.

A.3.4 Pressure Transducer

For the second set of experiments, a Validyne DP-7 pressure transducer with diaphragm #1-20 was used with a Validyne CD23 signal demodulator. The 0-10V output was read directly by the computer. Due to the small internal volume of the transducer and the small flow volume required to change the output, the system came to equilibrium an order of magnitude or more rapidly than the manometer used previously. The time required for

calibrations was therefore shortened by an order of magnitude. Also, since the transducer was read electronically, user errors were eliminated.

The transducer output is extremely linear. It is only necessary to know the voltage at two (widely spaced) pressures in order to get the pressure from the voltage. The transducer demodulator controls allow setting the voltage output at zero pressure and full scale. These were set once and left. Between experiments, the output of the transducer was calibrated against a water column in the manometer used previously for pressure measurement. Valves were provided so that this calibration could easily be done, and also so that the lines could readily be cleaned of bubbles. Some drift of the offset was occasionally observed. This drift was usually caused by overloads which were accidentally placed across the transducer while clearing the lines. This drift could be carefully observed since the electronic set points were never changed. A program was written to save two extreme points on the calibrated curve, so that the readings of voltage could be automatically converted to pressure or velocity by software, using the latest calibration. It was very easy to overload the transducer since the instrument reads 3.0 inches of water at full scale. A typical plot of voltage vs. pressure is attached as Figure A.13.

This pressure was monitored during the experiments to check on the drift of freestream velocity with time. It should be noted that a new tunnel motor driver was also installed between the first and second set of runs. The new driver yielded a stable velocity within about 1% over the course of a series of runs, as determined by looking at the output of the pressure transducer over time during one of these runs.

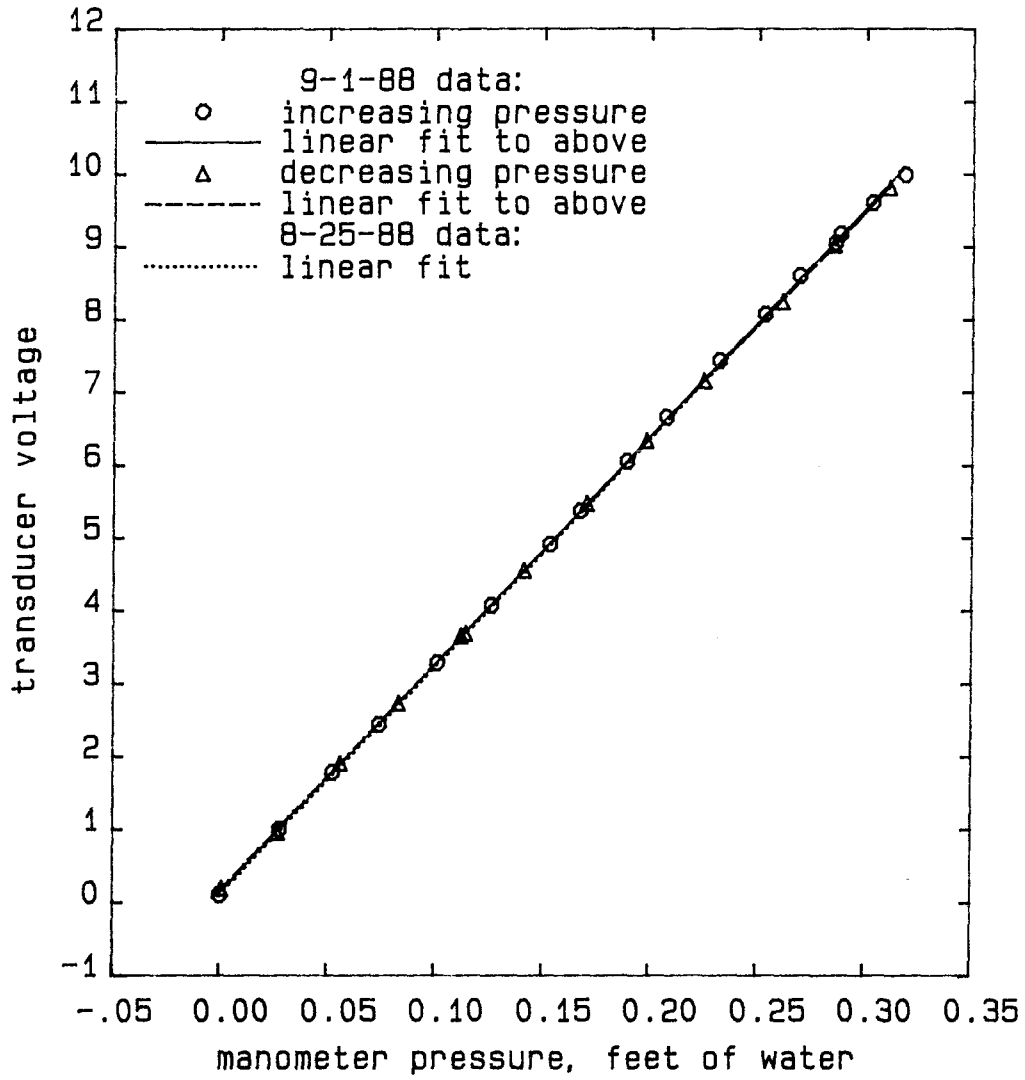


Figure A.13: Pressure Transducer Calibrations

Appendix B

Detailed Description of Experimental Procedures

B.1 Measurement of Freestream Turbulence

Much experimental effort went into reduction of the freestream turbulence in the FSWT so that the experiment could be carried out. This appendix is primarily a description of how the freestream turbulence was measured, once the final configuration was found.

It was found to be important that the tunnel water level be maintained fairly high and that the 20 mesh 0.5 blockage ratio screen on the upstream face of the tunnel honeycomb be kept free of debris. For the experiment discussed here, the water level was brought to 1.93 ft with no flow, a value within the 1.9 to 2.0 ft region of normal operation. The tunnel test section was empty, except for the hot film probe and its mount. The honeycomb screen had been cleaned just a week previously.

The freestream velocity was measured with a cylindrical hot film probe, TSI model 1261-10W, mounted to the bottom of a long sting assembly which was supported from above the free surface of the tunnel by a heavy automatic traverse¹. The probe was located 15.5 inches from the entrance of the test section and 8 1/4 inches from the bottom of the test section. This position was chosen to match the usual location of the flat plate leading edge in

¹FSWT Model Elevation Mechanism

the boundary layer experiments. The probe was mounted perpendicular to the flow direction, horizontally, and thus served to measure primarily the component of the velocity in the freestream direction.

The freestream turbulence is a small quantity and thus difficult to measure. The signal on the output of the hot film anemometer connected to the probe is composed of noise from at least four sources: electrical noise, probe vibrations, collection of dirt on the probe, and freestream turbulence. Considerable efforts were made to reduce the first three, but they may still remain. Most of the electrical noise is at high frequencies or occurs at multiples of the power line frequency, 60 Hz, and so can fairly easily be filtered or ignored. The problem of probe vibration is not so simple, especially in water, whose high density makes for large forces on probe structures. After this problem was identified, the probe was always observed with a small 9 power stand mounted telescope, with which it was easily possible to observe vibrations with an amplitude as small as 0.05 inches. Probe vibration is an even more important effect because it was observed that probe vibrations could give rise to broadband spectra that are not easily distinguished from true turbulence, as a resonant vibration could be. The third source of extraneous noise was dirt, specifically lint, which collected occasionally on the probe, and also gave rise to a large broadband increase in the noise level. This lint was small enough that at best it could only be seen by looking carefully through the telescope. The lint also affected the calibration curves. It was removed when observed, using a small brush, but the use of an air jet would have been wiser. The tunnel has a filter that runs full-time, but it apparently does not filter all of the water because the lint escaped. Given all these noise sources, it is possible to give only an upper bound for the freestream turbulence.

The probe sting finally used was made from a piece of aluminum, 19 inches long x 3.5 inches wide x 0.25 inches thick. The aluminum was cut into a smoothed double wedge airfoil shape and angled 45 degrees forward into the flow. A fitting was mounted on its end to accept a forward pointed sting, to which was attached another double wedge airfoil, 15/16 x 3 x 3/16 inches thick, pointing vertically downward, into the end of which was mounted the TSI boundary layer type probe. All these materials were salvaged from already existing mounts and were carefully aligned. With the tunnel in operation at the flow speeds of interest, no probe vibrations could be observed with the telescope.

The probe was run at constant temperature using the anemometers used in the preliminary work, which were adapted from those of Robey [34]. The overheat was roughly 70°C, as recommended by TSI. The signal from the anemometer was passed to a preamplifier with a gain of 100 and 3db/octave filter points of 0.1Hz and 1000Hz. The signal was digitized at 5000Hz for 6.4 sec, and the mean was at the same time monitored with an averaging voltmeter (HP Model 5326B). The tunnel speed was varied and monitored using the pitot tube and manometer described in Appendix B.2.

The variation of velocity with anemometer voltage should constitute a smooth calibration curve, and should follow King's law,

$$V^2 = A(Re)^n + B,$$

at least to first approximation (see, e.g., Fingerson [7, p. 111]). Occasionally a piece of lint was picked up by the probe, and a large change occurred in the probe response; even after cleaning the probe, a significant shift in the calibration would then be found. A consecutive set of five points was found, however, during which the probe was well-behaved, and from these

five points, a calibration curve could be obtained that fitted King's law well. An exponent of $n = 0.5$ was used for the results presented here; the results change less than 5% when an exponent of 0.3 is used.

The rms freestream turbulence level between 0.2Hz and 2500Hz was determined by direct operation on the voltage record, to be 0.15%. King's law was locally linearized in order to convert the rms voltage to u'_{rms}/U_{∞} . The lower frequency portion of the spectrum is shown in the attached Figure B.1. It can be seen that the power decreases roughly exponentially with increasing frequency, up to about 180 Hz. This decay with increasing frequency is similar to that reported by Leehey et al. [24, p. 284]. At higher frequency the signal approaches a noise floor composed apparently of vibration and electrical noise. The peak at 130 Hz seems to be caused by probe vibration since it changes with small changes in tunnel speed. The peak at 180 Hz is evidently caused by 60 Hz line noise. Neither of these outside noise sources contributes significantly to the rms, and even the first is an order of magnitude in amplitude below the low frequency turbulence. The peak at DC is residual from the large amount of DC in the hot film voltage corresponding to the freestream speed and is incompletely removed by the high-pass filter. The reason for the spectral distribution is not known; waves present on the free surface may have contributed, although measurements of the boundary layer instability waves on the plate did not appear to be sensitive to the free surface waves.

No extensive surveys of the flow uniformity were made. Earlier surveys made without the turbulence damping screen, and before a recently completed tunnel overhaul, showed nonuniformities to be significant only in the wakes behind the turning vanes of the last turn. These turning vanes were rebuilt during the tunnel overhaul. These expectations of good flow unifor-

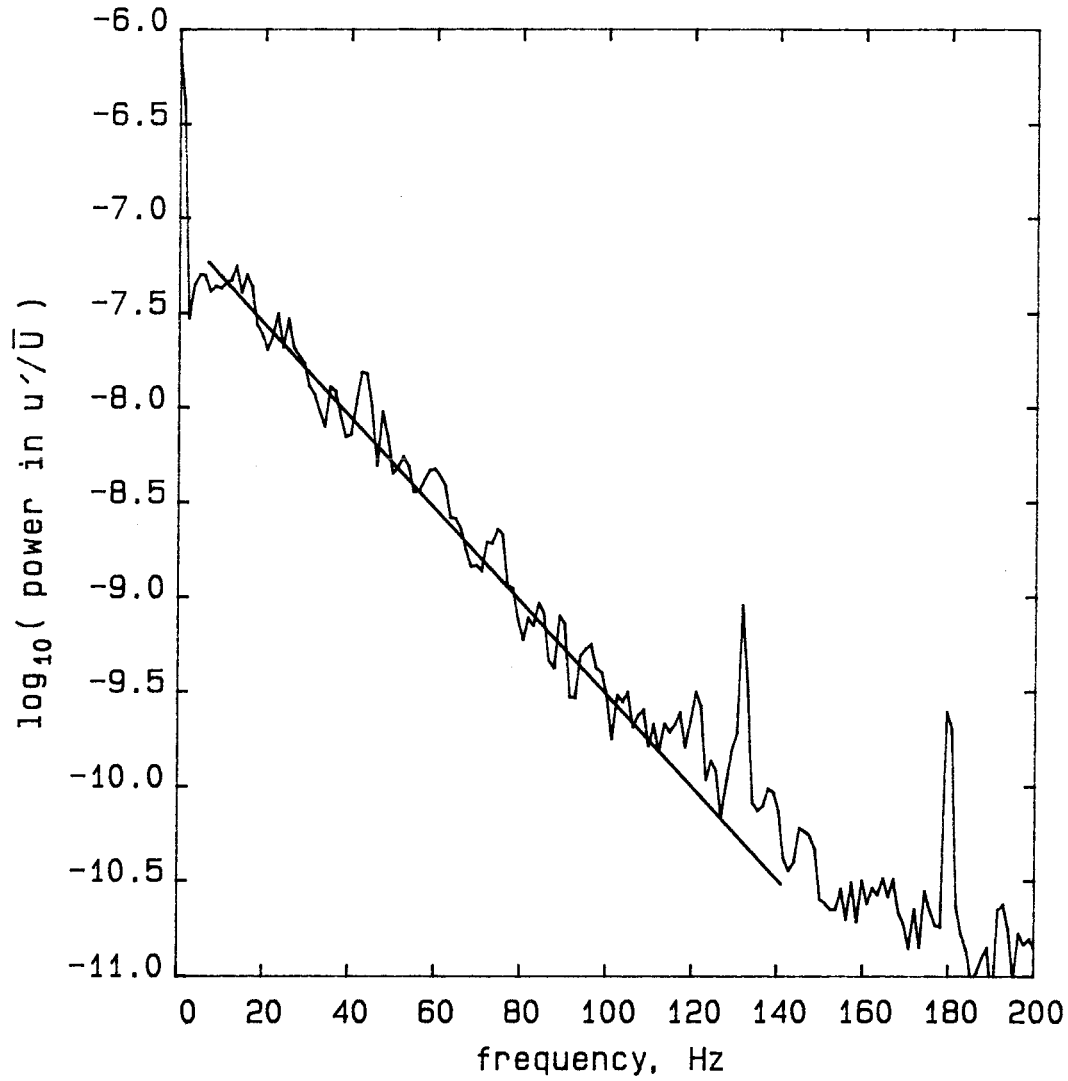


Figure B.1: Spectrum of Freestream Turbulence in FSWT
 $u'_{rms}/\bar{U} = 0.12\%$ in frequency range 1-2500Hz
 $U_{\infty} = 3.2$ fps, 8-4-87 run03

mity were confirmed by noting that hydrogen bubble wire flow visualization of the freestream did not show any large nonuniformities.

B.2 Calibration of Wall Shear Sensors

All quantitative measurements were made with hot film wall shear sensors. These were of two types: the old type, made from TSI model 1268W flush mount sensors, epoxied into a stainless steel insert; and the new type, made from TSI Model 1237W sensors inserted into a snug-fitting hole reamed into a brass insert, and fastened with a set screw. All of the experiments discussed in this thesis were done using the anemometers described in Appendix A.3.1.

The calibration procedure was as follows: The plate was mounted in the tunnel accurately parallel to the bottom wall at the standard height. A pitot-static tube² was used to measure the freestream velocity in tandem with a precision water manometer built at the GALCIT Hydrodynamics Laboratory³. The manometer has a vernier scale that can measure to 0.001 ft of water. The manometer lines were carefully flushed to clear them of bubbles, and the manometer zero was checked before and after every experiment. The pitot tube was mounted carefully so that the tip did not vibrate, and the tip was located 17 inches from the bottom of the tunnel and 12 inches from the entrance to the test section. The angle was aligned carefully so that the pitot tube pointed directly into the flow within about 2 degrees. The tunnel velocity was varied through a range of roughly 10 values below and up to the operating speed, and at each speed a computer program sampled each anemometer channel for 41 seconds at 100Hz, computing the rms and mean of the voltage on each anemometer channel at each tunnel velocity.

²United Sensor Model PBC-24-G-22-KL

³The pressure transducer was used for later experiments.

This procedure was repeated before and after each experiment.

From Taylor [43, p. 17], or from Brown [2], we expect that

$$V^2 = c_1 \tau^{1/3} + c_2. \quad (\text{B.1})$$

If we assume that the boundary layer is given by the Blasius formula from the leading edge, we know that

$$\tau = \gamma U^{3/2}. \quad (\text{B.2})$$

Thus we can expect that

$$V^2 = c_1 \gamma^{1/3} U^{1/2} + c_2. \quad (\text{B.3})$$

Plots of V^2 vs. $U^{1/2}$ were therefore made for each sensor for each run, including the data taken both before and after each experiment. A sample plot of a good set of data is shown as Figure B.2, along with a linear least-squares fit to the data. It can be seen that the data fit a straight line very well, but that there is some drift in the sensors during the experiment. This drift is used to estimate the error in the sensor calibrations.

These data were used in two different ways. The fluctuating wall shear was the quantity of interest, and in the majority of cases, the amplitude of the fluctuations was small compared to the mean value. The calibration formula, equation B.1, was thus linearized to small fluctuations around a known mean. Using a Taylor series approximation near the mean, one can show that

$$\frac{\tau'}{\bar{\tau}} = 6 \frac{\bar{V}}{\bar{V}^2 - c_2} V' + 3 \frac{5\bar{V}^2 - c_2}{(\bar{V}^2 - c_2)^2} V'^2 + h.o.t..$$

For the laminar instability wave data, V'/\bar{V} was of the order of a few percent or less, and so the second-order term was small compared to the first and was ignored. Also for these data, the mean was filtered out by the analog

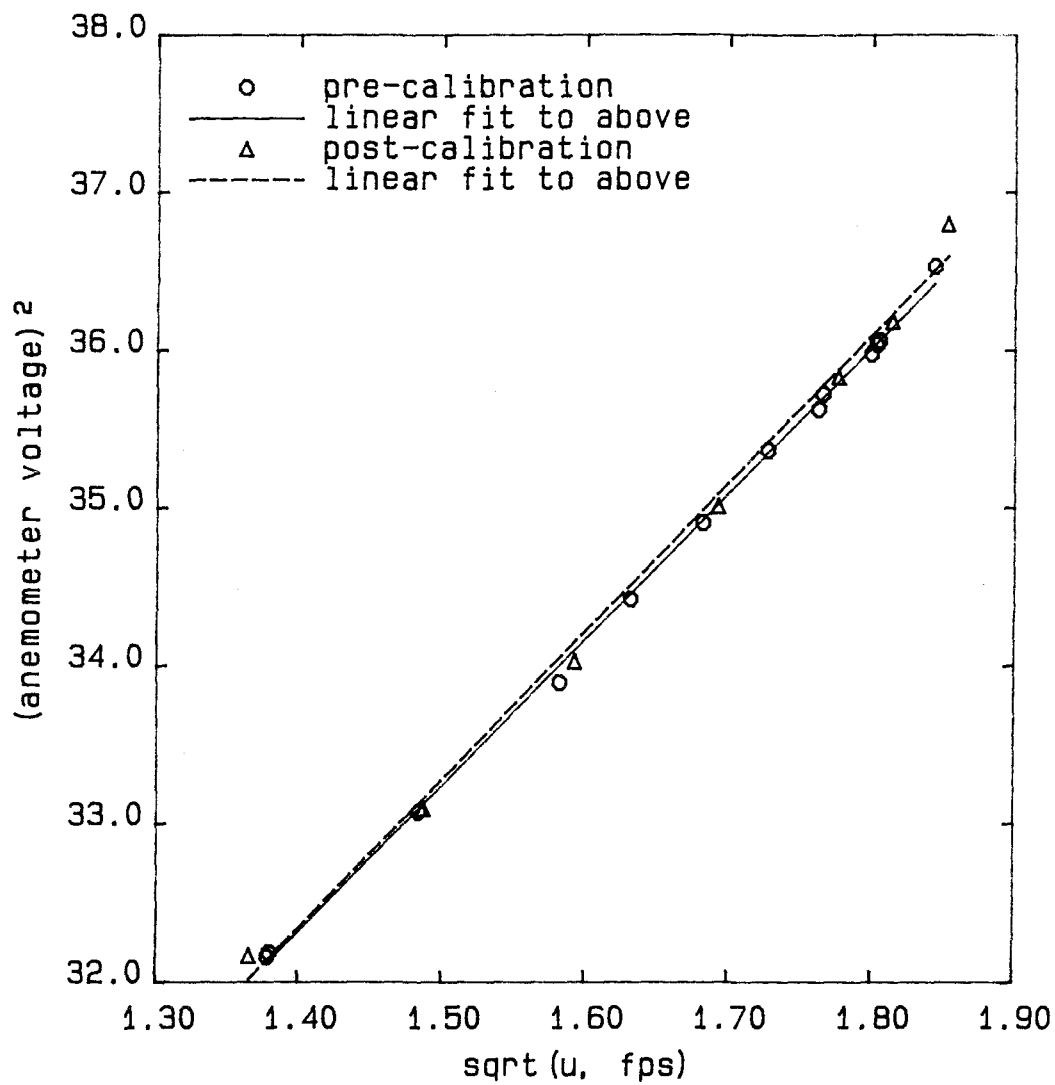


Figure B.2: Sample Calibration of Wall Shear Sensors
2nd sensor on Ch4, 9-14-88, S3'

electronics before the signal was amplified and digitized. Thus, it was only necessary to compute the linear multiplication factor for V' to get $\tau'/\bar{\tau}$, which is the form in which the data is presented. This method also allowed the calibration error to be estimated from the difference in the calibration constant between the before and after calibrations; this error was usually about 1 to 10%. The calibration drift seemed to be the largest error in the wall shear data. However, the wall shear on nearby sensors sometimes seemed to be different by more than could be accounted for using linear theory, and extra difference could not always be accounted for using the calibration drift as estimated above. The linear fit parameters were computed from the mean between the fits to the before and after calibrations, and might thus be expected to be more accurate than either. It is curious that the slope of the fit does not enter into the conversion formula using this method. This property seems to be tied into the form of the formula used.

A second calibration method was used for downstream sensors placed in the intermittent region, which contained fluctuations in wall shear of the order of the laminar value (incipient turbulent spots, and spots). For these cases, the small fluctuation approximation was no longer valid. These signals were not high-pass filtered, either, since the filters disturbed the spot signature. Both conditioned and unconditioned signals were monitored for such downstream sensors, and the mean and rms of the unconditioned signals were saved along with the complete conditioned signals, which had a DC voltage bucked into them, and were then amplified. The amplifier gains were recorded, and the DC offsets were recovered from the difference between the means of the conditioned and unconditioned signals. The full anemometer voltages could thus be used for the complete unapproximated conversion of the voltage to wall shear. It was desired to present the data in a normalized

formula, however, as close as possible in form to the previous data. For these data, the wall shear could be recovered using

$$\tau = \frac{(V^2 - c_2)^3}{c_1^3}.$$

The voltage for the undisturbed nominally laminar flow shear was recorded during the calibration, at the same speed,

$$\tau_{laminar} = \frac{(\bar{V}^2 - c_2)^3}{c_1^3}.$$

Dividing the two, we find that

$$\frac{\tau}{\tau_{laminar}} = \frac{(V^2 - c_2)^3}{(\bar{V}^2 - c_2)^3},$$

where the slope of the fit again drops out. This is the formula used for computing the wall shear when high-amplitude fluctuations were present.

Errors in the wall shear signals can come from several sources. Calibration errors should be seen in the differences between the before and after calibrations, and this drift is used to estimate the sensor errors as discussed above. A second source of error comes from the possibility that the quasi-steady response of the hot film might differ from its response to fluctuating signals, possibly because of substrate effects. A third source of error would be caused by differences between the theoretical boundary layer used for calibration and the actual boundary layer. These differences might be due to errors in the freestream velocity measurement or to small changes in the pressure gradient, fluid temperature, leading edge stagnation point position (which could be changed by obstructions on upper side of plate), freestream turbulence, and so on. This third source of error varied considerably between days but was fairly constant during a single experiment. This implies that comparisons among different forcing cases during a single experiment are

much more accurate than comparisons for the same forcing case repeated on different days.

The errors in the wall shear data can perhaps best be estimated from the repeatability of the data among different runs for different days, as included in several figures to allow the reader to judge for himself. In general, the accuracy is good for the changes in behavior for different forcing cases on the same day, and this is what the experiment was designed to measure. The scatter among different runs on different days is much larger, and would require more experimental development to reduce.

It should be noted that errors in the nonlinear calibration can result in the presence of false higher harmonics in spectra of the wall shear, since one would then be computing not the spectra of the wall shear but spectra of some nonlinear function of the wall shear, which would not be a pure sine wave even if the wall shear is. However, the second harmonics seen in the data are generally not at the same phase as the fundamental, an effect that would be expected if this error were the source of the higher harmonics.

Appendix C

Detailed Description of Analysis Methods

C.1 Computation of Leading Edge Pressure Gradient Effects

Computations were made of the pressure gradient and boundary layer thickness on the plate using a 2D panel method code and a Thwaites method code.

The panel method program was written following the methods of Smith and Pierce [39]. One major change was made. The paper cited uses a unusual coordinate system instead of x-y coordinates so that there are no special cases where the general integral solution becomes singular. These special cases are easily handled by a FORTRAN IF statement, which chooses a different closed form integral solution when appropriate. The program thus uses x-y coordinates directly, greatly simplifying the coding and understanding of the method. The symmetry of the flow was not used in the solution of the problem, since a matrix solver for general matrices was easily available from the *Numerical Recipes* book [33], while a symmetric matrix solver was not. A total of 170 panels were used for the solution, distributed tightly near the leading edge and farther and farther apart downstream, the last point being at $40L$, where L is the length of the leading edge half-ellipse. The panel method code was checked against the theoretical solution (see, e.g., Schlichting [37]) for flow over an ellipse, with which it agreed very well.

Results were also compared against the solutions for flat plates with elliptical leading edges computed by Hess and Smith [14, p. 125]. Also, the sum of all the source panel elements is very nearly the amount required by theory, to within 0.6%.

From the values for the surface velocity, the boundary layer pressure gradient parameters λ and (Falkner-Skan) β can be computed, using the methods of Thwaites (see, e.g., Thwaites [44]). A table look-up method with interpolation, using the tables in [44], was used to convert λ to h to β . These parameters are independent of Reynolds number in the current approximation, where the pressure gradient depends only on the inviscid flow over the plate, the surface of which is not corrected for the boundary layer displacement thickness. The Thwaites method was also used to compute the boundary layer thickness on the plate. The code was checked against the Blasius solution for the flat plate. No corrections were made for the approximately 5% blockage ratio which the plate represents. Further corrections based on the blockage would have to take into account the free surface above the plate.

One of the items of interest is the difference in pressure gradient for elliptical leading edges of different bluntness. In the recent boundary layer instability wave forcing work published by Caltech workers, the heater strip has been located immediately behind the plate leading edge, as in the present work. The amount of power that has been required in order to achieve a given amplitude of instability wave at some position down the plate has been highly variable. Nosenchuck [32, p. 46ff] quotes a power input of 20-25W for most of his work, in which he cancelled T-S waves, creating waves of a few percent at some position downstream. Robey [34, p. 96] quotes power inputs of up to 700W, yielding T-S waves apparently up to about 6% at $Re_{\delta^*} = 1250$. In

the present case, the maximum power used was about 200W (in a 50% wider channel), and the maximum waves created were about 5% at $Re_{\delta^*} = 1500$. Much of the difference in power requirements has been attributed to the different leading edges used by the different workers. The argument can be understood by reference to Figure C.1, which shows the surface velocity computed with INVISCID for flat plates with elliptical leading edges of three different bluntness ratios. The 4:1 case corresponds to the leading edge used in the experiments of Nosenchuck, the 6:1 case corresponds to the leading edge used in the experiments of Robey, and the 8:1 corresponds to the present work.

It can be seen that the surface velocity increases rapidly for the inviscid flow as the flow rounds the corner and then overshoots before it recovers to the freestream value far down the plate. It can be seen that the overshoot is far greater for the 4:1 elliptical leading edge than for the more slender 8:1. The portion of interest is really the recovery region where the surface velocity returns to the freestream value from the overshoot. Here, the velocity is decreasing, so that the pressure is increasing; thus we have a region of adverse pressure gradient, where the instability waves have a much greater growth rate. This can be better seen if the local Falkner-Skan pressure gradient parameter β is computed, as has been done in Figure C.2.

Here one can see that β approaches the nominal value for separation ($\beta_{sep} = -0.1988$) as the flow approaches the shoulder of the ellipse, where the half-ellipse meets the flat portion of the plate and the local adverse gradient has a maximum. For the 4:1 case, in fact, β actually reaches β_{sep} , and the computation clips the β values there. The growth rates for instability waves depend roughly exponentially on the value of the pressure gradient parameter (see, for example, Wazzan, Okamura, and Smith [47]). Since

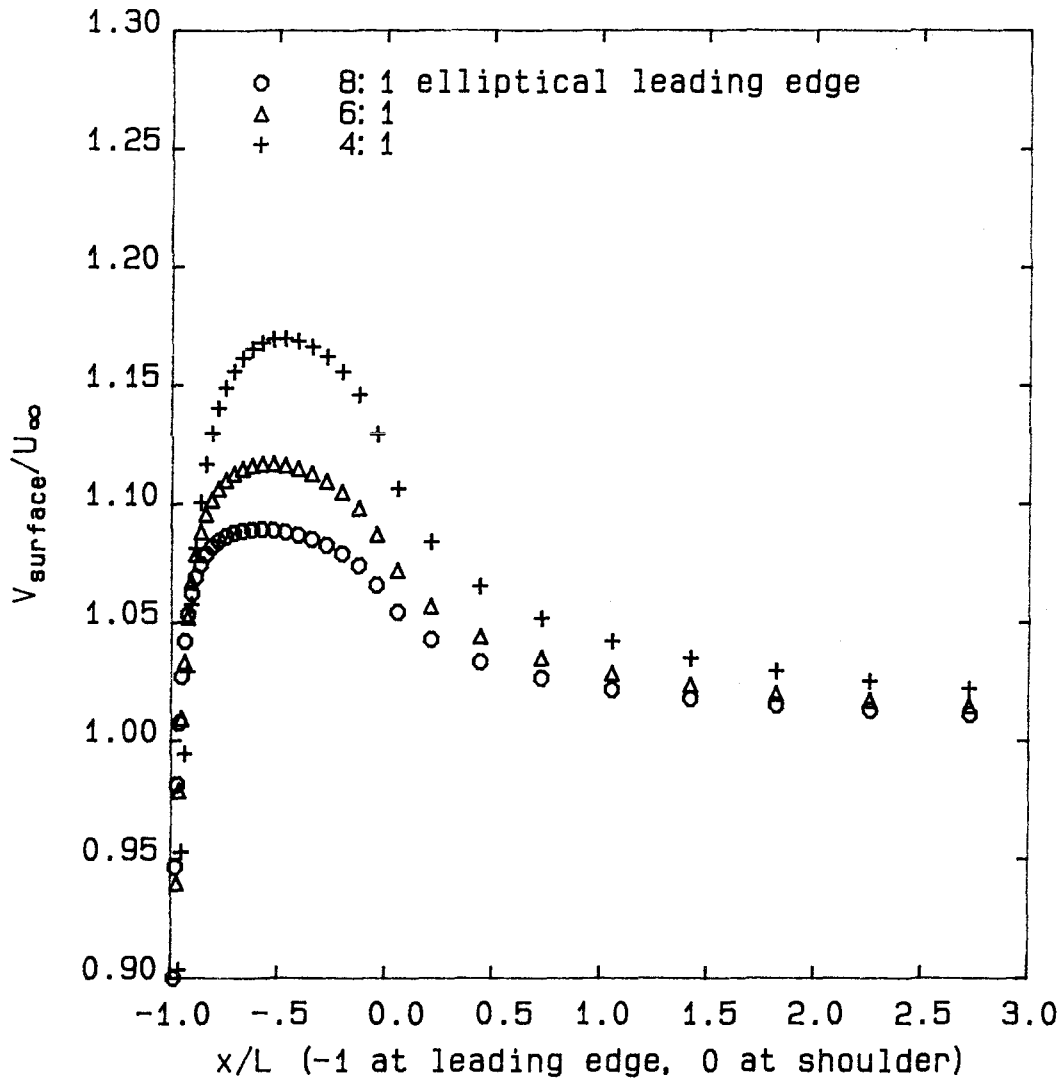


Figure C.1: Surface Velocity Computed for Flat Plate Leading Edge using INVISCID, 170 panels

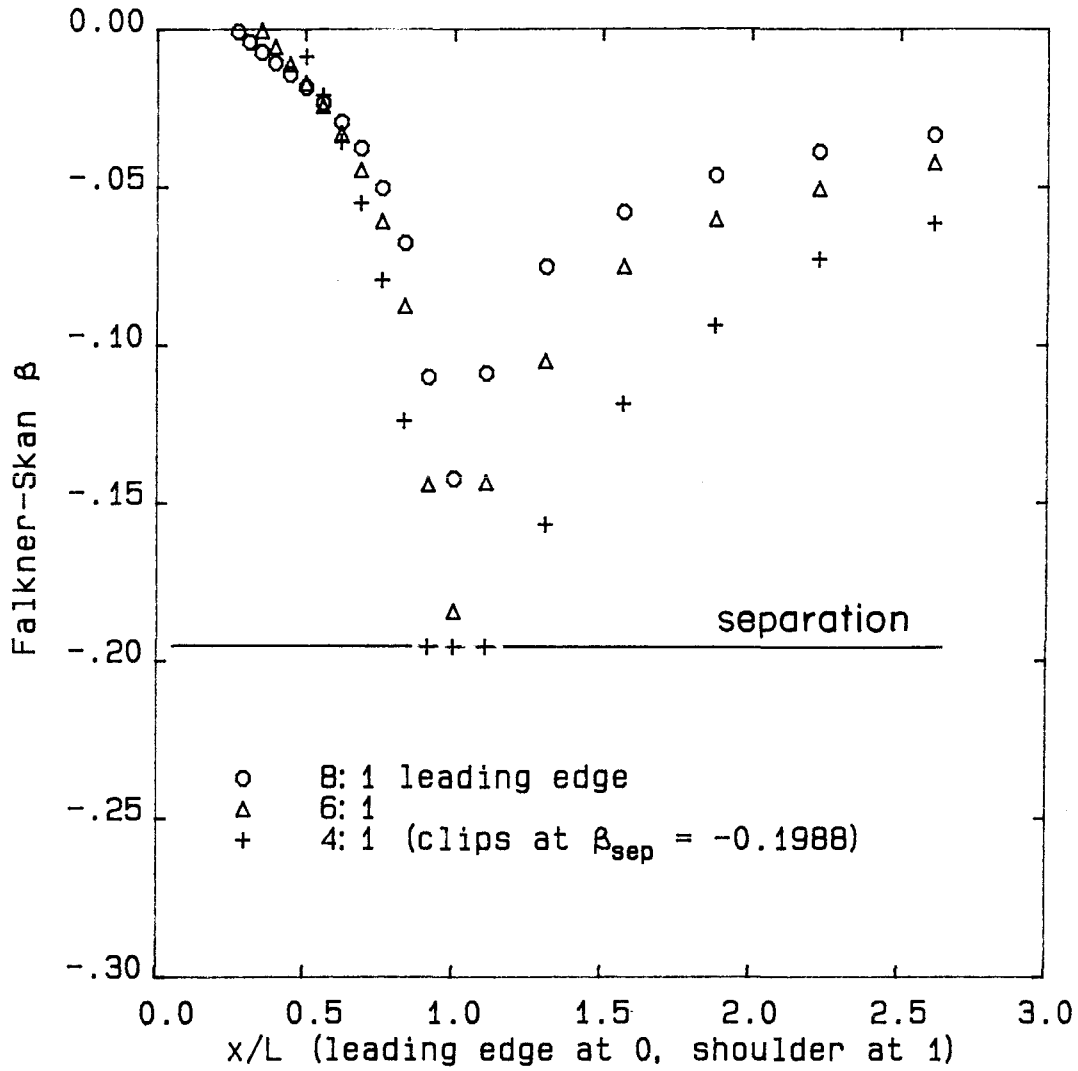


Figure C.2: Falkner-Skan β for Flat Plate Leading Edge
 $Re/inch = 3.075 \times 10^4$, elliptical leading edges
all 1 inch thick, L for 8:1 is 3.74 inches

the heaters are located just behind the shoulder, roughly at $x/L = 1.3$ in the notation used in the figure, the local adverse gradient has an important effect in the growth of the waves. In particular, it may be that this effect is sufficient to account for the differences in amplification of the disturbances introduced by Nosenchuck, Robey, and the current author.

The other reason for doing the computations described in this appendix is to better estimate the boundary layer thickness on the plate, for generating Reynolds numbers at different plate locations, so that the data can be compared to that of other researchers. For this purpose, a typical boundary layer thickness growth plot is shown as Figure C.3. It can be seen that the local adverse gradient caused by the bluntness of the elliptical leading edge has a significant effect of the growth of the boundary layer. Although the boundary layer thickness was never measured, the pressure gradient was very small, so this well-tested theoretical method should give fairly good results. In particular, the correction of the boundary layer thickness for pressure gradient effects caused by the leading edge is about a 10% change from the simple Blasius which is sometimes used and should improve the accuracy. All the results in the text and plots have been corrected for this effect and show Re_{δ^*} obtained in this manner. The plate leading edge is very accurately an 8:1 ellipse, with thickness 0.935 inches (it was made using nominally 1 inch plexiglas). The streamwise length thus comes out 3.74 inches. Since the leading edge section is still 4 inches long (actually 3.98 inches) the rest of the leading edge section is flat on both sides. The center of the heater strip is about 1.39 inches¹ behind the actual shoulder of the ellipse-flat plate junction. Thus a perturbation produced by the heater strip travels through the part of the pressure gradient behind this point.

¹ $0.24 + 1.04 + \frac{0.22}{2} \approx 1.39$

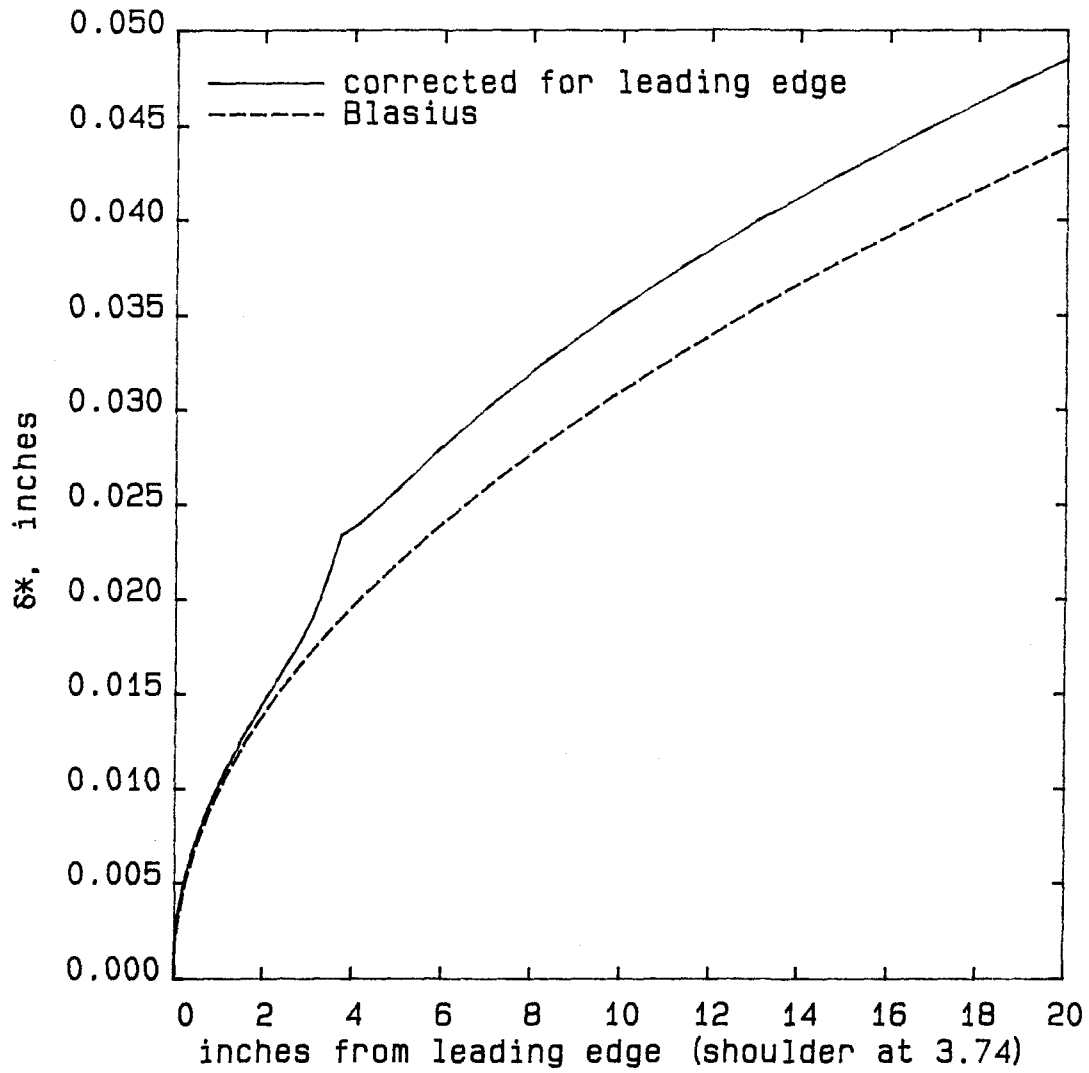


Figure C.3: Boundary Layer Thickness Corrected for Leading Edge
 $Re/\text{inch} = 3.075 \times 10^5$, 8:1 elliptical leading edge

Theoretical work sometimes draws attention to the curvature discontinuity involved in the junction between a flat plate and an elliptical leading edge, claiming that this causes a singularity in the instability behavior. It is worth noting that attempts were made to design a new leading edge shape that avoids this behavior. Designs can be arrived at that have pressure gradients no worse than the elliptical leading edge, while having curvatures matched at all junctions. However, the best curvature-matched design found differed from the elliptical leading edge by at most 0.001 inches in a leading edge of 0.935 inches thickness. Thus the two designs were the same to the accuracy with which the leading edge is normally machined. Theoretical work that addresses the effect of discontinuities in curvature should supply an estimate of the amount of curvature change over some length which is required for some significant effect to occur. The jump in curvature here is believed to be small.

C.2 Computation of Intermittency

The computation of intermittency for the flow at a position in the boundary layer is not a well-defined procedure (see Narasimha [31]). Fortunately, the wall shear time traces available using the current experimental apparatus are the best traces possible for computing intermittency since the velocity away from the wall is a less precise signal to use [31]. The length of record required in order to get a statistically well-approximated intermittency does not seem to have been studied, and even the best procedure for computing intermittency from a given trace is not yet well-defined.

Two procedures were tried out on a part of the current data, and one of the two was then used for the rest of the computations. The first procedure was suggested by D. Coles and is called the ϵ procedure, for want of a better

name. This procedure picks out the high frequency portions of a digitally recorded trace without a great deal of computation and works as follows: A straight line is fitted to three neighboring points in the data. The difference between the fitted line and the actual points gives an error parameter, ϵ , which is the actual distance between two of the points and the line, and half the distance for the third. This parameter is basically the local 2nd derivative or curvature of the line, to within a constant. This ϵ is trivial to compute from linear combinations of the 3 data points and reflects surprisingly well the high-frequency portions of the record. The maximum value for ϵ in laminar portions of the record is determined, and a cutoff in ϵ is set somewhere above this value, such that the points in the time trace that have ϵ above the threshold are called turbulent. Call this trace of provisional turbulence/non-turbulence, $i(t)$. Smooth $i(t)$ using a window that passes over the data, and within which the center point is called turbulent when the majority of points in the window are turbulent. This smoothed trace is called $I(t)$, and labels the parts of the record to be called turbulent. The parameters, namely the threshold in ϵ and the window width, are selected so that the routine calls turbulent the parts of the record that appear turbulent, i.e., the parts that have high-frequency content. The average value of $I(t)$ over the record is called the intermittency.

The second procedure follows an idea used by Hansen and Hoyt [11] and advocated by Narasimha in [31]. This procedure picks out the portion of the record where the fluctuating wall shear is high and calls that portion turbulent. This procedure works as follows: A probability density function (PDF) is computed for the data records by binning the fraction of digitized points that have a certain shear (see Figure C.4). The fraction of the probability distribution above a certain shear reflects the amount of time

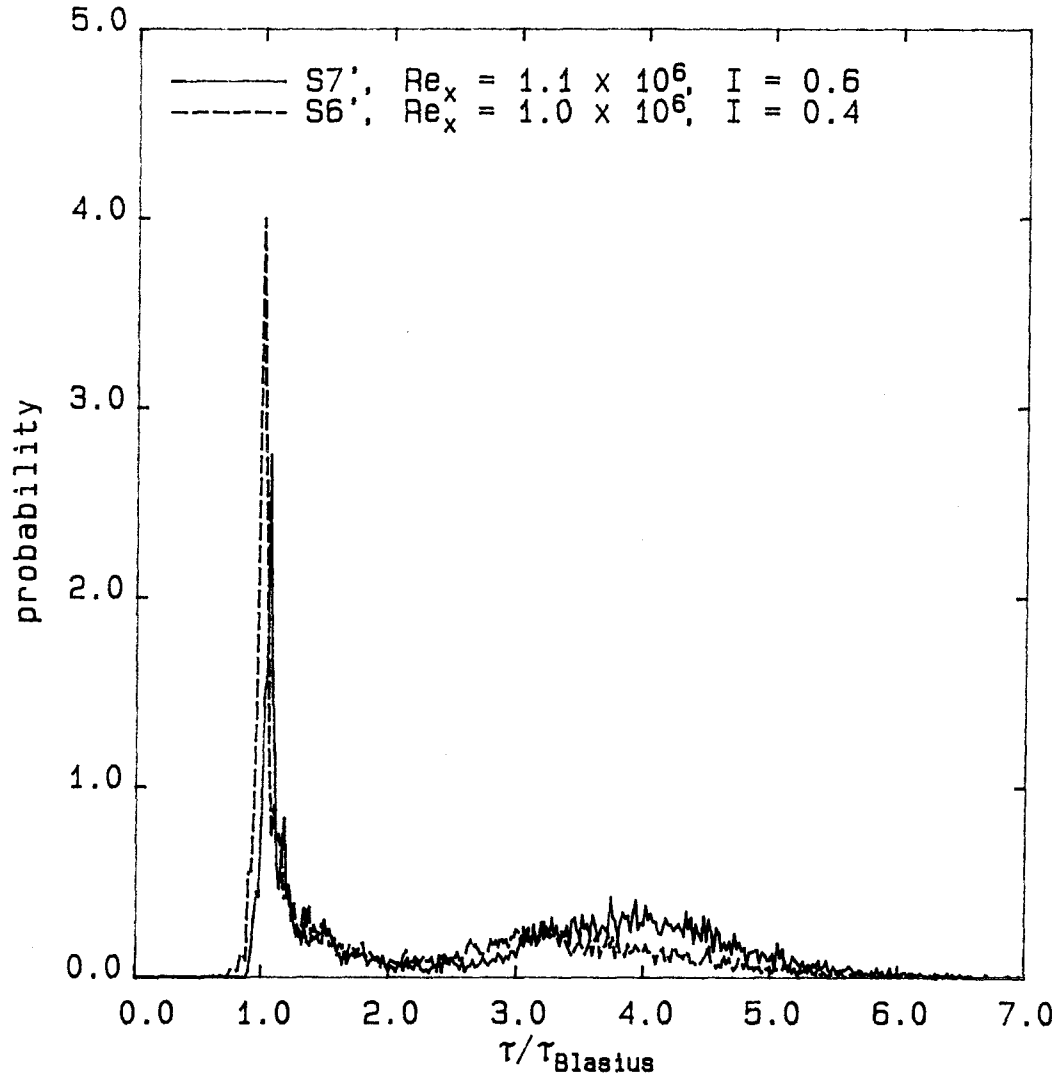


Figure C.4: PDF of Shear for Intermittent Signal
20Hz 163 watt 2D forcing, 9-2d2

the trace spends with a shear above that threshold. Normally, a valley is found in the PDF between a large peak at the laminar shear and another peak around a common value of the shear for turbulent records. The location of this valley is chosen as a threshold, and the fraction of the PDF above this valley represents the proportion of time the shear has a value greater than the cutoff, and so is the intermittency. The method presented in [11] was here refined to give the cutoff explicitly in terms of the actual shear stress, so that the method used here can actually be repeated by other observers using different equipment. The cutoff of $2\tau_{blasius}$ was chosen because it is roughly at the minimum that occurs for PDF's with large intermittency, like Figure C.4, and because it is a round number well above any value found in smooth laminar flow.

The two procedures are compared for a sample set of data in Figure C.5. Both procedures pick out similar portions of the record to call turbulent. When the two procedures were used to compute intermittency for a few dozen records, they both yielded similar trends. The parameters in the ϵ technique were chosen to fit visual observations of the data without reference to the other technique. The PDF technique was used for the data presented here, since it is also computationally efficient and has the advantage of being a technique in which the adjustable cutoff parameter is at least well-defined in terms of a repeatable specification.

C.3 Computation of Power Spectra and Peak Amplitudes

Power spectra were computed using the methods described in Press et al. [33]. Most of the wall shear data consisted of 8192 points sampled at 1000Hz. Spectra were computed using 2048 point Fast Fourier Transforms of Parzen

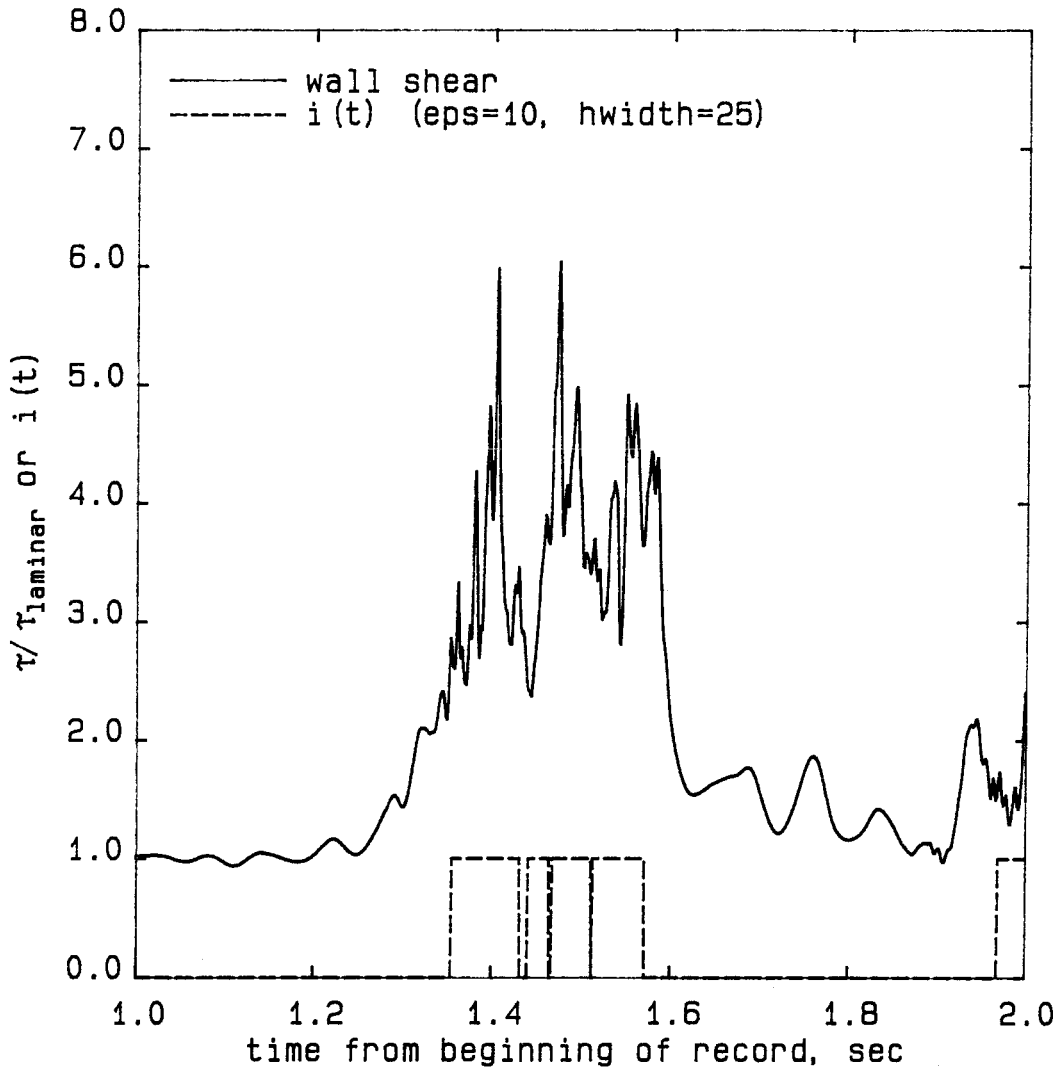


Figure C.5: Comparison of Intermittency Computation Procedures
20Hz 3 degree oblique waves, 192 watts, 4-13a
S8, $Re_{\delta^*} = 1750$
'eps' and 'hwidth' are cutoff and smoothing parameters

windowed data, overlapped as described in the reference, in order to get maximum smoothing from the data. The spectral resolution was thus 0.48 Hz. Spectral resolution for other results was generally similar. In some cases longer data records were collected, and in these cases the extra data was generally used to smooth the spectra through further averaging. The amplitudes of the peaks obtained from the spectral program were checked against those expected for a sample computer generated sine wave signal.

It was necessary to compute the amount of power present in the spectral peaks automatically because of the large amount of data collected. For the plots of spectral power, the data was first analyzed using the power spectral routine described above. Another program then searched the spectral data for peaks that might be present near specific frequencies of interest. The location of the peak was found by interpolation around a local maximum in the spectral points, using a method proposed by Hildebrand [15, p. 75]. The program integrated the amount of power present over a specified bandwidth near the peak. This bandwidth was selected based on the parameters used in the spectral computation. The resulting peak power was not sensitive to the bandwidth selected, due to the spiky nature of the forced spectra; the amount of power outside a narrow region around the peak is small. The program decided if the amount present was significantly above the local background, using an arbitrary criterion based on visual examination of the spectra. The same criterion was used for all spectra in which the parameters for spectral computation were the same. Small changes in the criterion had little effect on the results.